Alma Mater Studiorum · Università di Bologna

Scuola di Scienze
Dipartimento di Astrofisica e Cosmologia
Corso di Laurea Magistrale in Astrofisica e Cosmologia

The innermost regions of the Seyfert 2 galaxies NGC613 and NGC1808: the X-ray and millimeter view

Relatore:
Prof. Cristian Vignali

Correlatori:
Dr.ssa Viviana Casasola
Dr. Mauro Dadina

Presentata da:
Elisa Romandini

Sessione IV
A. A. 2019/2020

Per aspera sic itur
ad astra...

Abstract

One of the goals of modern astrophysics concerns the formation and the evolution of super massive black holes (SMBHs), which interact with their host galaxies in a the so-called co-evolution scenario. The accretion process of SMBH is characterized by intense energy production and represents a key phase of their evolution. This accretion phenomenon inside active galactic nuclei (AGN) can be associated with large obscuration that makes them difficult to be studied. This fact is amplified at high redshift, where there is a larger quantity of gas available.

Starting from the observed obscuration and hence from the width of the lines detected in optical spectra, AGN are subdivided into two main classes: Type 1 and Type 2. In the X-ray band, they are classified as unobscured and obscured, respectively. X-rays offer a unique tool to study the properties of the obscuring material since, given their penetrating power, they are able to pierce the absorbing structures allowing the study of the central engine of Type 2 AGN.

One of the main goals of this Thesis is to verify whether the gas traced by the CO transitions in millimeter band can be considered responsible for the obscuration measured in X-ray observations. This multi-band analysis could give information on the characteristic scales where AGN obscuration occurs. In particular, we carried out the multi-frequency study of the local galaxies NGC613 (z = 0.0049) and NGC1808 (z = 0.0033), which belong to the Seyfert 2 galaxies class. These two sources were selected from the sample of 7 galaxies, analyzed in Combes et al. 2019, where a comprehensive study of the morphological and kinematics properties of the molecular torus was carried out. Our selection was based on the available data: since NGC613 and NGC1808 have both been observed with *Chandra* and XMM-*Newton*, in the X-ray band, and ALMA, in the millimeter band, they represent an ideal benchmark for multi-wavelengths analyses. We are interested, in particular, in the study of their obscuring medium (likely associated with the torus) by comparing the properties as obtained in the millimetric band with those derived in X-rays band.

The X-ray spectral analysis of the sources were carried on in the energy bands $0.3-7.0$ keV (*Chandra)* and $0.3-10$ keV (XMM-*Newton*). The combination of the data from these two satellites allows us to study not only the main features of the obscuring molecular torus, but also the underlying AGN continuum emission and estimate its intrinsic luminosity. The higher resolution (FWHM$\sim 0.5''$) granted by *Chandra* allows us to identify the nuclear emission in both sources, which are characterized also by the extended emission, being quite prominent in NGC1808.

From the studies of light curves no variability was found within the individual X-ray observations over timescales of the observations ($42-49$ ks for NGC613, and $3-43$ ks for NGC1808). Moreover, comparing the fluxes, for the two X-ray datasets, we found no significant variability for long-term timescales of ~ 4 yr and ~ 8 months, for NGC613 and NGC1808, respectively. The X-ray spectral analysis was carried out using different approaches for the two sources, in virtue of their different number of spectral counts.

For the spectral study of NGC613, both the phenomenological models, which provide the general properties of the galaxy emission, and the X-ray physically motivated models (`MYTorus` and `borus02`), which allow for a better characterization of the intrinsic physical and geometric properties of the obscuring torus, were adopted. The physically motivated

models are based on Monte-Carlo codes that simulate the structure of the obscuring material and its interaction with the radiation. `MYTorus` distinguish among the l.o.s. column density and the average one and assumes a clumpy distribution of obscuring material; `borus02` provides not only the average column density, but also the covering factor, i.e., the half-opening angle of the torus. Moreover, it assumes uniform density for the obscuring material.
The intrinsic absorption along the line of sight of the source is measured through the column density, which was found to be $\sim 3 - 4 \times 10^{23}\ cm^{-2}$, indicating that NGC613 hosts a heavily obscured AGN. By using `MYTorus` model, we obtained a value of the "global average" column density of the torus of $2.9 \times 10^{24}\ cm^{-2}$ for NGC613, indicative of its Compton-thick nature.
The X-ray spectral analysis for NGC1808, thanks to the high angular resolution provided by *Chandra*, was mainly (but not only) focused on the study of the nuclear source region. The intrinsic absorption along the line of sight is found to be $\sim 2 - 3 \times 10^{23}\ cm^{-2}$, i.e., NGC1808 hosts a heavily obscured AGN. We calculated the star formation rate (SFR) ($\sim 5 - 10\ M_{\odot}/yr$) from which we estimated the contribution of the HMXBs to the total X-ray luminosity. This contribution is up to 50-60% in both X-ray datasets.
The galaxies under examination were observed in the millimetric band as well, by using the ALMA (Atacama Large Millimeter/submillimeter Array) interferometer. The high angular resolution and sensibility of this facility allow us to investigate physical and geometrical properties of the obscuring torus (on scales of $\sim pc$) through CO observations, which is a good tracer of the molecular gas. We used data from ALMA Science Archive in Band 7 (345 GHz) which were obtained in Cycle 3 for NGC613 and in Cycle 4 for NGC1808, with an angular resolution of $0.14''$ and $0.30''$, respectively. In particular, we used data of the CO (3–2) emission line, which is emitted at 0.87 mm (345 GHz), in order to obtain an estimate of the column density (N_H) under the assumption of spherical symmetry for the gas. This estimate was calculated by using the CO-to-H_2 conversion factor α_{CO}; a univocal value of α_{CO} for NGC613 and NGC1808 is not known (as for many galaxies), hence we used two reasonable values: $\alpha_{CO} = 0.8\ (K\ km\ s^{-1}\ pc^2)^{-1}$ and $\alpha_{CO} = 3.2\ (K\ km\ s^{-1}\ pc^2)^{-1}$, corresponding to typical values for ultra-luminous infrared galaxies (ULIRGs) and for spiral galaxies, respectively. In this way, we obtained a range of possible values for N_H, to be compared with the those obtained from X-ray spectral analyses. We obtain agreement between ALMA data and X-ray ones by using `MYTorus` models, which assume a *clumpy* distribution of the obscuring material. We then conclude that the most plausible geometry of the molecular torus is patchy, instead of uniform and doughnut-like, for both sources.

Sommario

Uno dei propositi dell'astrofisica moderna è la comprensione della formazione e dell'evoluzione dei buchi neri super massivi (SMBHs), che convivono e interagiscono con la galassia ospite in uno scenario così detto di co-evoluzione. Il processo di accrescimento di materiale sul SMBH, caratterizzato da un'intensa produzione di energia, rappresenta una fase chiave della loro evoluzione. Spesso questa fase di forte accrescimento all'interno dei nuclei galattici attivi (AGN) è legata ad un alto oscuramento che ne rende difficoltoso lo studio, in particolare ad alto redshift, dove sono presenti grandi quantità di gas.
In base all'oscuramento osservato, e quindi alla largezza delle righe osservate negli spettri ottici, gli AGN vengono suddivisi in due classi principali: Tipo 1 e Tipo 2. In banda X, gli AGN di Tipo 1 e 2 vengono identificati rispettivamente come non oscurati e oscurati. I raggi X offrono uno strumento unico per studiare le proprietà del materiale oscurante poiché, dato il loro potere penetrante, sono in grado di attraversare le strutture assorbenti permettendo lo studio del motore centrale degli AGN di Tipo 2.
Uno degli scopi principali di questo lavoro di Tesi è verificare se il gas tracciato dalle transizioni CO nella banda millimetrica possa considerarsi responsabile per l'oscuramento misurato nelle osservazioni X. Questa analisi multibanda può dare informazioni sulle scale caratteristiche alle quali avviene l'oscuramento degli AGN. In particolare, abbiamo condotto uno studio multifrequenza delle galassie locali NGC613 (z = 0.0049) e NGC1808 (z = 0.0033), appartenenti alla classe delle galassie Seyfert 2. Queste due sorgenti sono state selezionate da un campione di 7 galassie analizzate in Combes et al.(2019) dove è stato svolto uno studio approfondito delle proprietà morfologiche e cinematiche dei tori molecolari. La nostra scelta si è basata sui dati a disposizione: visto che sia NGC613 che NGC1808 sono state osservate con *Chandra* e XMM-*Newton* nella banda X e ALMA nella banda millimetrica, esse rappresentano un banco di prova ideale per l'analisi multifrequenza. In particolare, siamo interessati allo studio del loro materiale oscurante (presumibilmente associato al toro) comparando le proprietà ottenute in banda millimetrica con quelle ricavate in banda X.
L'analisi spettrale in banda X delle sorgenti viene effettutata nelle bande $0.3 - 7.0$ keV (*Chandra*) e $0.3 - 10$ keV (XMM-*Newton*). La combinazione di questi due strumenti ci permette di studiare non solo le proprietà principali del toro molecolare oscurante, ma anche l'emissione del continuo sottostante dell'AGN e stimare la sua luminosità intrinseca. Inoltre, grazie alla miglior risoluzione angolare di *Chandra* (FWHM$\sim 0.5''$), abbiamo potuto identificare l'emissione nucleare in entrambe le sorgenti, che sono caratterizzate anche da emissione estesa, particolarmente prominente in NGC1808.

Dagli studi delle curve di luce non è stata trovata variabilità nelle singole osservazioni X considerando i loro tempi scala ($42-49$ ks per NGC613 e $3-43$ ks per NGC1808). Inoltre, comparando i flussi per i due datasets X abbiamo dedotto che entrambe le sorgenti non mostrano variabilità nemmeno su tempi scala lunghi di ~ 4 anni per NGC613 e ~ 8 mesi per NGC1808. L'analisi spettrale è stata condotta utilizzando differenti approcci per le due sorgenti, in virtu del loro numero di conteggi differente.

Per lo studio spettrale di NGC613 sono stati adotatti sia i modelli fenomenologici, che forniscono le proprietà generali dell'emissione della galassia, sia i modelli fisicamente motivati

(`MYTorus` e `borus02`), i quali forniscono una migliore caratterizzazione delle proprietà fisiche e geometriche intrinseche del toro oscurante. I modelli fisicamente motivati (`MYTorus` e `borus02`) sfruttano codici di Monte-Carlo per simulare la struttura del materiale oscurante e l'interazione con la radiazione. `MYTorus` distingue tra la densità di colonna lungo la linea di vista e quella media, assumento una distribuzione non omogenea del materiale oscurante; `borus02` fornisce non solo la densità di colonna media, ma anche il covering factor, cioè l'angolo di mezza-apertura del toro. Inoltre assume densità uniforme per il materiale oscurante.

La quantità di assorbimento intrinseco lungo la linea di vista della sorgente viene misurata attraverso la densità di colonna, che risulta essere circa $3-4\times10^{23}\ cm^{-2}$, indice del fatto che NGC613 ospita un AGN molto oscurato. Utilizzando il modello `MYTorus`, abbiamo ottenuto un valore della densità media del toro dell'ordine di $2.9\times10^{24}\ cm^{-2}$ per NGC613, indicativo della natura Compton-thick del toro oscurante.

L'analisi spettrale in banda X di NGC1808, grazie all'alta risoluzione angolare fornita da *Chandra*, si è concentrata principalmente (ma non solo) sullo studio della regione nucleare della sorgente. La quantità di assorbimento intrinseco lungo la linea di vista risulta essere circa $2-3\times10^{23}\ cm^{-2}$; NGC1808 ospita un AGN molto oscurato. Al fine di andare a determinare la luminosità X fornita dalla sola componente nucleare, abbiamo calcolato il tasso di formazione stellare (SFR) ($\sim 5-10\ M_{\odot}/yr$) dal quale abbiamo stimato il contributo delle HMXBs alla luminosità X totale che risulta essere al più del 50-60%, in entrambi i datasets X.
Entrambe le galassie in esame sono state osservate anche in banda millimentrica con l'interferometro ALMA (Atacama Large Millimeter/submillimeter Array). L'alta risoluzione angolare e l'alta sensisbilità offerte dai dati ALMA permettono di indagare le proprietà fisiche e geometriche del toro oscurante (su scale dell'ordine del pc) attraverso l'osservazione del CO, tracciante del gas molecolare. Abbiamo usato i dati dell'archivio ALMA in Banda 7 (345 GHz) che sono stati ottenuti nel Ciclo 3 per NGC613 e nel Ciclo 4 per NGC1808, con risoluzioni angolari rispettive di $0.14''$ e $0.30''$. In particolare, abbiamo utilizzato i dati della riga CO(3–2) emessa a $0.87\ mm$ (345 GHz) per stimare la densità di colonna (N_H), con l'assunzione di simmetria sferica per il gas. Questa stima è stata calcolata utilizzando il fattore di conversione CO-to-H_2 α_{CO}; non sono noti valori univoci di α_{CO} per NGC613 e NGC1808 (così come per molte galassie), così abbiamo usato due valori ragionevoli: $\alpha_{CO}=0.8(K\ km\ s^{-1}\ pc^2)^{-1}$ e $\alpha_{CO}=3.2(K\ km\ s^{-1}\ pc^2)^{-1}$ che corrispondono rispettivemente a valori tipici per ultra-luminous infrared galaxies (ULIRGs) e per galassie a spirale. In questo modo abbiamo ottenuto un intervallo di valoti possibili per N_H da comparare con i valori ottenuti nelle analisi spettrali X. Si noti che otteniamo un buon accordo tra i dati ALMA e X usando i modelli `MYTorus` che assumono una distribuzione disomogenea per il materiale oscurante. Abbiamo quindi concluso che la geometria più plausibile del toro molecolare è quella irregolare per entrambe le sorgenti, rispetto a quella a ciambella uniforme.

Contents

Chapter 1

Active Galactic Nuclei

Introduction

Almost every galaxy hosts a *Super Massive Black Hole* (SMBH) of mass in the range $10^6 - 10^{10}$ $M_\odot$ (Ferrarese et al. 2000). A few up to 10% of them are *active*: a galaxy is defined active if its nuclear emission can be attributed to physical processes of non-stellar origin. In such a case, we say that the galaxy is hosting an *Active Galactic Nucleus* (AGN) and its bolometric luminosity can reach values up to $L \sim 10^{14-15}$ $L_\odot$ (e.g., Woo et al. 2002).
AGN are interesting, energetic and powerful objects in the Universe and they represent one of the best example of matter to energy converter. The radiation of AGN covers the entire electromagnetic spectrum, from radio to gamma rays. Thus, in order to study the complex physical processes that concern AGN, it is necessary to carry out multi-band studies.

1.1 The structure of AGN

In this section we will introduce the main structures that define an AGN: the central SMBH, its accretion disc, the hot corona, the molecular torus, the jets and Broad and Narrow Line Regions. In Fig. 1.1, we report the previously described AGN components as a function of the distance from the SMBH.

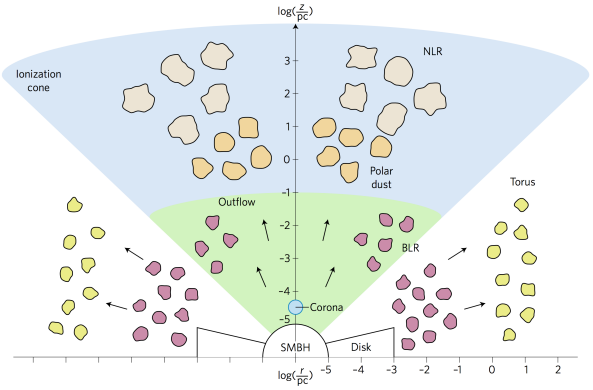

Figure 1.1: Schematic representation of the AGN structure and the main components, from the SMBH to the outer NLR (from Ramos Almeida & Ricci 2017).

Super Massive Black Hole

One of the evidences of the presence of a SMBH in the center of an AGN is given by the combination of two facts (e.g., Ho et al. 2000): they emit high quantities of energy ($L \sim 10^{40} - 10^{46}\ erg/s$) from their central regions and the nuclear luminosities may be comparable or even larger than the one of the whole galaxy itself; the AGN dimensions must be very small since their emission varies on very short time scales (of the order of some minutes-days, e.g., Pacholczyk et al. 1994). This is know as *Black Hole paradigm* (e.g., Ho et al. 2000). Therefore, SMBH have been considered the most likely driving powers of the activity in AGN sources (e.g., Ho et al. 2000). These indications are suggestive of the high efficiency of the energy production mechanism in AGN. The accreting gas surrounding the SMBH, loosing angular momentum, tends to fall inward onto the SMBH with a mass accretion rate $\dot{M} = dM/dt$. The total energy released by this accretion is given by:

$$L_{acc} = \eta \dot{M} c^2 \ , \tag{1.1}$$

where c is the speed of light in vacuum and η is the mass-to-energy conversion efficiency.
The defining feature of a black hole is the *event horizon*, i.e., a boundary in the space-time through which nothing, not even light, can escape from it. This means that if an event occurs within the boundary, information from that event cannot reach an outside observer, making it impossible to determine whether such an event occurred. It is possible to define the *Schwarzschild radius*, i.e., the radius of the event horizon of a Schwarzschild black hole and for a BH of a given mass M_{BH} we have:

$$r_S = \frac{2GM_{BH}}{c^2} \ = 3 \times 10^{13} M_8 \ cm \ , \tag{1.2}$$

where G is the universal gravitational constant and M_8 is the BH mass in units of $10^8\ M_\odot$. In addition to the Schwarzschild radius, we can introduce another scale length, the *gravitational radius* $r_g = r_S/2$.

Accretion disk

AGN represent one of astrophysical laboratory to study accretion processes (e.g., Reynolds et al. 2005). As stated above, the large luminosities observed in these objects are due to the efficient conversion of gravitational energy into radiation in the accretion disk surrounding the central SMBH.
The accreting gas surrounding the black hole forms two different kinds of disk: the *Shakura-Sunyaev Disk* (SSD) (Shakura & Sunyaev 1973) and the *Advection Dominated Accretion Flow* (ADAF) (Narayan & Yi 1994, Abramowicz et al. 1994, Chen et al. 1995, Ichimaru 1977). The first is a geometrically thin, optically thick disc with a temperature of $T \sim 10^5\ K$ and emits as a *multi-color black body* (e.g., Mitsuda et al. 1984). This means that the disc emission is considered as a superposition of black body emissions with different temperatures, with an emission peak in UV band. SSD is associated with efficient and high-luminosity accreting AGN.
ADAF is a geometrically thick, optically thin accretion disk with a temperature of $T \sim 10^9\ K$ and emits thermal radiation, often with a high energy Compton radiation. It is often associated with low-efficiency AGN (with respect to SSD's).

Assuming a gas of fully ionized hydrogen with spherical symmetry distribution, the forces acting on it are, in first approximation, the force of the pressure radiation F_{rad} and the gravitational force F_g. The radiation force is defined by

$$F_{rad} = \frac{\sigma_T L}{4\pi r^2 c} \ , \tag{1.3}$$

where σ_T is the Thompson cross-section, L is the luminosity and r is the radial distance from the central BH.
Competing with F_{rad} there is the gravitational force, which pulls the gas towards the center of the system and is defined by

$$F_g \simeq \frac{GM_{BH}m_p}{r^2} \ , \tag{1.4}$$

where m_p is the proton mass and where the mass of the electron has been neglected.
An upper limit for the luminosity for the accretion disc of a black hole of mass M_{BH} is given by the Eddington luminosity L_{Edd}. This luminosity is reached when the radiation pressure balances the gravitational pull of the black hole, so we have

$$F_{rad} \leq F_g \ \rightarrow \ L \leq L_{Edd} = \frac{4\pi M_{BH} m_p c}{\sigma_T} \simeq 1.26 \times 10^{38} \left(\frac{M_{BH}}{M_\odot}\right) \ erg/s \ . \tag{1.5}$$

Therefore, the Eddington Luminosity imposes a limit on the amount of matter per time unit that fall in the BH, as it follows from equation (1.1):

$$\dot{M}_{Edd} = \frac{L_{Edd}}{\eta c^2} \ . \tag{1.6}$$

η can be expressed in terms of the *compactness* of the accreting object, namely the ratio M_{BH}/R_{ISCO}, as:

$$\eta = \frac{GM_{BH}}{R_{ISCO}c^2} = \frac{R_s}{2R_{ISCO}} \ , \tag{1.7}$$

where R_{ISCO} is the radius of the *Innermost Stable Circular Orbit* (ISCO), i.e., is the last stable circular orbit beyond which a particle will fall onto the BH. For a non-spinning black hole, we have:

$$R_{ISCO} = \frac{6GM_{BH}}{c^2} \ . \tag{1.8}$$

Typically, $\eta \sim 0.1$ (e.g., Raimundo et al. 2011) but theoretically it can reach values of 0.42 (to be compared, for example, with $\eta \sim 0.007$ of proton-proton chain reaction in stars) for Kerr BH with $a = 1$ (e.g., Davis et al. 2011).

Hot corona

The production of X-rays in AGN is thought to occur in a *hot corona* via thermal Comptonization of seed UV-photons. The most striking evidence of the existence of such structure is most probably the detection of a high-energy cut-off in the spectra of nearby Seyferts (e.g., Zdiarzky et al. 1995, Perola et al. 2000, Dadina 2007 and 2008) and, in recent years, also in distant quasar (e.g., Dadina et al. 2016, Lanzuisi et al. 2020). According to *two-phase model*, originally proposed by Liang (1979), and revived by Haardt & Maraschi (1991) and

(1993), X-rays are produced via Compton up-scattering of seed UV-photons by means of a corona made of electrons at high temperature. In this process a high energy cut-off corresponding to a fraction of the temperature of the plasma is impressed in the outgoing X-ray spectra (e.g., Petrucci et al. 2001, Fabian et al. 2015).
The geometry of the Comptonizing corona generating the primary powerlaw-like continuum has been considered in various ways. Haardt & Maraschi (1991) suggested a simple model, where a uniform plane corona "sandwiches" the accretion disc. In the disc-corona scenario, the inner region of an AGN is essentially composed by two phases: a hot, optically thin, X-ray-emitting corona, located above a cold, optically thick, UV-emitting accretion disc.

Broad Line Region

One of the most common signatures of activity in a galactic nucleus is the presence of broad emission lines, originated into *Broad Line Regions* (BLRs), with *Full Width at Half Maximum* (FWHM) corresponding to the velocity range $10^3 - 10^4$ km/s (e.g., Laor 2003). Since the electron densities are sufficiently high, all the forbidden lines are suppressed by collision, therefore the BLR emits only the permitted lines. The absence of broad forbidden lines indicates that the density of the matter responsible for the emission of the broad lines should be high enough ($n \sim 10^{9-10}$ cm^{-3}, e.g., Laor 2003) to suppress, via collisional up-ionization, the productions of such lines.
The BLR is a region located beyond the accretion disk, approximately 0.1−1 pc from the center of the system. This structure is composed of cold ($T \sim 10^4$ K), high density clouds (e.g., Laor 2003). BLRs lay deep inside the gravitational spheres of influence of SMBHs and their kinematics is strictly connected to the mass of the black holes, so they offer a precious insight of the physical properties of the inner circum-nuclear medium.

Molecular torus

The presence of a molecular torus was postulated by Antonucci (1993) to explain the variety of AGN classification and, in particular, the differences observed among Type 1 (unobscured) and Type 2 (obscured) AGN.
The molecular torus surrounding the central engine of AGN consists of molecular gas and dust (e.g., Pier & Krolik 1993). It is expected to have an absorption column density higher than 10^{24-25} cm^{-2} (e.g., Netzer 2013), it is extended for $1 - 100$ pc at distances about $1 - 30$ pc by the central AGN (e.g. Jaffe et al. 2004, Hickox & Alexander 2018) and has densities ranging from 10^4 to 10^6 particles per cm^3.
From the historical point of view, the simplest structure of torus was first described as a smooth homogeneous and doughnut-like distribution (e.g., Krolik & Begelman 1988) of dust. In this description, the darkening of the source depends only on the geometry of the torus, i.e., it results to be obscured if its radiation intercepts the obscuring material.
More elaborated structures, made of clumps and inter-clump material, are preferred by observations (e.g., Nenkova et al. 2002, Jaffe et al. 2004, Tristram & Schartmann 2011, Burtscher et al. 2013). The observations suggest that tori are irregular and formed by clumps and dust between them (e.g., Combes et al. 2019). The gas in the inner radius of the torus is ionized by the central source. In this region, the torus contains dusty molecular gas; the temperature is not homogeneous, given a certain line of sight (l.o.s.), since the

illuminated part of the clumps is hotter than the one further from the central source, hence they radiates differently. This model is called *clumpy (or patchy) torus* (e.g., Almeida et al. 2009).

Narrow Line Region

The *Narrow Line Region* (NLR) is located at a distance from the AGN that may vary from ~ 10 *pc* to ~ 1 *kpc*. The typical density of clouds of the NLR is $10^3 - 10^6$ cm^{-3}, then the gas can emit forbidden lines; the gas velocity is $300 - 1000$ km/s (e.g., Bennert et al. 2002). Since the density in the NLR is lower than the one in the BRL, the NLR must be much larger than the BLR in order to be not transparent for the incoming radiation. This determines the boundary of the region of direct influence of the AGN. Low density and hot ($T \sim 10^4$ K) gas in this extended region is ionized by high-energy photons from the inner AGN regions (e.g., Bennert et al. 2002). The ionized NLR gas can be anisotropically distributed in an *ionization cone*, because of the doughnut-like geometry of the central regions (e.g., Das et al. 2006).
The NLR is resolved by ground-based observations in several AGN in the local Universe, showing dimensions of 100 *pc* to scales of some *kpc* (e.g., Rice et al. 2005).

Jets

Relativistic plasma jets are present in less than 10% of AGN (e.g., Kellermann et al. 1989). They are observed typically in *Radio-Loud* AGN and extend over distances of Mpc with (apparently) superluminal motions. These jets are extremely collimated outflows, with its base perpendicular to the plane of the disc, of high-energy charged particles produced in the inner region of the AGN. These particles emit from radio to γ-rays band and the main emission mechanisms are synchrotron radiation and Inverse Compton (IC) (e.g., Blandford & Znajek 1977, Blandford & Payne 1982). One of the most accredited model is that of the *magnetic tower*, in which the plasma is expelled by means of a dynamo effect produced by the rotating material (e.g., Lebedev et al. 2005). The simulations show that relativistic jets would be generated in the presence of magnetic field in the accretion disk. Since the accretion disk rotates differentially, it generates a magnetic field around which the jet spirals, directed towards the hot corona (e.g., Lebedev et al. 2005). Therefore, the generation of relativistic jets seems to depend in first approximation by the presence of strong magnetic fields that originate in the accretion disk and from the spin of a BH.
Jets interact with the surrounding environment, sometimes creating lobes and hot spots that emit mainly in the radio band.

1.2 AGN classification

The classification of AGN is still an open topic: it is indeed difficult to reconcile the different phenomena of this type, observed at very different wavelengths, in a single classification.
Historically, the first to recognize the existence of some objects that could not be categorized as standard galaxies was C. Seyfert, in 1943 (Seyfert 1943). Their spectra showed broad emission lines, up to hundreds of kilometers per second, with high excitation and very high luminosity. These objects were named of *Seyfert galaxies*. In the fifties, the first surveys in the radio band identified sources that in the optical band were catalogued as galaxies or stellar-like sources, but which showed unknown emission lines. These lines were then identified as already known lines, but strongly redshifted (Schmidt 1963). Since the nature of these objects was not understood at that time, they took the name of *quasars* (QUASi-stellAR radio sources).
The classification of AGN in the literature is very diversified and depends also on the observation band, hence it is not unique. Another factor that makes the classification of AGN difficult is the possible presence of an obscuring torus that makes it difficult to determine the intrinsic characteristics of the AGN (e.g., Antonucci 1993, Urry & Padovani 1995, Netzer 2015).
The peculiar features usually present in AGN, not necessary at the same time, are (e.g., Netzer 2013):

- AGN contain a compact nuclear region with higher emission than expected from stellar processes typical of the galaxies;
- they show line and/or continuum variability, especially in the X-ray band;
- they have unresolved nuclei with small angular sizes;
- their nuclear emission often dominates the galaxy emission, over a wide portion of the electromagnetic spectrum;
- their nuclear emission shows a high level of polarization with respect to normal galaxies;
- many AGN, not all, have very intense emission lines not common to normal galaxies.

We now briefly describe the main classes of AGN.

1.2.1 Radio classification

One of the common ways to provide a classification of AGN is based on radio emission, in particular on the ratio R_{r-o} of the rest frame flux density in the 5 GHz radio band and that in the optical band at 4400 Å (e.g., Kellermann et al. 1989). AGN with $R_{r-o} > 10$ are defined as *Radio-Loud*, while those with $R_{r-o} < 10$ as *Radio-Quiet* (e.g., Schmidt et al. 1970, Kellermann et al. 1989).
However, there are other quantities that may allow to discriminate radio-loud from radio-quiet AGN, such as the relationship between radio band and X-ray band brightness (e.g., Terashima & Wilson 2003). This is not affected by extinction due to dust (typically present in the optical and ultraviolet emission), therefore it can provide solid information on the

radio dichotomy presented. This ratio discriminates between radio-quiet and radio-loud sources as follows:

$$\log\left(\frac{\nu L_{\nu\ 5\ GHz}}{L_{2-10\ keV}}\right)\begin{cases} > -4.5 & \Longrightarrow \quad \text{Radio-Loud ,} \\ < -4.5 & \Longrightarrow \quad \text{Radio-Quiet .} \end{cases}$$

However, this classification turned out to be obsolete (e.g., Padovani et al. 2017), as these objects do not only present an observational difference but also, and above all, intrinsic and physical ones. Radio-Loud AGN emit most of their energy with non-thermal mechanisms, associated with the presence of powerful relativistic jets, while the multi-frequency emission of Radio-Quiet AGN is dominated by thermal emission, proper of the accretion disk, without jets. Therefore, a more appropriate classification should distinguish among *jetted* and *non-jetted* AGN, depending on the presence or absence of relativistic jets.
Another classification was given by Fanaroff & Riley (1974) according to the morphology and emission power of the radio galaxy. They divided radio galaxies into two classes, using the ratio of the distance between the regions of highest surface brightness on opposite sides of the central galaxy to the total extent of the source up to the lowest brightness contour: *Fanaroff-Riley I* (FRI) and *Fanaroff-Riley II* (FRII).
The former are sources whose luminosity decreases as the distance from the central galaxy increases and the jets emission is dominant with respect to that of the lobes. FRI have a power $P_{1.4GHz} < 10^{24.5}\ W/Hz$. FRII exhibit increasing luminosity in the lobes which dominate the emission. FRII have a power $P_{1.4GHz} > 10^{24.5}\ W/Hz$. This morphology reflects the efficiency in transporting energy in the two sources: FRII have jets that are able to transport much energy at the end of the lobes, while the FRI have an higher dispersion (e.g., Ledlow & Owen 1996).
A further classification is based on the presence (or absence) of high excitation emission lines. An *High-Excitation Galaxy* (HEG) is an AGN which presents these emission lines and has efficient accretion properties ($0.01 < L/L_{Edd} < 1$). AGN not presenting those lines are *Low-Excitation Galaxies* (LEG): they appear to have redder optical colors and are characterized by inefficient accretion around the black hole due to a low ratio L/L_{Edd} (e.g., Hine & Longair 1979).

1.2.2 Optical classification

From an optical point of view, AGN are classified on the basis of their spectral characteristics. In particular, if the source shows both narrow lines (up to $\sim 10^3\ km/s$) and broad lines (up to $\sim 10^4\ km/s$) and has a spectrum with a very bright continuum, it is classified as *Type 1* AGN. Broad and narrow emission lines are generated in the BLR and NLR, respectively. If both line types are present, the AGN is not obscured and, accordingly with the *Unified Model* of AGN, we are looking it directly in the nuclear region.
If there are only narrow lines and a faint continuum, the AGN is classified *Type 2*. In the framework of Unified Model of AGN, the fact that only narrow lines are observed means that the AGN is obscured by the molecular torus and therefore there is darkening along the l.o.s. and the BLR is obscured.

1.3 Unified Model

The unification of the wide range of objects described so far under a single classification, using a few fundamental parameters, is a very important goal in the study and understanding of AGN. The *Unified Model*, as developed today (e.g., Antonucci 1993, Urry & Padovani 1995, Bianchi et al. 2012), proposes that the various types of AGN are actually a single type of object observed at different angles of view, hence with a different contribution of the dusty torus. The only intrinsic difference is the presence of powerful radiojets. In Fig. 1.2, we note the intrinsic division of AGN into two large groups: AGN with and without jets.
For each of these families of objects the same differentiation is applicable based on the inclination of the AGN. If, on the one hand, the plane of the AGN is almost perpendicular to the l.o.s., then the AGN is not obscured by the dusty torus and it is possible to observe the central regions with wide lines (BLRG and Seyfert 1, or Type 1 AGN).
On the other hand, if the plane of the AGN is placed right along the line of sight, the torus hides the central region, then it is possible to see only the NLR, which produces narrow lines (NRLG and Seyfert 2, or Type 2 AGN). The observed source with an angle within few degrees with respect to the direction of the jets will have the characteristics of *Blazars*, where the jet predominates over all the other components.

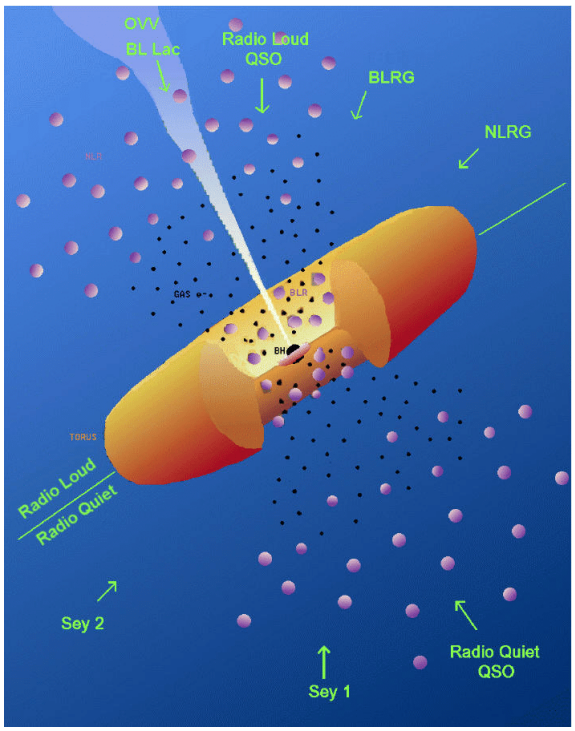

Figure 1.2: Representation of the Unified Model of the AGN. Different classes and subclasses of AGN are represented with respect to the line of sight and the various components of the model. The plane of the disk and the torus of dust is called the AGN plane (adapted by Polletta, from Urry & Padovani 1995).

In Fig. 1.2, the central SMBH is surrounded by an accretion disk of infalling material. The accretion disk is surrounded by a dusty torus. Clouds of gas also extend from the central regions and are divided into the closer and denser BLR and the further and rarefied NLR.

The observed differences in their optical spectra are attributed to different viewing angles: Type 1, i.e., unobscured AGN, are nearly face-on objects, and the nucleus can be directly seen; Type 2, i.e., obscured AGN, have larger angles, thus the line of sight intercepts the obscuring medium surrounding the nucleus.

1.4 Multi-wavelength properties of AGN

AGN emission covers the entire electromagnetic spectrum and a typical *Spectral Energy Distribution* (SED) is shown in Fig. 1.3. Each band of spectrum has peculiar and different emission processes, which will be described in this section. In particular, we will focus on the X-ray band which is crucial for the study of nuclear regions of an AGN, the main topic of this Thesis.

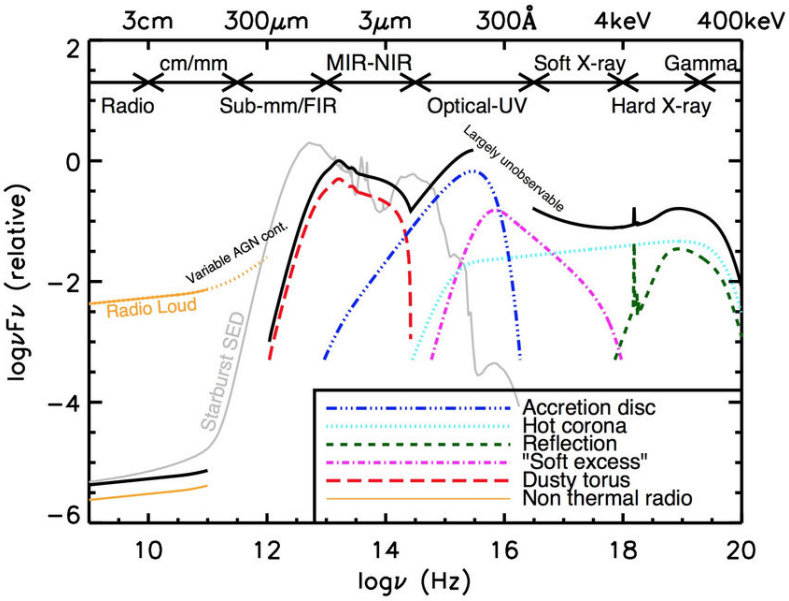

Figure 1.3: A schematic representation of an AGN's SED. The black solid curve represents the total SED and the various colored curves represent the individual components (from Harrison 2014).

Radio Emission

The emission of AGN in the radio band is of non-thermal type, produced by synchrotron emission. The process is due to relativistic electrons, of mass m_e and Lorentz factor γ, which are accelerated by a magnetic field $\mathcal{B}$, hence producing the emission of photons with frequency $\nu \propto \mathcal{B}E^2$, where the energy is calculated as usual $E = \gamma m_e c^2$. Assuming a powerlaw distribution for electrons, we have

$$N(E)dE \propto E^{-\delta}dE \ , \tag{1.9}$$

where $N(E)$ is the number of electrons with energy between E and $E + dE$. We obtained the powerlaw spectrum of the synchrotron emission

$$F_\nu \propto \nu^{-\alpha} \ , \tag{1.10}$$

where $\alpha = \frac{\delta-1}{2}$, represents the spectral index of the energy distribution and typically its value is $\alpha \sim 0.7$.
Equation (1.10) is valid only for $\nu > \nu_c$, where ν_c is called *critical frequency*, and its value depends on the density of the medium and the size of the source. Below this value, electrons reabsorb the low-energy photons emitted, in a process called *self-absorption*. In this case, the synchrotron emission has a pattern of the type: $F_\nu \propto \nu^{2.5}$.
Both Radio-Loud and Radio-Quiet AGN show nuclear point-like radio emission from the compact nucleus (*flat spectrum*); moreover, in the case of AGN Radio-Loud, the predominant radio emission is not the one coming from the central region, but that coming from jets, lobes and hot spots (*steep spectrum*).

Infrared emission

The infrared wavelengths are roughly divided into three bands: Near-Infrared (NIR) $1 - 3\ \mu m$, Middle-Infrared (MIR) $3 - 50\ \mu m$, and Far-Infrared (FIR) $50 - 200\ \mu m$[1].
This subdivision identifies three emission peaks produced by different components. The component closely linked to the AGN shows a peak typically in the range $10 - 20\ \mu m$, corresponding to a temperatures $T < 1000 - 2000\ K$, beyond which the dust sublimes. This is a thermal type emission linked to the absorbed radiation, coming from the inner walls of the dusty torus and/or from the inner BLR clouds directly exposed to the ionizing continuum coming from the central engine. For the Radio-Loud AGN, at these wavelengths, a non-thermal component may also be present, produced by the same synchrotron emission which is present in the radio band.
The other two peaks, at $\sim 1.6\ \mu m$ and $\sim 100\ \mu m$, refer to the stellar emission of the old red stars and to the cold dust present in the host galaxy, respectively. These thermal emission components must be taken into consideration, because they will overlap the AGN emission from the torus.
The infrared emission has an important role in the search and characterization of obscured AGN, as will be explained in the next section.

Optical-UV emission

The main characteristic of the optical/UV emission is an peak, between $\sim$ 300 Å and $\sim$ 3000 Å, called *Big Blue Bump* (BBB) (e.g., Malkan et al. 1982). This emission is the result of the overlap of black body spectra at different temperatures of the accretion disk, which can be approximated with a series of powerlaws (e.g., Malkan et al. 1982).
In addition to the thermal continuum (e.g., Berk et al. 2001, Telfer et al. 2002), in the optical/UV band it is possible to observe the presence of narrow and broad lines coming from the NLR and BLR, respectively. Through the study of these broad lines it is possible to derive the mass of the SMBH using the virial hypothesis and estimate the intrinsic emission of the AGN.

X-ray emission

The X-ray radiation allows to study the more energetic phenomena that take place in the innermost and closest regions to the SMBH. This emission extends from 0.1 keV up to

[1]Notice that actually these ranges may vary in different textbooks and references.

energies of $100 - 300\ keV$ (e.g., Dadina 2008). In Fig. 1.4 we show the typical spectrum of a Type 1 AGN, made of various components.

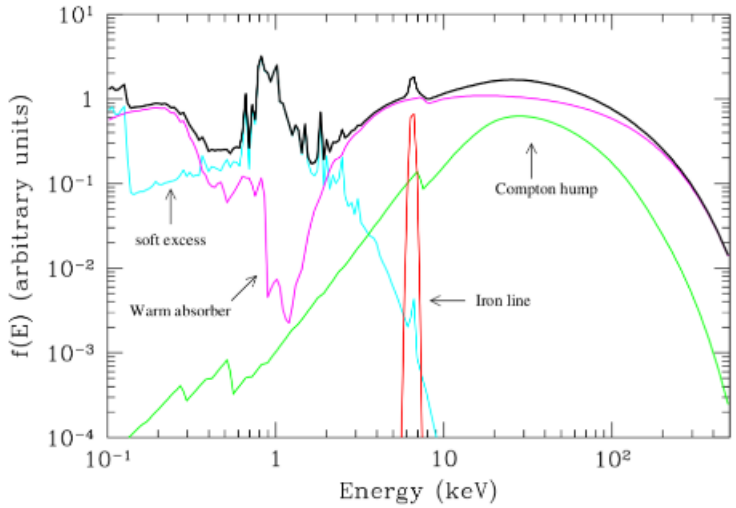

Figure 1.4: Typical spectrum of a Type 1 AGN in X-ray band (from Risaliti & Elvis 2004). The magenta line indicates the powerlaw with the cut-off at $100 - 300\ keV$ plus the presence of warm-absorber; the blue line indicates the soft excess; the green line indicates the Compton hump, which is the reflection component; the red line indicates the fluorescence line of neutral iron at $6.4\ keV$; the black line represents the sum of all the components. All energies are to be considered in the AGN rest reference system.

Primary emission

The main powerlaw component, extended in the range $1 - 300\ keV$, is produced by Inverse Compton processes involving relativistic electrons from the hot corona ($T \sim 10^9\ K$) and thermal photons from the accretion disk ($T \sim 10^{5-6}\ K$). The electrons, being much more energetic, give part of their energy to the thermal photons of the accretion disk, bringing them up to hundreds of keV (e.g., Haardt & Maraschi 1991). Thus, the resulting spectrum is composed by these IC up-scattered photons, which give rise to the primary powerlaw distribution $N((E) \propto E^{-\Gamma}$, where Γ is called *photon index*. Typical values are $\Gamma \approx 1.8 - 2$ (e.g., Risaliti & Elvis 2004).
The exponential drop around $100 - 300\ keV$ occurs when the energy of the photons coming from the accretion disk reaches the same energy as the electrons of the hot corona. This happens since photons have lost a great amount of energy because of numerous scatterings. At this point the electrons cannot transfer more energy to the photons and, consequently, a cut-off in the spectrum is created.

Soft Excess

As already mentioned, soft excess is still a much debated component and is present in almost all AGN spectra. It could be an extension of the Big Blue Bump at high energies (Czerny & Elvis 1987) or a colder part of hot corona which, again for IC, brings the photons from the disk to energies $< 1 - 2\ keV$ (e.g., Boissay et al. 2016). In some AGN, part of this emission can be traced back to emission from the host galaxy, associated with star formation events.

Warm Absorber

It is an absorption component between $1 - 2\ keV$ observed in $\sim 50\%$ of local AGN and quasars (e.g., Blustin et al. 2005, Piconcelli et al. 2005). It has a column density $N_H \sim 10^{21} - 10^{23}\ cm^{-2}$ with a temperature in the range $T \sim 10^4 - 10^5\ K$ (e.g. Kaastra et al. 2000, Ebrero et al. 2016). The material that constitutes the warm absorber is probably in the outflow phase with speeds of $10^2 - 10^3\ km/s$, possibly related to winds with high speeds at the base of the accretion disk (e.g., Tombesi et al. 2013).

Compton Hump

The IC process between photons of the disk and electrons of the hot corona produces photons in an isotropic way. Part of these photons is then reflected on the disk or on the torus, by Compton scattering. The reflected component generates a hump shape, called *Compton hump* (e.g., Ghisellini et al. 1994). This process occurs if the reflecting medium is optically thick, otherwise the photons would pass through it without interacting with the medium itself. This component is mainly characterized by an emission peak at $\sim 30 - 40\ keV$ and by a low energy cut-off between $4 - 5\ keV$, which is caused by photoelectric absorption of the radiation at lower energy.

Iron fluorescent emission line

It is one of the most important features of X-ray spectra. This line is produced by fluorescence mechanisms generated in the accretion disk or in the torus.
If an energetic photon ($E_\gamma > 7.1\ keV$) hits an iron atom, it can extract, by photoelectric effect, an electron in the $K - shell$. Thus, the iron atom goes to an ionized state. At this point, by de-excitation, an electron from the upper levels (M or L shell) moves to occupy the vacancy in the K shell.
If the electron that fills the hole comes from the L shell (the most probable case), a K_α photon of energy 6.4 keV is emitted, while if the electron comes from the M shell a K_β photon of 7.05 keV energy will be emitted. This phenomenon is called *fluorescence*.
If K_α or K_β photons are reabsorbed by an electron from a more external shell, which will be ejected from the atom, the process that takes place is called the *Auger effect*.
The probability that there is emission of a photon K_α versus the emission of an electron due to the Auger effect is given by the *fluorescence yield* Y:

$$Y \propto \frac{Z^4}{Z^4 + const}\ , \tag{1.11}$$

where Z is the atomic number of the element that produces fluorescence. So, the higher the atomic number, the higher the probability of emission of a K_α photon. Iron, with $Z = 26$, is the element with the highest probability of emission by fluorescence, among the most abundant ones. This is the reason for which the K_α emission line of neutral iron at 6.4 keV is so important.
The radiation produced by the hot corona through IC processes is sufficiently energetic to to produce K_α photons. This radiation will be partly reflected by the disk or by the torus, and partly involved in the emission of the iron line. We assume that the iron line is produced in the disc, then several effects are expected on this line (see Fig. 1.5): the profile

of an intrinsically narrow emission line is modified by the interplay of Doppler/Special and General relativity (e.g., Fabian et al. 2000).

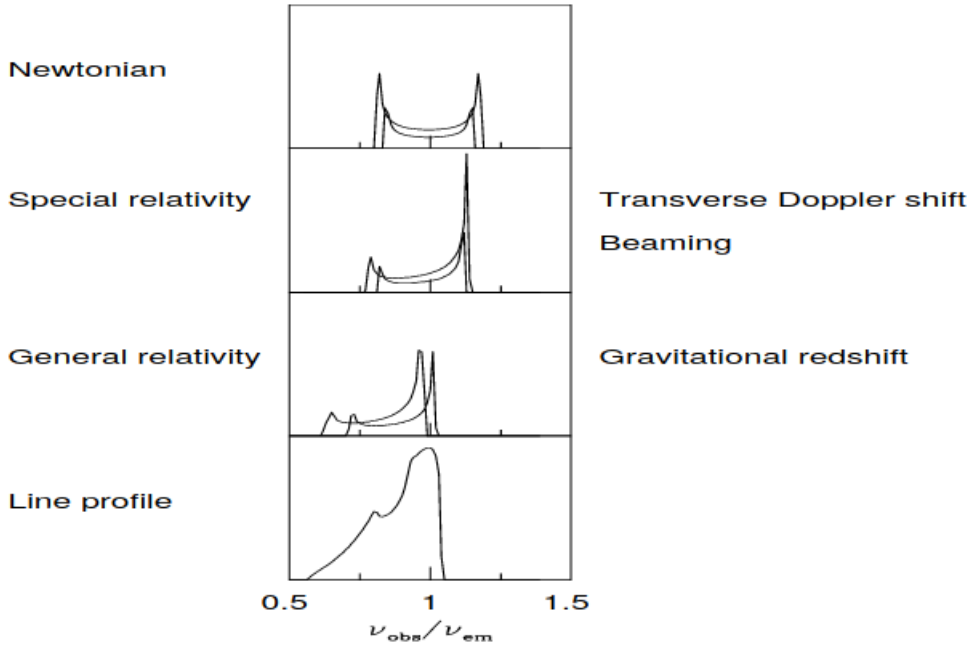

Figure 1.5: Effects expected on the line produced in the accretion disk. In the upper panel we see classic Doppler effect due to the rotating disk; in the second panel the relativistic Doppler effect that amplifies the blue peak and attenuates the red one; in the third panel the effect of gravitational redshift that shifts the line to lower energies. In the lower panel the sum of all contributions is shown (from Fabian & Miniutti 2005).

The iron line is the sum of the contributions of the single iron atoms in the accretion disk; it will have two components: one with positive speed and one with negative speed, with respect to the observer, which will Doppler shift the line towards red and towards blue, respectively, producing the double-peaked profile of the line. This effect produces a classical, or *Newtonian*, deformation of the line.
The effects of amplification of the bluest part of the line and de-amplification of the reddest part must be included. They take the name of *Doppler shift beaming*, due to the relativistic rotation speed of the accretion disk.
Finally, in the regions close to the SMBH the photons are subjected to a high gravitational force. This causes a redshift of the entire profile of the line which takes the name of *gravitational redshift*.

γ-ray emission

The γ band emission is divided into *High Energy* (HE), from $\sim 100\ MeV$ to $\sim 100\ GeV$, and *Very High Energy* (VHE), from $\sim 50\ GeV$ to $\sim 10\ TeV$. This emission is typical for Blazars, that is, for "face-on" AGN in which the l.o.s. intercepts the emission cone of the jet. This configuration of AGN means that jets are strongly amplified by relativistic effects, up to the point of dominating the entire emission. By defining the Doppler Factor as:

$$\delta = [\gamma(1 - \cos\theta)]^{-1} \ , \tag{1.12}$$

where γ is the Lorentz factor and θ is the angle between the axis of the jet and the line of sight. Thus, we find an amplified monochromatic flux of:

$$F_\nu = \delta^{3+\alpha} \; F'_\nu \; , \tag{1.13}$$

where α is the spectral index, F'_ν is the intrinsic flux of the source and F_ν is the observed one, amplified by the value of $\delta^{3+\alpha}$.
The characteristic emission of these objects ranges from radio to γ and shows a characteristic double-peaked emission, called *Blazar sequence* (see Fig. 1.6) (e.g., Fossati et al. 1998, Donato et al. 2001) .

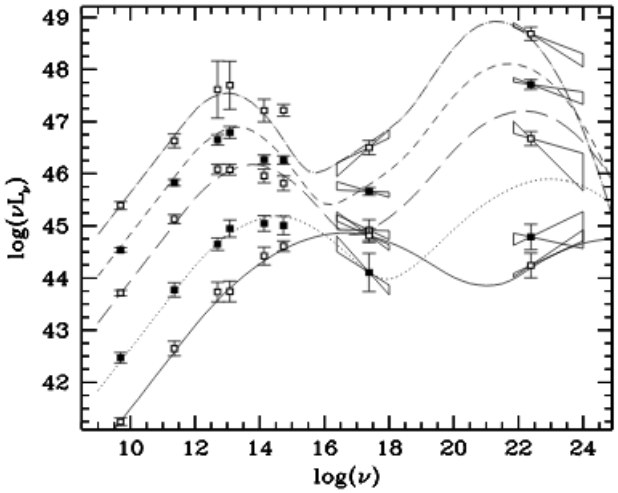

Figure 1.6: Average SED of Blazars with different luminosity (from Fossati et al. 1998).

Blazars can be distinguished in *High* and *Low frequency Blazars* if the second peak falls in the VHE or HE band, respectively. The first peak is due to the synchrotron emission produced by the relativistic electrons of the jet; the second peak can have two origins: via IC, where the electrons of the jet interact with the same photons generated by synchrotron, in a process called *Synchrotron Self Compton* (SSC); via interaction with photons coming from the disk or from external regions, in a process called *External Compton* (EC).

1.5 Obscured AGN

An obscured AGN is an AGN that is partially, or largely, covered by material along the l.o.s. that absorbs the radiation coming from the SMBH activity (e.g., Hickox & Alexander 2018). Obscured AGN are common objects both in the nearby and in the distant Universe. Locally, they are ~ 4 times more numerous than the unobscured ones and this number seems to grow with redshift (e.g., Vito et al. 2014). The most used wavelengths for studying and researching these objects are mid-infrared, optical and X-ray bands.

MIR emission

In the framework of Unified Model (see Section 1.3), we should expect that the optical/UV emission is strongly attenuated in obscured AGN. Within this scenario, in fact, the line of sight intercepts the dusty torus that absorb and thermalize optical/UV photons (e.g., Elitzur 2008). Type 2 objects do not display broad lines and BBB (e.g., Prieto et al. 2009). On the contrary, a strong mid-IR bump is present. Therefore, IR is a fundamental observation band for the study of obscured AGN (e.g., Draine et al. 2003b). The dusty torus has an emission peak between $10 - 20\ \mu m$, which makes the MIR the ideal band for identifying this type of objects (e.g., Netzer et al. 2015, Elitzur et al. 2008), as seen in Section 1.4.
In this band, the AGN emission can be distinguished from the host galaxy emission, even if star forming galaxies (SFGs) can cover or dilute the AGN emission. From a photometric point of view, this problem is tackled by considering the difference between the AGN and the SFGs SEDs, which are very different. Comparing the SEDs, the one of the AGN is more reddened at wavelengths shorter than the MIR (e.g., Shanks et al. 2020), as shown in Fig. 1.7

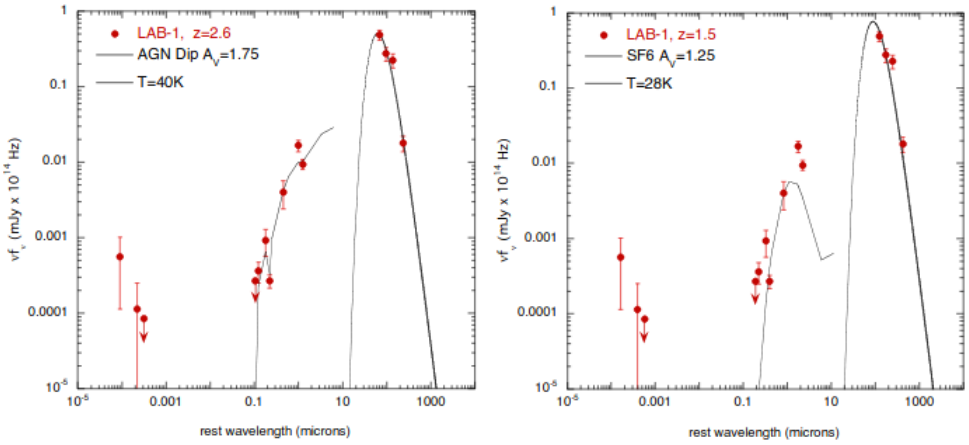

Figure 1.7: SED comparison of best-fitting quasar and star forming galaxy templates; LAB-1 shows weak absorbed X-ray emission and strong FIR emission. Radio emission is not detected. The main fitted parameters were the dust extinction A_V in the optical-NIR, the dust temperature T in the FIR and the redshift z of the two templates. The SED of an AGN is reddened with respect to that of a SFG, as can be verified at wavelengths shorter than the MIR (from Shanks et al. 2020).

The spectroscopy in MIR constitutes a more complete and reliable method for the distinction of obscured AGN by SFGs, due to the low optical depth in this band. In fact,

the environment surrounding the former is hotter than the one surrounding the latter and, consequently, an obscured AGN presents high excitation emission lines such as $[OIV]$ at 25.9 μm, $[NeVI]$ at 7.6 μm and $[NeV]$ at 14.3 μm and 24.3 μm (e.g., Pereira-Santaella et al. 2010).
Spectroscopy is also useful in order to study the *Polycyclic Aromatic Hydrocarbons* (PAHs[2]) emission lines of AGN and SFGs. These lines have a higher FWHM than those with high excitation, hence easier to identify. The PHA lines are less prominant or absent in the presence of high radiation fields. As a first approximation, if the silicate feature Si at 9.7 μm and at 18 μm is in emission we have a Type 1 AGN and if it is in absorption we have a Type 2 (e.g., Draine & Lee 1984).

Optical/NIR emission

The emission in optical/UV band is dominated by the thermal emission of the accretion disk made of the material surrounding the central black hole (see Section 1.4). If this radiation passes through the torus, it can be easily attenuated, since the optical depth τ significantly increases at short wavelengths (e.g., Draine et al. 2003b).
Thanks to spectroscopy in NIR/optical band, Seyfert galaxies have been discovered and AGN have been divided into Type 1 and Type 2 (Weedman et al. 1977). Thanks to the presence of many emission lines, we can build *diagnostic diagrams* that allow to distinguish AGN from others astrophysical sources using intensity line ratios (Baldwin et al. 1981). Diagnostic diagrams, shown in Fig. 1.8, allow to distinguish AGN from others astrophysical sources: the AGN are located in the upper right corner, where the degree of ionization of the gas is higher, while the HII regions are located in the left side and are more concentrated towards the low, in the area with the lowest degree of ionization.

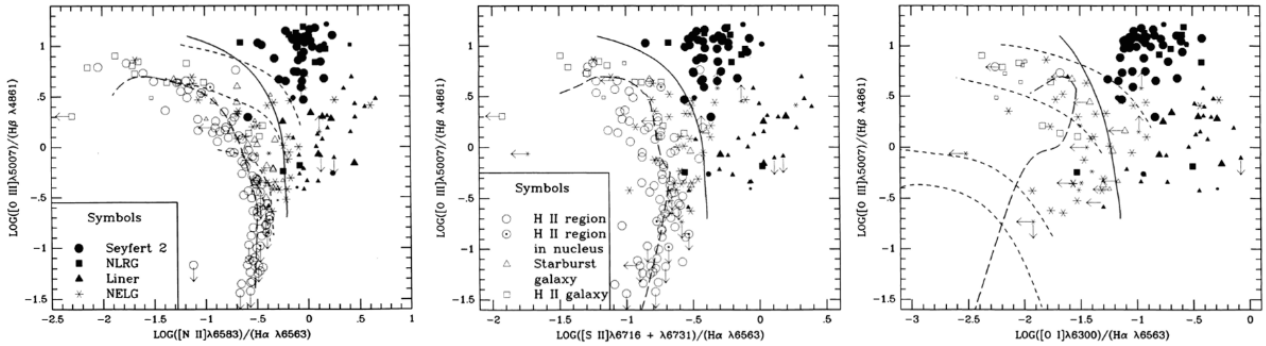

Figure 1.8: Diagnostic diagrams obtained by Veilleux and Osterbrock on a sample of 264 objects. From left to right we observe [OIII]/H_β in relation to [NII]/H_α, [SII]/H_α, [OI]/H_α. The empty symbols represent objects with a similar emission to HII regions, while darker symbols represent AGN. The dashed curves represent HII region models and the solid curve divides AGN from HII region-like objects. (from Veilleux & Osterbrock 1987).

An example is the *Balmer decrement*, based on the intensity of the hydrogen emission lines in different excitation states: from the variation of the ratio between the intensities of the lines, we deduce the amount of darkening. For example, in the ratio H_α/H_β, H_β results to

[2]PAH are molecules composed by carbon and hydrogen, which produce emission lines at MIR wavelengths (e.g., 6.2, 7.7, 8.6 and 11.3 μm).

be attenuated (e.g., Gaskell & Martin 2017).
The photometry in these bands can be used to study the properties of the host galaxy. The obtained results are to be compared with other bands for the search of obscured AGN.
In Optical/NIR band, photometry and spectroscopy constitute a reliable, although incomplete, method of searching for AGN.

X-ray emission

Obscured AGN can be divided into different classes based on the absorbing column density N_H, i.e., the amount of material that produces the obscuration (see Fig. 1.9).

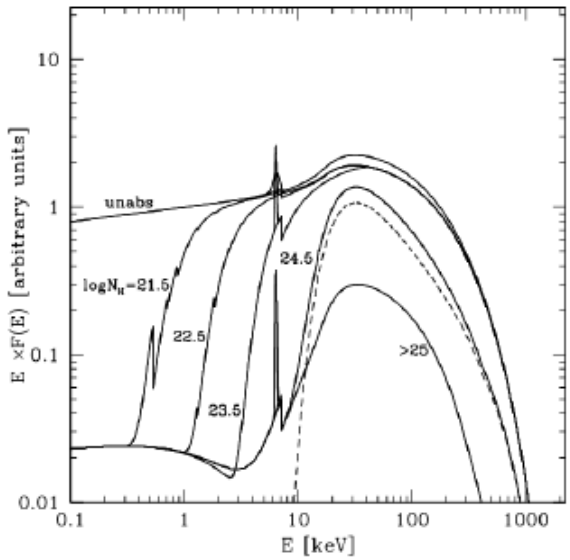

Figure 1.9: AGN SEDs obscured in X-ray band. High column densities strongly suppress radiation for energies below 10 keV so that the iron line at 6.4 keV becomes more prominent. The dashed line corresponds to the reflection component (from Gilli et al. 2007).

When considering the X-ray band, an AGN is called *unabsorbed* if $N_H < 10^{22}\ cm^{-2}$, *absorbed* if $N_H > 10^{22}\ cm^{-2}$ (e.g., Gilli et al. 2007). An obscured AGN is classified as *Compton-thin* if $N_H \sim 10^{22-24}\ cm^{-2}$; if $N_H \sim 10^{24-25}\ cm^{-2}$, the AGN is defined as *Compton-thick* and if $N_H > 10^{25}\ cm^{-2}$ the source is an *Heavily Compton-thick* AGN (e.g., Gilli et al. 2007).
Obscured AGN have different spectral characteristics with respect to the classic unobscured AGN. The intrinsic emission is influenced by the amount, composition and geometry of the column density (e.g., Risaliti & Elvis 2004). AGN have an integrated brightness $L_X = 10^{40-46}\ erg/s$, between $0.5 - 10\ keV$. If $L_X \lesssim 10^{42}\ erg/s$, AGN are identified as *Low Luminosities AGN* (LLAGN) (e.g., Contini 2011), if $L_X > 10^{44}\ erg/s$ they are defined as *High Luminosities AGN* (HLAGN). X-rays are particularly suited to study the inner regions of absorbed AGN. Their penetrating power, in fact, allow a direct, even if attenuated, view of the central engine (e.g., Brandt & Alexander 2015) and, for column densities of $2 \times 10^{24}\ cm^{-2}$, the photons emerge at a few tens of keV. As we have seen, AGN can be classified according to the amount of absorbing material in terms of N_H. If $N_H > 10^{25}\ cm^{-2}$ ($\tau \gg 1$, heavily Compton thick) all the radiation is depressed by the multiple scattering in the obscuring material, which decreases the energy of photons up to photoelectric absorption

(e.g., Wilms et al. 2000). In this case, only the reflection component, if present, can emerge in the typical X-ray observing band. If the column density is between $N_H \sim 10^{24-25}\ cm^{-2}$, part of the radiation with energies $> 10 - 15\ keV$ can penetrate the obscuring material and reach the observer (e.g., Vignali 2014).
As it can be seen in Fig. 1.9, for energies between $\sim 0.1 - 10\ keV$ the extinction is dominated by the photoelectric absorption of the nuclear radiation (e.g., Comastri 2004), which progressively attenuates it. This effect creates a cut-off, which moves to higher energies as N_H increases. At energies larger than $\sim 10\ keV$, Compton scattering becomes the dominant process, which in turn extinguishes the radiation as a function of N_H. Moreover, starting from these energies the reflected component contribution of the primary powerlaw emerges, the Compton Hump (see Section 1.4).
Another characteristic of the X-ray spectrum is the presence of the Fe K_α line (with a peak at $E \sim 6.4\ keV$). The contributions to the Fe K_α line are of various kinds: transmission and reflection from the accretion disk component, a contribution from the dusty torus, which, invested by the radiation of the primary powerlaw, can emit photons of iron fluorescence (e.g., Gilli et al. 1999). In the case of Compton-thin AGN the nuclear emission is observed directly and the iron line has values of $EW \sim 10 - 100\ eV$. By contrast, in the Compton thick cases, where the reflection component and the contribution of the torus dominate, we have $EW \sim 1keV$ (e.g., Bauer et al. 2015).

Cosmic X-ray background

Because of the strong obscuration, Type 2 AGN are not easy to detect. Different techniques are used for their detection, such as the measurement of the column density N_H (e.g., Lanzuisi et al. 2013), the analysis of the hardness ratio, i.e., the ratio between hard and soft fluxes (e.g., Brusa et al. 2009) or the analysis of X-ray colors (e.g., Iwasawa et al. 2012). The census and the study of this class of objects have, in fact, an important role in several research areas, including the *Cosmic X-Ray Background* (XRB) and the understanding of phases in the cosmological evolution of AGN. The CXB is the diffuse emission observed between 0.5 and 300 keV in the X-ray band (Giacconi et al. 1962).
Thanks to X-ray surveys carried by XMM-*Newton* and *Chandra* satellites, it was possible to resolve $\simeq 50\% - 80\%$ of the XRB in the $0.1 - 10\ keV$ band in point-like sources, the majority of which are AGN (e.g., Hickox & Markevitch 2006). At energies higher than $10\ keV$, the X-ray background is partially resolved (leaving the possibility for the presence of an undetected fraction of obscured AGN, e.g., Gilli 2013), with a peak at $\sim 30\ keV$. This can be reproduced through AGN synthesis models (see Fig. 1.10), which predict a large number of unresolved Compton-thin sources, as well as a large number of Compton-thick AGN, capable to reproduce XRB at high energies, providing a contribution of $\sim 30\%$ to the total XRB (e.g., Gilli et al. 2007). The fraction of obscured AGN is known with good accuracy for the local Universe only (e.g., Burlon et al. 2011). It also seems that their number decreases as their luminosity increases, up to $z \sim 3$ (e.g., Ueda et al., 2014). Many uncertainties still persist at high redshifts, mainly due to the strong extinction of these objects which makes them very difficult to detect, especially at high redshift. Despite these observation difficulties, Vito et al. (2014) present a sample of AGN at $3 < z < 5$, 50% about of it represents AGN with strong obscuration ($N_H > 10^{23}\ cm^{-2}$).
Comparing this sample with Burlon et al. (2011), a positive correlation was found between strongly obscured AGN and the redshift (see Fig. 1.11), especially for high luminosities.

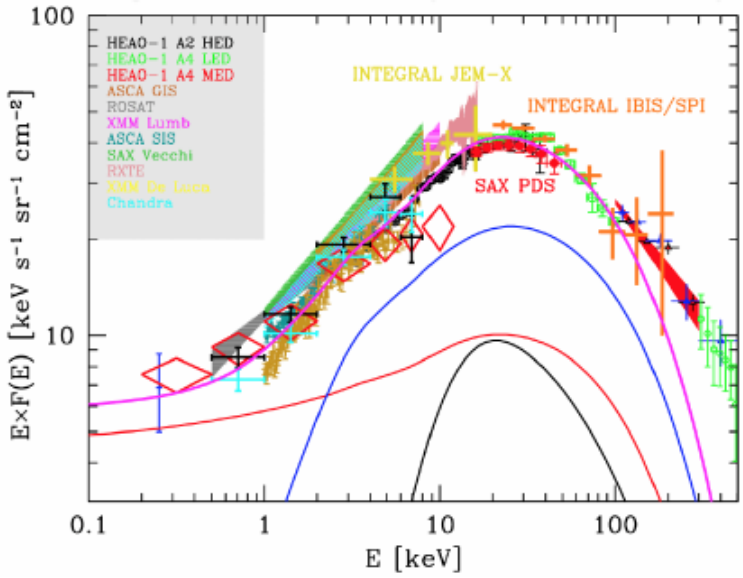

Figure 1.10: Cosmic X-ray background given by the sum (magenta line) of AGN unobscured (red line), AGN Compton-thin (blue line) and AGN Compton-thick (line black); data from various X-ray satellites are also shown (from Gilli et al. 2007).

The increasing in the fraction of obscured AGN as a function of redshift may be due to the large amount of gas available at high z (e.g., Vito et al. 2018), making these objects very interesting for studying the growth of SMBH. In particular, with a multiwave-length approach which also includes X-rays, recent studies (e.g., Gilli et al. 2014, Circosta et al. 2019, D'Amato et al. 2020) have found that high redshift obscuration can be produced not only by the molecular torus, but also by the gas present in the host galaxy. These sources are usually compact, with scales of a few kpc (e.g., Circosta et al. 2019).

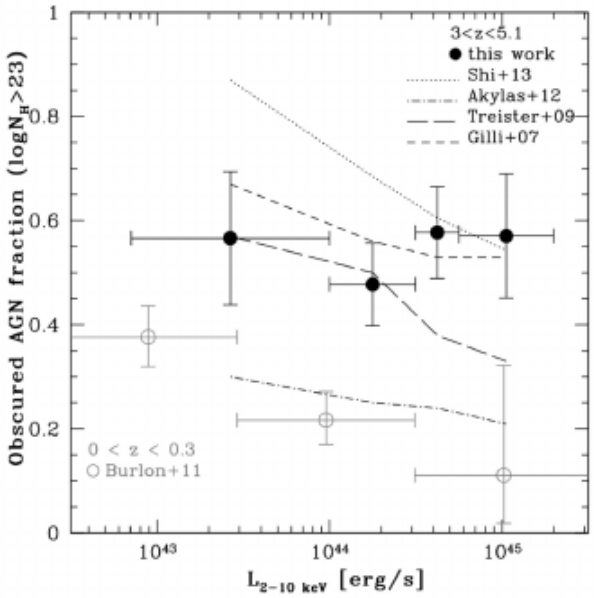

Figure 1.11: Fraction of obscured AGN as a function of luminosity, for samples at different redshifts. The black points represent the binned estimates obtained by Vito et al. 2014; the dotted, dot-dashed, long-dashed and short-dashed lines are the predictions from various X-ray background synthesis models (e.g., short-dashed lines are Gilli et al. 2007 synthesis models). The positive correlation between the fraction of obscured AGN and the redshift is in agreement with the results of synthesis of AGN populations for XRB, within the errors (from Vito et al. 2014).

1.6 The samples and the goal of this Thesis

In this Thesis we will present a multiwavelength study of the nuclear regions of NGC613 and NGC1808. These galaxies were selected from a sample of 7 sources observed with ALMA in Cycle 3 and 4 in Combes et al. (2019). Thanks to its high angular resolution and sensibility, it was possible to observe the molecular gas distribution (the torus) which is the main goal of this work. In this Thesis we focused our attentions to two the Seyfert 2 galaxies, NGC613 and NGC1808, having both ALMA and X-ray observations. This allowed us to compare the results in the two spectral ranges, and thus investigate the properties of the cold gas surrounding the SMBH. Due to limited time available, we could not expand the work to the other sources of the sample.

NGC613

NGC613 is a barred $SB(rs)bc$ galaxy (de Vaucouleurs et al. 1991) at a distance of 17.2 Mpc ($1'' = 83$ pc), i.e., $z = 0.0049$. Many multi-band observations have already been carried out for this source, shedding light on various spectral and morphological features. NGC613 has a composite nucleus (e.g., Veron-Cetty & Veron 1986) with an AGN that interacts with the galaxy through outflows, an ionized cone, and a radio jets, as well as a circumnuclear ring of HII regions that has a radius of 300 pc (e.g., Hummel & Jorsater 1992, Falcón-Barroso et al. 2014, Audibert et al. 2019). The galaxy contains an AGN, confirmed by the detection of high-ionization emission line, such as $[NeV]$ an $[OIV]$, observed with

Spitzer space telescope (e.g., Goulding & Alexander 2009). The AGN in NGC613 is of low luminosity with $L_{2-10\ kev} = 8.9 \times 10^{40}\ erg/s$ (e.g., Castangia et al. 2013) and a bolometric correction of 20 (e.g., Vasudevan et al. 2010), Davies et al. (2017) determined that the AGN bolometric luminosity is $L_{bol} \sim 1.6 \times 10^{42}\ erg/s$. From the analysis of the XMM-*Newton* data, Castangia et al. (2013) obtained an intrinsic column density of $N_H \sim 36^{+5}_{-4} \times 10^{22}\ cm^{-2}$. With *Very Large Array* (VLA) observation at 6 *cm* and 20 *cm*, the radio jets show a structure extending along 5″ with *Position Angle* (PA) of 6° (Hummet et al. 1987). Three blobs were detected in the central *kpc* (e.g., Hummet & Jorsater 1992).
ALMA observations of molecular lines revealed that the nucleus emits compatibly with Seyfert/LINER galaxies. There are very energetic molecular outflows (their kinetic power corresponds to $P_{K,out} = 20\%\ L_{AGN}$) that are possibly fossils from a phase when this AGN was in a higher activity and they are also associated with the radio jet, possibly being driven by it (Audibert et al. 2019).

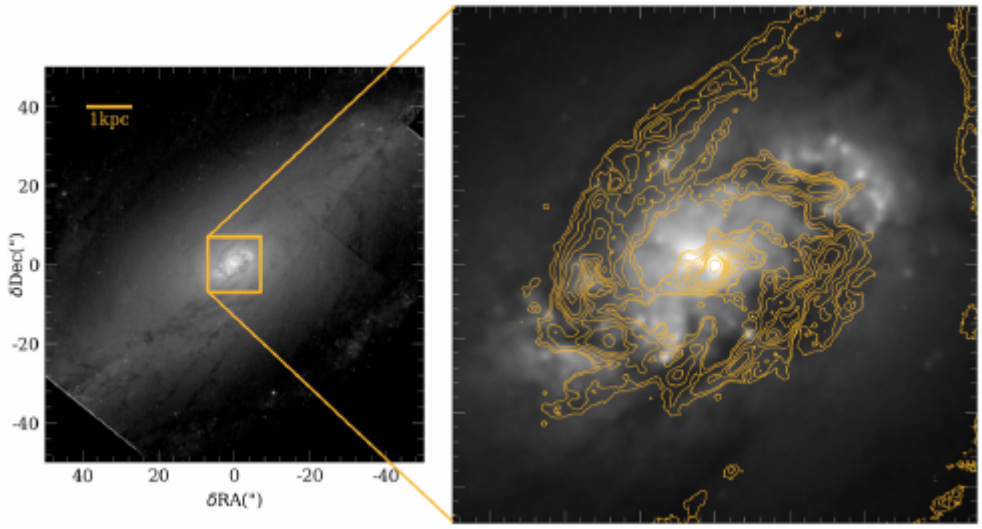

Figure 1.12: *Left panel*: WFC/F814W HST image showing the nuclear ring and the sets of spiral arm structures at large scales. The scale is indicated in the upper-left corner. *Right panel*: there are a 14″ square zoom showing the CO(3–2) contours overlaid on the same image, from Falcón-Barroso et al. (2014).

According to Böker et al. (2007) and (2008) and Falcón-Barroso et al. (2008) and (2014), the circumnuclear ring of NGC613 is formed by seven *HII* regions. This ring can also be observed in radio wavelengths (e.g., Hummel & Jorsater 1992, Miyamoto et al. 2017 and 2018, Audibert et al. 2019) and, if its structure is circular, the inclination should be $55° \pm 5°$ (Hummel & Jorsater 1992). Combes et al. (2019) and Audibert et al. (2019) found that this ring connected to the bar in two points, at NW and SE, as Bökeret al. (2008) previously estimated by using the HST images, and that the ring is indeed clumpy (Falcón-Barroso et al. 2014, see Fig. 1.12). There is also a nuclear spiral of molecular gas connected with the ring in two different spots (Audibert et al. 2019).

NGC1808

NGC1808 is classified as an *SABb* (de Vaucouleurs et al. 1991) and is located at a distance of 9.3 Mpc ($1'' = 45\ pc$), corresponding to a redshift of $z = 0.0033$. It is a starburst galaxy; according to Véron-Cetty & Vèron (1985) it exhibits Seyfert 2 characteristics as well. Awaki & Koyama (1993) detected X-ray emission of a Seyfert nucleus with the *Ginga* satellite. North of the central starburst region, NGC1808 shows clear signature of a nuclear outflow with a maximum length $\sim 3.8\ kpc$ (e.g., Laustsen et al. 19897, Koribalski et al. 1993). The kinematics of this outflow has been studied in the optical, e.g., by Forbes et al. (1992) and Phillips (1993), who found outflow velocities on the order of 500 km/s. The soft X-ray emission, detected by *ROSAT*, suggests the presence of diffuse hot ionized gas in its disk, associated with supernova activity in the star forming (SF) regions in the central 1 kpc (Dahlem et al. 1990, 1994).
VLA radio data by Saikia et al. (1990) revealed the existence of a compact core and ring of SF regions encompassing the core. There are several optical blobs associated with HII regions (Sérsic & Pastoriza 1965). The luminous and compact knots detected in radio and infra-red (IR) images (Saikia et al. 1990, Kotilainen et al. 1996) that do not coincide with the optical hot spots are probably supernova remnants (SNRs). Dust filaments were found perpendicular to the central disk plane (see Fig.1.13); this can be explained as outflowing material driven by supernovae (Heckmanet al. 1990). A recent interaction of NGC1808 with its companion NGC1792 could explain both the intense star formation activity and its peculiar morphology (Dahlem et al. 1990, Koribalski et al. 1993). Near-infrared integral-field spectroscopy with SINFONI by Busch et al. (2017) showed a large gas reservoir and a disturbed gas velocity field that indicates signs of inflowing streaming motion in the central ∼100 pc. Jiménez-Bailón et al. (2005) proved the co-existence of thermal diffuse plasma and non-nuclear unresolved point-like sources associated with the starburst activity. ALMA observations by Salak et al. (2017) and Combes et al. (2019) have shown the nuclear ring and two spiral arms.

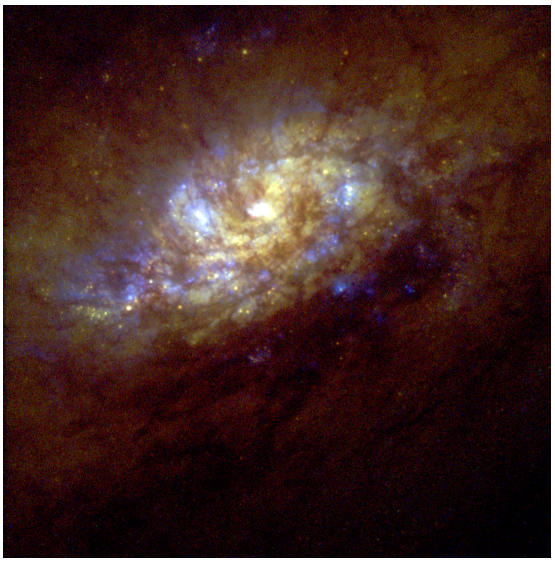

Figure 1.13: WFPC2 HST image of nuclear starburst galaxy NGC1808 (from Flood & Mutchler 1997).

Therefore, multiwavelength analysis has shown that the galaxies NGC613 and NGC1808 have rich nuclear regions, making this environment interesting to be studied and challenging to be understood.

Chapter 2

X-rays satellites and data reduction

In this chapter we will present the main characteristics of X-ray telescopes. We will then discuss about the two X-rays telescopes, *Chandra* and XMM-*Newton*, used in this Thesis for observations of the sources studied.
In the second part of the chapter, we will describe the process of data reduction.

2.1 X-ray telescopes

Because of absorption by Earth's atmosphere, which is opaque to X-rays and γ-rays, high-energy observations of celestial sources must be made from satellites placed outside the atmosphere. The basic principle of X-rays detection is the *grazing incidence* (e.g., Eisenberger et al. 1981): if the angle between the incoming photons and the reflecting layer is "small enough" even high-energy photons may be reflected (see Fig. 2.1).

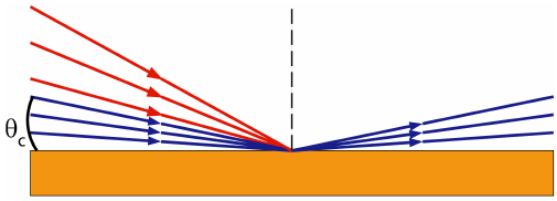

Figure 2.1: Total reflection at an angle lower than θ_C, the critical angle, which depends mainly on the density of the material used for the coating of the optics and on the energy of the incoming photon.

By Snell's law it is possible to define a critical angle θ_c such that this phenomenon occurs:

$$\theta_c \approx \frac{28}{E}\sqrt{\frac{\rho Z}{A}}\ , \tag{2.1}$$

where ρ is the density of the material used for optics coating, (Z/A) is the ratio between the atomic number and the atomic weight of the coating material and E is the energy of the incoming photon. In order to be detected, photons must have an incidence angle less than the critical angle. Therefore, in order to have the largest critical angle as possible, the mirrors are coated with a high density material.
X-ray telescopes are essentially described by their:

- effective area,
- angular resolution,
- spectral resolution,
- sensitivity.

Effective area

The effective area quantifies the capability of an instrument to collect photons; it is defined as

$$A_{eff}(E,\theta,x,y) = A_{geometric} \times R(E) \times V(E,\theta) \times QE(E,x,y)\ ,\ [A_{eff}] = [cm^2]\ , \qquad (2.2)$$

where $A_{geometric}$ is the cross section of the telescope or, analogously, the transverse section at the point of intersection of the optics, $R(E)$ is the *reflectivity*, i.e., the fraction of photons reflected by the mirrors, $V(E,\theta)$ is the *vignetting*, i.e., the fraction of effective area loss due to the off-axis angle and $QE(E,x,y)$ is the *quantum efficiency*, i.e., the fraction of incident photons registered by detectors. E is the incoming photon energy, (x,y) represents the position on the detector and θ is the off-axis angle.
It is worth noting here that all the quantities in equation (2.2) are energy-dependent. Essentially all the X-ray telescopes are intrinsically spectrometers as well, even if with poor energy resolution. This is because these facilities are always able to register, for each single incoming photon, its position, arrival time and energy.

Angular resolution

The angular resolution is the capability of the detector to distinguish between objects separated by small angular distances: the highest the angular resolution, the finest the distinction of details. It is usually reported as *Point Spread Function* (PSF), which describes how the light of a point-like object is distributed on the detector. The PSF is a function of the energy and off-axis angle of the incoming photons: if the off-axis angle and the energy increase, the shape of the PSF becomes wider, hence worsening the angular resolution. The highest image quality is obtained in an area close to the optical axis of the telescope (the so-called *aimpoint*). Furthermore, the PSF is sharper at low energies. The PSF is usually described by one of the following two parameters, the FWHM or the *Half Energy Width* (HEW). The FWHM is the width of the PSF at half of its highest value, the HEW is the amplitude which contains half of incident photons.
Another parameter related to the PSF and widely used by X-ray astronomers is the *Encircled Energy Fraction* (EEF), i.e., the fraction of photons collected within a given extraction radius.

Spectral resolution

The spectral (energy) resolution, or resolving power, is the capability of a detector of discriminating photons at different energies, i.e., to distinguish spectral features at close energies. In the ideal case, the detected pulse is a Dirac delta distribution, in the real case it is a

Gaussian distribution. The energy resolution is defined by (we assume a Poisson distribution for the photons' statistics)

$$R_{Poisson} = \frac{FWHM}{H_0} \simeq \frac{2.35\sigma}{KN} = \frac{2.35K\sqrt{N}}{KN} = \frac{2.35}{\sqrt{N}} \ , \tag{2.3}$$

where $H_0 = KN$ is the incident photon energy peak, K is a normalization constant, N is the number of recorded photons and σ is the standard deviation of the Gaussian distribution. The event distribution cannot be considered as purely Poissonian, since the events cannot be considered really independent. We then introduce in equation (2.3) a corrective term, the *Fano Factor* (F):

$$R_F = 2.35\sqrt{\frac{F}{N}} \ , \tag{2.4}$$

where F is linked to the ratio between the measured and expected Poisson variance. A typical average value of F for CCD's is ~ 0.13 (e.g., Kotov et al. 2018).

Sensitivity

Sensitivity is the minimum detectable flux, i.e., the faintest source that we can detect in a field. It is related to the signal-to-noise ratio

$$SNR = n_\sigma = \frac{C_S}{\sqrt{C_S + C_B}} \ , \tag{2.5}$$

where C_S is the source count and C_B is the background count. They can be expressed as

$$\begin{aligned} C_S &= \epsilon A_{eff} \Delta E F_{src} \ , \\ C_B &= A_{eff} \Delta E F_{bkg} \ , \end{aligned} \tag{2.6}$$

where ϵ is the efficiency in source counts detection, A_{eff} is the effective area, T is the exposure time, ΔE is the observing energy range, F_{src} and F_{bkg} are source and background fluxes ($photons/cm^2 s\ keV$), respectively. Therefore, equation (2.5) becomes

$$n_\sigma = \frac{C_S}{\sqrt{C_S + C_B}} = \frac{\epsilon\ A_{eff}\ T\ \Delta E\ F_{src}}{\sqrt{A_{eff}\ T\ \Delta E\ (F_{bkg} + F_{src})}} \ . \tag{2.7}$$

The minimum detectable flux is obtained from equation (2.7) when the source flux is negligible with respect to the background flux:

$$F_{min} = \frac{n_\sigma}{\epsilon} \sqrt{\frac{F_{bkg}}{A_{eff} T \Delta E}} \ . \tag{2.8}$$

2.1.1 Chandra telescope

Chandra X-ray Observatory (Weisskopf et al. 1999), which inherits its name by the Nobel laureate Subrahmanyan Chandrasekhar, is a NASA telescope developed for high energy observations in the X-ray spectrum. It was launched in orbit in July, 1999 and despite its mission was supposed to finish observing in 2004, the telescope is still operating nowadays. In Table 2.1 we collect the main characteristics of *Chandra*.

Optics	Wolter Type-I
Mirror coating	Iridium
Mirror maximum diameter	1.23 m
Mirror lengths	84 cm
Focal length	(10.070 ± 0.003) m
PSF FWHM	$< 0.5''$
Effective Area	800 cm^2 (0.25 keV)
	400 cm^2 (5.0 keV)
	100 cm^2 (8.0 keV)

Table 2.1: *Chandra* main characteristics. From *Chandra proposers' observatory guide.*

Currently, it is the best X-ray telescope in terms of high-resolution imaging and spectroscopy in the band $0.1 - 10$ keV and in terms of angular resolution (see Table 2.1).
The telescope is made by four pair of parabolic and hyperbolic nested mirrors assembled into a support structure called *High Resolution Mirror Assembly* (HRMA)[1], shown in Fig. 2.2. Mirrors, coated with iridium, focus the incoming X-rays and convey it on the focal plane.

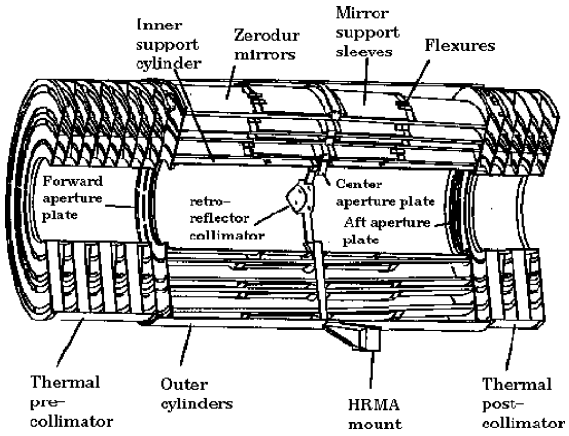

Figure 2.2: The four nested HRMA mirror pairs and associated structures. From *Chandra proposers' observatory guide.*

In Fig. 2.3 we show the encircled energy fraction at different energy levels as a function of the extraction radius for an on-axis point-like source, as reported in Sections 3.1−3.2. Considering that the EEF depends on photons energies and positions on the detector, it will be taken into consideration in choosing the size of the extraction regions of the source. The EEF is used as a representative of the PSF, which is used to determine the size and shape of the target. Approximately 90% of the encircled energy lies within $2''$ at 1.5 keV and within $2.5''$ at 6.4 keV.

[1] *https://cxc.harvard.edu/proposer/POG/html/chap4.html*

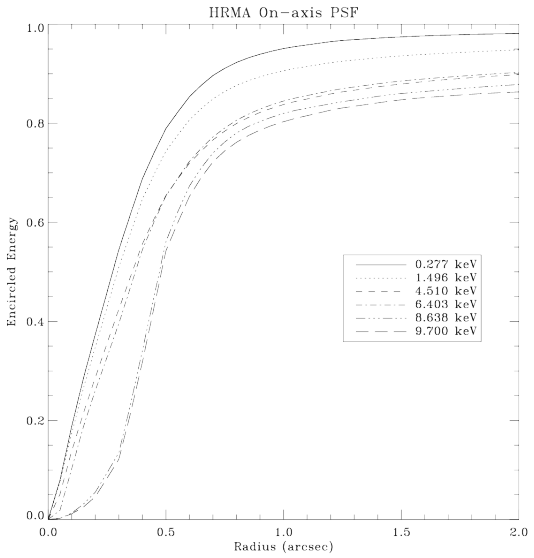

Figure 2.3: The EEF of *Chandra* HRMA as a function of angular radius, calculated for an on-axis source, at selected X-ray energies. The EEF is different at different energies, in particular, given a certain radius, the EEF is higher at low energies. From *Chandra proposers' observatory guide.*

The *Chandra* focal-plane detectors are combined to capture the images formed by the mirrors and to give information about the incoming X-rays: their number, position, energy and time of arrival. Onboard *Chandra* there are four different science instruments[2]:

- *High Resolution Camera* (HRC)(Weisskopf et al. 1999). HRC has two micro-channel plates in different configurations: the HRC-I configuration is used for imaging, the HRC-S configuration for spectroscopy, with field-of-view's of $\sim 30 \times 30\ arcmin^2$ and $\sim 6 \times 90\ arcmin^2$, respectively. Its temporal resolution is about 16 ms and spatial resolution is lower than $0.5''$.

- *High and Low Energy Transmission Gratings* (HETG and LETG) (Weisskopf et al. 1999). HETG and LETG are two sliding gratings inserted behind the exit aperture of the HRMA. They are dedicated to high resolution spectroscopy at ranges $0.4 - 10\ keV$ and $0.07 - 0.2\ keV$, respectively.

- *Advanced CCD Imaging Spectrometer* (ACIS) (Weisskopf et al. 1999). ACIS, in Fig. 2.5, is an X-ray imager made of a set of CCDs divided in two different arrays: *ACIS-I* and *ACIS-S*. ACIS offers the capability to simultaneously acquire high-resolution images, moderate resolution spectra and moderate time resolution. When it is used with HETG or LETG it obtains higher resolution spectra. The effective area of the imaging instruments are shown in Fig. 2.4.

[2] *https://chandra.harvard.edu/about/science_instruments.html*

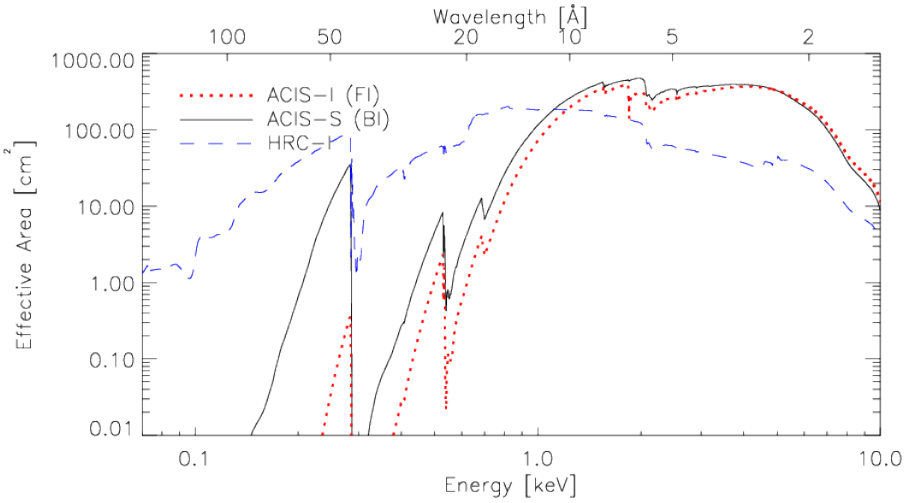

Figure 2.4: *Chandra* effective area as a function of energy for ACIS and HRC (logarithmic scale). From *Chandra proposers' observatory guide*.

ACIS-I is composed by four square front illuminated CCDs ($I0 - I3$) and is used for large fields (16×16 $arcmin^2$); ACIS-S is composed by a string of six front and back illuminated CCDs ($S0 - S5$) and it is used also with the HETG (and less commonly with the LETG) for high resolution spectroscopy.
ACIS operates in the energy range $0.2 - 10$ keV and when the photons hit the camera, they are detected individually and their position, energy and arrival time are recorded. NGC613 and NGC1808 were observed using the ACIS-I and ACIS-S imagers, respectively.

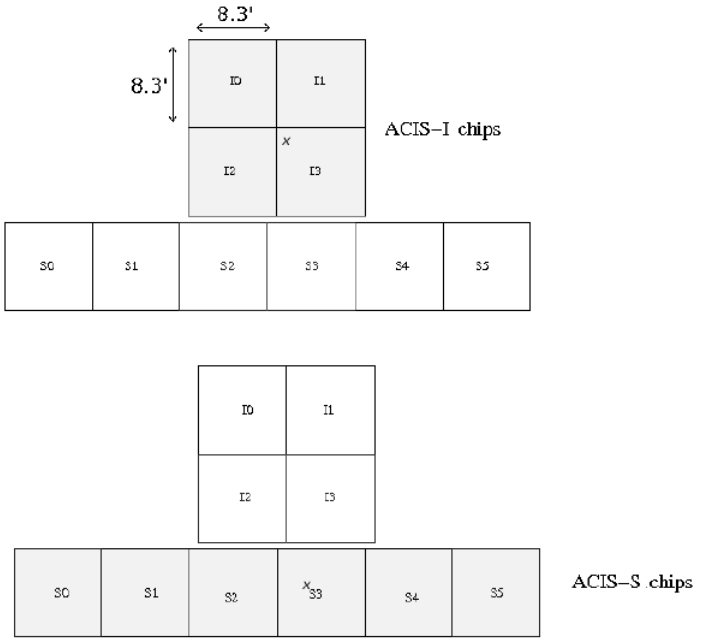

Figure 2.5: Scheme of ACIS-I (top) and ACIS-S (bottom).

2.1.2 XMM-Newton telescope

X-ray Multi Mirrors-Newton, which inherits its name by physicist and astronomer Sir Isaac Newton, is a ESA spatial telescope for X-rays detection (Aschenbach et al. 2000). It was launched in orbit in December, 1999 and despite initially funded for two years, the telescope remains in good health and has received repeated mission extensions. In Fig. 2.6, we show the XMM-*Newton* spacecraft[3].

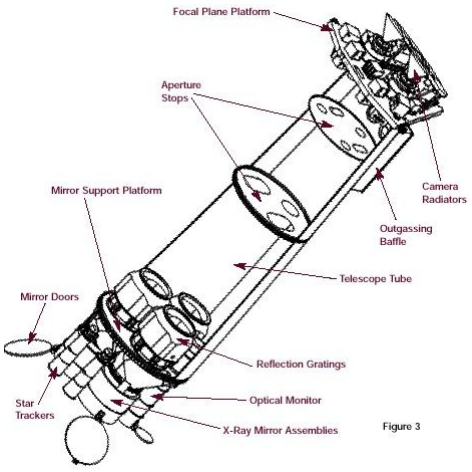

Figure 2.6: The different components of the XMM-*Newton* spacecraft. From XMM-*Newton technical details*.

The collecting area of XMM-*Newton*[4] is shown in Fig. 2.7. Currently, XMM-*Newton* is the best X-ray telescope in terms of effective area and, with a length of 10 m, spacecraft is the largest scientific satellite ever launched by the ESA. It comprises three telescopes and its main characteristic are collected in Table 2.2. It covers the energy range $0.1 - 12\ keV$.

Optics	Wolter Type-I
Mirror coating	Gold
Mirror maximum diameter	70 m
Mirror lengths	60 cm
Focal length	7.5 m
PSF FWHM	$< 6''$
Effective Area	1400 cm^2 (2 keV)
	900 cm^2 (6.0 keV)

Table 2.2: XMM-*Newton* main characteristics. From XMM-*Newton users handbook*.

Thanks to its large effective area, the main strength of XMM-*Newton* is its capability to detect and collect a large number of photons.

[3] $https://www.cosmos.esa.int/web/xmm-newton/technical-details-spacecraft$
[4] $https://xmm-tools.cosmos.esa.int/external/xmm\_user\_support/documentation/uhb/effareaonaxis.html$

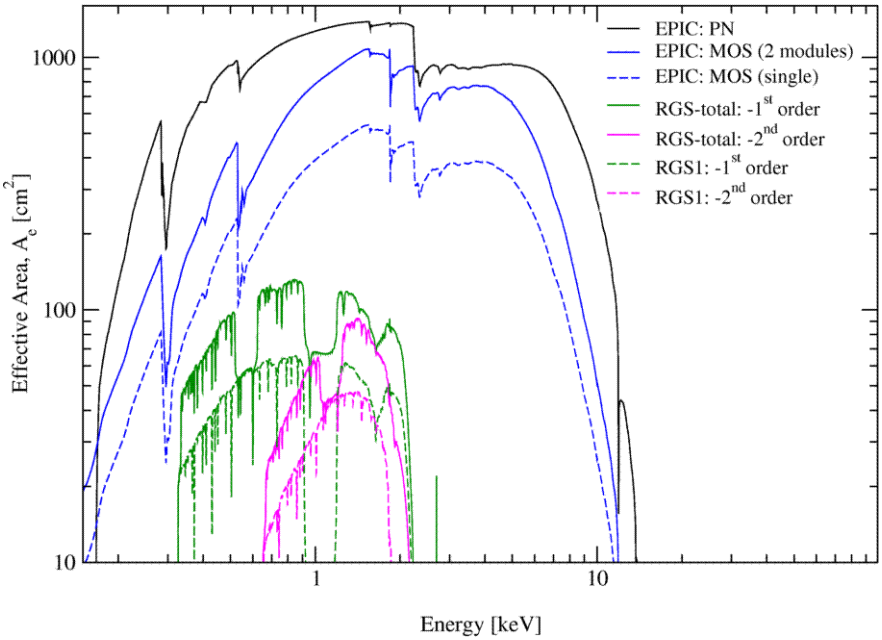

Figure 2.7: The effective area of all XMM-*Newton* X-ray telescopes, EPIC and RGS (logarithmic scale). From XMM-*Newton users handbook*.

The instruments on XMM-*Newton* observatory are[5]:

- *European Photon Imaging Cameras* (EPIC) (e.g., Ferrando et al. 2002). EPIC are the main camera aboard XMM-*Newton* for X-ray imaging. The system, in Fig. 2.8, consists of two MOS-CCD cameras (*MOS1* and *MOS2*) and a single pn-CCD camera. The XMM-*Newton* EPIC cameras offer the possibility to perform extremely sensitive imaging observations over a field of view of 30 *arcmin* and the energy range $0.2 - 12$ *keV*, with moderate spectral ($E/\Delta E \sim 20 - 50$) and angular resolution ($\sim 6''$ FWHM; $\sim 15''$ HEW).

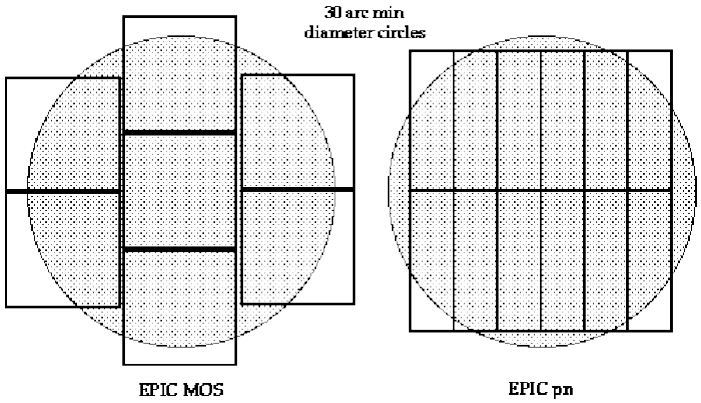

Figure 2.8: Scheme of XMM-*Newton* EPIC cameras: MOS (left) and pn (right). The shaded circle represents a 30 *arcmin* diameter area. From XMM-*Newton users handbook*.

[5] *https* : *//www.cosmos.esa.int/web/xmm − newton/technical − details*

Each EPIC MOS camera is composed by seven individual identical silicon front-illuminated CCDs. The cameras receive typically $\sim 44\%$ of the incoming radiation, because the light is divided into two directions, MOS cameras and the RGS, so the effective areas of the two MOS cameras are lower than that of the pn. MOS1 HEW is $13.6''$ at 1.5 keV and $12.5''$ at 8 keV; MOS2 HEW varies in the range $12.8'' - 12.2''$ in the energy range $1.5 - 8$ keV.
EPIC pn camera is realized by the monolithic fabrication of twelve pn-CCDs on a single wafer. The pn HEW varies from $15.1'' - 14.8''$ in the energy range $1.5 - 8$ keV. All instruments work together simultaneously.
Similarly to *Chandra* ACIS cameras, EPIC cameras allow to develop imaging, light curve analysis and moderate-resolution X-ray spectral analysis.
The XMM-*Newton* EPIC cameras have been designed to minimize the variation of the PSF, hence the encircled energy fraction (EEF), across the field of view and the range of observed photon energies. MOS and pn cameras have different EEF.
In Fig. 2.9 and in Fig. 2.10 we show the EEF for XMM-*Newton* MOS and pn cameras[6] as a function of the radius for an on-axis point-like source for different energies.

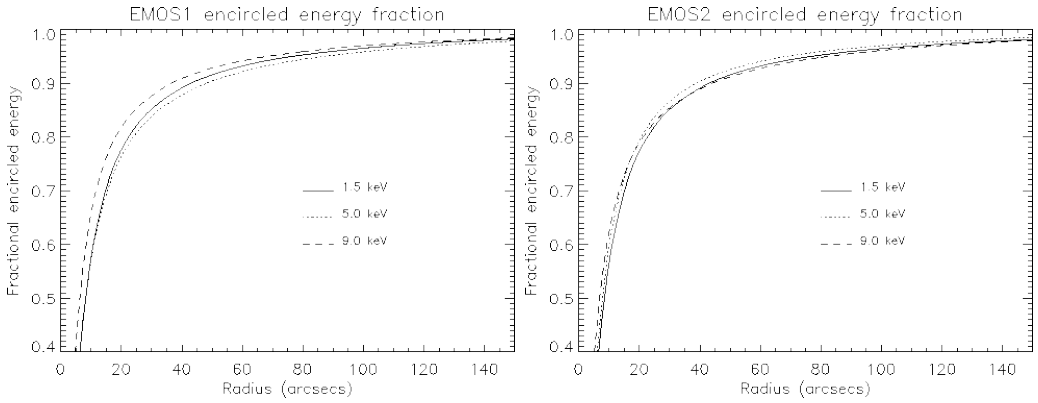

Figure 2.9: The EEF for the XMM-*Newton* MOS cameras as a function of angular radius (on-axis) at different energies. Curves corresponding to the three different energies are plotted with different curves: 1.5 keV, 5.0 keV and 9.0 keV are represented by a solid, dashed and dotted line, respectively. In order to have $\sim 90\%$ of the photons, a circular region with radius of $\sim 40''$ must be selected. From XMM-*Newton users handbook*.

The MOS and pn cameras were used to observe the sources analyzed in this Thesis.

- *Reflection Grating Spectrometers* (RGS). Each RGS consists of an array of reflection gratings which diffract the X-rays to an array of dedicated CCD detectors and only two of the three telescopes are equipped with these RGSs. Each unit is composed by the Reflection Gratings Assemblies (RGAs) and the RGS Focal Cameras (RFCs). RGSs, associated with EPIC MOS cameras, contain 182 identical diffraction gratings and are used to diffract light. RFCs consist of nine MOS-CCD devices mounted in a row and are used for the detection of diffracted X-rays. The RGS system operates in the $0.35 - 2.5$ keV range.

[6] *https://xmm-tools.cosmos.esa.int/external/xmm_user_support/documentation/uhb/onaxisxraypsf.html*

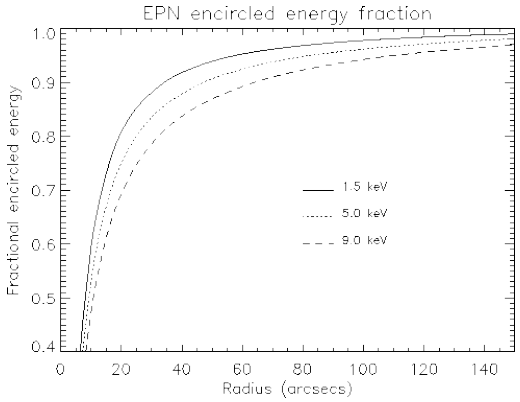

Figure 2.10: The EEF for the XMM-*Newton* pn camera as a function of angular radius (on-axis) at different energies. Curves corresponding to the three different energies are plotted with different curves: 1.5 keV, 5.0 keV and 9.0 keV are represented by a solid, dashed and dotted line, respectively. The EEF is different at different energies, in particular, given a certain radius, the EEF is higher at low energies. From XMM-*Newton users handbook*.

- *Optical Monitor* (OM) (Mason et al. 2000). OM is a 30 cm optical/ultraviolet telescope designed to provide simultaneous observations alongside the spacecraft's X-ray instruments. Its spectral working range is $170 - 650$ nm and it permits multi-wavelength observations of X-ray, ultraviolet and optical bands.

2.2 X-ray data reduction

In order to have the best possible control of the data acquired during a scientific pointing, it is necessary to select only that integration periods for which the operation of the instrument was "nominal", i.e., performed within all the expected range of functioning. The individuation of such periods is usually called *data reduction* and is fairly standard. In the following paragraphs we will introduce the datasets used for this Thesis and the basic procedures for the data cleaning.

2.2.1 The data

We searched in the *Chandra archive*[7] and XMM-*Newton archive*[8] for observations of NGC613 and NGC1808. We found two observations per source (see Table 2.3) available for our purposes. For NGC613, the observations were taken ~ 4 years apart and had similar duration, ≈ 40 ks for XMM-*Newton* and ≈ 50 ks for *Chandra*. *Chandra* data were acquired on the ACIS-I with a standard read-out mode. XMM-*Newton* EPIC data were acquired in FULL-FRAME mode with the Medium filter applied. The observations of NGC1808 were taken in the same year and lasted ≈ 43 ks for *Chandra* and ≈ 4 ks for XMM-*Newton*. *Chandra* data were acquired using the ACIS-S imager, and XMM-*Newton* EPIC data were acquired in FULL-FRAME mode with the Thin1 filter applied.

[7] $https://cda.harvard.edu/chaser/$
[8] $http://nxsa.esac.esa.int/nxsa-web/\#search$

Source	Telescope	Obs.ID	Start Date	Duration (ks)	PI name
NGC613	*Chandra*	16351	2014-08-21	48.85	Garmire
	XMM-*Newton*	0654800501	2010-12-30	41.81	Castangia
NGC1808	*Chandra*	3012	2002-12-19	42.88	Maloney
	XMM-*Newton*	0110980801	2002-04-06	4.36	Jansen

Table 2.3: Obs.ID, start date and nominal duration of the observations for the *Chandra* and XMM-*Newton* telescopes.

Chandra and XMM-*Newton* measurements are associated by their own software and tools to make data reduction and analysis, *Chandra Interactive Analysis of Observations* (CIAO) and *Science Analysis System* (SAS), respectively.

2.2.2 Chandra data reduction

Data reduction consists in cleaning the raw data. The *Chandra* archives have reprocess data, but in order to have the best possible control of the data under examination and apply the latest calibrations, we re-applied the *calibration files* using CIAO tools. All steps for data reprocessing are made using the script `chandra_repro`[9] which acquires event files and information about parameters of the downloaded data and creates:

- a new bad pixel file, i.e., a list of pixels identified as "bad" which are excluded from the analysis;
- a new event file (*evt2.fits*) containing all the events, filtered and corrected, recorded during the observation;
- a new *Pulse Height Amplitude* (PHA) file, to encode the properties of incident photons such as energy, position and time of arrival.

NGC613 was observed with the ACIS-I detector and in *very faint mode*[10], i.e., for each detected event are provided position, time, total pulse height and pixel values in a 5×5 region surrounding the event, then we used `check_vf_pha=yes`. NGC1808 was observed with the ACIS-S imager and in *faint mode* instead, i.e., for each detected event the same quantities provided to the very faint mode are given, but in a 3×3 region surrounding the event. We then used `check_vf_pha=no`.
From this point on, data reduction is performed in the same way for both sources. The data were then filtered to remove the possible background flares: these components change very slowly in time and therefore can be statistically recognized and, consequently, removed. For

[9] *http://cxc.harvard.edu/ciao/ahelp/chandra_repro.html*
[10] *http://cxc.cfa.harvard.edu/proposer/threads/acis_notes*

this purpose the data have been filtered in order to take in exam only photons at energies $0.3 - 7.0\ keV$.
In order to remove hot and bad pixels, we applied the *Good Time Intervals* (GTI) at the new event file. The GTI contain all the information of the time intervals in which the events, detected during observation, are deemed acceptable.
Using the task `dmcopy`, we created an image of the source with a selected energy range; in particular, we divided the energy band into three ranges: $0.3 - 2.0\ keV$, $2.0 - 7.0\ keV$ and $0.3 - 7.0\ keV$. These energy selections were made in order to maximize the contribution of the diffuse component ($0.3 - 2.0\ keV$ band), that of the nuclear component ($2.0 - 7.0\ keV$ band) and in order to have the total emission contribution of the galaxy ($0.3 - 7.0\ keV$ band): see Section 3.1 for the extraction regions.
Once the final file of calibrated and filtered events was obtained, we proceeded with the selection of the galaxy regions to study the spectrum.

2.2.3 XMM-Newton data reduction

XMM-*Newton* data reduction produces images, light curves and spectral data from *Observation Data File* (ODF). Since the properties of the XMM-*Newton* telescopes are known to slowly vary, it is necessary to best calibrate the analyzed observation using the files related to the epoch during which it was obtained. Therefore, in order to process the ODF dataset, SAS must identify the *Current Calibration Files* (CCF): this operation is known as the generation of the *Calibration Index File* (CIF) and is performed by the `cifbuild` task. The output of previous task is the *ccf.cif* file and it is a FITS file which can be examined with any FITS viewer, as for example the `fv` from *HEASOFT*. It contains references to all CCF files which are required by own ODF set.
Subsequently, we created the event calibrated file for MOS and pn cameras, using the tasks `emproc` and `epproc`; it is then possible remove bad pixels, cosmic rays and out-of-field events.
At this is point, we created and visualized the light curve of the entire field of view for both sources. In particular, we extracted the light curve in the energy range of $10 - 12\ keV$ in order to check for background flares: XMM-*Newton* orbit can intercept and interact with Earth's magnetosphere soft protons clouds, which increase the level of background.
Therefore, with the task `tabgtigen` we selected a threshold for the count rate in order to remove the intervals of the observation affected by the previous significant noise. This is one of the methods to remove flared regions. The standard threshold value for MOS is 0.35 (cts/s), while that for pn is 0.4 (cts/s). In our case, these values are unsatisfactory and we chose different threshold values for both sources: 0.12 (cts/s) for the MOS cameras for both NGC613 and NGC1808 and 0.36 (cts/s) for NGC613 and 0.30 (cts/s) for NGC1808 for the pn camera. In Fig. 2.11-Fig. 2.13 we show the light curves of NGC613 and NGC1808, where the flares have been highlighted in a red rectangle; in Fig. 2.12-Fig. 2.14 we show the light curves resulting from the flare removal.

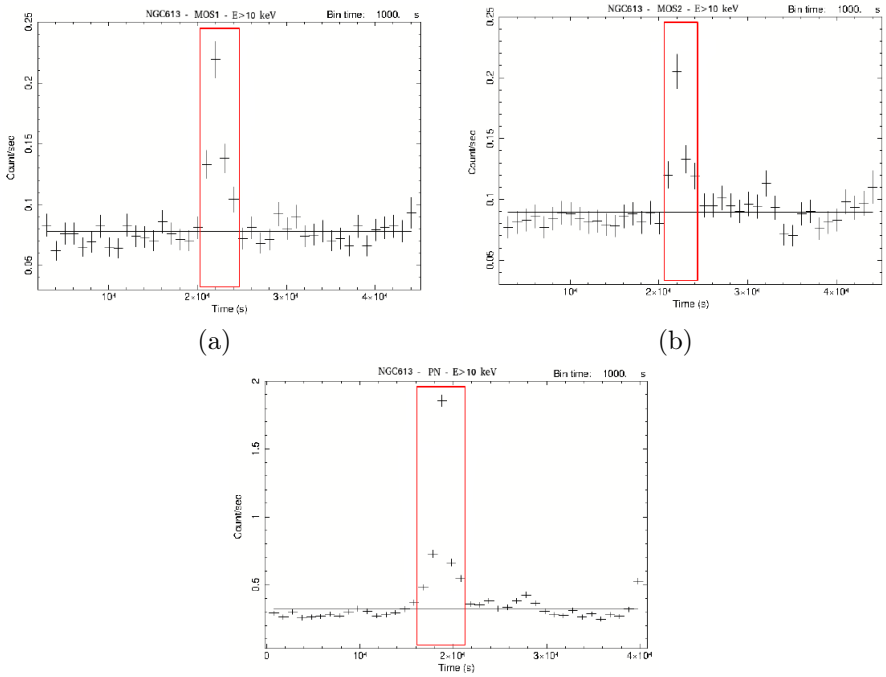

Figure 2.11: Light curves of NGC613 for MOS1 (a), MOS2 (b) and pn (c) cameras before cleaning the data to remove flaring-background periods. The flares are highlighted in red rectangles. In all three light curves we noticed an increase in the count rate at about half of the integration time. Light curves have been extracted with a time binning of 1000 s.

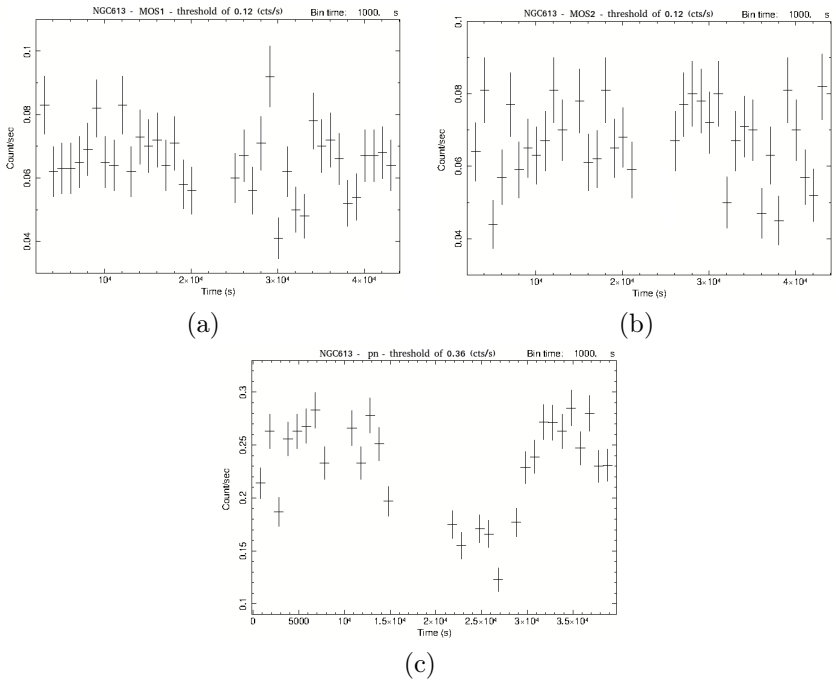

Figure 2.12: Light curves of NGC613 for MOS1 (a), MOS2 (b) and pn (c) cameras after removing the period with the flare. Light curves have been extracted with a time binning of 1000 s.

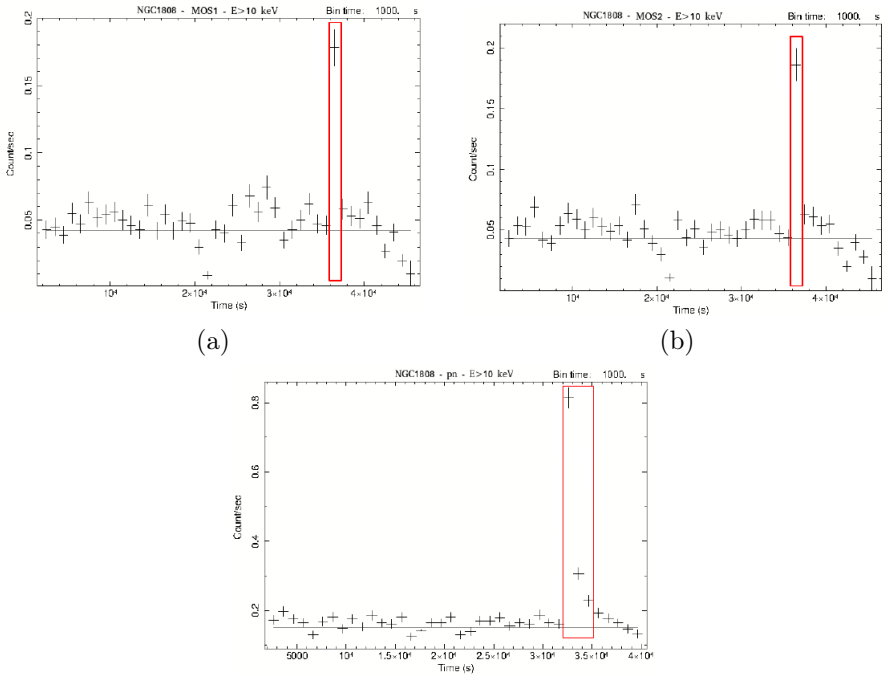

Figure 2.13: Light curves of NGC1808 for MOS1 (a), MOS2 (b) and pn (c) cameras before cleaning the data to remove flaring-background periods. The flares are highlighted in red rectangles. In all three light curves we noticed an increase in the count rate at about half of the integration time. Light curves have been extracted with a time binning of 1000 s.

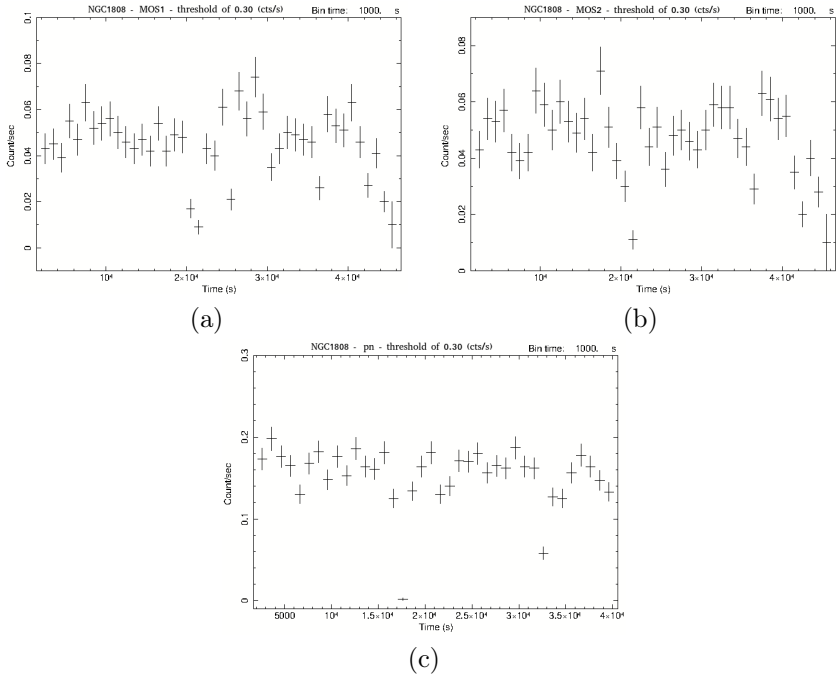

Figure 2.14: Light curves of NGC1808 for MOS1 (a), MOS2 (b) and pn (c) cameras after removing the period with the flare. Light curves have been extracted with a time binning of 1000 s.

In Table 2.4 we report the exposure time and counts before and after data cleaning for both sources.

		Before	After
		Exposure Time (ks)	Exposure Time (ks)
NGC613	MOS1	40.96	35.55
	MOS2	41.00	32.47
	pn	35.00	24.07
NGC1808	MOS1	36.45	38.34
	MOS2	39.63	38.73
	pn	31.85	30.44

Table 2.4: Exposure time before and after cleaning for NGC613 and NGC1808.

Then, we generated a new cleaned event file for both sources which contains the events below the selected threshold only and, in analogy to *Chandra* data reduction, we divided the cleaned event file into three energies ranges: $0.3-2.0\ keV$, $2.0-10.0\ keV$ and $0.3-10.0\ keV$.

Chapter 3

X-ray data analysis

3.1 Chandra data analysis

For each source, the event file which was created from data reduction (see Section 2.2.2), is visualized with the *ds9* viewer which was used to select the regions of interest. In particular, we defined nuclear, source and background regions for both sources. The size of nuclear and source regions must be chosen by taking into account the instrument PSF and, in particular, the associated EEF (see Section 2.1). The background region must be selected excluding other sources and in the same chip of the source.
Throughout this Thesis distances and luminosity have been computed assuming a ΛCDM cosmology: $H_0 = 70\ km/sMpc$, $\Omega_M = 0.27$, and $\Omega_\Lambda = 0.73$.

NGC613

In order to investigate the individual components within the galaxy (e.g., nucleus and host galaxy emission), we chose various regions (see Fig. 3.1).
Thanks to *Chandra* high resolution and sensitivity, from Fig. 3.1 it is possible to distinguish the nuclear component from the diffuse one of the galaxy. We defined a region with a radius of $2''$ (the blue circle in Fig. 3.1(b)) to focus on the nuclear component, a region with a radius of $6.5''$ (cyan circle in Fig. 3.1(b)) to study the diffuse and nuclear components and an annular region with $R_{min} = 2''$ and $R_{max} = 6.5''$ to study the diffuse component only (green annulus in Fig. 3.1(c)). Finally, considering the elongation of the source, we chose an elliptical extraction region in order to maximize the signal-to-noise ratio. The elliptical region has as major semiaxis $a = 7.4''$, a minor semiaxis $b = 5.9''$ and an inclination angle of $\theta = 31°$ (magenta ellipse in Fig. 3.1(b)). For the background region we chose an extraction radius of $20''$ close to NGC613 and avoided any contamination from other sources (yellow circle in Fig. 3.1(a)). 1" corresponds to $\sim 83\ pc$, when evaluated at the redshift of the source ($z \simeq 0.0049$).
As anticipated in Section 2.2.2, we divided the energy band into three ranges: $0.3-2.0\ keV$, $2.0-7.0\ keV$ and $0.3-7.0\ keV$. In the soft band ($0.3-2.0\ keV$), we have the maximum contribution of the diffuse component, since the nuclear emission is absorbed. In the hard band ($2.0-7.0\ keV$), we have the dominant contribution of the nuclear component and in the full band ($0.3-7.0\ keV$), we have the total emission contribution of the galaxy. In Table 3.1 we show the counts for each energy band for the different extraction regions.

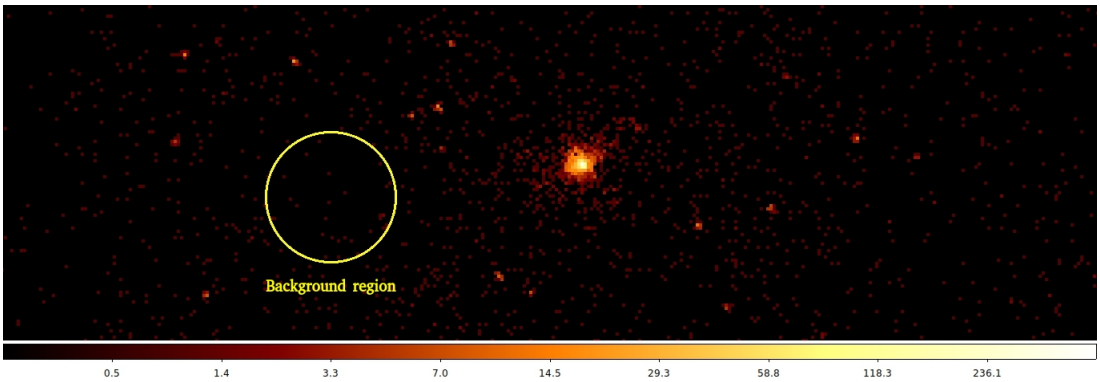

(a)

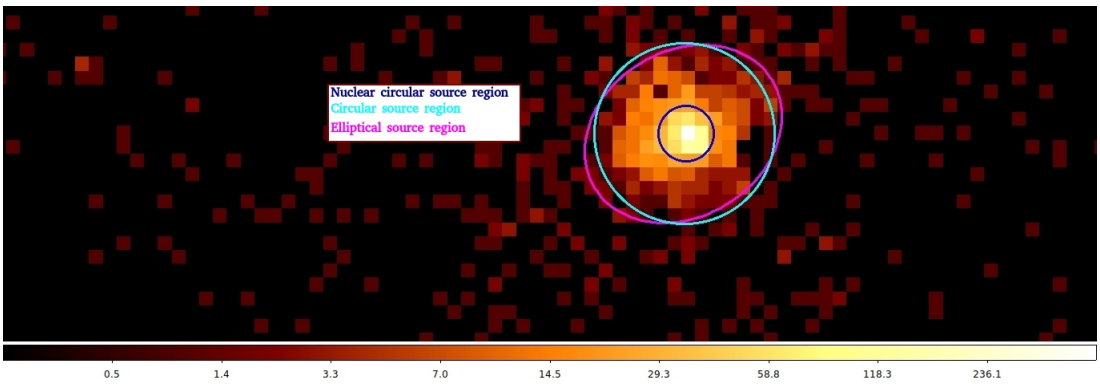

(b)

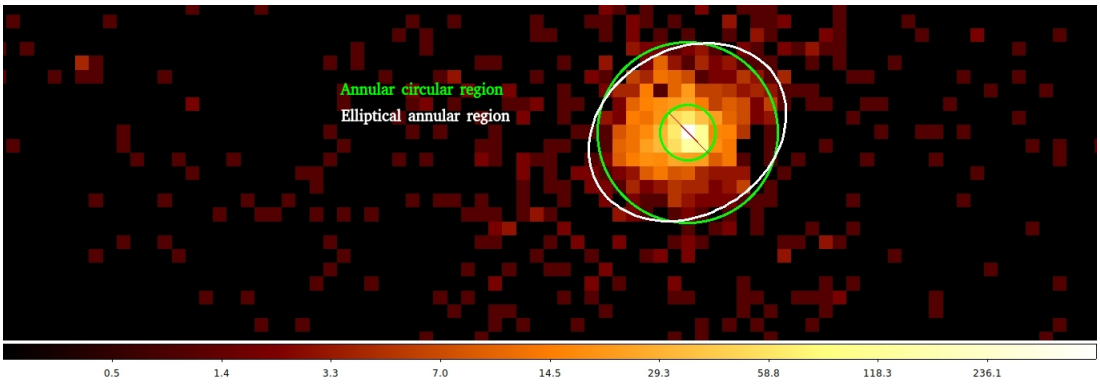

(c)

Figure 3.1: The choice of different extraction regions for the NGC613 *Chandra* observation at energy of $0.3 - 7.0\ keV$. In (a) we show the background region in yellow; in (b) we show the nuclear region ($r = 2''$) in blue, the circular source region ($r = 6.5''$) in cyan and the elliptical source region ($a = 7.4''$ and $b = 5.9''$) in magenta. These regions were selected in order to investigate the nuclear and the total emission, respectively. In (c) we show the annular region in green and the elliptical annular region in white. These two regions were selected in order to study the diffuse emission of the source.

Energy range (keV)	Extraction radius ($''$)	counts (cts)
$0.3 - 2.0$	2	338 ± 18
	6.5	982 ± 31
$2 - 7$	2	878 ± 30
	6.5	999 ± 32
$0.3 - 7.0$	2	1216 ± 35
	6.5	1981 ± 44
	$2 < R < 6.5$	762 ± 28
	$a = 7.4$, $b = 5.9$	1993 ± 45
	$a_{min} = b_{min} = 2$, $a_{max} = 7.4$, $b_{max} = 5.9$	775 ± 28

Table 3.1: NGC613 background-subtracted counts in the selected extraction regions, in each energy range considered.

From the previous regions we extracted and visualized the background-subtracted light curves. They show how the flux of the source varies during the observation.
The light curves are fitted with constant models to check the variability of NGC613. In Fig. 3.2 we show the light curves of NGC613 for the nuclear region in three energy ranges. In Fig. 3.3 we show in (a),(b),(c) the light curves for the circular source region in the three energy ranges and in (d) for the elliptical source region in the full energy band. In Fig. 3.4 we show in (a) the light curves for annular regions and in (b) for the elliptical annular region in the energy range $0.3 - 7.0$ keV.
By observing the light curves, we deduced that the variability is mainly influenced by the nuclear part of the source. Indeed, it drastically decreases if we exclude the nucleus by using annular regions, for which there is not variability at all. Light curves corresponding to the soft part of the spectrum $0.3 - 2.0$ keV do not show variability ($\sim 0.3\sigma$); therefore, the observed variability in the energy range of $0.3 - 7.0$ keV is mainly governed by that of the nuclear component. AGN exhibit rapid, high-amplitude stochastic flux variations across the entire electromagnetic spectrum on time-scales ranging from hours to years (e.g., Smith 1996, Kasliwal et al. 2016). Hence, variability is a typical feature of AGN. In Table 3.2, we report the statistical significance of variability for the previously selected light curves.
Finally, with the task `specextract` we extracted the source and background spectra, and produced the response matrices, i.e., the *Redistribution Matrix File* (RMF) and the *Auxiliary Response File* (ARF). The RMF associates to each instrument channel the energy of the detected photons, while the ARF is related to the effective area (described in Section 2.1). Using this task we also grouped 25 counts for each bin of the spectrum, in order to have enough counts in each bin to be in the Gaussian regime, hence to apply the χ^2-statistics.

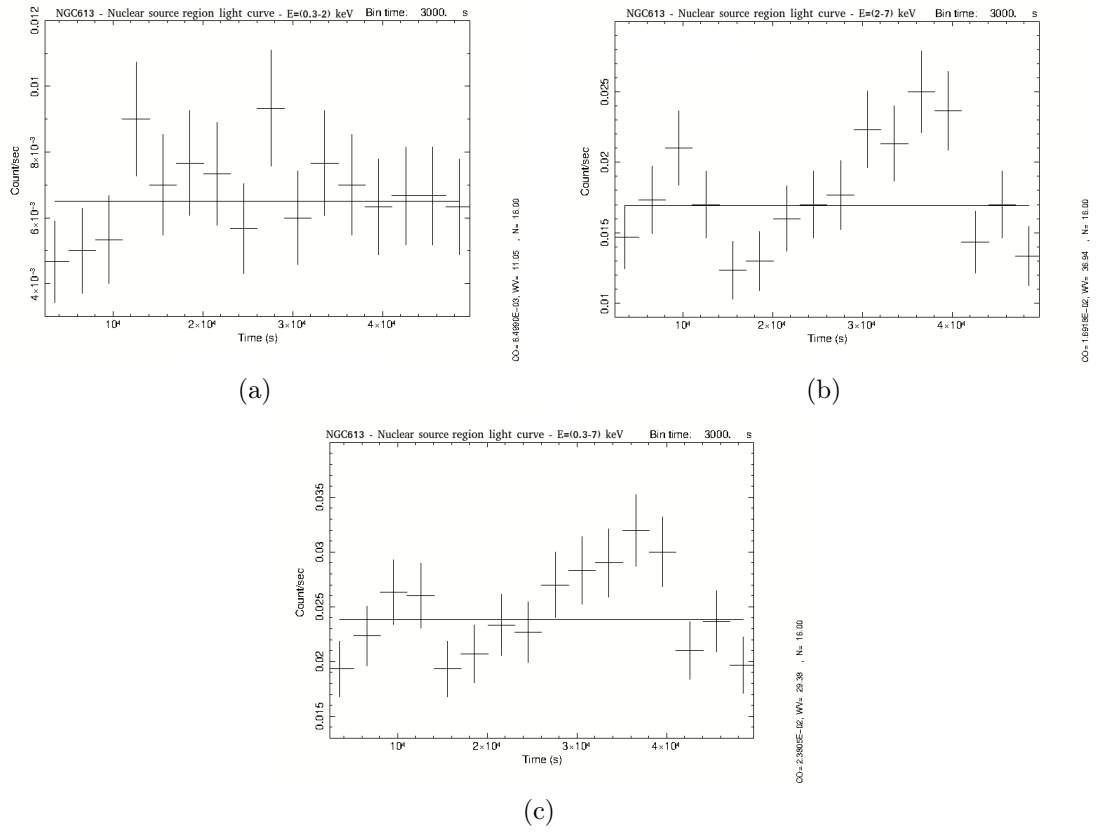

Figure 3.2: Light curves for the nuclear region (extraction radius of $2''$) in the different energy ranges considered. Light curves have been extracted with a time binning of 3000 s.

Table 3.2: Variability and its statistical significance for the selected regions in each energy range considered for NGC613.

Region	Energy range (keV)	$dof^{(1)}$	$CO^{(2)}$	χ^2	$(1-Q^{(3)})$
Nuclear	$0.3-2.0$	15	6.5×10^{-3}	11.1	$25.10\% \approx 0.3\sigma$
	$2-7$	15	1.69×10^{-2}	36.9	$99.88\% \approx 3.0\sigma$
	$0.3-7.0$	15	2.38×10^{-2}	29.4	$98.57\% \approx 2.4\sigma$
Source	$0.3-2.0$	15	1.93×10^{-2}	6.3	$25.40\% \approx 0.3\sigma$
+	$2-7$	15	1.94×10^{-2}	38.1	$99.92\% \approx 3.5\sigma$
Nuclear	$0.3-7.0$	15	3.94×10^{-2}	21.8	$88.63\% \approx 1.5\sigma$
	$0.3-7.0$	15	3.95×10^{-2}	23.1	$91.70\% \approx 1.7\sigma$
Annular region	$0.3-7.0$	15	1.52×10^{-2}	7.6	$6.22\% \approx 0.0\sigma$
		15	1.54×10^{-2}	7.0	$4.30\% \approx 0.0\sigma$

(1) Number of *degrees of freedom*, i.e., the number of data-points minus the number of free parameters.
(2) Fitting constant, i.e., the value of the average count rate.
(3) *Chance probability*, i.e., the probability that the source is variable. Our acceptance threshold of variability of 99.9%.

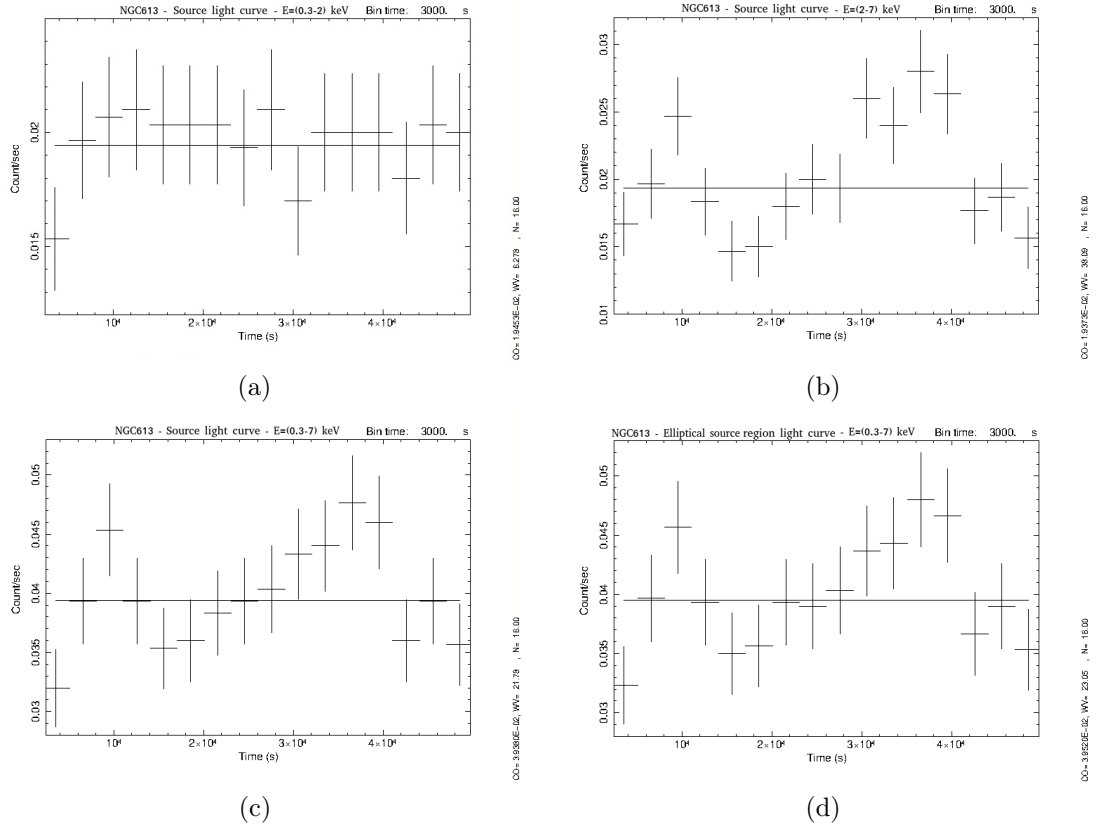

Figure 3.3: Light curves for the source region (extraction radius of 6.5″) in the three energy band (a), (b), (c) and for the elliptical region (extraction major semiaxis $a = 7.4''$ and minor semiaxis $b = 5.9''$) (d) in the full energy range. Light curves have been extracted with a time binning of 3000 s.

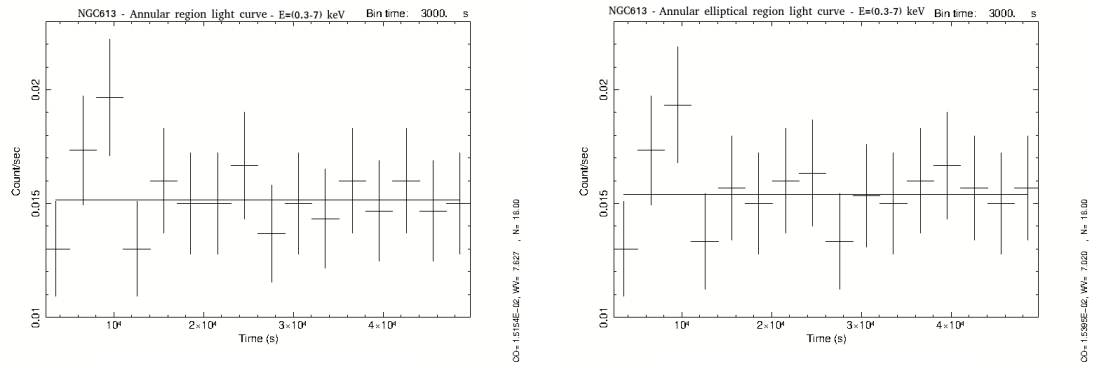

Figure 3.4: Light curves for the annular region ($2'' < R < 6.5''$) (a) and elliptical annular region ($a_{min} = b_{min} = 2''$, $a_{max} = 7.4''$, $b_{max} = 5.9''$) (b) in the full energy range. Light curves have been extracted with a time binning of 3000 s.

NGC1808

The *Chandra* image clearly show that the X-ray emission of central regions NGC1808 is most probably a mixture of diffuse and blob-like structures (see Fig. 3.5).

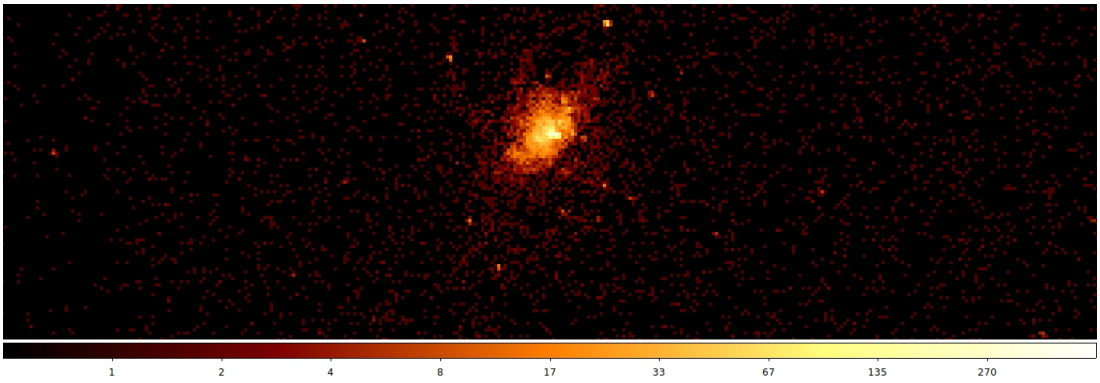

(a)

Figure 3.5: Zoom of the NGC1808 central 300×100 $arcsec^2$ in the energy range of 0.3−7.0 keV.

In order to study both the nuclear properties and the total emission, we have selected various regions to perform the spectral analysis. In particular, we chose the background region (the yellow circle in Fig. 3.6(a)) with a radius of $40''$, the source nuclear region (the blue circle in Fig. 3.6(b)) with a radius of $1.5''$ and the source region (the magenta ellipse in Fig. 3.6(a)). In order to maximize the signal-to-noise ratio, the source region representative of the galaxy has been chosen elliptical with a major semiaxis $a = 15''$, a minor semiaxis $b = 7.5''$ and an inclination angle of $\theta = 45$. $1''$ corresponds to ~ 45 pc, when evaluated at the redshift of the source ($z \simeq 0.0033$).

Unlike NGC613, the nuclear region is selected with an extraction radius of $1.5''$. It should be noted that, even in the hard band, there are various emission blobs, most likely due to X-ray binaries, typical of starburst sources such as NGC1808 (e.g., Forbes et al. 1992, Collison et al. 1994, Jiménez Bailón et al. 2005, Bush et al. 2017, Salak et al. 2018). Therefore, we decided to select the brightest hard X-ray source as the core of the galaxy, taking into account also the position of the continuum emission peak obtained from the ALMA map at 345 GHz. For this source we have chosen a smaller radius with respect to the one of NGC613 in order to obtain the contribution of nuclear emissions only, limiting the contribution of the non-nuclear blobs previously described. We analyzed NGC1808 *Chandra* data in the full $0.3 - 7.0$ keV energy band. We also divided it in two ranges: $0.3 - 2.0$ keV (the soft band), in which the emission of diffuse component is expected to be dominant, and $2 - 7$ keV (the hard band), in which the nuclear component, if any, is expected to be dominant. Table 3.3 shows the counts for each energy band for the different extraction regions.

In order to study the variability of NGC1808, we extracted the light curves from the previously discussed regions and tested its behaviour against a constant rate. Figures 3.7 and 3.8 show the light curves of NGC1808 for the nuclear source region and the elliptical source region in three energy ranges, respectively.

From the study of light curves, we observed that NGC1808 does not show a statistically significant variability. Furthermore, the hard band shows a variability with a maximum of 2.0σ confidence level for the nuclear region, which governs the observed variability in the

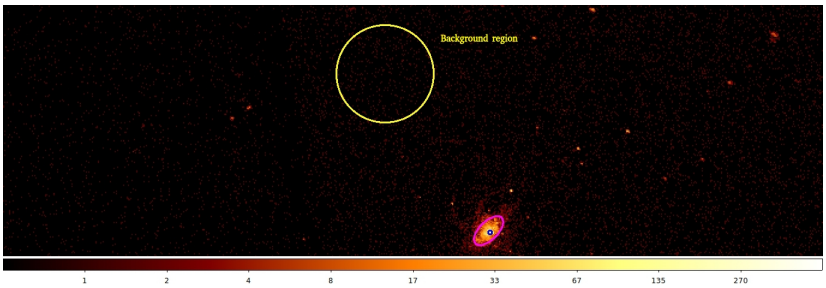

(a)

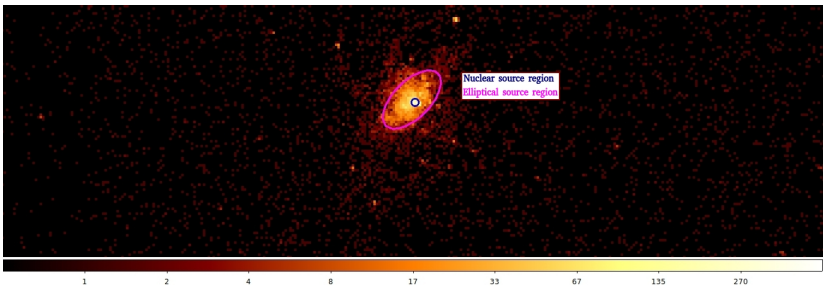

(b)

Figure 3.6: The choice of different extraction regions for the NGC1808 *Chandra* observation at energy of $0.3 - 7.0\ keV$. In (a) we show the background region ($r = 40''$) in yellow; in (b) we show the source nuclear region ($r = 1.5''$) in blue and the elliptical source region ($a = 15''$ and $b = 7.5''$) in magenta. These regions were selected in order to investigate the nuclear and the total emission, respectively.

Energy range (keV)	Extraction radius ($''$)	counts (cts)
$0.3 - 2.0$	1.5	887 ± 30
	$a = 15,\ b = 7.5$	5899 ± 77
$2 - 7$	1.5	219 ± 15
	$a = 15,\ b = 7.5$	1343 ± 37
$0.3 - 7.0$	1.5	1106 ± 33
	$a = 15,\ b = 7.5$	7242 ± 85

Table 3.3: NGC1808 background-subtracted counts in the selected extraction regions, in each energy range considered.

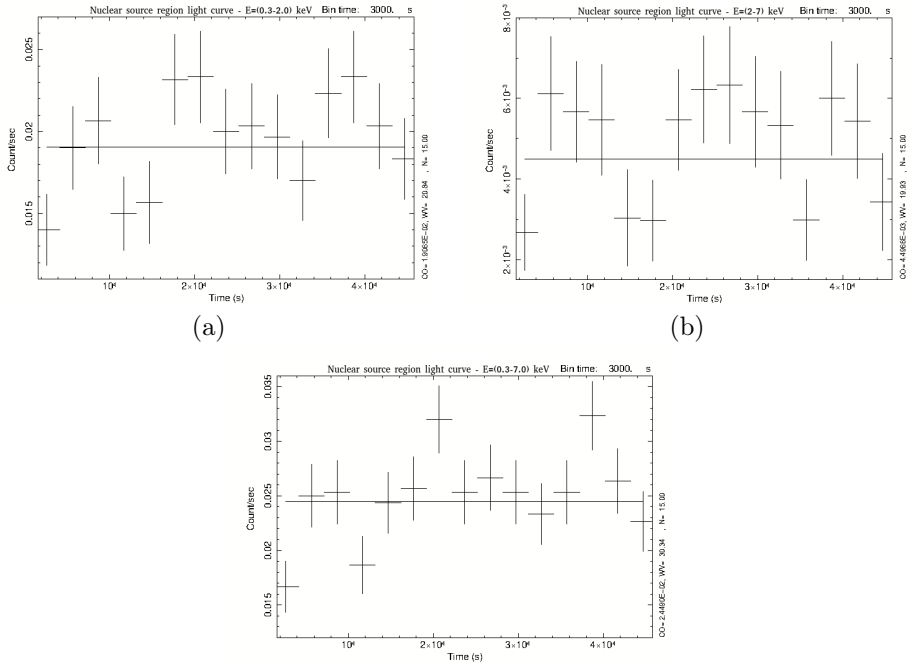

Figure 3.7: Light curves for the nuclear region (extraction radius of 1.5″) in the different energy ranges considered. Light curves have been extracted with a time binning of 3000 s.

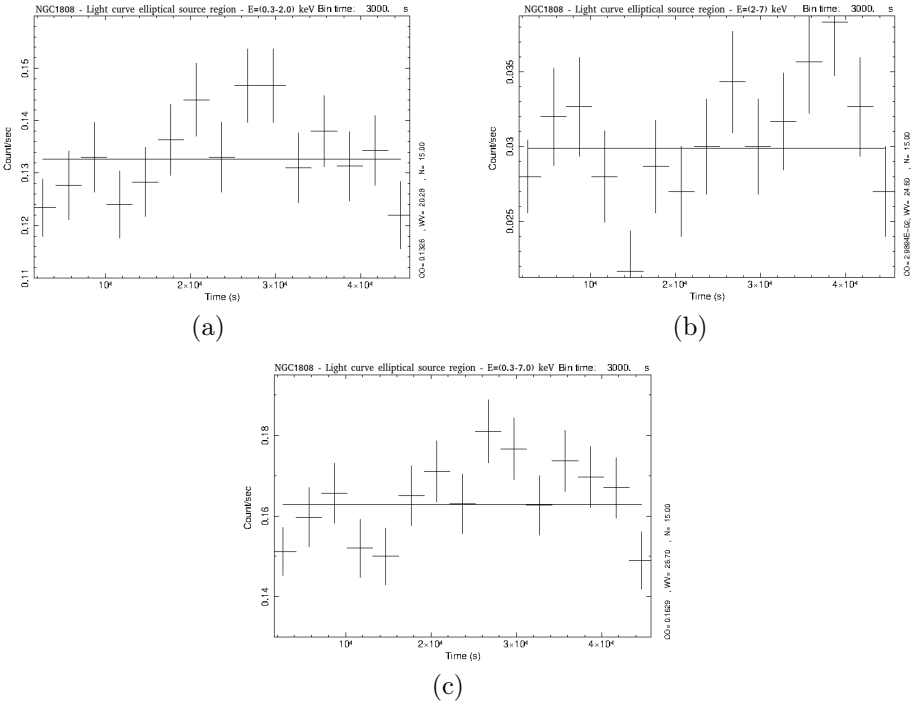

Figure 3.8: Light curves for the source region (extraction major semiaxis $a = 15''$ and minor semiaxis $b = 7.5''$) in the different energy ranges considered. Light curves have been extracted with a time binning of 3000 s.

energy range of $0.3 - 7.0\ keV$.
In Table 3.4, we report the statistical significance of variability for the previously selected light curves.

Table 3.4: Variability and its statistical significance for the selected regions in each energy range considered for NGC1808.

Region	Energy range (keV)	$dof^{(1)}$	$CO^{(2)}$	χ^2	$(1 - Q^{(3)})$
Nuclear	$0.3 - 2.0$	15	1.91×10^{-2}	20.8	$89.42\% \approx 1.6\sigma$
	$2 - 7$	15	4.50×10^{-3}	19.9	$86.77\% \approx 1.5\sigma$
	$0.3 - 7.0$	15	4.45×10^{-2}	30.3	$99.32\% \approx 2.7\sigma$
Source	$0.3 - 2.0$	15	0.13	20.3	$87.85\% \approx 1.5\sigma$
+	$2 - 7$	15	2.99×10^{-2}	24.6	$96.13\% \approx 2.0\sigma$
Nuclear	$0.3 - 7.0$	15	0.16	26.7	$97.90\% \approx 2.3\sigma$

(1) Number of *degrees of freedom*, i.e., the number of data-points minus the number of free parameters.
(2) Fitting constant, i.e., the value of the average count rate.
(3) *Chance probability*, i.e., the probability that the source is variable. Our acceptance threshold of variability of 99.9%.

Finally, we extracted the source and background spectra, produced the response matrices (RMF and ARF) and, in order to apply the χ^2-statistics, we grouped the photons in order to have at least 25 counts in each bin of the spectrum.

3.2 XMM-Newton data analysis

For each source, we visualized the cleaned event file (see Section 2.2.3) with the *ds9* viewer; as we carried out for *Chandra*, we used *ds9* to select the regions of interest. In particular, we defined source and background regions. Despite the FWHM of XMM-*Newton* is higher than that of *Chandra* (see, e.g., Tables 2.1 and 2.2), in Fig. 3.9-3.13 it is possible to distinguish both the nuclear emission and the diffuse one. The latter can be visualized on much larger scales with respect to *Chandra*, thanks to the possibility of XMM-*Newton* to collect a large number of photons (see Fig. 2.7).

NGC613

The radius of the source region was chosen by taking into account the PSF, and the associated EEF; we decided to use an aperture which contains 90% of the total energy at 5.0 keV: 37.6″ in the case of MOS1, 38.4″ for MOS2 and 31.4″ in the pn case. The background region was selected with the same criteria described above. We proceeded separately for the three cameras; in Fig. 3.9 we show the previously described regions.

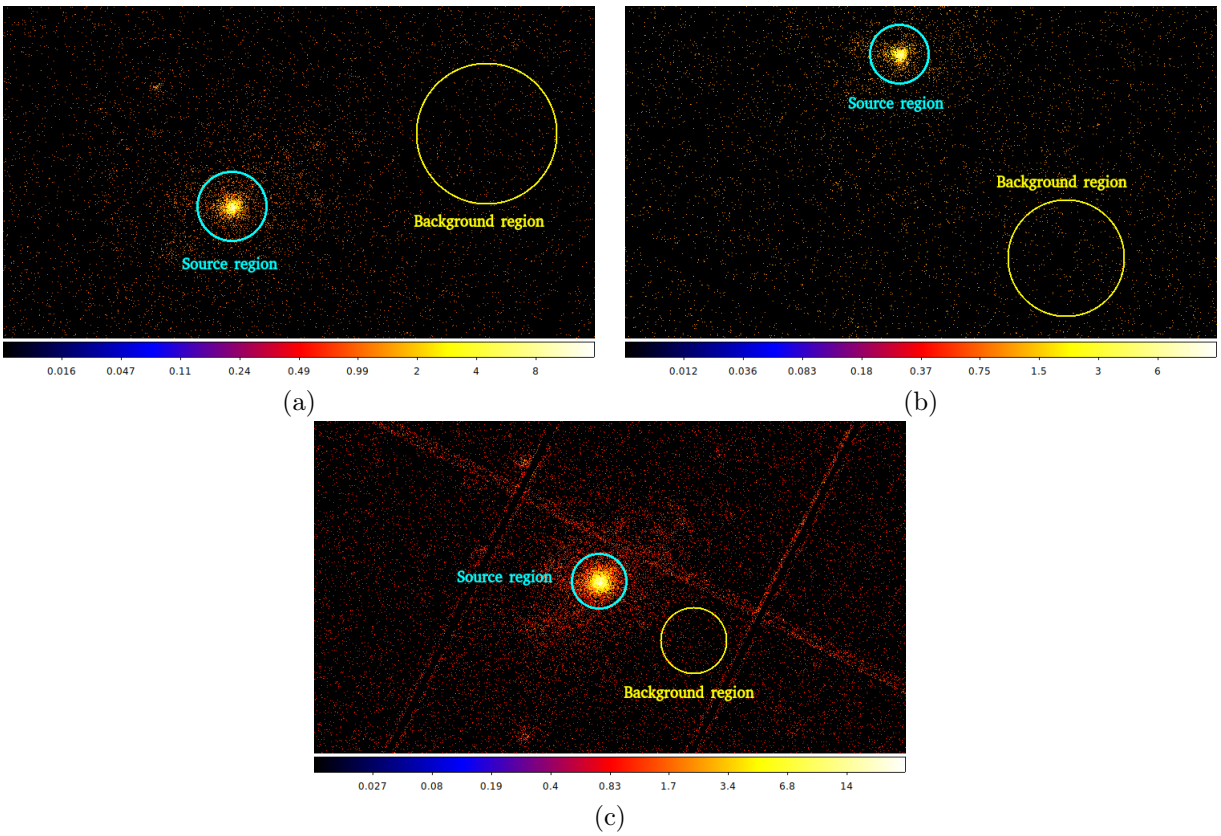

Figure 3.9: Extraction regions for NGC613 XMM-*Newton* observation in the energy range $0.3 - 10$ keV. The circular source region is shown in cyan and the background region in yellow for MOS1 (a), MOS2 (b) and PN (c) cameras. The sizes of the extraction regions are reported in the text.

In Table 3.5 we report the counts for NGC613 the source extraction regions.

Energy range (keV)	Camera	Region	Extraction radius (″)	counts (cts)
0.3 − 2.0	MOS1	Source	37.6	1779 ± 42
		Background	70.0	55 ± 7
	MOS2	Source	38.4	1515 ± 39
		Background	70.0	42 ± 7
	pn	Source	31.4	4514 ± 67
		Background	33.0	117 ± 11
2 − 10	MOS1	Source	37.6	744 ± 27
		Background	70.0	71 ± 8
	MOS2	Source	38.4	2218 ± 47
		Background	70.0	53 ± 7
	pn	Source	31.4	1757 ± 42
		Background	33.0	105 ± 10
0.3 − 10.0	MOS1	Source	37.6	2543 ± 50
		Background	70.0	126 ± 11
	MOS2	Source	38.4	3733 ± 61
		Background	70.0	95 ± 10
	pn	Source	31.4	6271 ± 79
		Background	33.0	222 ± 15

Table 3.5: Source and background counts in each energy range considered for MOS and pn cameras.

We extracted and visualized the background-subtracted light curves for the three source regions. In Fig. 3.10−3.12, we show the source light curves for MOS and pn cameras in the three energy ranges. Analogously as for *Chandra* light curves, the trend of the curves shows that the variability is mainly influenced by the hard emission of the source. The soft part variability is negligible and "fluctuations" appear to be largely governed by the core itself. Pn and MOS2 cameras show a similar trend of variability, with a confidence level of 4.0σ.Finally, we do not observe a significant variability for MOS1 camera (in the hard band the confidence level is below 2.5σ).
In Table 3.6, we report the statistical significance of the variability for the various light curves.
Finally, we extracted the source and background spectra. With the task `backscale` we re-scaled the background area to that of the source area. With the tasks `rmfgen` and `arfgen` we created the two response matrices, (RMF) and (ARF). In order to apply the χ^2-statistics with the task `grppha` we included at least 25 counts in each bin of the spectrum.

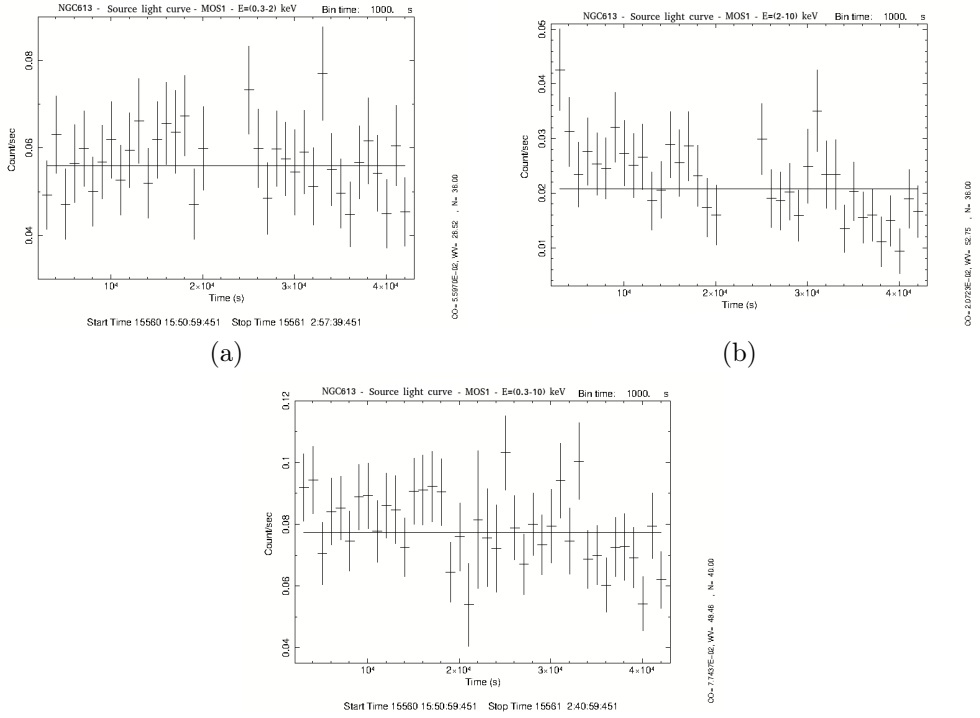

Figure 3.10: Light curves of MOS1 camera for the source region $r = 37.6''$ in the three energy ranges. Light curves have been extracted with a time binning of 1000 s.

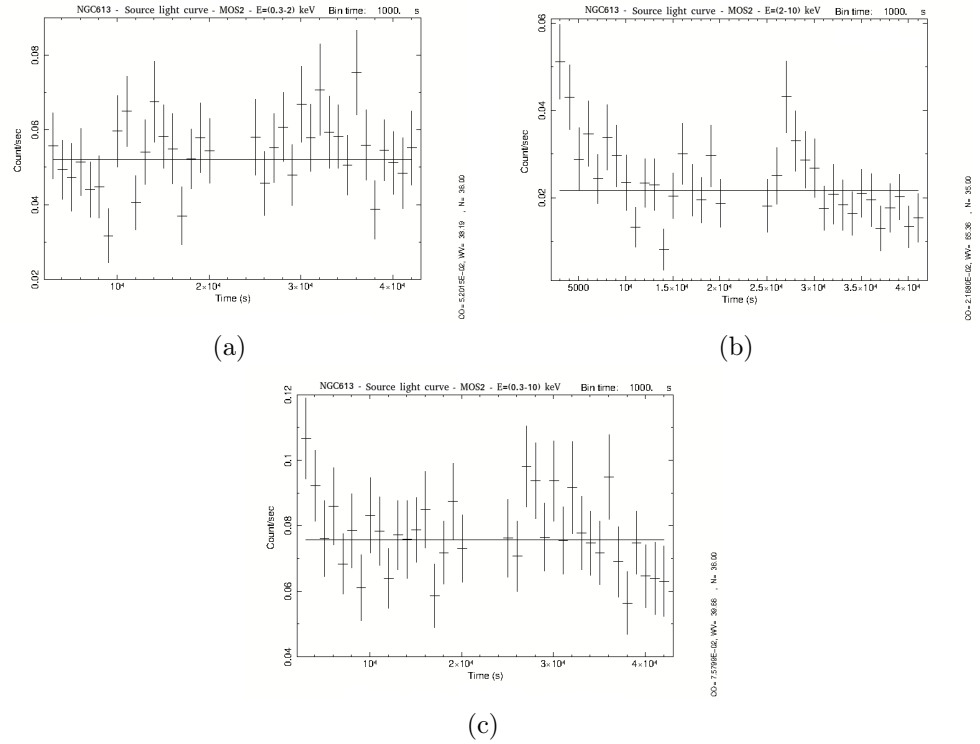

Figure 3.11: Light curves of MOS2 camera for the source region $r = 38.4''$ in the three energy ranges. Light curves have been extracted with a time binning of 1000 s.

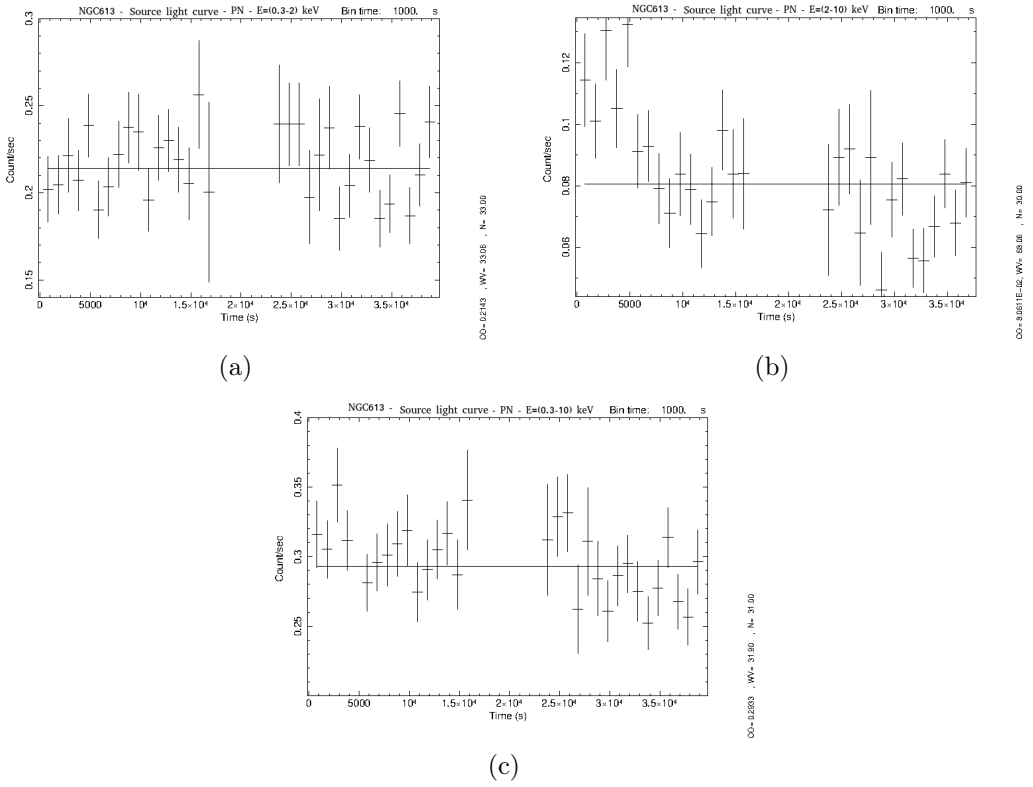

Figure 3.12: Light curves of pn camera for the source region $r = 31.4''$ in the three energy ranges. Light curves have been extracted with a time binning of 1000 s.

Table 3.6: Variability and its statistical significance for the selected regions in each energy range considered.

Camera	Region	Energy range (keV)	$dof^{(1)}$	$CO^{(2)}$	χ^2	$(1 - Q^{(3)})$
MOS1	Source	$0.3 - 2.0$	35	5.60×10^{-2}	26.5	$15.21\% \approx 0.1\sigma$
		$2 - 10$	35	2.07×10^{-2}	52.8	$97.25\% \approx 2.2\sigma$
		$0.3 - 10.0$	34	7.85×10^{-2}	42.0	$83.71\% \approx 1.4\sigma$
MOS2	Source	$0.3 - 2.0$	35	5.20×10^{-2}	38.2	$67.35\% \approx 0.9\sigma$
		$2 - 10$	34	2.17×10^{-2}	65.4	$99.91\% \approx 3.5\sigma$
		$0.3 - 10.0$	35	7.58×10^{-2}	39.7	$73.01\% \approx 1.1\sigma$
pn	Source	$0.3 - 2.0$	32	0.21	33.1	$58.49\% \approx 0.8\sigma$
		$2 - 10$	29	8.06×10^{-2}	63.1	$99.99\% \approx 4.0\sigma$
		$0.3 - 10.0$	30	0.29	31.9	$62.79\% \approx 0.9\sigma$

(1) Number of *degrees of freedom*.
(2) Fitting constant.
(3) *Chance probability*. Our acceptance threshold of variability of 99.9%.

NGC1808

We chose an elliptical source and circular background regions, following the criteria described above (see Fig. 3.13): we selected an elliptical shape in order to represent the source region with major semiaxis $a = 40.0''$, minor semiaxis $b = 33.0''$ and an inclination angle of $\theta = 52°$ for the MOS1 camera, $a = 42.0''$, $b = 32.0''$ and $\theta = 52°$ for the MOS2 camera and $a = 33.5''$, $b = 21.5''$ and $\theta = 52°$ for the pn camera. For the background region we selected a circular shape with a radius of $r = 70''$ for both MOS cameras and $r = 30''$ for pn camera. The three cameras were analyzed separately, as for NGC613.

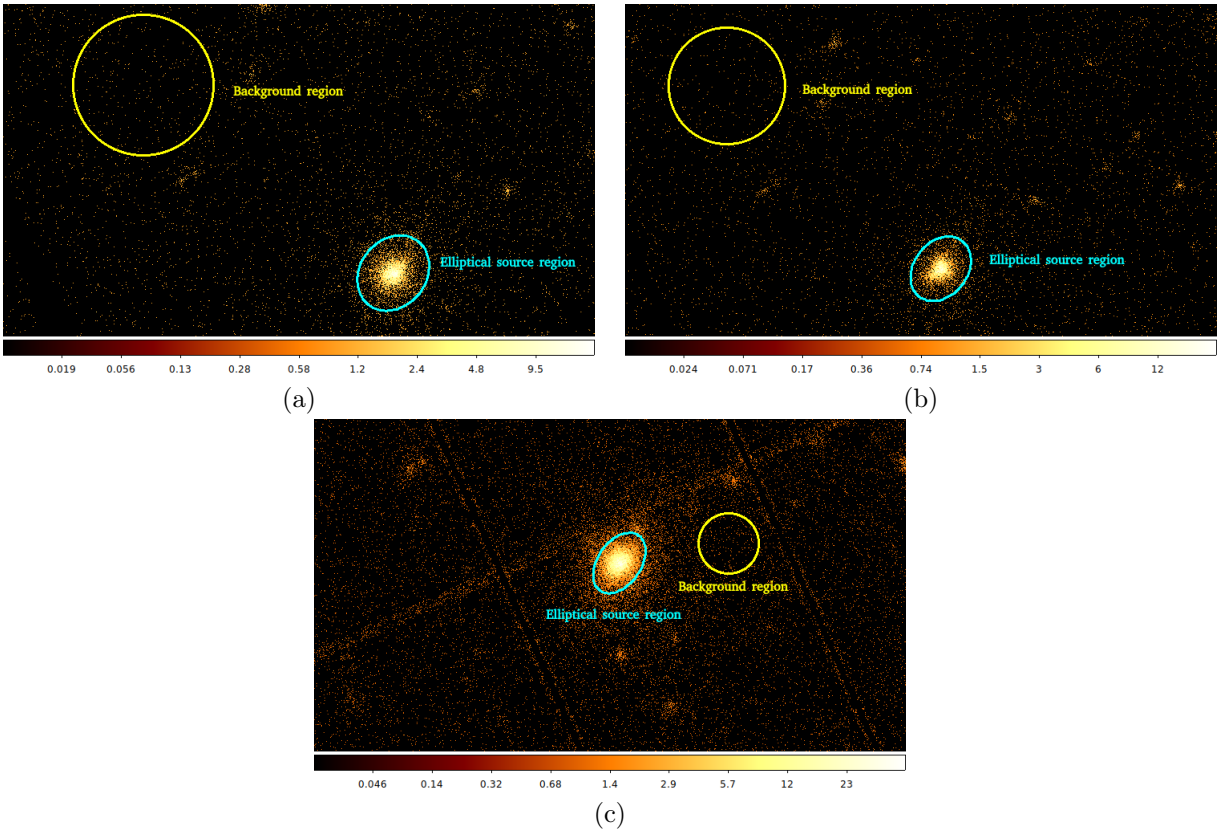

Figure 3.13: Extraction regions for NGC1808 XMM-*Newton* observation in the energy range $0.3 - 10\ keV$. The elliptical source region is shown in cyan and the background region in yellow for MOS1 (a), MOS2 (b) and pn (c) cameras. The sizes of the extraction regions are reported in the text.

Table 3.7 shows the counts corresponding to the different extraction regions for NGC1808. In Fig. 3.14−3.16, we show the extracted source light curves for MOS and pn cameras in the three energy ranges.
Since the variability in the hard band is $\leq 1.4\sigma$ and that the hard band is the one from which we hypothesize the higher variability, NGC1808 variability is negligible. In Table 3.8, we report the statistical significance of the variability for the various light curves.

Energy range (keV)	Camera	Region	Extraction radius ($''$)	counts (cts)
$0.3 - 2.0$	MOS1	Source	$a = 40$, $b = 33$	4065 ± 64
		Background	70.0	53 ± 7
	MOS2	Source	$a = 42$, $b = 32$	4297 ± 66
		Background	70.0	69 ± 8
	pn	Source	$a = 33.5$, $b = 21.5$	10081 ± 100
		Background	30.0	102 ± 10
$2 - 10$	MOS1	Source	$a = 40$, $b = 33$	1214 ± 35
		Background	70.0	34 ± 6
	MOS2	Source	$a = 42$, $b = 32$	1277 ± 36
		Background	70.0	31 ± 6
	pn	Source	$a = 33.5$, $b = 21.5$	2784 ± 53
		Background	30.0	70 ± 8
$0.3 - 10.0$	MOS1	Source	$a = 40$, $b = 33$	5279 ± 73
		Background	70.0	87 ± 9
	MOS2	Source	$a = 42$, $b = 32$	5574 ± 75
		Background	70.0	100 ± 10
	pn	Source	$a = 33.5$, $b = 21.5$	12865 ± 113
		Background	30.0	172 ± 13

Table 3.7: Source and background counts in each energy range considered for MOS and pn cameras.

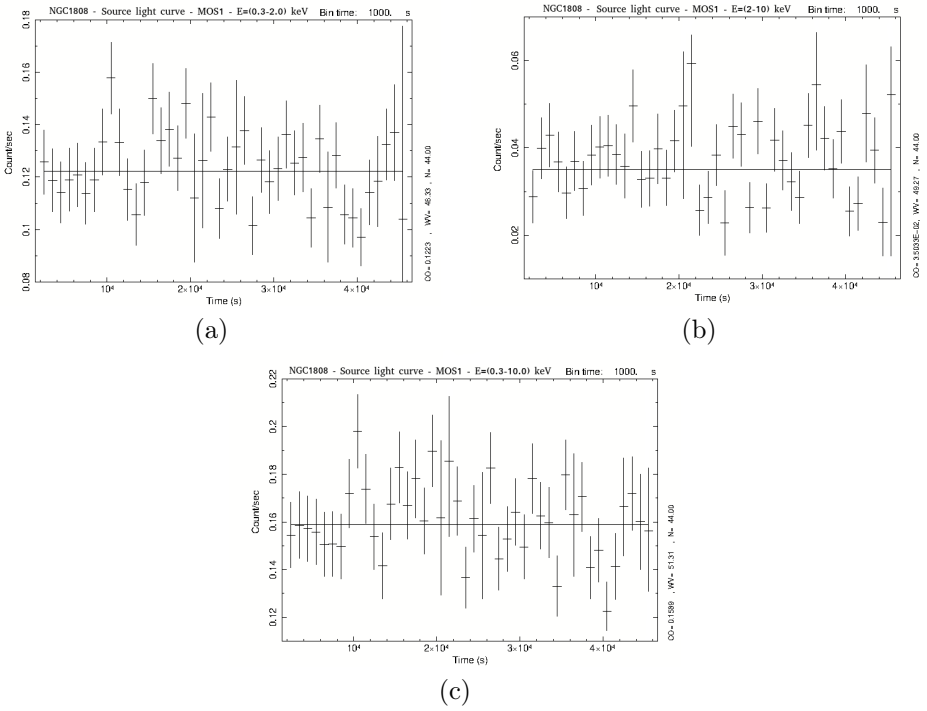

Figure 3.14: Light curves of MOS1 camera for the elliptical source region $a = 40.0''$, $b = 33.0''$ in the three energy ranges. Light curves have been extracted with a time binning of 1000 s.

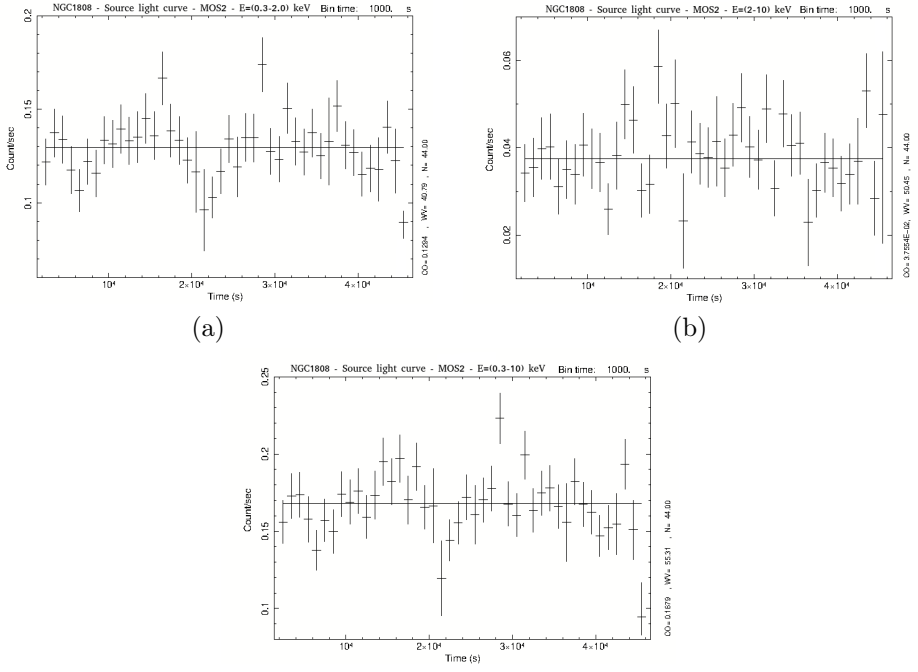

Figure 3.15: Light curves of MOS2 camera for the elliptical source region $a = 42.0''$, $b = 32.0''$ in the three energy ranges. Light curves have been extracted with a time binning of 1000 s.

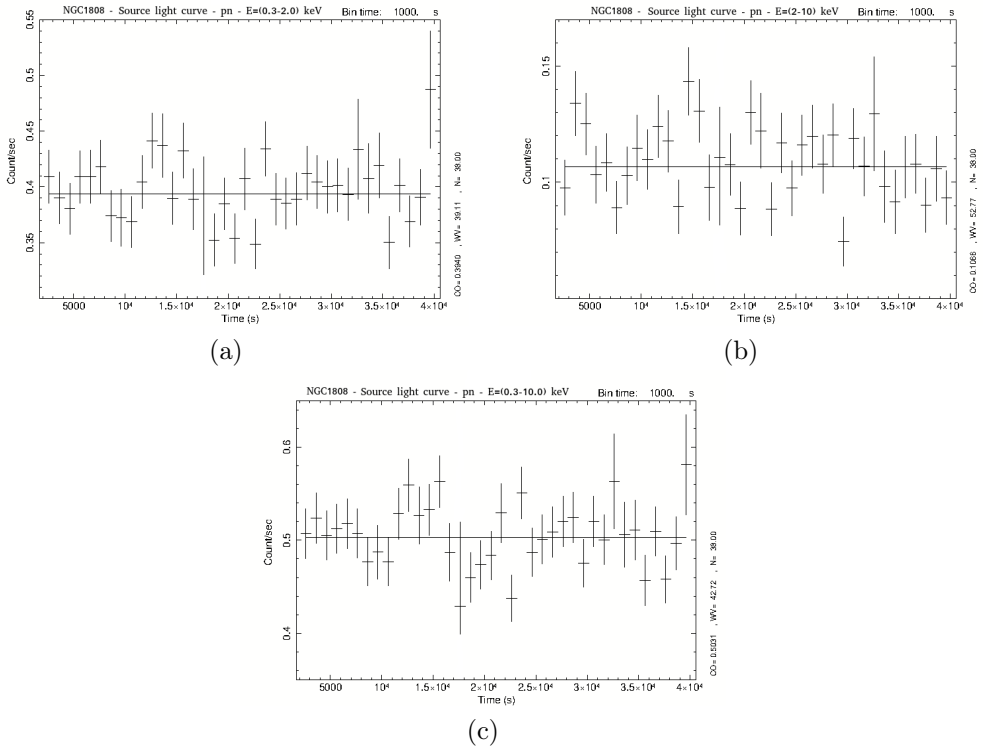

Figure 3.16: Light curves of pn camera for the elliptical source region $a = 33.5''$, $b = 21.5''$ in the three energy ranges. Light curves have been extracted with a time binning of 1000 s.

Table 3.8: Variability and its statistical significance for the selected regions in each energy range considered.

Camera	Region	Energy range (keV)	$dof^{(1)}$	$CO^{(2)}$	χ^2	$(1 - Q^{(3)})$
MOS1	Source	$0.3 - 2.0$	43	0.12	46.3	$66.34\% \approx 0.9\sigma$
		$2 - 10$	43	3.50×10^{-2}	49.3	$76.33\% \approx 1.1\sigma$
		$0.3 - 10.0$	43	0.16	51.3	$82.00\% \approx 1.3\sigma$
MOS2	Source	$0.3 - 2.0$	43	0.12	40.8	$42.25\% \approx 0.5\sigma$
		$2 - 10$	43	3.76×10^{-2}	50.5	$79.74\% \approx 1.2\sigma$
		$0.3 - 10.0$	43	0.16	55.3	$90.13\% \approx 1.6\sigma$
pn	Source	$0.3 - 2.0$	43	0.39	39.1	$35.94\% \approx 0.4\sigma$
		$2 - 10$	43	0.11	52.8	$85.40\% \approx 1.4\sigma$
		$0.3 - 10.0$	43	0.50	42.73	$51.71\% \approx 0.7\sigma$

(1) Number of *degrees of freedom*.
(2) Fitting constant.
(3) *Chance probability*. Our acceptance threshold of variability of 99.9%.

Finally, we extracted the source and background spectra, re-scaled the background area to that of the source area, generated the RMF and ARF and, in order to apply the χ^2-statistics we grouped at least 25 counts in each bin of the spectrum.

3.3 X-ray spectral models

In the first part of this Section, we will describe the components of the *phenomenological* best-fit models. They are obtained from the composition of various individual components, each of which describes a different spectral property. In the second part, we will present the *physically motivated* models used in order to obtain more detailed physical analysis. The phenomenological approach is important in order to describe the general properties of the source while the physical approach allows for the geometric description.
The spectral analysis and its fitting has been conducted with the `Xspec` software[1], version 12.11.1 (Arnaud et al. 1996).

3.3.1 Phenomenological model components

Here we briefly describe the individual components used in the phenomenological best-fit models.

Absorption components: wabs, phabs

The absorbed emission in heavily obscured AGN, as described in Section 1.5, is considered by using a photoelectric absorption (Morrison et al. 1983) component located at the redshift of the source (`zwabs`, `zphabs`). This component can be express as

$$M(E) = exp[-N_H \sigma(E[1+z])] \ , \tag{3.1}$$

where N_H is the hydrogen column density in units of 10^{22} $atoms/cm^2$, σ is the photoelectric cross-section (not including Thomson scattering) in units of cm^2, depending on the observed energy and on the redshift z.
In order to take into account the Galactic absorption (i.e., the absorption by the Milky Way), we must consider another absorption component. In this case, $N_H = 1.56 \times 10^{20}$ cm^{-2} for NGC613 and $N_H = 2.33 \times 10^{20}$ cm^{-2} for NGC1808 (Kalberla et al. 2005) is considered as a fixed component in all modelings.

Partial absorption component: zpcfabs

In order to take into account the complex internal structure (extended hard X-ray emission) of NGC1808, we used a partial covering fraction absorption component `zpcfabs`. It is parametrized as:

$$M(E) = f \exp[-N_H \sigma(E[1+z])] + (1-f) \ , \tag{3.2}$$

where $\sigma(E)$ is the photoelectric cross-section, N_H is the equivalent hydrogen column (in units of 10^{22} atoms cm^{-2}), f is the dimensionless covering fraction ($0 < f \leq 1$) and z is the redshift. For NGC1808 we used this component in order to take into account either an intrinsically patchy nature of the (absorber) torus or a double powerlaw component, one due to the nucleus and one due to the binaries. In fact, when binaries are not in high accretion phase, their emission is dominated by a hard powerlaw due to Comptonization.

[1] https://heasarc.gsfc.nasa.gov/xanadu/xspec

Primary emission: zpowerlaw

In order to consider the main powerlaw described in 1.4, we use a simple photon `powerlaw`. The `zpowerlw` variant takes into account a redshifted spectrum and it is parametrized as

$$A(E) = K[E(1+z)]^{-\Gamma} \ , \tag{3.3}$$

where K is the powerlaw normalization constant in unit of $photons/keV/cm^2/s$ at 1 keV and Γ is the photon index of the powerlaw (dimensionless). K and Γ are free parameters and $z = 0.0049$[2] for NGC613 and $z = 0.0033$ for NGC1808 are kept fixed.
To reproduce the contribution to the soft part of the spectrum of the scattered and unabsorbed photons, we also used a second powerlaw, with the same photon index of the primary one, but different normalization.

Thermal emission component: mekal

The `mekal` component is representative of the thermal emission from hot diffuse gas (Mewe et al. 1985). In first approximation, the soft emission (below $\sim 2-3$ keV) in the X-ray spectrum of AGN can be represented by this component. This model also includes some emission lines such as C, N, O and Si. The main `mekal` parameters are: plasma temperature kT expressed in keV, hydrogen density in cm^{-3}, metal abundances, redshift and normalization constant. We used two `mekal` components to reproduce complex thermal emission.

Emission line component: zgauss

This component is added to the model with the aim of modeling the emission lines which are present in the AGN X-ray spectrum. The emission lines can be modeled using a Gaussian line profile (`zgauss`) at the fixed redshift of the source:

$$A(E) = K\frac{1}{(1+z)\sigma \times \sqrt{2\times\pi}} \exp\left(\frac{-(E(1+z)-E_l)^2}{2\sigma^2}\right) \ , \tag{3.4}$$

where E_l is the line energy expressed in keV, σ is the line width in keV and K is the normalization constant.

Reflection component: pexmon

`Pexmon` is an `Xspec` component used to reproduce an exponential cut-off of the powerlaw spectrum, reflected from neutral material (i.e., the `pexrav`, Magdziarz & Zdziarski 1995). `pexmon` comprises `pexrav` by adding self-consistent Fe and Ni lines. It is the sum of the primary powerlaw and the reflection component. This component has several parameters: the powerlaw photon index Γ, the cut-off energy E_c in keV, the scaling factor for reflection, the redshift, the abundance of elements heavier than He relative to Solar values, the inclination angle and the normalization.

[2] $https://ned.ipac.caltech.edu/$

3.3.2 Physically motivated models

In this subsection we will describe the physically motivated models used for the analysis of NGC613. Both `MYTorus` and `borus02` are designed to reproduce X-ray spectra supported by Monte-Carlo simulations. The two models can provide estimates for the intrinsic column density of the obscuring torus and information on its geometry, e.g., the inclination angle (`MYTorus`) and the covering factor (`borus02`).

MYTorus

`MYTorus` (Murphy & Yaqoob 2009) was designed for modeling X-ray spectra of active galaxies, in particular for spectral fittings of Compton-thick sources. It is used for column densities in the range $10^{22} - 10^{25}$ cm^{-2}. `MYTorus` was developed to be used in the `Xspec` environment and based on a combination of additive and multiplicative tables. It simulates the interaction between the obscuring material and the radiation. This model adopts a doughnut-like, azimuthally symmetric geometry for the torus, assuming that the reprocessing material is uniform, neutral and cold. In Fig. 3.17 we illustrate the main geometrical parameters of the obscuring torus used in this model.

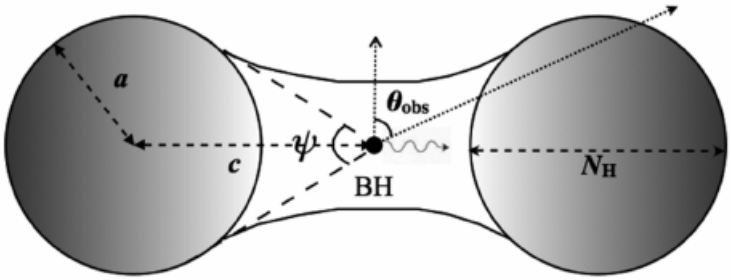

Figure 3.17: Geometrical parameters of `MYTorus`. The BH (filled circle) is located at the center of the torus and is assumed to be coincident with the (isotropically) illuminating X-ray source. θ_{obs} is the inclination angle. N_H is the equatorial column density of the torus, defined along the diameter of the section of the doughnut. c is the distance of the BH to the center of the torus section and a is the radius of the torus section (from Murphy & Yaqoob 2009).

We can calculate the line of sight column density $N_{H_{l.o.s}}$ as

$$N_{H_{l.o.s}} = N_H \left[1 - \left(\frac{c}{a}\right)^2 \cos^2 \theta_{obs}\right]^{\frac{1}{2}} , \tag{3.5}$$

where N_H is the equatorial column density, i.e., the equivalent hydrogen column density through the diameter of the doughnut-like torus, θ_{obs} is the observation angle, i.e., the angle between the observer's line of sight and the symmetry axis of the torus ($\theta_{obs} \in [0°, 90°]$). If $\theta_{obs} = 0°$, the observer looks directly at the nucleus which is in the *face-on configuration*; if $\theta_{obs} = 90°$, the observer line of sight intercepts the torus equator which is in the *edge-on configuration*. The torus half opening angle represents the fraction of the sky as seen from the center and is defined as $\alpha = [(\pi - \psi)/2] = 60°$. a is the radius of the torus section and c is the distance of the SMBH to the center of the torus section (see Fig. 3.17).
There are three groups of model components that combine to produce the total spectrum:

- **zeroth-order continuum (MYTZ)**: this component, also known as *direct component*, is composed by the incident photons that do not interact (absorbed or scattered) with the torus and escape it. The column density of this component represents $N_{H_{l.o.s.}}$;
- **scattered continuum (MYTS)**: this component, also known as *reprocessed component*, takes into account the escaping photons scattered in the reprocessing medium at least once. The column density of this component represents N_H;
- **fluorescent emission lines (MYTL)**: this component takes into account the possibility of having the Fe K_α and K_β fluorescence emission lines (`MYTorus` models consider these two emission lines only). The line emission component combines the zeroth-order and the scattered.

`MYTorus` can been used in two different configurations, *coupled* and *decoupled*. In the former, N_H is fixed to be equal to $N_{H_{l.o.s.}}$, therefore it is not possible to characterize the internal structure of the torus. In the latter, the inclination angle of the direct continuum is fixed to 90° and its column density is a pure line of sight quantity. In this way, the column density of the scattered component is untied from the direct component and represents the average column density. From the ratio between the line of sight and the global average column densities, it is possible to characterize the torus structure: if the ratio is different from 1, then the torus clumpy structure is favored over the smooth one. Based on Yaqoob et al. 2015, in order to reproduce the edge-on and face-on geometry, we fix the MYTS and MYTL inclination angles to be $\theta_{S=L} = 90°$ and $\theta_{S=L} = 0°$, respectively. In Fig. 3.18 we show the difference between the geometry of the reprocessor in the edge-on and the face-on configurations; the former represents the reprocessed photons by the obscuring material, the latter mimics the reprocessed emission coming from the back-side of the torus.

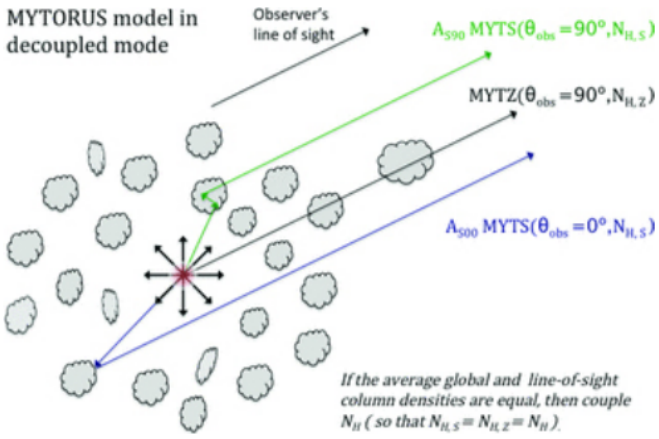

Figure 3.18: Geometry of the torus in the `MYTorus` decoupled configuration. The black arrow represents the zeroth-order component with fixed $\theta_{obs} = 90°$; the blue and the green arrows mimic the scattered component in face-on and edge-on configurations, respectively (from Yaqoob 2012).

borus02

The `borus02` model, developed by Baloković et al. 2018, is an improvement of the `BNtorus` model (Brightman & Nandra 2011). `borus02` is based on template tables computed with

Monte-Carlo simulations of radiative transfer. This model assumes an X-ray point-like source emitting a powerlaw spectrum located at the center of a toroidal distribution of gas. The medium is characterized by a biconical, uniform distribution of matter and the line of sight column density does not depend on the inclination angle of the observer. In Fig. 3.19 we show the main geometrical parameters of the obscuring torus of this model.

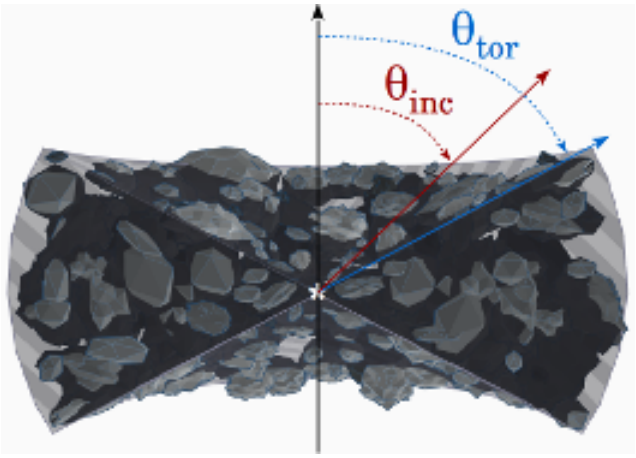

Figure 3.19: The model geometry assumed by `borus02`. The white star represents the central X-ray source. The blue arrow represents the torus opening angle and the red arrow is the torus inclination angle (from Baloković et al. 2018).

The half-opening angle of the biconical distribution θ_{tor}, measured from the symmetry axis clockwise, ranges from 0° to 84°, corresponding to a covering factor range from 0.1 to 1. The covering factor is defined as the cosine of θ_{tor}. θ_{inc} is the torus inclination angle with respect to the symmetry axis and it ranges in [18° - 87°]. Contrary to `MYTorus`, in `borus02` the average column density of the torus and its covering factor are free parameters of the spectral analysis. The main differences with respect to `MYTorus` are related to the possibility to have a free opening angle of the torus (i.e. the covering factor): this is a crucial advantage of this model. Instead of the three tables of `MYTorus`, `borus02` is composed by a single additive table which takes into account the reprocessed emission component and the fluorescent line emission component, such as K_α and K_β lines. In order to take into account the l.o.s. absorption and the losses out of the l.o.s. due to Compton scattering, which are not considered in `borus02`, we must add to the model the combination of Xspec components `zphabs` $*$ `cabs`. In order to reproduce the total spectrum of the NGC613 based on the previous spectral analysis (see Sections 3.4.1 and 3.4.2), `borus02` is implemented with the addition of further components. The primary powerlaw emission multiplied by the previous expression, is represented by `cutoffpl1`; the parameters related to this component (photon index, cut-off energy and normalization) must be tied to those of `borus02` table component. Furthermore, in order to model the scattered unabsorbed reflection of the intrinsic continuum, we add a second cut-off powerlaw represented by `cutoffpl2`. Finally, we also add two thermal components to reproduce the emission at soft energies.

For references where these models have been used see, e.g., Zhao et al. (2019a,b).

3.4 NGC613: X-ray spectral analysis

In this section, we will apply the models discussed in Sections 3.3.1-3.3.2 and report the spectral analysis of NGC613 for both X-ray observations. At first, we build the phenomenological models and the corresponding best-fit is obtained starting from a simple model, enriched step by step by adding further components. The statistical significance of the inclusion of a new component is evaluated through the use of the F-test. In order to give a geometric description of the material surrounding the source, we will then apply `MYTorus` and `borus02`.

3.4.1 Chandra spectral analysis

Let us describe the various steps that led to the construction of the final *Chandra* model. We decided to proceed by adding the components one by one in order to verify their contribution in the spectrum as well as its statistical significance. In the following subsection we will describe the same procedure for the XMM-*Newton* model, by skipping the details which will be analogous to those which we are about to describe for *Chandra*.
The best-fit model for *Chandra* observation of NGC613 was created for each extracted region (see Section 3.1); here we report the models for the elliptical extraction region only, since it is the region with largest statistics, which can allow modeling both the nuclear and the diffuse emission. Unless stated otherwise, errors will be reported at the 90% confidence level for any parameter of interest.
We began with a simple spectral model composed by the main emission powerlaw affected by Galactic absorption. This powerlaw takes into account the primary nuclear emission of the AGN (see Section 1.4). The χ^2_ν results to be 11.4, the resulting spectral fitting is shown in Fig. 3.20 and the residuals plot suggests which additional components are needed.

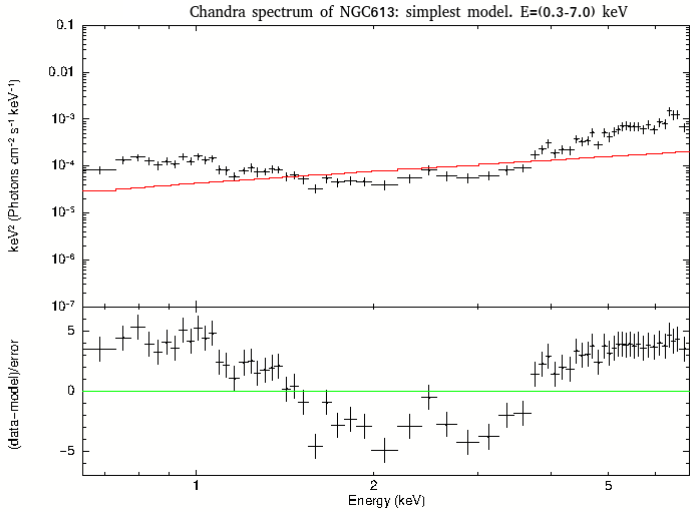

Figure 3.20: The starting model (*wabs*zpo*) applied to *Chandra* spectrum of NGC613. Upper panel: spectral fitting; lower panel: plot of residuals, defined (here and in the following figures) as (data − model)/error, in unit of the error σ. The red line is the best-fit model.

The upper panel of Fig. 3.20 represents the spectral fitting, while the lower panel shows the *residuals*, i.e., the difference between the observed data and the model, in units of the

error σ associated with each spectral datapoint. The second plot represents the statistical significance (χ), parametrizing the "goodness" of the chosen model to fit the data. The residuals in Fig. 3.20 suggest that a more complex model is needed. This first basic model is then expanded by adding new components and the relevance of the new components is carried out through the F-test.
From the residuals plot in Fig. 3.20, it is evident that the model should be corrected to take better account for the soft and the hard parts of the spectrum. Let us focus on the soft part first. The soft emission is governed by two main components: the scattering one, which is expected for obscured AGN, and the host galaxy one, which can be directly observed. In fact, the residuals in Fig. 3.20 show the presence of an absorbed direct component which decreases below 2 keV and a structured component which is prominent below ~ 1 keV (i.e., at the energy of the FeL complex). This could be the imprint of a thermal component. We expanded then the starting model with a second powerlaw with the same Γ of the primary powerlaw (the final photon index results to be $\Gamma = 1.93^{+0.52}_{-0.55}$). This new powerlaw represents the scattering by warm gas in the polar regions, that is, those not covered by the torus. We assume the two photon indices to be identical, since we are dealing with Thompson scattering. The relative intensity is two order of magnitude smaller than the primary one. For this second model we obtained $\chi^2_\nu = 2.5$. In Fig. 3.21 we show the resulting spectral fit.

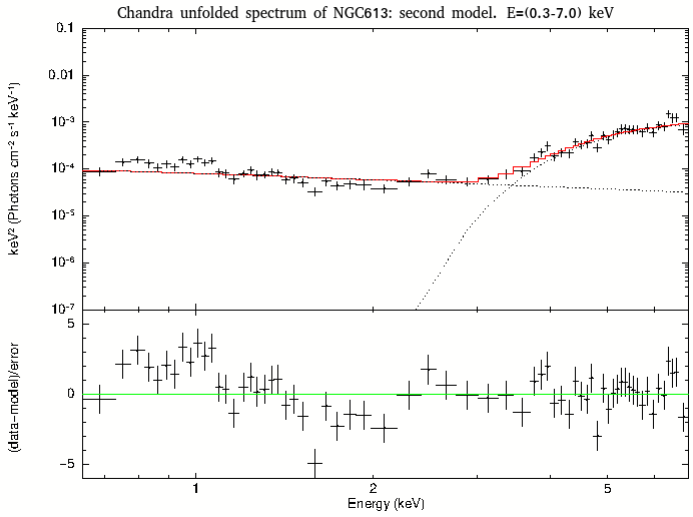

Figure 3.21: The second model (*wabs*(zpo+zwabs*(zpo))*) applied to *Chandra* spectrum of NGC613. Upper panel: spectral fitting; lower panel: residuals plot, i.e., the difference between the observed data and the model, in units of the error σ. The red line is the best-fit model.

From Fig. 3.21 we observe that the soft part of the spectrum is not entirely described by the new component. Therefore, we replaced the soft powerlaw with a thermal component (`mekal`) (see Fig. 3.22) and the reduced chi-squared turned out to be $\chi^2_\nu = 3.0$.
From the residuals in Figures 3.21 and 3.22, we may infer that perhaps both `zpo` and `mekal` components are necessary in order to reproduce the data in the soft part of the spectrum. We then added a powerlaw; this model reproduces fairly well the $0.3 - 7.0$ keV spectrum of NGC613 and we obtained $\chi^2/\text{dof} = 94.1/60$.

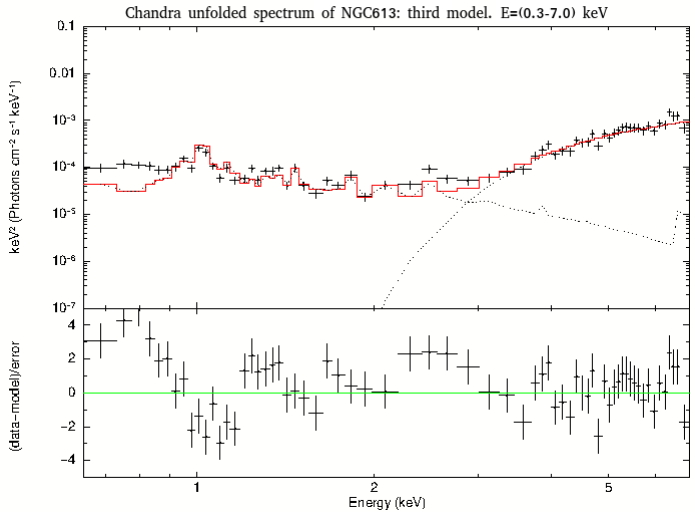

Figure 3.22: The third model (*wabs*(mekal+zwabs*(zpo))*) applied to *Chandra* spectrum of NGC613. The upper panel represents the spectral fitting and the lower panel shows the residuals in terms of data-model in units of σ. The red line is the best-fit model.

For this reason we used this model as our *baseline* in order to reproduce the analyzed source emission (see Fig. 3.23).

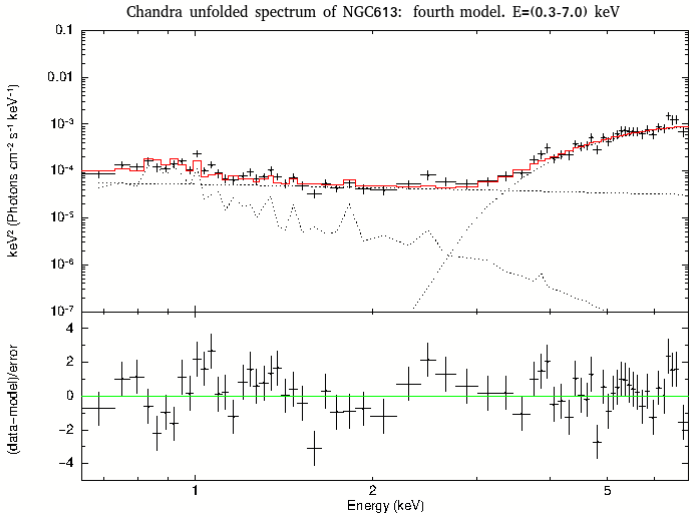

Figure 3.23: The fourth model (*wabs*(zpo+mekal+zwabs*(zpo))*) applied to *Chandra* spectrum of NGC613. Upper panel: spectral fitting; lower panel: residuals plot in terms of data-model in units of σ. The red line is the best-fit model.

In Fig. 3.23 there are some residuals at low energy, thus we tested the addition to the baseline model of a second thermal component to reproduce the presence of a more structured plasma. We obtained $\chi^2/\text{dof} = 78.4/58$. Since this model fits consistently the soft part of the spectrum, we can focus on the hard part. In Fig. 3.23, we can observe some residuals around $6.4keV$: the Fe K_α neutral emission line. In order to reproduce this Gaussian line, we added a `zgauss` component. We found the corresponding energy to be $6.41^{+0.09}_{-0.10}$ keV with an equivalent width of $EW = 0.22^{+0.12}_{-0.13}$ keV. The resulting χ^2/dof is 70.1/56, hence

this component does not improve the fit significantly. However, we decided not to remove this component, since it represents a typical feature of AGN. The results reported in Table 3.9 and displayed in Fig. 3.24 indicates that this may be indeed a consistent representation of the NGC613 data.
Considering the χ^2/dof and the F-test in Table 3.9, we have chosen the following phenomenological model

$$Chandra\_Model = wabs(zpo + mekal + mekal + zwabs(zpo + zgauss)) \quad .$$

In Fig. 3.24, we show the resulting spectral fitting (a) and the unfolded spectrum (b), i.e., the theoretical source spectrum unfolded through the instrumental response. The best-fit model is represented by the red line.

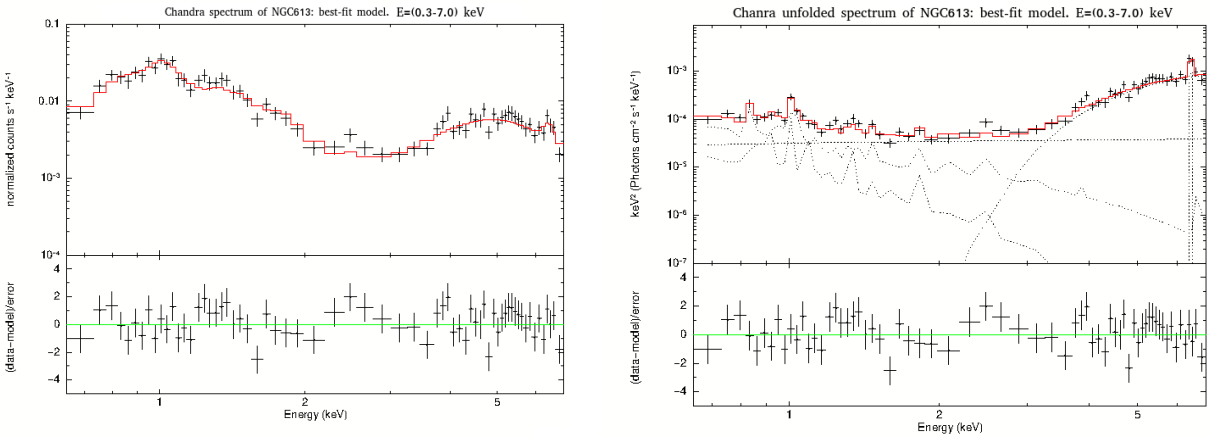

(a) (b)

Figure 3.24: The best-fit model applied to *Chandra* spectrum of NGC613. We show in (a) the resulting spectral fitting and in (b) the unfolded spectrum. Upper panel: spectral fitting; lower panel: residuals plot in terms of data-model in units of σ. The red lines are the best-fit models.

Table 3.9: The final steps used to create the phenomenological best-fit model for *Chandra* spectrum of NGC613.

Models	wabs(zpo+ +mekal) +zwabs(zpo))	wabs(zpo+ +mekal+mekal+ + zwabs(zpo)	wabs(zpo+ mekal+mekal zwabs(zpo+zgauss))
Γ^1	$2.43^{+0.40}_{-0.44}$	$1.68^{+0.48}_{-0.38}$	$1.93^{+0.52}_{-0.55}$
$Norm^2_{\Gamma_1}$ $(photons/keV/cm^2/s)$	$5.51^{+1.57}_{-1.47} \times 10^{-5}$	$3.83^{+1.55}_{-1.12} \times 10^{-5}$	$3.31^{+1.68}_{-1.19} \times 10^{-5}$
$Norm^3_{\Gamma_2}$ $(photons/keV/cm^2/s)$	$3.27^{+0.42}_{-0.19} \times^{-3}$	$7.85^{+2.89}_{-2.41} \times 10^{-4}$	$1.13^{+0.32}_{-0.74} \times 10^{-3}$
kT^4_1 (keV)	$0.83^{+0.19}_{-0.08}$	$0.44^{+0.06}_{-0.12}$	$0.44^{+0.13}_{-0.12}$
$Norm^5_{kT1}$ (cm^{-5})	$3.39^{+0.92}_{-0.94} \times 10^{-5}$	$3.85^{+1.10}_{-0.96} \times 10^{-5}$	$2.62^{+1.09}_{-1.04} \times 10^{-5}$
kT^6_2 (keV)		$1.12^{+0.17}_{-0.13}$	$1.12^{+0.17}_{-0.14}$
$Norm^7_{kT2}$ (cm^{-5})		$(3.85^{+1.32}_{-1.18}) \times 10^{-5}$	$3.70^{+1.26}_{-1.21} \times 10^{-5}$
$N^8_H(10^{22}\ cm^{-2})$	$35.3^{+3.9}_{-3.8}$	$31.5^{+4.4}_{-3.8}$	$30.1^{+4.3}_{-3.6}$
$LineE^9$ (keV)			$6.41^{+0.09}_{-0.10}$
$Norm^{10}_{zg}$ $(photons/cm^2/s)$			$7.25^{+3.62}_{-2.66} \times 10^{-6}$
EW^{11} (keV)			$0.22^{+0.12}_{-0.13}$
σ^{12} (keV)			0.01
$(\chi^2/dof)^{13}$	94.1/60	78.4/58	72.1/56

(1) Photon index; (2) and (3) powerlaw normalizations; (4) and (6) temperatures in keV of the `mekal` component; (5) and (7) normalizations of the `mekal` component; (8) column density in units of $10^{22}\ cm^{-2}$; (9) and (10) energy in keV and normalization of the Gaussian line, respectively; (11) equivalent width of the Gaussian line in keV; (12) line width in keV, fixed at 0.01 keV; (13) ratio between χ^2 and the number of degrees of freedom.
The errors are computed at the 90% confidence level for each parameter of interest (Avni 1976).

Chandra phenomenological best-fit spectral model is composed by the main emission powerlaw with $\Gamma = 1.93^{+0.52}_{-0.55}$, which represents the primary nuclear emission of the source, affected by Galactic absorption $N_H = 1.56 \times 10^{20}\ cm^{-2}$ (Kalberla et al. 2005). The value obtained for Γ is compatible with the theoretical predictions for AGN which are around 1.8 (e.g., Risaliti & Elvis 2004). We used two thermal emission components with different temperatures $kT_1 = 0.44^{+0.13}_{-0.12}\ keV$ and $kT_2 = 1.12^{+0.17}_{-0.14}\ keV$ and different intensities, to reproduce the soft part of the spectrum. This indicates that the soft part could be structured with the gas at different temperatures in the considered region. There is a further emission powerlaw with the same photon index as the first one but different normalization. This second powerlaw is used to reproduce the contribution to the soft part of the spectrum of the scattered unabsorbed photons (usually it is a fraction of a few % of primary nuclear power). Finally, there is a Gaussian emission line at $6.41^{+0.09}_{-0.10}\ keV$ with an $EW = 0.22^{+0.12}_{-0.13}\ keV$, which describes the Fe K_α emission line, typical of AGN X-ray spectra (see Section 1.4). From spectral analysis, the amount of intrinsic absorption of the source was estimated, by measuring a column density of $N_H = 30.1^{+4.3}_{-3.6}\ cm^{-2}$. The high value for the column density suggests an indirect view of the central nucleus and for this reason NGC613 is classified as a Seyfert 2 galaxy. Figure 3.25 shows the confidence contours of the column density versus the powerlaw photon index.

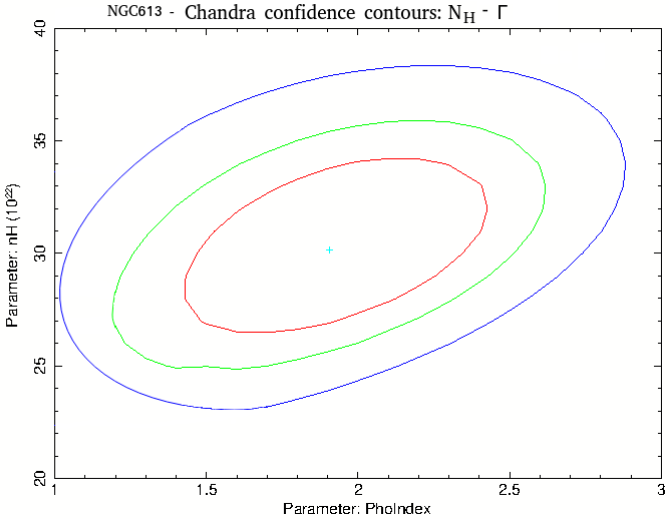

Figure 3.25: $N_H - \Gamma$ contour plot for *Chandra* data. The levels of confidence are shown as: 99% in blue, 90% in green and 68% in red.

The flux corresponding to the best-fit model is $F_{(2-10)\ keV} = (1.10^{+0.58}_{-0.19}) \times 10^{-12}\ erg/s\ cm^2$. The de-absorbed (i.e., corrected for the amount of obscuration) rest-frame luminosity is $L_{(2-10)\ keV} = (5.76^{+0.05}_{-0.05}) \times 10^{40}\ erg/s$.

After the phenomenological analysis of the source, we moved to a more detailed analysis through the use of physically motivated models. The first model used is `MYTorus`. This model was built using all three Tables of `MYTorus` and, in order to reproduce the scattered emission at lower energies, we added a second powerlaw component (in analogy to phenomenological analysis of the source spectrum). Both the photon index and the normalization of the second powerlaw have been set to be equal to those of the primary powerlaw,

and the fraction of the scattered emission is taken into account through the constant f_s, multiplying the second powerlaw. Based on the previous analysis, to take into account the thermal emission in the soft part of the spectrum, two `mekal` components have been added to the model. Finally, in order to consider the possible different normalization of the two components `MYTS` and `MYTL` with respect to `MYTZ`, two further constants A_S and A_L have been added to the model. Therefore the `MYTorus` model used is:

$$\text{Chandra\_}MYT=phabs(zpo1*MYTZ+A_S*MYTS+A_L*MYTL+f_s*zpo2+2*mekal) \quad .$$

This model has been applied to both versions of `MYTorus` (described in Section 3.3.2), *coupled* and *decopuled*. `MYTorus` in the coupled version is the first physically motivated model we used. In this configuration, all the parameters of the three `MYTorus` tables are placed equal to each other. In particular, the observation angle of the torus θ_{obs} is fixed at 90° and the column density is only representative of the column density along the line of sight $N_{H_{l.o.s.}}$. The geometric characterization of the torus was instead obtained by applying the decoupled version of `MYTorus` to the dataset in two different configurations: *edge-on* and *face-on*.
Table 3.10 compares the main spectral parameters obtained from the best-fit model of `MYTorus` in the three different configurations adopted. The three models are statistically equivalent in terms of χ^2_ν.
The values of the main parameters and those obtained from the phenomenological models are in agreement. In particular, the photon indices obtained from the three models are $\Gamma_{coupled} = 1.93^{+0.25}_{-0.24}$, $\Gamma_{edge-on} = 1.91^{+0.32}_{-0.29}$ and $\Gamma_{face-on} = 2.13^{+0.12}_{-0.13}$, and they are all compatible with the photon index value $\Gamma_P = 1.93^{+0.52}_{-0.55}$ found by the phenomenological model. The respective temperatures of the two thermal components are also consistent with what was previously obtained ($kT_{1,P} = 0.44^{+0.13}_{-0.12}$ keV and $kT_{2,P} = 1.12^{+0.17}_{-0.14}$ keV). The values of the column density along the line of sight are all in agreement with $N_{H,P} = 0.30^{+0.04}_{-0.04} \times 10^{24}$ cm^{-2}. The values of the "average global" column densities are $N_{H_{edge-on}} = 2.97^{+0.05}_{-0.09} \times 10^{24}$ cm^{-2} and $N_{H_{face-on}} = 2.90^{+0.06}_{-0.05} \times 10^{24}$ cm^{-2}, comparable within errors. Considering the edge-on and face-on configurations, the column density along the l.o.s was found to be lower than the average column density of the torus, thus obtaining a ratio between these two quantities lower than 1, within the errors, indicative of a clumpy structure of the torus. In particular, the line of sight intercepts an obscuring material whose column density is about 10% of the average one.
Despite the χ^2/dof of the three models reported in Tab. 3.10 are statistically almost equivalent, we have chosen as the best-fit model the model given by `MYTorus` decoupled in the face-on configuration in which the continuum emission is dominated by the reprocessed emission from the back-side of the torus. In Fig. 3.26 we show the *Chandra* unfolded spectrum with the `MYTorus` model (a) and the contours plot between the "global average" column density (N_H) and the photon index (Γ).
Note that the three values of Γ for the three `MYTorus` models are all consistent with what is expected for an AGN. The value of the column density along the l.o.s. is not representative of the average value column of the torus that turns out to be much larger, by a factor ~ 10. This means that if seen from a different angle or at different epochs, NGC613 should be classified as a Compton-thin AGN. In other words, the ratio $N_{H_{l.o.s.}}/N_H \simeq 0.10$ suggests a clumpy scenario for the torus in which nuclear emission is observed through a region with low column density of the obscuring material.

Table 3.10: Comparison between the main parameters of Chandra `MYTorus` models.

	coupled	decoupled edge-on	decoupled face-on
Γ^1	$1.93^{+0.25}_{-0.24}$	$1.91^{+0.32}_{-0.29}$	$2.13^{+0.12}_{-0.13}$
$f_s^2(10^{-2})$	$2.84^{+0.23}_{-0.13}$	$2.11^{+0.13}_{-0.11}$	$1.74^{+0.72}_{-0.77}$
$A_S = A_L^3$	$2.84^{+4.49}_{-1.98}$	$3.21^{+3.62}_{-1.88}$	$1.52^{+0.24}_{-0.11}$
kT_1^4 (keV)	$0.44^{+0.14}_{-0.12}$	$0.44^{+0.13}_{-0.11}$	$0.44^{+0.15}_{-0.11}$
kT_2^5 (keV)	$1.12^{+0.17}_{-0.14}$	$1.10^{+0.18}_{-0.12}$	$1.11^{+0.18}_{-0.14}$
$N^6_{H_{l.o.s}}(10^{24}\ cm^{-2})$	$0.30^{+0.04}_{-0.04}$	$0.33^{+0.09}_{-0.13}$	$0.32^{+0.04}_{-0.03}$
$N_H^7(10^{24}\ cm^{-2})$	$0.30^{+0.04}_{-0.04}$	$2.97^{+0.05}_{-0.09}$	$2.90^{+0.06}_{-0.05}$
$\theta^8_{obs,Z}$	90°	90°	90°
$(\chi^2/dof)^9$	71.0/57	72.7/57	70.5/57

(1) Photon index; (2) fraction of the scattered component; (3) normalization between the the zeroth-order continuum and reprocessed component; (4) and (5) temperatures in keV of the `mekal` components; (6) line of sight column density in units of $10^{24}\ cm^{-2}$; (7) "global average" column density in units of $10^{24}\ cm^{-2}$; (8) inclination angle of the torus (fixed for all three configurations); (9) ratio between χ^2 and the number of degrees of freedom.
The errors are computed at the 90% confidence level for each parameter of interest (Avni 1976).

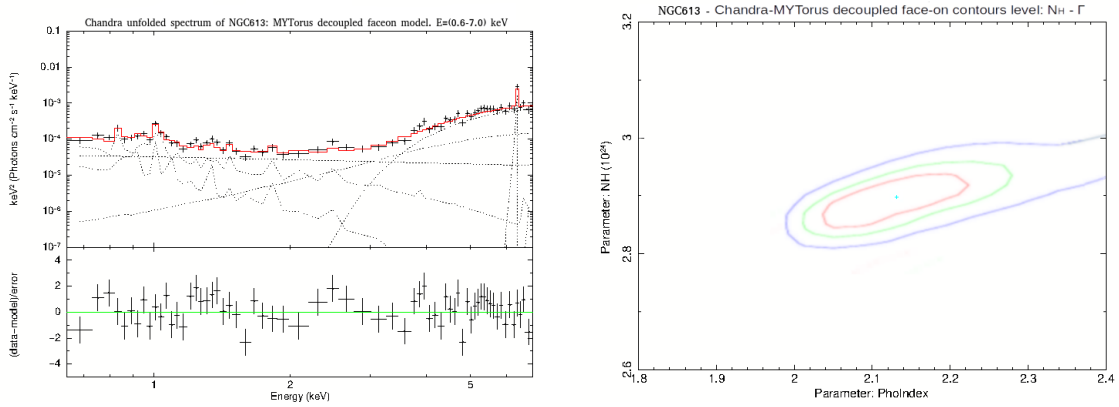

(a) (b)

Figure 3.26: (a) The *Chandra* unfolded spectrum of NGC613 modeled with `MYtorus` decoupled in face-on configuration. (b) contours plot between the "global average" column density and the photon index; the levels of confidence are shown as: 99% in blue, 90% in green and 68% in red.

Using `borus02` to model the *Chandra* dataset, we obtained the same conclusions. The model was built using the information provided by the models studied above: in order to consider the scattered photons of the Compton-thin medium, the second powerlaw was added to the absorbed primary powerlaw (zphabs∗cabs∗cutoffpl1). Finally, in order to reproduce the emission observed in the soft spectrum, we added two thermal components `mekal`. Therefore, the resulting model is:

$$\text{Chandra\_}\mathit{borus}{=}\mathit{phabs}{*}(\mathit{borus02}{+}\mathit{zphabs}{*}\mathit{cabs}{*}\mathit{cutoffpl1}{+}\mathit{C2}{*}\mathit{cutoffpl2}{+}\mathit{2}{*}\mathit{mekal}) \quad .$$

The values of the main parameters of the model are shown in Table 3.11.
This model has a photon index $\Gamma = 1.98^{+0.15}_{-0.16}$ and a Compton-thin l.o.s. column density $N_{H_{l.o.s.}} = 0.32^{+0.02}_{-0.05} \times 10^{24}\ cm^{-2}$. The average column density is $N_H = 2.57^{+0.08}_{-0.06} \times 10^{24}\ cm^{-2}$, consistent with what obtained before. Photon index, $N_{H_{l.o.s.}}$ and N_H are consistent with the values obtained with `MYTorus` (see Table 3.10). The covering factor is $C_{TOR} = 0.27^{+0.07}_{-0.06}$ and this value suggests that the structure of the torus is most likely geometrically thin. The temperatures of the thermal components are also in agreement with those reported above. In Fig. 3.27, we show the spectrum related to the `borus` model (a) and the confidence contours of the covering factor versus the "global average" column density of the torus (b).

Therefore, based on the study of the *Chandra* dataset, we found that NGC613 has a spectrum with a typical photon index value (i.e., as expected from AGN) and a column density along the line of sight consistent with Compton-thin models. The average column density, which provides more detailed information on the structure of the obscuring torus, is found to be in the thick range ($> 10^{24}\ cm^{-2}$). Therefore, we can infer that NGC613 is a Compton-thin AGN, observed through a region of the torus which has an associated lower column density. The covering factor also shows that the portion of the sky subtended by the torus is small. Finally, soft excess is well described by two thermal components with different temperatures.

Table 3.11: Chandra `borus02` model.

	`borus02`
Γ^1	$1.98^{+0.15}_{-0.16}$
$N^2_{H_{l.o.s}}(10^{24}\ cm^{-2})$	$0.32^{+0.02}_{-0.05}$
$N_H{}^3(10^{24}\ cm^{-2})$	$2.57^{+0.08}_{-0.06}$
C^4_{TOR}	$0.27^{+0.07}_{-0.06}$
$f^5_s(10^{-2})$	$1.74^{+0.78}_{-0.65}$
$kT^6_1\ (keV)$	$0.44^{+0.11}_{-0.11}$
$kT^7_2\ (keV)$	$1.13^{+0.14}_{-0.10}$
$(\chi^2/dof)^8$	69.9/56

(1) Photon index; (2) line of sight column density in units of $10^{24}\ cm^{-2}$; (3) "global average" column density in units of $10^{24}\ cm^{-2}$; (4) torus covering factor; (5) fraction of the scattered component; (6) and (7) temperatures in keV of the `mekal` components; (8) ratio between χ^2 and the number of degrees of freedom.
The errors are computed at the 90% confidence level for each parameter of interest (Avni 1976).

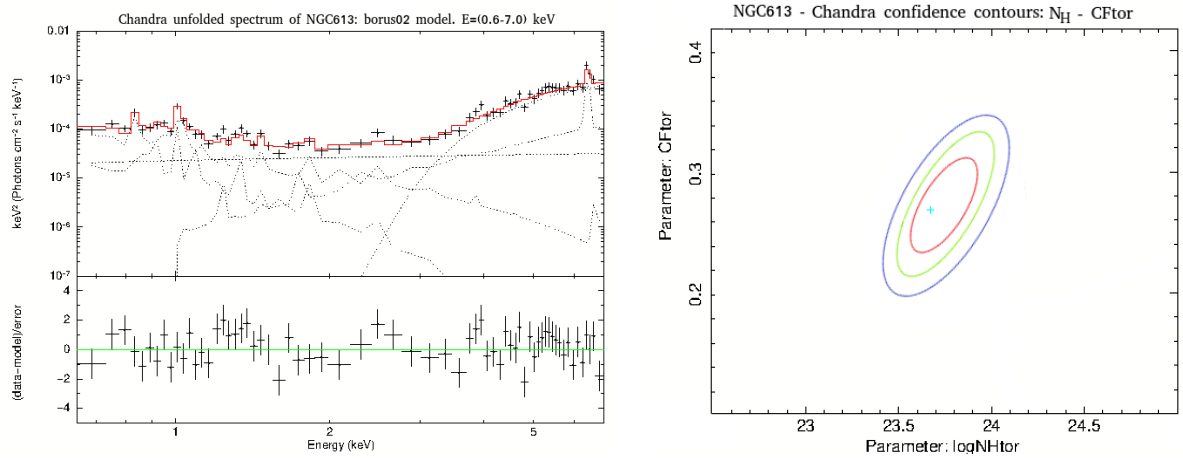

(a) (b)

Figure 3.27: (a) The *Chandra* unfolded spectrum of NGC613 modeled with `borus02`. (b) $C_{TOR} - log(N_H)$ contour plot; the levels of confidence are shown as: 99% in blue, 90% in green and 68% in red

3.4.2 XMM-Newton spectral analysis

In this section we describe the spectral analysis for XMM-*Newton*. Since XMM-*Newton*'s PSF is larger than *Chandra*'s one, we choose extraction regions which are larger than those we considered for *Chandra*. Please remind that the large effective area (see Section 2.7) of XMM-*Newton* allows to collect a large number of photons, hence to investigate the diffuse emission on larger scales. However, despite such emission would be of great interest, it is not the main goal of this thesis. We want to focus our attention on the column density of the innermost regions of the galaxy, in order to compare it with the molecular gas distribution obtained with ALMA observations, which are limited to the nuclear part of the galaxy ($FoV \sim 18''$).

The spectral analysis for XMM-*Newton* is carried out in analogy with that of *Chandra*: we start from a basic model and then refine it by adding components which minimize the residuals plot. Since the spectra for the two telescopes and the corresponding fluxes are consistent, the resulting final models will be similar. In Fig. 3.28 we show the XMM-*Newton* spectrum of NGC613 in the energy band $0.3 - 10\ keV$. For the sake of clarity, we will show the spectral analysis of the pn camera only. The same analysis has been carried out (in terms of presentation of the spectra) for the other two cameras as well; in the last part of this section we report the best-fit models for all the three cameras.

As we mentioned above, the logic steps that led to the best-fit model are the same we deeply described for *Chandra*. We will then limit ourselves to report some key steps. A preliminary model for both the soft and the hard parts of the spectrum, including the components `zpo`, `mekal`, `zwabs` and `zpo`, is shown in Fig. 3.29, with $\chi^2_\nu = 1.4$.

From the residuals plot of Fig. 3.29, we observe that the model does not provide a good representation of the data around $2\ keV$. Hence the model can be refined by adding a second thermal component which should consider the presence of a structured plasma, exactly as in *Chandra*. In the hard energy range, it is possible to observe two peaks at $6.4\ keV$ and $7.1\ keV$, respectively, which indicate two Gaussian emission lines.

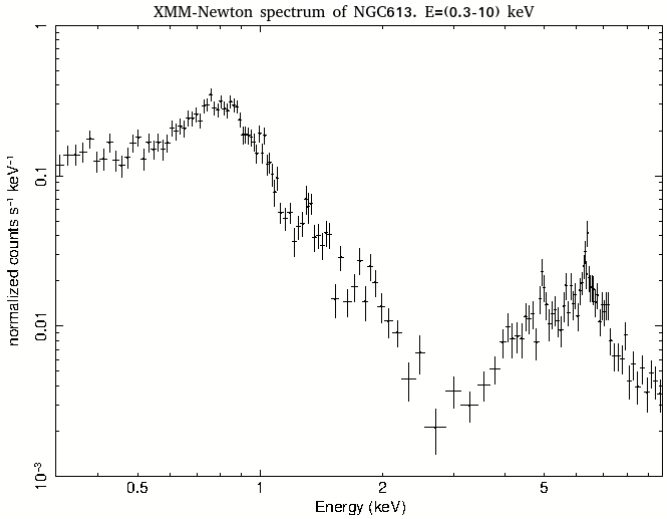

Figure 3.28: XMM-*Newton* spectrum of NGC613 in the energy band $0.3-10$ keV (pn data only here).

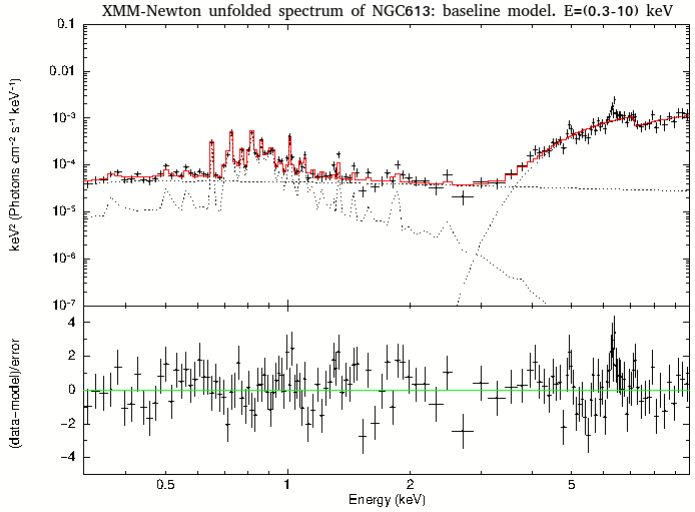

Figure 3.29: Modeling with wabs*(zpo+mekal+zwabs*(zpo)) applied to XMM-*Newton* spectrum of NGC613 (pn data only here). Upper panel: spectral fitting; lower panel: residuals plot in terms of data-model in units of σ. The red line is the best-fit model.

These are Fe K_α neutral emission line at $6.37^{+0.04}_{-0.04}$ keV, with an equivalent width of $EW = 0.26^{+0.07}_{-0.07}$ keV (χ^2/dof=164.1/133), and the Fe K_β emission line at $7.17^{+0.09}_{-0.09}$ keV with $EW = 0.12^{+0.07}_{-0.08}$ keV (χ^2/dof=158.5/130). Notice that, in contrast to *Chandra*, it was possible to detect the latter line thanks to the capability of XMM-*Newton* to collect a large number of photons at hard energies. Since the addition of the second Gaussian line, although expected on the basis of physics, is not statistically highly significant (only 1.6σ), we have removed it from the following models. The resulting spectral fitting, with a χ^2/dof=152.5/130, is shown in Fig. 3.30.

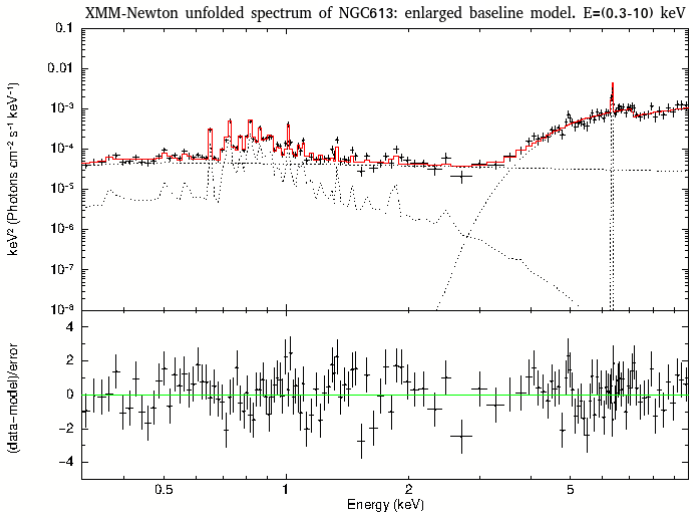

Figure 3.30: Modeling of XMM-*Newton* pn spectrum of NGC613 adopting wabs*(zpo+mekal+mekal+zwabs*(zpo+zgauss)) model. Upper panel: spectral fitting; lower panel: residuals plot. The red line is the best-fit model.

Driven by the detection of the discussed Fe K_α line and from the residuals around 2 keV, we introduce in the model a reflection component `pexmon`, obtaining χ^2/dof=150.3/131. We have assumed the reflection component to be produced by a pure reflector. Thus, the reflection scaling factor is set to be $R = -1$; moreover, the inclination angle is fixed to be 30°, matching the inclination angle of the source (see Section 3.2), and the cut-off energy is fixed to $E_{cut} = 500$ keV. Summing up, this component keeps track of the two Fe emission lines (hence we removed the `zgauss` factor since it is yet included in `pexmon`) and the reflection continuum. In Table 3.12, we report the data of the two final models.

Table 3.12: The two final steps used to produce the best-fit model for pn camera of XMM-*Newton* spectrum of NGC613.

	wabs(zpo+mekal+mekal +zwabs(zpo+zgauss))	wabs(zpo+mekal+mekal +zwabs(zpo+pexmon))
Γ^1	$2.13^{+0.12}_{-0.13}$	$2.17^{+0.13}_{-0.13}$
$Norm^2_{\Gamma_1}$ $(photons/keV/cm^2/s)$	$4.09^{+0.43}_{-0.43} \times 10^{-5}$	$4.08^{+0.42}_{-0.42} \times 10^{-5}$
$Norm^3_{\Gamma_2}$ $(photons/keV/cm^2/s)$	$2.32^{+0.42}_{-0.43} \times 10^{-3}$	$1.79^{+0.58}_{-0.46} \times 10^{-3}$
kT^4_1 (keV)	$0.42^{+0.18}_{-0.20}$	$0.42^{+0.08}_{-0.09}$
$Norm^5_{kT_1}$ (cm^{-5})	$4.82^{+0.76}_{-1.32} \times 10^{-5}$	$4.82^{+0.74}_{-1.64} \times 10^{-5}$
kT^6_2 (keV)	$0.79^{+0.13}_{-0.18}$	$0.79^{+0.20}_{-0.17}$
$Norm^7_{kT_2}$ (cm^{-5})	$2.29^{+1.70}_{-1.42} \times 10^{-5}$	$2.29^{+0.76}_{-1.35} \times 10^{-5}$
N^8_H $(10^{22}\ cm^{-2})$	$43.1^{+4.4}_{-3.9}$	$40.2^{+4.4}_{-4.0}$
E^9_1 (keV)	$6.37^{+0.04}_{-0.04}$	
$Norm^{10}_{E_1}$ $(photons/cm^2/s)$	$1.12^{+0.33}_{-0.32} \times 10^{-5}$	
$EW^{11}_{E_1}$ (keV)	$0.26^{+0.07}_{-0.07}$	
$\sigma^{12}_{E_1}$ (keV)	0.01	
$Norm^{13}_{pex}$ $(photons/keV/cm^2/s)$		$3.55^{+1.85}_{-1.28} \times 10^{-3}$
$(\chi^2/dof)^{14}$	153.5/130	150.3/131

(1) Photon index; (2) and (3) powerlaw normalizations; (4) and (6) temperatures in keV of the `mekal` component; (5) and (7) normalizations of the `mekal` component; (8) column density in units of 10^{22} cm^{-2}; (9) and (10) energy in keV and normalization of the Gaussian line, respectively; (11) equivalent width of the Gaussian line in keV; (12) line width in keV, fixed at 0.01 keV; (13) normalization of the `pexmon` component; (14) ratio between χ^2 and the number of degrees of freedom. The errors are computed at the 90% confidence level for one parameter of interest (Avni 1976).
As seen in Section 3.3.1, the `pexmon` component directly includes the Fe Gaussian line that we considered using the `zgauss` component in the other models.

Hence, the final phenomenological model is:

$$XMM\text{-}Newton\_Model{=}wabs(zpo{+}mekal{+}mekal{+}wabs(zpo{+}pexmon)) \quad .$$

In Fig. 3.31 we show the resulting spectral fitting (a) and the unfolded spectrum (b) for the three cameras used.

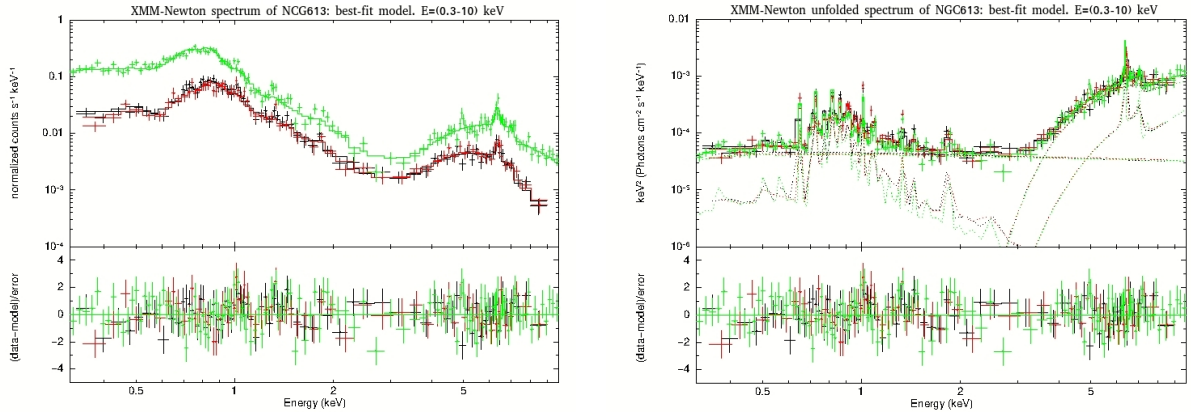

(a) (b)

Figure 3.31: The phenomenological best-fit model applied to the XMM-*Newton* spectrum of NGC613. We show in (a) the resulting spectral fitting and in (b) the unfolded spectrum. Upper panel: spectral fitting; lower panel: residuals plot in terms of data-model in units of σ. In both figures, the green and the red crosses are the pn and MOS cameras data points, respectively; the green and the red lines are the best-fit model for the pn and MOS cameras, respectively.

The XMM-*Newton* phenomenological best-fit spectral model is composed by the primary nuclear emission of the source with $\Gamma = 2.17^{+0.13}_{-0.13}$, affected by Galactic absorption $N_H = 1.56 \times 10^{20}\ cm^{-2}$ (Kalberla et al. 2005). This primary powerlaw is apparently steeper than that of *Chandra*, but the photon indices are compatible within their errors. The soft part of the spectrum is described by two thermal emission components with different temperatures $kT_1 = 0.42^{+0.08}_{-0.09}\ keV$ and $kT_2 = 0.79^{+0.20}_{-0.17}\ keV$ and different intensities. kT_2 is not compatible with the corresponding value found for *Chandra*; however, since $kT_1 \neq kT_2$ we confirm the presence of a "structured" plasma. The contribution of scattered unabsorbed photons is reproduced by the second powerlaw with the same photon index as the first one, but having different normalization, exactly as in *Chandra*. Differently from *Chandra* spectral analysis, the XMM-*Newton* best-fit model has been obtained using the reflection component `pexmon`, which takes into account the reflection continuum, which is an expected component of AGN spectra (see Section 1.4), and directly includes both the Gaussian lines. This difference can be linked to the higher capacity of XMM-*Newton* to collect photons in hard band (i.e., higher A_{eff}, see Section 2.1.2) with respect to *Chandra*. We estimated the amount of intrinsic absorption of the source and we obtained a Compton-thin column density of $N_H = 40.2^{+4.4}_{-4.0}\ cm^{-2}$. This result confirms the classification of NGC613 as a Seyfert 2 galaxy. In Fig. 3.32 we show the contour plot of the column density versus the powerlaw photon index.

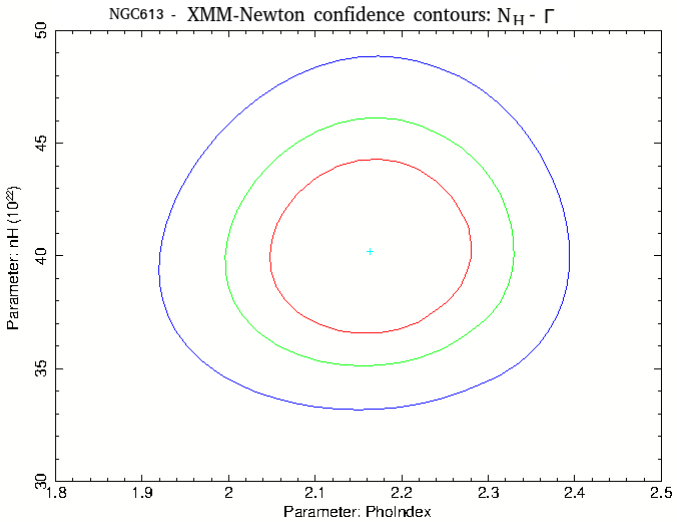

Figure 3.32: $N_H - \Gamma$ contour plot for XMM-*Newton* data. The levels of confidence are shown as: 99% in blue, 90% in green and 68% in red.

The flux corresponding to the best-fit model is $F_{2-10\ keV} = (1.09^{+0.08}_{-0.08}) \times 10^{-12}\ erg/s\ cm^2$; the de-absorbed rest-frame luminosity is $L_{2-10\ keV} = (5.72^{+0.06}_{-0.05}) \times 10^{40}\ erg/s$. These values show no significant variability between the two datasets taken four years apart. In fact the fluxes of the two instrument are compatible within errors evaluated 90% confidence levels

In analogy with *Chandra* spectral analysis, after completing the study of the phenomenological model, we applied `MYTorus` and `borus02` to the XMM-*Newton* dataset. `MYTorus` was built by adding to the three available Tables two powerlaw components (to reproduce both the primary emission of the AGN and the scattered emission) and two thermal components (to reproduce the soft excess). In both versions of `MYTorus`, *coupled* and *decopuled* (see Section 3.3.2), we then applied the following model:

$$XMM\_MYT{=}phabs(zpo1{*}MYTZ{+}A_S\ {*}MYTS{+}A_L\ {*}MYTL{+}f_s\ {*}zpo2{+}2mekal) \quad .$$

The main results of this model, applied in the three different `MYTorus` configurations, are compared in Table 3.13.
As reported Table 3.13, the values of the main results are compatible within the errors not only when compared with each other, but also when compared with those obtained from the phenomenological models (see Table 3.12). In particular, the photon index for the three models, $\Gamma_{coupled} = 1.91^{+0.21}_{-0.23}$, $\Gamma_{edge-on} = 1.87^{+0.21}_{-0.21}$ and $\Gamma_{face-on} = 1.96^{+0.26}_{-0.25}$, is compatible with $\Gamma_P = 2.17^{+0.13}_{-0.13}$. The value of $\Gamma_{face-on}$ obtained from the analysis of the XMM-*Newton* data was found to be less than that obtained in *Chandra*, but still consistent within the errors. There are also compatible values for the column density along the l.o.s. (remember that the column density of the phenomenological model is $N_{H,P} = 0.40^{+0.04}_{-0.04} \times 10^{24}\ cm^{-2}$). The values of the "average global" column densities are $N_{H_{edge-on}} = 2.83^{+0.09}_{-0.07}$ and $N_{H_{face-on}} = 2.83^{+0.08}_{-0.07}$. As found for the *Chandra* dataset, the column density along the l.o.s was found to be lower than the average column density of the torus and, in particular, we obtained $N_{H_{l.o.s.}} = 0.16 N_H$.
The best-fit model in terms of χ^2_ν is given by `MYTorus` decoupled in the face-on configuration.

Table 3.13: Comparison between the main parameters of XMM-*Newton* physically motivated models.

	coupled	decoupled edge-on	decoupled face-on
Γ^1	$1.91^{+0.21}_{-0.23}$	$1.87^{+0.21}_{-0.21}$	$1.96^{+0.26}_{-0.25}$
$f_s^2(10^{-2})$	$2.21^{+0.88}_{-0.62}$	$1.58^{+0.56}_{-0.43}$	$1.53^{+0.76}_{-0.55}$
$A_S = A_L^3$	$2.39^{+0.56}_{-0.52}$	$1.42^{+0.08}_{-0.10}$	$1.12^{+0.43}_{-0.34}$
kT_1^4 (keV)	$0.47^{+0.04}_{-0.06}$	$0.47^{+0.04}_{-0.06}$	$0.47^{+0.04}_{-0.05}$
kT_2^5 (keV)	$0.93^{+0.12}_{-0.13}$	$0.93^{+0.12}_{-0.12}$	$1.10^{+0.05}_{-0.05}$
$N^6_{H_{l.o.s}}(10^{24}\ cm^{-2})$	$0.41^{+0.04}_{-0.03}$	$0.44^{+0.04}_{-0.03}$	$0.44^{+0.05}_{-0.04}$
$N_H^7(10^{24}\ cm^{-2})$	$0.41^{+0.04}_{-0.03}$	$2.83^{+0.09}_{-0.07}$	$2.83^{+0.08}_{-0.07}$
$\theta^8_{obs,Z}$	90°	90°	90°
$(\chi^2/dof)^9$	269.0/247	296.7/246	266.6/246

(1) Photon index; (2) fraction of the scattered component; (3) normalization between the the zeroth-order continuum and the reprocessed component; (4) and (5) temperatures in keV of the `mekal` components; (6) line of sight column density in units of $10^{24}\ cm^{-2}$; (7) "global average" column density in units of $10^{24}\ cm^{-2}$; (8) inclination angle of the torus; (9) ratio between χ^2 and the number of degrees of freedom.
The errors are computed at the 90% confidence level for one parameter of interest (Avni 1976).

Fig. 3.33 shows the XMM-*Newton* unfolded spectrum (a) and the contour plot between the "global average" column density (N_H) and the photon index (Γ) (b).

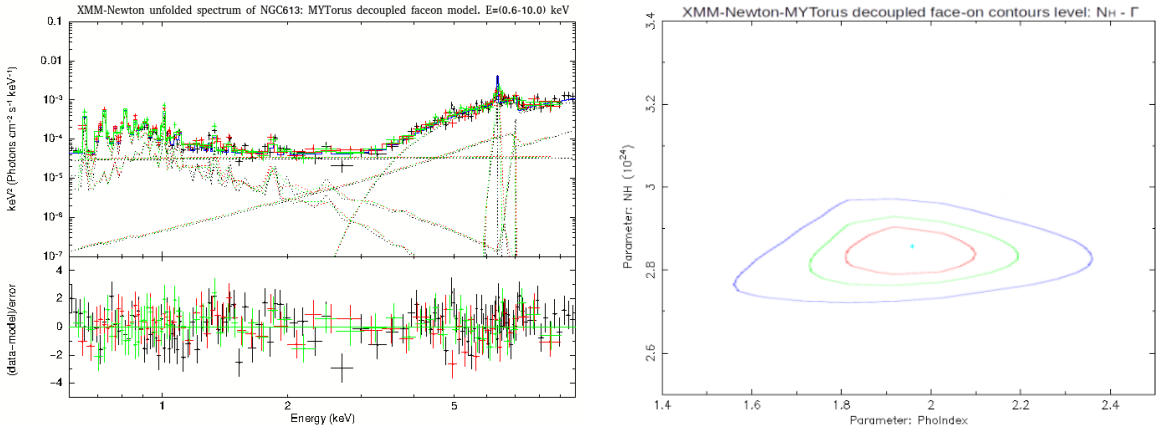

(a) (b)

Figure 3.33: (a) The XMM-*Newton* unfolded spectrum of NGC613 modeled with `MYtorus` decoupled in face-on configuration. (b) contours plot between the "global average" column density and the photon index; the levels of confidence are shown as: 99% in blue, 90% in green and 68% in red.

From the analysis of these models, we reach similar conclusion as from the analysis of *Chandra*: the material along the line of sight is Compton-thin, while the average column density ($\sim 10 N_{H_{l.o.s.}}$) suggests a Compton-thick material around the AGN. The relation between these two quantities reconfirms a clumpy scenario for the assumed geometry of the torus.
Finally, we applied `borus02` to the XMM-*Newton* dataset. Also in this case, we added to the model an absorbed primary powerlaw (zpha∗cabs∗cutoffpl1), a second powerlaw and two thermal components `mekal`. Therefore, the model applied is:

$$XMM\_borus{=}phabs{*}(borus02{+}zphabs{*}cabs{*}cutoffpl1{+}C2{*}cutoffpl2{+}2mekal) \quad .$$

The main results of the model are reported in Table 3.14. We obtain a photon index and a Compton-thin l.o.s. column density about $\Gamma = 1.78^{+0.22}_{-0.24}$, $N_{H_{l.o.s.}} = 0.43^{+0.04}_{-0.04} \times 10^{24}\ cm^{-2}$, respectively. The "global average" column density is $N_H = 2.24^{+0.10}_{-0.11} \times 10^{24}\ cm^{-2}$, lower than the `MYTorus` N_H, but consistent with a Compton-thick scenario and the covering factor is $C_{TOR} = 0.25^{+0.07}_{-0.04}$. Γ and $N_{H_{l.o.s}}$ are compatible with the values from `MYTorus` (see Table 3.13).
In Fig. 3.34 we show spectral results obtained using `borus` spectrum (a) and the confidence contour between the covering factor and the average column density of the torus (b). From the analysis of the XMM-*Newton* dataset, we came to the same conclusions of the previous analysis: NGC613 is a Compton-thin AGN observed through a region of the torus that has a lower density than the average density. The torus subtends a small portion of the sky and the geometry suggested by the spectral results is of the clumpy type.

Table 3.14: XMM-*Newton* `borus02` model.

	`borus02`
Γ^1	$1.78^{+0.22}_{-0.24}$
$N^2_{H_{l.o.s}}(10^{24}\ cm^{-2})$	$0.43^{+0.04}_{-0.04}$
$N_H{}^3(10^{24}\ cm^{-2})$	$2.24^{+0.10}_{-0.11}$
C^4_{TOR}	$0.25^{+0.07}_{-0.04}$
$f^5_s(10^{-2})$	$1.64^{+0.90}_{-0.60}$
$kT^6_1\ (keV)$	$0.47^{+0.04}_{-0.05}$
$kT^7_2\ (keV)$	$1.00^{+0.10}_{-0.06}$
$(\chi^2/dof)^8$	585.5/246

(1) Photon index; (2) line of sight column density in units of $10^{24}\ cm^{-2}$; (3) "global average" column density in units of $10^{24}\ cm^{-2}$; (4) torus covering factor; (5) fraction of the scattered component; (6) and (7) temperatures in keV of the `mekal` components; (8) ratio between χ^2 and the number of degrees of freedom.
The errors are computed at the 90% confidence level for each parameter of interest (Avni 1976).

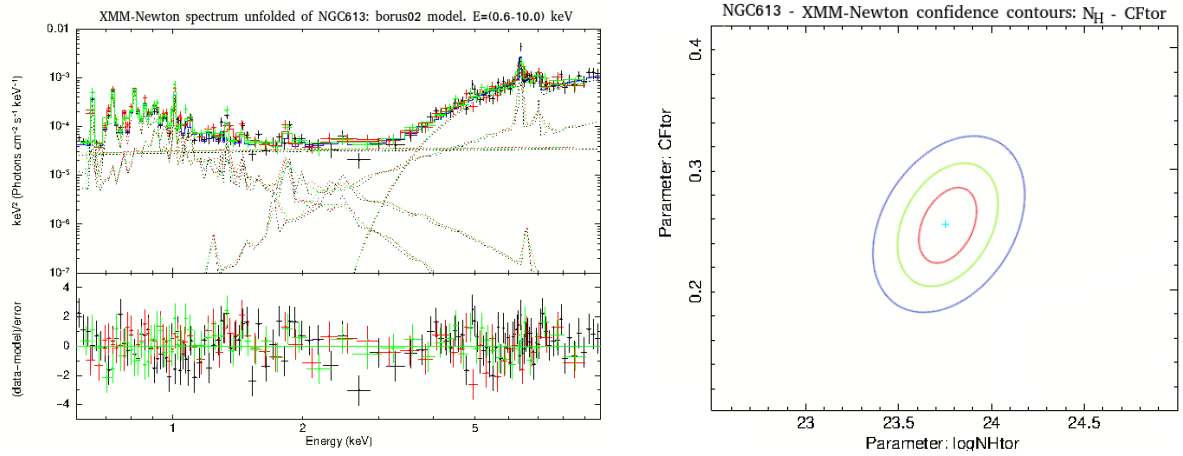

(a) (b)

Figure 3.34: (a) The XMM-*Newton* unfolded spectrum of NGC613 modeled with `borus02`. (b) $C_{TOR} - log(N_H)$ contour plot; the levels of confidence are shown as: 99% in blue, 90% in green and 68% in red

3.5 NGC1808: X-ray spectral analysis

In this section we will present the spectral analysis of NGC1808. Since this galaxy has various substructures (e.g., the blobs described above) in its central regions and it seems to host a weak nucleus ($L_{[2-10]keV} \sim 10^{40}$ (erg/s), see, e.g., Dahlem et al. 1990, Jiménez-Bailón et al. 2005), we will follow a different approach with respect to NGC613 to study its spectrum. In fact, the core emission may be "diluted" by that the global galaxy emission; for this reason, we started from studying the inner and central region that we assume to be, if any, most probably dominated by the nuclear emission and then moved on to the galaxy in its total emission. Taking advantage of the superb *Chandra* angular resolution, we thus adopted, at first, an extraction region for the nucleus of $r = 1.5''$, so as to increase the probability to spot the AGN contribution among the diffuse emission. Once the nuclear emission is characterized, we will study the total emission of the galaxy. Furthermore, since NGC1808 is classified as an LLAGN (see, e.g., Dahlem et al. 1990, Jiménez-Bailón et al. 2005), we preferred to adopt only phenomenological models both for *Chandra* and XMM-*Newton* spectral analyses. Furthermore, for this source we are also limited by the low statistic, which prevents the implementation of solid physically motivated models.

3.5.1 Chandra spectral analysis

Firstly, we focused our analysis on the nuclear source region in order to investigate the core emission. In Fig. 3.35 we show the *Chandra* spectrum of the nuclear region ($r = 1.5''$) in the energy band 0.3−7.0 keV. The first model applied on the spectrum is composed by an emission powerlaw component, which takes into account the primary nuclear emission of AGN, affected by the Galactic absorption $N_{H,gal} = 2.33 \times 10^{20}$ cm^{-2} (Kalberla et al. 2005). The resulting spectral fitting is shown in Fig. 3.36, with $\chi^2_\nu = 5.3$.

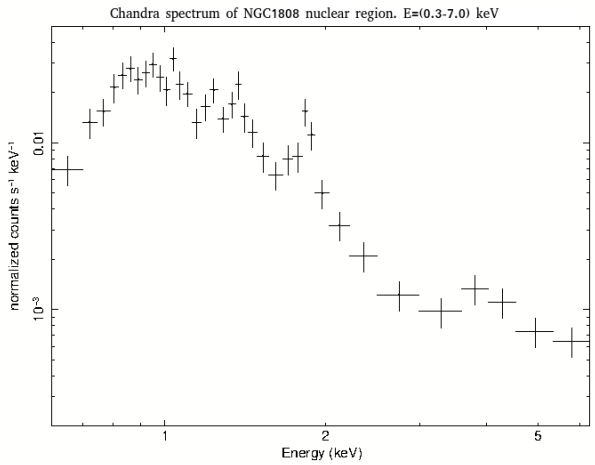

(a)

Figure 3.35: *Chandra* spectrum of NGC1808 nuclear source region ($r = 1.5''$).

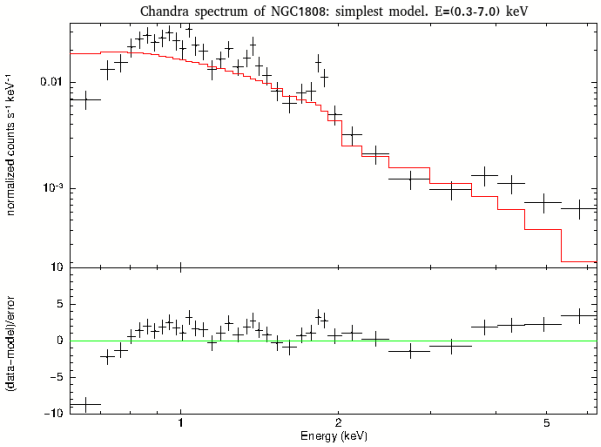

(a)

Figure 3.36: Starting model ($phabs_{gal}$*zpo) applied to *Chandra*'s spectrum of NGC1808. Upper panel: spectral fitting; lower panel: residuals plot. The red line is the best-fit model.

We thus added a further absorption component `zphabs` to this model, in order to consider the gas obscuration in the soft part (below 0.5 keV) of the spectrum. The addition of this component seems to be justified by HST images, where the presence of dust lanes up to the inner regions of the galaxy is clearly detected (see, e.g., Flood & Mutchler 1997). Therefore, it is reasonable to think that the gas associated with the dust extinction observed in the optical can be responsible for the extra-absorption component in the X-ray spectrum of NGC1808. The χ^2_ν results to be 3.6. From the residuals plot in Fig. 3.36, we noted the presence of a structured component which is prominent below $\sim 2keV$: this could be the imprint of a thermal component. We then expanded the model with a `mekal` component: the origin of this thermal component is non-nuclear (see Jiménez-Bailón et al. 2005) and it is ascribable to SN activities. This soft emission is then dominated by the host galaxy contribution in the 0.3−2 keV band, although we did our best to limit this emission by choosing a small source extraction region. Figure 3.37 shows the second model, with $\chi^2_\nu =$

1.7, applied to the *Chandra* dataset.

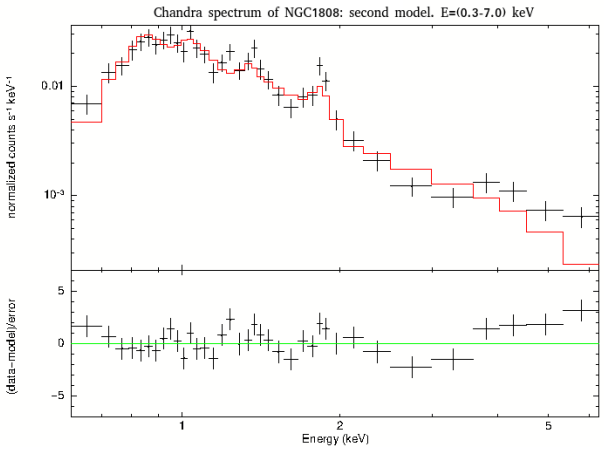

(a)

Figure 3.37: Second model (*zphabs*[phabs$_{gal}$*(mekal+(zpo))]*) applied to *Chandra*'s spectrum of NGC1808. Upper panel: spectral fitting; lower panel: residuals plot. The red line is the best-fit model.

From the residuals plot in Fig. 3.37 we noticed that the soft part is now well described, but there are some residuals above 3 keV.
The complexity of the hard part of the spectrum, given by the intrinsically patchy torus (if present) and/or by a double powerlaw component (core + binaries, see Section 3.1), is taken into account through a partial covering absorption component `zpcfabs`. Therefore the emission in the hard band is attributable to obscured AGN emission.
We chose the following model in order to reproduce the whole *Chandra* nuclear spectrum:

$$Chandra\_Nuclear\_Model{=}zphabs*[phabs_{gal}*(mekal{+}zpcfabs*(zpo))] \ .$$

In Table 3.15, we show the main parameters of the *Chandra* nuclear best-fit spectral model. In Fig. 3.38, we show the unfolded spectrum (b) for the nuclear source region and the $N_{H,zpcf} - CvrFract$ contours plot.

Table 3.15: The best-fit model for *Chandra* spectrum of NGC1808 nuclear region.

	zpha[pha$_{gal}$(mekal+ +zpcfabs(zpo))]
$N^1_{H,gas}(10^{22}\ cm^{-2})$	$0.71^{+0.15}_{-0.17}$
$kT^2(keV)$	$0.58^{+0.05}_{-0.11}$
$Norm^3_{kT}\ (cm^{-5})$	$1.71^{+1.27}_{-0.80} \times 10^{-4}$
$N^4_{H,zpcf}(10^{22})$	$33.9^{+43.7}_{-16.1}$
CvrFract[5]	$0.83^{+0.11}_{-0.14}$
Γ[6]	2
$Norm^7_{\Gamma}\ (photons/keV/cm^2/s)$	$1.95^{+4.06}_{-0.88} \times 10^{-4}$
(χ^2/dof)[8]	38.3/31

(1) Gas/dust column density in units of $10^{22}\ cm^{-2}$; (2) and (3) temperature in keV and normalization of the `mekal` component, respectively; (4) and (5) column density in units of $10^{22}\ cm^{-2}$ and covering factor of the `zpcfabs` component, respectively; (6) and (7) photon index (fixed) and powerlaw normalization, respectively; (8) ratio between χ^2 and the number of degrees of freedom. The errors are computed at the 90% confidence level for one parameter of interest (Avni 1976).

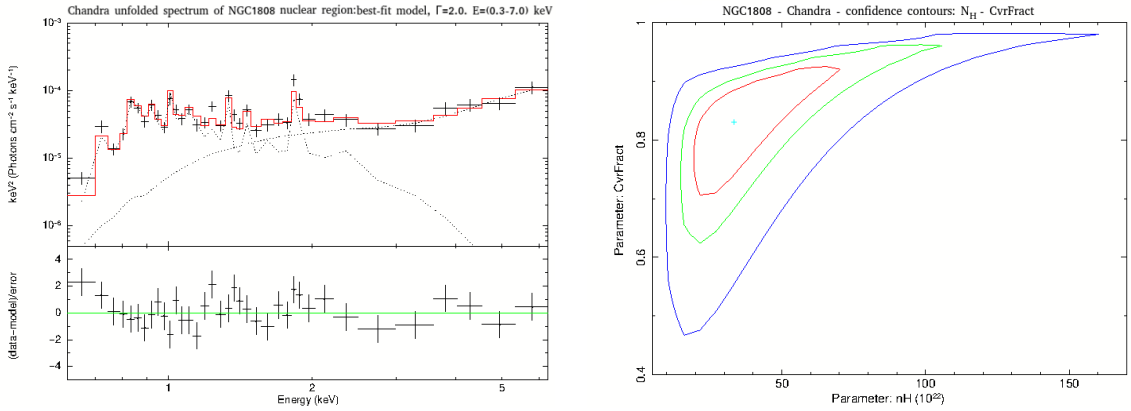

(a) (b)

Figure 3.38: (a) The best-fit model applied to *Chandra*'s unfolded spectrum of NGC1808 nuclear source region. Upper panel: spectral fitting; lower panel: residuals plot in terms of data-model in units of σ. The red lines are the best-fit models. (b) $N_{H,zpcf} - CvrFract$ contour plot; the levels of confidence are shown as: 99% in blue, 90% in green and 68% in red.

To conclude, we can summarize the findings of this as analysis as follow. The X-ray spectrum of the inner region of NGC1808 is dominated at low energy ($E < 3\ keV$) by a thermal component most probably related to some hot gas in the host galaxy. The nucleus seems to emerge at larger energies. Because of both the $\Gamma - N_H$ degeneracy and the limited statistics for this selected region ($\sim 1000\ cts$), the photon index was fixed at 2, in order to be reproduced by reasonable AGN models. Indeed, we observed that if the photon index was left free to vary, one always obtained values higher than 2.8, which are not physical. We obtained a column density ($N_{H,gas}$) of $0.71^{+0.15}_{-0.17} \times 10^{22}\ cm^{-2}$ for the presumably galaxy-scale, and a temperature of $0.58^{+0.05}_{-0.11}\ keV$ for the thermal emission component. These two components reproduce the soft emission. At these low energies, the thermal component is most probably due to the gas heated by SNRs and/or hot bubbles in the central star forming region. This suggests that the stellar activity in the nuclear region may significantly contribute to the observed soft X-ray emission. NGC1808 is known to show spectral evidence for weak ($L_{2-10 keV} \sim 10^{40}\ (erg/s)$) Seyfert-like activity in the nucleus (SFR$\sim 4\ (M_\odot/yr)$), which is surrounded by a extended starburst regions ($\approx 1\ kpc$) in the center of the galaxy (e.g., Junkes et al. 1995, Jiménez-Bailón et al. 2005).
The thermal component dominates in the soft X-ray band, while the powerlaw is dominant in the 2−7 keV band. We obtained a hydrogen column density of $N_{H,zpcf} = 33.9^{+43.7}_{-16.1} \times 10^{22}\ cm^{-2}$ and a covering fraction (CvrFract), i.e., a geometrical parameter that determines whether the absorber completely or partially covers the inner AGN engine or covers only part of the continuum source, of $0.83^{+0.11}_{-0.14}$ for the `zpcfabs` component.

The flux corresponding to the best-fit model is $F_{(2-10)\ keV} = (1.87^{+0.10}_{-0.37}) \times 10^{-13}\ erg/s\ cm^2$. The de-absorbed (i.e., corrected from the obscuration) AGN luminosity is $L_{(2-10)\ keV} = (1.22^{+0.14}_{-0.13}) \times 10^{40}\ erg/s$.

To complete our analysis and provide more details of the emission of NGC1808, we studied

the total emission of the galaxy; we considered the elliptical source region chosen in Section 3.1, in order to study the overall galaxy emission. The best-fit model for this extended region is built on the basis of the one obtained for the nuclear region. In Fig. 3.39 we show *Chandra*'s spectrum of the elliptical source region modeled with the same best-fit model of the nuclear region. The χ^2_ν results to be 1.4.

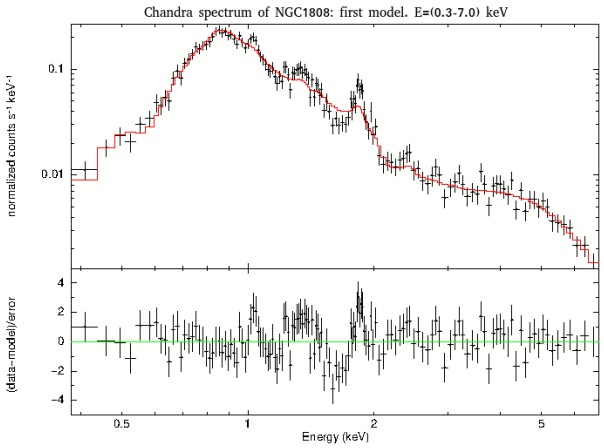

(a)

Figure 3.39: Fist model (*zphabs*[phabs$_{gal}$*(mekal+zpcfabs*(zpo))]*) applied to *Chandra* spectrum of NGC1808 source region. Upper panel: spectral fitting; lower panel: residuals plot in terms of data-model in units of σ. The red lines are the best-fit models.

In Fig. 3.39, we noticed that we have some residuals around 1.3 keV and 1.8 keV. In contrast to the nuclear region, since here we have a higher photon statistics, we were able to model these lines. Following Jiménez-Bailón et al. (2005), we added to the model two `zgauss` components in order to reproduce the MgXI and SiXIII Gaussian emission lines. These lines are attributable to a thermal emission which is lead by the stellar activity that, at these low energies, play an important role. We report in Table 3.16 the properties and the statistical significance of the two emission lines found in the *Chandra* spectrum.

Table 3.16: Theoretical line energy (from Turner et al. 1997), observed line energy and statistical significance of the lines.

	Theoretical line energy	Observed line energy	Statistical significance
MgXI	1.34 (keV)	$1.34^{+0.02}_{-0.02}$ (keV)	3.5σ
SiXIII	1.85 (keV)	$1.84^{+0.02}_{-0.02}$ (keV)	5σ

Since both lines result to be statistically significant, we finalize the following best-fit model for *Chandra*'s source spectrum:

$$Chandra\_Source\_Model{=}zphabs{*}[phabs_{gal}{*}(mekal{+}zgauss{+}zgauss{+}zpcfabs{*}(zpo))] \ .$$

In Table 3.17 we displayed the main parameters of the *Chandra* best-fit model for the elliptical source region.

Table 3.17: The best-fit model of *Chandra* spectrum of NGC1808 source region.

	zpha[pha$_{gal}$(mekal+zgauss+ +zgauss+zpcfabs(zpo))]
$N^1_{H,gas}$ $(10^{22}\ cm^{-2})$	$0.22^{+0.04}_{-0.04}$
kT^2 (keV)	$0.63^{+0.02}_{-0.02}$
$Norm^3_{kT}$ (cm^{-5})	$2.05^{+0.26}_{-0.23} \times 10^{-4}$
$E^4_1(keV)$	$1.34^{+0.02}_{-0.02}$
$Norm^5_{E_1}$ $(photons/cm^2/s)$	$7.69^{+2.27}_{-2.36} \times 10^{-6}$
$EW^6_{E_1}$ (keV)	$0.05^{+0.01}_{-0.01}$
$\sigma^7_{E_1}$ (keV)	0.01
E^8_2 (keV)	$1.84^{+0.02}_{-0.02}$
$Norm^9_{E_2}$ $(photons/cm^2/s)$	$5.81^{+1.63}_{-1.92} \times 10^{-6}$
$EW^{10}_{E_2}(keV)$	$0.09^{+0.01}_{-0.01}$
$\sigma^{11}_{E_2}$ (keV)	0.01
$N^{12}_{H,zpcf}$ $(10^{22}\ cm^{-2})$	$20.5^{+10.2}_{-6.0}$
CvrFract[13]	$0.72^{+0.08}_{-0.11}$
Γ[14]	$1.93^{+0.26}_{-0.25}$
$Norm^{15}_{\Gamma}$ $(photons/keV/cm^2/s)$	$5.68^{+3.28}_{-2.09} \times 10^{-4}$
(χ^2/dof)[16]	136.2/129

(1) Gas/dust column density in units of $10^{22}\ cm^{-2}$; (2) and (3) temperature in keV and normalization of the `mekal` component, respectively; (4) and (8) energy in keV of the Gaussian lines; (5) and (9) normalization of the Gaussian lines; (6) and (10) equivalent width of the Gaussian lines in keV; (7) and (11) line widths in keV, fixed at 0.01 keV; (12) and (13) column density in units of $10^{22}\ cm^{-2}$ and covering factor of the `zpcfabs` component, respectively; (14) and (15) photon index and powerlaw normalization, respectively; (16) ratio between χ^2 and the number of degrees of freedom. The errors are computed at the 90% confidence level for one parameter of interest (Avni 1976).

The best-fit model, with $\chi^2_\nu = 1.1$, includes the main emission powerlaw with $\Gamma = 1.93^{+0.26}_{-0.25}$, affected by Galactic absorption. The soft part of the spectrum is represented by the gas absorption with $N_{H,gas} = 0.22^{+0.04}_{-0.04} \times 10^{22}\ cm^{-2}$, by the thermal component with temperature of $0.63^{+0.02}_{-0.02}\ keV$ and by two Gaussian emission lines. The former, with an energy of $1.34^{+0.02}_{-0.02}\ keV$ and an EW of $0.05^{+0.01}_{-0.01}\ keV$, represents the MgXI emission line, the latter, with an energy of $1.84^{+0.02}_{-0.02}\ keV$ and an EW of $0.09^{+0.01}_{-0.01}\ keV$, represents the SiXIII emission line. As in *Chandra* nuclear model, the hard part of the spectrum is reproduced using a partial covering absorption with a hydrogen column density of $20.5^{+10.2}_{-6.0} \times 10^{22}\ cm^{-2}$ and a covering fraction of $0.72^{+0.08}_{-0.11}$. The absorption measured in the *Chandra* spectral analysis, both in the nuclear and in the elliptical source regions, is compatible with a typical value of Compton-thin obscuration. On the one hand, the temperature, the `zpcfabs` hydrogen column density ($N_{H,zpcf}$) and the covering fraction obtained in this model are compatible, within their errors, with what we obtained for the nuclear region model; on the other hand, the hydrogen column density due to the gas absorption is less than the one obtained for the nuclear region model. This is clear since the hydrogen is expected to be dense in the inner regions and diluted in the outer regions. In Fig. 3.40 we show the *Chandra* best-fit model for the source region.

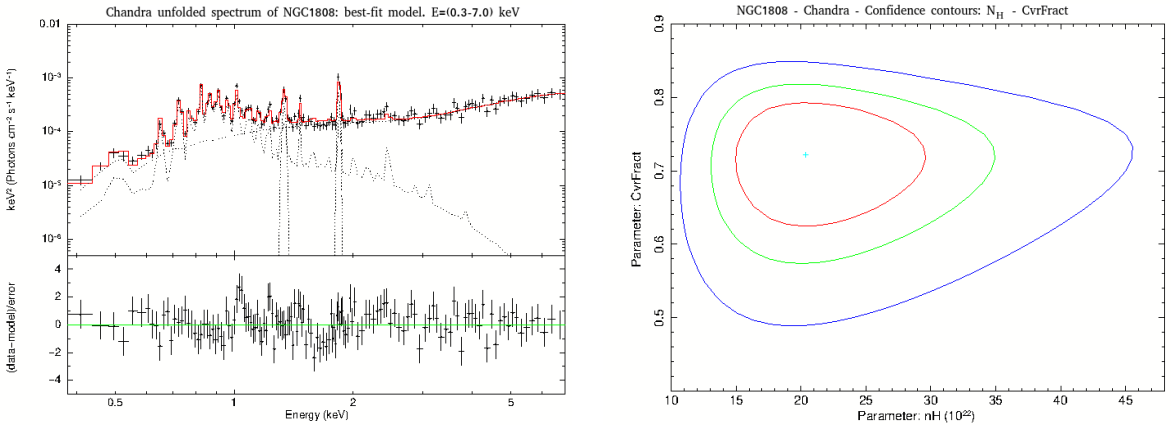

(a) (b)

Figure 3.40: (a) The best-fit model applied to *Chandra* unfolded spectrum of NGC1808 source region. Upper panel: spectral fitting; lower panel: residuals plot in terms of data-model in units of σ. The red lines are the best-fit models. (b) $N_H - CvrFract$ contour plot; the levels of confidence are shown as: 99% in blue, 90% in green and 68% in red

The flux corresponding to the best-fit model is $F_{(2-10)\ keV} = (8.71^{+0.41}_{-0.82}) \times 10^{-13}\ erg/s\ cm^2$. The de-absorbed (i.e., corrected for the obscuration) rest-frame luminosity is $L_{(2-10)\ keV} = (3.88^{+0.21}_{-0.22}) \times 10^{40}\ erg/s$.

Given the estimated low luminosity of the primary powerlaw and the known high SFR of NGC1808, it is important to investigate if what we are indeed observing obscuration related to the torus. The powerlaw component, in fact, could be due to, at least in part, also to binaries laying in the inner 1.5″. We thus tried to estimate the SFR contribution to the X-ray emission also above 3 keV so as to be able to firmly associate the measured column to the putative nuclear obscuring torus.

Hereafter, we consider the possible sources of X-ray emission in a starburst scenario and their contributions to the total luminosity of the X-ray emission, in order to estimate the nuclear emission contribution only. Following Mineo et al. (2012), we calculated the star formation rate (SFR) for NGC1808 in order to estimate the contribution of the HMXBs to the total X-ray luminosity.
In general, the present SFR of a galaxy is mainly measured by the light emitted by highly massive stars: given their short lifetime, their collective luminosity is, in first approximation, proportional to the rate at which new stars are currently forming within the galaxy. Since the evolutionary time scale of HMXB does not exceed $\sim 10^7$ years, their X-ray emission reproduces the SFR of the galaxy itself quite well (e.g., Shtykovskiy & Gilfanov 2007). This makes them a good potential tracer of recent star forming activity in the host galaxy.
The total SFR (SFR_{tot}) is calculated by taking into account both the UV light escaping the galaxy and the IR emission of the dust heated by young stars (e.g., Bell 2003, Hirashita, Buat & Inoue 2003, Iglesias-Páramo et al. 2004, 2006). From Mineo et al. 2012, we evaluated the total SFR as

$$SFR_{tot} = SFR^0_{NUV} + (1-\eta)SFR_{IR} \ , \tag{3.6}$$

where η is the *cirrus correction*, i.e., the fraction of IR luminosity due to the old stellar population. It depends on the type of galaxy and in general is very difficult to determine; we use the average values obtained by Hirashita et al. (2003):

$$\eta \approx \begin{cases} 0.4 & \text{for normal disk galaxies,} \\ 0 & \text{for starbursts.} \end{cases} \tag{3.7}$$

SFR^0_{NUV} and SFR_{IR} in equation (3.6) are obtained assuming a Salpeter initial mass function (IMF) for the mass range 0.1−100 $\mathrm{M}_\odot$. From Iglesias-Páramo et al. 2006, we evaluated the individual contributions to the total SFR by

$$SFR^0_{NUV}\ (M_\odot/yr) = 1.2\times10^{-43}\times L_{NUV,obs}\ (erg/s) \ , \tag{3.8}$$
$$SFR_{IR}\ (M_\odot/yr) = 4.6\times10^{-44}\times L_{IR}\ (erg/s) \ , \tag{3.9}$$

where $L_{UV,obs}$ is the observed NUV luminosity (2312 Å), i.e., uncorrected for dust attenuation, and L_{IR} is the 8−1000 μm luminosity.
For $L_{UV,obs}$ and L_{IR}, we used the literature values: from Gil De Paz et al. (2006) we found $L_{UV,obs} = (2.69\pm0.40)\times10^{42}$ (erg/s); for L_{IR}, in virtue of the extensive literature, we chose two values in order to have upper and lower boundaries: we found $L_{IR,D} = (9.18\pm2.30)\times10^{43}$ (erg/s) and $L_{IR,S} = (1.96\pm0.39)\times10^{44}$ (erg/s) from Dhalem et al. (1990) and from Sanders et al. (2003), respectively. In Table 3.18 we reported the SFR_{IR} for L_{IR}, SFR^0_{NUV}, and SFR_{tot}, using equations (3.6), (3.9) and (3.9).
Considering the higher L_{IR}, we have obtained a value for the total SFR for NGC1808 which turns out to be $\sim 10(M_\odot/yr)$. This total SFR is in agreement with other values in the

SFR_{IR} $(M_\odot/yr)$	SFR^0_{NUV} $(M_\odot/yr)$	SFR_{tot} $(M_\odot/yr)$
$(4.23 \pm 1.06)_{L_{IR,D}}$	0.32 ± 0.05	4.55 ± 1.06
$(9.03 \pm 1.81)_{L_{IR,S}}$		9.35 ± 1.81

Table 3.18: SFR_{IR}, SFR^0_{NUV}, and SFR_{tot} using equations (3.6), (3.9) and (3.9). SFR_{IR} is computed considering both the upper $L_{IR,S}$ and lower $L_{IR,D}$ IR luminosities. The subscripts D and S refer to the luminosities found by Dahlem et al. (1990) and Sanders et al. (2003), respectively.

literature (see, e.g., Junkes et al. 1995, Jiménez-Bailón et al. 2005, Busch et al. 2017). As discussed above, HMXBs are good tracers of recent star forming activity in the host galaxy. From Mineo et al. (2012), their collective luminosity is found to be proportional to the SFR:

$$L^{HMXB}_{[0.5-8.0]\ keV}\ (erg/s) = 2.61 \times 10^{39} \times SFR_{tot}\ (M_\odot/yr)\ . \tag{3.10}$$

The dispersion around the best-fit relationship is $\sigma = 0.43\ dex$.

Furthermore, the collective luminosity of X-ray binaries correlates also with the IR luminosity of the host galaxy. From Mineo et al. (2012), we have:

$$L^{HMXB}_{[0.5-8.0]\ keV}\ (erg/s) = 1.75 \times 10^{-4} \times L_{IR}\ (erg/s)\ . \tag{3.11}$$

The dispersion around the best fit is $\sigma = 0.54\ dex$, notably worse than for the $L^{HXRB}_{[0.5-8.0]\ keV}$-SFR.

From equations (3.10) and (3.11) we estimated the value of X-ray luminosity of HMXBs. In particular, if we considered a SFR$\sim$ 10 $(M_\odot/yr)$, we obtained an upper boundary of $\sim 3 \times 10^{40}\ (erg/s)$. The total X-ray luminosity, derived in the best-fit model of the *Chandra* extended source spectrum, was obtained by setting the normalization of the `mekal` component to zero, in order to obtain the luminosity corresponding to the powerlaw alone, i.e., the primary emission component of the AGN. We obtained $L_{X,tot} = 6.30^{+0.31}_{-0.25} \times 10^{40}\ (erg/s)$. All the luminosities have been estimated in the energy range of 0.5−8.0 keV. We can estimate that $L^{HMXB}_{[0.5-8.0]\ keV}$ contributes to the total X-ray luminosity up to 50%. This confirms that the nuclear emission is "diluted" from the emission of the host galaxy, as mentioned above, and supports our choice to present the nuclear spectral properties adopting a small extraction radius.

3.5.2 XMM-Newton spectral analysis

To complete our presentation of the X-ray properties of NGC1808, even if the main purpose of the analysis of this source is the study of the nuclear region, we have also studied its total emission. Considering the XMM-*Newton* PSF (see Section 2.1.2), the XMM-*Newton*

spectral analysis is performed only on the elliptical (i.e., extended) extraction region chosen in Section 3.2. We built the best-fit model lead by the results obtained from the *Chandra* spectral analysis of the extended region. In fact, we verified that the best-fit model of *Chandra* for the elliptical source region is the statistically best model for XMM-*Newton*, with $\chi^2_\nu = 1.2$:

$$XMM\_Source\_Model{=}zphabs{*}[phabs_{gal}{*}(mekal{+}zgauss{+}zgauss{+}zpcfabs{*}(zpo))] \ .$$

As in *Chandra*, the addition of the two Gaussian lines to the basic model is statistically significant ($\geq 4\sigma$). In Table 3.19, we report the properties of the two emission lines found in the XMM-*Newton* spectrum.

Table 3.19: The theoretical line energy (from Turner et al. 1997), the observed line energy and the statistical significance of the lines.

	Theoretical line energy	Observed line energy	Statistical significance
MgXI	1.34 (keV)	$1.33^{+0.01}_{-0.01}$ (keV)	5σ
SiXIII	1.85 (keV)	$1.87^{+0.02}_{-0.02}$ (keV)	4σ

Table 3.20 shows the main parameters of the XMM-*Newton* best-fit model for the elliptical source region. For the sake of clarity, here (and below) we report the spectral analysis and the results obtained for the pn camera only.
The spectral analysis of XMM-*Newton* data supports the scenario outlined by *Chandra* spectral analysis. The XMM-*Newton* best-fit model is composed by the main emission powerlaw with $\Gamma = 1.78^{+0.18}_{-0.18}$, affected by the Galactic absorption ($N_{H,gal} = 2.33 \times 10^{20}\ cm^{-2}$, from Kalberla et al. 2005). The powerlaw results to be flatter than those found in *Chandra*, but compatible within the errors. The soft part of the spectrum is described by the contribution of several components: the gas absorption below $\sim 0.5\ keV$, likely associated with the abundant presence of dust in the considered regions, is represented by the addition of a further absorption component `zphabs`, with a Compton-thin column density of $0.11^{+0.02}_{-0.02} \times 10^{22}\ cm^{-2}$, placed in front of the whole model; the thermal emission below $\sim 2\ keV$, likely to the stellar activity of the galaxy, is reproduced through the addition of a thermal component `mekal` with a temperature of $0.60^{+0.02}_{-0.02}\ keV$ (consistent with *Chandra* temperature); the emission peaks at 1.3 keV and 1.8 keV, are considered by adding two Gaussian emission lines `zgauss`. These lines, as in *Chandra*, are identified as the MgXI at $1.33^{+0.01}_{-0.01}\ keV$ with an EW of $0.069^{+0.004}_{-0.004}\ keV$, and SiXIII at $1.87^{+0.02}_{-0.02}\ keV$ with an EW of $0.08^{+0.01}_{-0.01}\ keV$, respectively.
The hard part of the spectrum is mainly described by two components: the primary emission powerlaw, which emerges only above $\sim 3\ keV$, and a partial covering absorption component `zpcfabs`, with a column density of $N_{H,zpcf} = 0.11^{+0.02}_{-0.02} \times 10^{22}\ cm^{-2}$, which describes a clumpy torus and/or the contribution of the binaries. In Fig. 3.41 we show the unfolded spectrum for pn camera (a) and the $N_{H,zpcf} - \Gamma$ contour plot.

The flux corresponding to the best-fit model is $F_{(2-10)\ keV} = (9.95^{+0.72}_{-0.53}) \times 10^{-13}\ erg/s\ cm^2$. The de-absorbed (i.e., corrected for the obscuration) rest-frame luminosity is $L_{(2-10)\ keV} = (3.82^{+0.20}_{-0.23}) \times 10^{40}\ erg/s$.

Table 3.20: The best-fit model of XMM-*Newton* spectrum of NGC1808 source region for pn camera only.

	zpha[pha$_{gal}$(mekal+zgauss+ +zgauss+zpcfabs(zpo))]
$N^1_{H,gas}$ (10^{22} cm^{-2})	$0.11^{+0.02}_{-0.02}$
kT^2 (keV)	$0.60^{+0.02}_{-0.02}$
$Norm^3_{kT}$ (cm^{-5})	$1.58^{+0.13}_{-0.11} \times 10^{-4}$
$E^4_1(keV)$	$1.33^{+0.01}_{-0.01}$
$Norm^5_{E_1}$ ($photons/cm^2/s$)	$8.85^{+1.96}_{-1.96} \times 10^{-6}$
$EW^6_{E_1}$ (keV)	$0.069^{+0.004}_{-0.004}$
$\sigma^7_{E_1}$ (keV)	0.01
E^8_2 (keV)	$1.87^{+0.02}_{-0.02}$
$Norm^9_{E_2}$ ($photons/cm^2/s$)	$4.81^{+1.56}_{-1.56} \times 10^{-6}$
$EW^{10}_{E_2}$ (keV)	$0.08^{+0.01}_{-0.01}$
$\sigma^{11}_{E_2}$ (keV)	0.01
$N^{12}_{H,zpcf}$ (10^{22} cm^{-2})	$15.69^{+3.83}_{-2.98}$
CvrFract[13]	$0.67^{+0.07}_{-0.10}$
Γ[14]	$1.78^{+0.18}_{-0.18}$
$Norm^{15}_{\Gamma}$ ($photons/keV/cm^2/s$)	$4.42^{+1.95}_{-1.36} \times 10^{-4}$
(χ^2/dof)[16]	243.8/195

(1) Gas/dust column density in units of 10^{22} cm^{-2}; (2) and (3) temperature in keV and normalization of the `mekal` component, respectively; (4) and (8) energy in keV of the Gaussian lines; (5) and (9) normalization of the Gaussian lines; (6) and (10) equivalent width of the Gaussian lines in keV; (7) and (11) line widths in keV, fixed at 0.01 keV; (12) and (13) column density in units of 10^{22} cm^{-2} and covering factor of the `zpcfabs` component, respectively; (14) and (15) photon index and powerlaw normalization, respectively; (16) ratio between χ^2 and the number of degrees of freedom. The errors are computed at the 90% confidence level for one parameter of interest (Avni 1976).

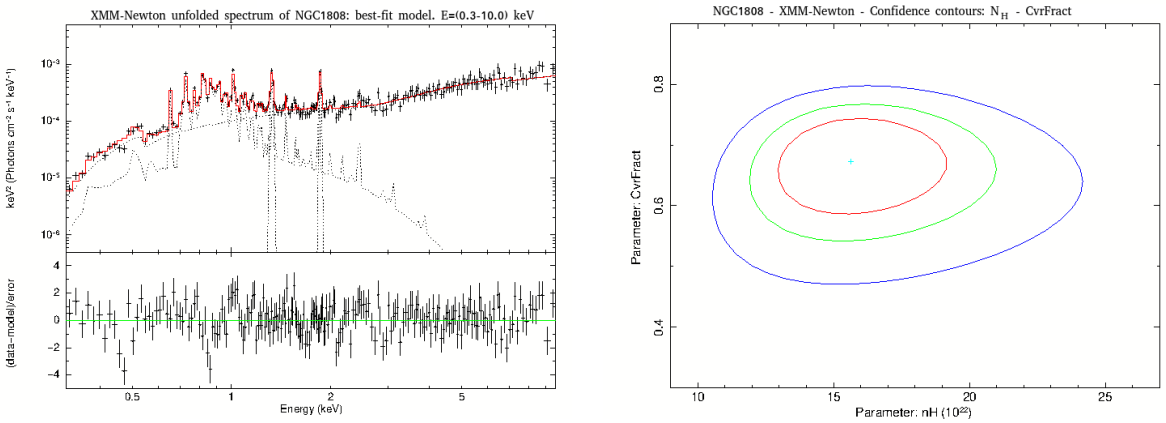

(a) (b)

Figure 3.41: (a) The best-fit model applied to XMM-*Newton* unfolded spectrum of NGC1808 source region, only pn camera. Upper panel: spectral fitting; lower panel: residuals plot in terms of data-model in units of σ. The red lines are the best-fit models. (b) $N_{H,zpcf} - CvrFract$ contour plot; the levels of confidence are shown as: 99% in blue, 90% in green and 68% in red

The total (de-absorbed) X-ray luminosity is of the order of 10^{40} (erg/s), compatible, within the errors, with the *Chandra* X-ray luminosity. In order to discriminate the contributions of the AGN and of the host galaxy to the total X-ray luminosity, we proceeded analogously to what we did in Section 3.5.1. By using the SFR reported in Table 3.18 we were able to compare the luminosities of interest, $L_{X,tot}$ and $L^{HXRB}_{[0.5-8.0]\ keV}$, directly.
The luminosity contribution associated to HMXBs calculated above, is confronted with the total X-ray luminosity ($L_{X,tot}$), derived in the best-fit model of the XMM-*Newton* source spectrum $L_{X,tot} = 5.61^{+0.24}_{-0.20} \times 10^{40}$ (erg/s). As in *Chandra*, the total X-ray luminosity was obtained by fixing the normalization of the `mekal` component to zero, in the energy range 0.5−8.0 keV. We can estimate the non-nuclear contribution to the total X-ray luminosity to be up to 60%.

Chapter 4

Radio data: instruments and data reduction

In the first part of the chapter we will review the principles of interferometry and present the used radio telescope ALMA. In the second part, we will describe the process of analysis and data reduction for the galaxies NGC613 and NGC1808.

4.1 The principles of interferometry

Interferometry is a technique that allows to obtain high angular resolutions in astronomical observations. It is based on Huygens-Fresnel principle and consists in collecting and combining signals from radio-telescopes, which can be at any distance. The incoming signal is processed as if it were observed by a single telescope having size equal to the distance between the individual antennas. In observations with a single telescope, the angular resolution θ is given by

$$\theta \approx 1.22\frac{\lambda}{D}\ [rad], \tag{4.1}$$

where λ is the observed wavelength, D is the antenna diameter, i.e., is the diameter of the circular section of the paraboloid identified by the telescope; similarly, in a simple interferometer (i.e., an interferometer made of two antennas) the angular resolution is given by

$$\theta \approx 1.22\frac{\lambda}{b}\ [rad], \tag{4.2}$$

where b is the *baseline*, i.e., the distance between the antennas that constitute it. Thanks to interferometry, one can obtain high angular resolutions by using single telescopes with a small diameter, thus overcoming the technological limits of the construction of large antennas.
Radioastronomers are able to obtain images with a very high angular resolution, high sensitivity and large *Field of View* (FoV) through the use of arrays of radio-telescopes such as the *Very Large Array* (VLA)[1] or the *Atacama Large Millimeter Array* (ALMA, discussed in detail in Section 4.3).

[1]The Very Large Array is an interferometric telescope composed of 27 antennas of 25 m located in Socorro, New Mexico. It works mostly on cm-wavelengths.
https : *//science.nrao.edu/facilities/vla/*

The FoV or *Primary Beam* is an important feature of an interferometric observation, defined as the angular distribution in which most of the radiation is received (or transmitted). It is typically approximated by a Gaussian function whose FWHM is:

$$\text{FoV} \simeq 1.13\frac{\lambda}{D}\ [rad], \tag{4.3}$$

where D is the diameter of the single aperture. The FoV is independent of the array configuration.
The maximum angular scale structure that may be recoverable from an interferometric observation is called *Maximum Recoverable Scale* (MRS) and is defined as:

$$\theta_{MRS} \simeq 0.6\frac{\lambda}{b_{min}}\ [rad], \tag{4.4}$$

where b_{min} is the minimum baseline of the array configuration. An interferometer is not sensitive to the large angular scales and cannot recover the total flux of resolved sources, therefore, from equation (4.4) the observed source is resolved if $\theta_{MRS} > \lambda/D$.
Another important angular scale of interferometers is the *Largest Angular Structure* (LAS), i.e., the largest scale structure observed in the source.
Actually, an interferometer is sensitive only to a range of angular sizes $\lambda/b_{max} < \theta < \lambda/b_{min}$, with an angular resolution λ/b_{max} over a FoV$\simeq \lambda/D$. In order to reconstruct the brightness of extended sources, one considers them as the sum of various point-like sources. Since a function can always be written as the sum of an even and an odd function, it follows that in order to detect all the brightness distributions of the source it is necessary to detect both the even and the odd part of the signal. A correlator which is sensitive both to the even and to the odd parts of the signal is called *complex correlator*; the response of a two-elements interferometer to an extended source with a brightness distribution $I(\hat{s})$ with a complex correlator is called *complex visibility*. It is defined as:

$$V = \int I(\hat{s})\ \exp\left(\frac{-2\pi i\vec{b}\cdot\hat{s}}{\lambda}\right)\ d\Omega, \tag{4.5}$$

where $\hat{s}$ is the direction of the vector pointing towards the observed source, $\vec{b}$ is the distance vector between two antennas and λ is the observation wavelength.
The visibility is a complex number, so it is characterized by a phase (ϕ) and an amplitude (A) and it can be expressed in the polar form:

$$V = A\ e^{-i\phi}. \tag{4.6}$$

In order to bring the complex visibility back to a two-dimensional Fourier transform, we can pass to a system of normalized Cartesian axis (u, v, w), by expressing the vectors $\vec{b}$ and $\hat{s}$ into their components $u = x/\lambda$, $v = y/\lambda$ and $w = z/\lambda$ and l, m, n, respectively. Finally, if one assumes the angular dimension of the source sufficiently small compared to the pointing angle, that is, $n = \cos(\theta) \approx 1$, equation (4.5) becomes:

$$V(u,v) \approx \int\int I_V(l,m)\ \exp\left[-2\pi i(ul+vm)\right] dl\ dm. \tag{4.7}$$

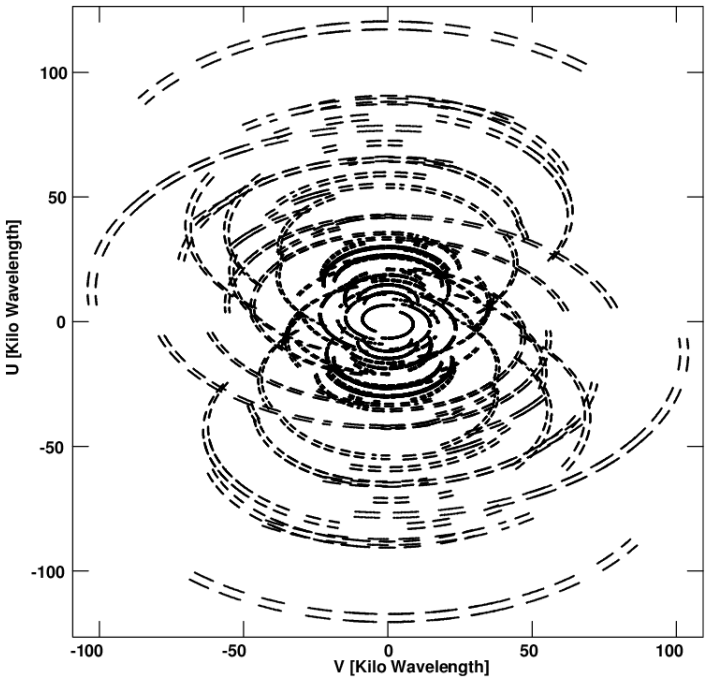

Figure 4.1: Example of uv plane coverage for a typical ALMA observation, from De Breuck et al. (2003).

The complex visibility measures the two-dimensional Fourier transform of the brightness distribution. The natural Cartesian coordinate system used to express the response of the correlator of an interferometer is called uv plane. An example of uv plane is shown in Fig. 4.1. This system represents the spatial distribution baselines as seen from the source and for the entire duration of the observation. The discretization of the uv plane determines the point spread function (PSF or beam), that is, the way in which the point-like source is seen by the acquisition system. In order to get an image that is as more similar as possible to the real one, the uv plane must be sampled as uniformly as possible: the denser the lattice of the uv plane, the better the reconstruction of the surface brightness of the source. Because the antenna diameter D must be smaller than the baseline b (otherwise the antennas would overlap), the angular frequency response cannot extend to zero and the interferometer cannot detect an isotropic source. This means that the closest regions of the uv plane cannot be sampled, leading to the so-called *missing short spacings problem* ($b < D$).
The brightness distribution is obtained through the Fourier inverse transform of equation (4.7) and it is, less then a multiplication factor, by:

$$I_V(l,m) \approx \int\int V(u,v)\, \exp\left[+2\pi i(ul+vm)\right] du\, dv. \tag{4.8}$$

Interferomery in practice

Each antenna measures and samples an electric signal V related to the electric field of the monochromatic incoming wave. The simplest interferometer is the one consisting of only two antennas, placed at a distance b from each other, pointing to the same source (as shown in Fig. 4.2): the voltages measured by each antenna are correlated by the correlator, which

multiplies the voltages between them and makes a temporal average. In this configuration, the wavefront of the incident radiation reaches the system with an angle θ, defined as the angle between the baseline and the direction of the source.

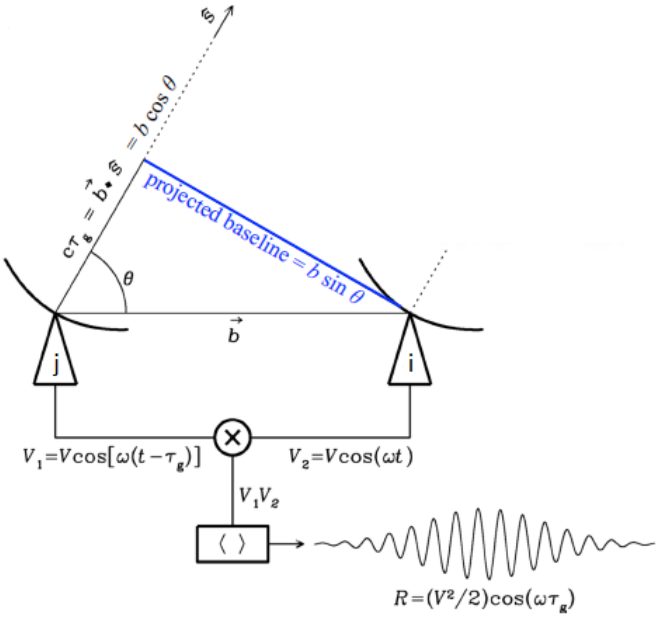

Figure 4.2: Scheme of two antennas interferometer (from Gitti 2020).

As shown in Fig. 4.2, the wavefront will not hit the two antennas simultaneously: antenna j will receive the signal later than antenna i. This delay is given by the different paths from the source and the two antennas, given by the *geometric delay* $\tau_g = b\cos(\theta)/c$. This geometric delay can be compensated by using devices called *cross-correlators*, which multiply the signal coming from the two antennas and make a temporal average, typically in intervals of few seconds. The output voltages of single antennas at a given time t will be obtained as

$$V_i = V\cos(\omega t), \tag{4.9}$$

$$V_j = V\cos[\omega(t-\tau_g)]. \tag{4.10}$$

The correlator multiplies the two outgoing voltages as

$$V_iV_j = V^2\cos[\omega(t-\tau_g)]\ \cos(\omega t) = \frac{V^2}{2}\left[\cos(2\omega t - \omega\tau_g) + \cos(\omega\tau_g)\right]. \tag{4.11}$$

Since $\omega\tau_g$ varies slowly, it can be approximated to be constant in the temporal mean; instead, ωt varies quickly, therefore, for a sufficiently long observation, the temporal average of the first term in equation (4.11) tends to zero. Note that, due to the terrestrial rotation, the considered source undergoes a shift in the plane of the sky. Therefore, during the observation θ will vary. Given these considerations, the correlator's output will be given by

$$R_{ij} = \langle V_iV_j\rangle = \left(\frac{V^2}{2}\right)\cos(\omega\tau_g). \tag{4.12}$$

The produced sine waves are called *interference fringes* and their phase ϕ is given by the argument of the sinusoidal function, so we have

$$\phi = \omega\tau_g = 2\pi\left(\frac{b}{\lambda}\right)\cos(\theta).$$

Since the baseline b is much larger than the observation wavelength λ, the phase of the fringes is extremely sensitive to the position of the source. For this reason ϕ is used as an observable for determining the position of the target. The correlator between the responses of the two antennas in equation (4.12) thus provides the *fringe visibility*. Given N antennas, the output number of visibilities depends on the number of baselines $N(N-1)/2$, on the polarization, on the number of sub-bands, on the number of channels and on the integration time.

4.2 Imaging process

Once the calibration process is done, in order to obtain the sky brightness distribution $I_t(l,m)$, the calibrated visibilities are Fourirer transforms. The function that takes the value of the true visibilities distribution $V_t(u,v)$ in each sampled point of the uv plane is called *sampling function* $S(u,v)$. From the convolution between $V_t(u,v)$, i.e. the ideal total coverage of the uv plane, and $S(u,v)$ we obtain the sampled visibilities distribution $V_S(u,v)$:

$$V_S(u,v) = V_t(u,v) * S(u,v). \tag{4.13}$$

From the inverse Fourier transform of the sampling function, we obtain the *dirty beam* $B(l,m)$, i.e. the interferometer response to the point-like source. Using the convolution Fourier transform theorem, we obtain the *dirty map* $I_D(l,m)$:

$$I_D(l,m) = FT^{-1}(V_S(u,v)) = I_t(l,m) * B(l,m). \tag{4.14}$$

Therefore, it is necessary to deconvolve the dirty map by the dirty beam, in order to obtain the map of the true brightness distribution $I_t(l,m)$.
The primary beam is corrected using the `clean` algorithm, in order to correct the image by the limited sampling of the uv plane and the synthesized beam sidelobes which can corrupt the image. The clean algorithm is an iterative process which makes a deconvolution of equation (4.14) with the goal of minimizing the effects of the incomplete spatial frequency sampling. At each iteration, the algorithm produces a *residual image* (RI), i.e., the image from which the brightest pixels have been subtracted and the final obtained image is a map of the diffused noise. In the latest RI no structure can be distinguished anymore. The last part of the cleaning process is called *restoring*. The fluxes and the positions of the points removed in the previous steps are stored in *clear components* (CC) tables. The `restore` algorithm convolves the cleaned components with the clean beam, i.e., the Gaussian fit for the main lobe of the dirty beam. Then, the algorithm sums the obtained values in the same pixels from which they were originally extracted from the final residual map. Thus, the *cleaned map*, i.e., the map cleaned by the effect of the secondary lobes, has been built.

4.3 ALMA radio telescope

The *Atacama Large Millimeter/submillimeter Array* (ALMA), shown in Fig. 4.3, is an astronomical interferometer made of 66 radio telescopes and one of the largest multi-national science projects nowadays. ALMA is an international partnership among Europe, United

States, Canada, Japan, South Korea, Taiwan, and Chile. The official inauguration took place on March, 13^{th} 2013, while the last antenna was delivered on October, 1^{st} 2013, with all 66 antennas fully operational at the end of that year. It is located in the Atacama Desert of northern Chile at an elevation of about 5000 m and at a latitude of $-23°$; this location was chosen for its high elevation and low humidity, crucial factors in order to decrease the noise signal[2].

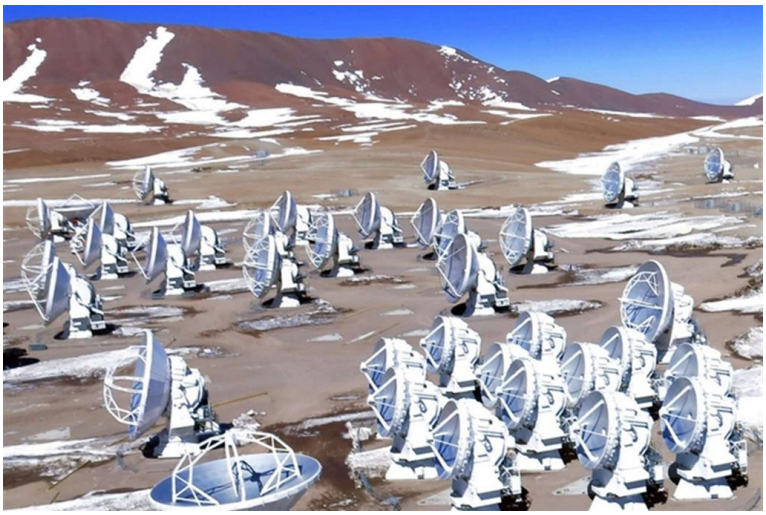

Figure 4.3: Atacama Large Millimeter/submillimeter Array.

ALMA combines 54 parabolic antennas with a diameter of 12 m (12 m *Array*), four among these antennas are used as single-dish (*Total Power Array*), and 12 parabolic antennas with diameter of 7 m (*Atacama Compact Array*, ACA). The antennas can be moved across the desert plateau over distances from 15 m to 16 km which allows to obtain angular resolutions ranging from 20 mas at 230 GHz to 43 mas at 110 GHz. The 12 m Array, whose baselines range from 15 m up to 16 km, is used for sensitive, high resolution imaging, while ACA, whose baselines range from 9 m to 30 m, is used for observation of wide field. The large number of ALMA's antennas allow a large number of baselines, a dense instantaneous uv plane coverage and a good imaging in short time.
The design of ALMA was driven by three key science goals:

- the possibility to detect spectral line emissions from carbon monoxide CO or ionized carbon [CII] in a normal galaxy (like the Milky Way) at a redshift of $z = 3$, in less than 24 hours;
- the possibility to create kinematic maps for gas in protostars and in protoplanetary disks around young Sun-like stars in the nearest molecular clouds (150 pc);
- the possibility to provide precise images at an angular resolution of $0.05''$.

ALMA is an incredibly powerful instrument at its full capabilities stage. Up to ten receiver bands are available, covering a wavelengths range from 0.3 mm to 3.6 mm ($84 - 950$ GHz), with possible extension to 10 mm (30 GHz).

[2] *https* : *//public.nrao.edu/telescopes/alma/*

4.3.1 ALMA Full capabilities

In Table 4.1 we summarized the ALMA full capabilities.

Table 4.1: ALMA Full Array Capabilities

						Compact		Extended	
Band	ν (GHz)	λ (mm)	**FoV**[(1)] ($''$)	**Maximum Scale**[(2)] ($''$)	**Continuum Sensitivity**[(3)] (mJy/beam)	**Angular Resolution**[(4)] ($''$)	ΔT_{line} (K)[(5)]	**Angular Resolution**[(6)]	ΔT_{line} (K)[(7)]
1^{+}	31.3 - 45	6.7 - 9.5	145 - 135	93	+	13 - 9	+	0.14 - 0.1	+
2^{+}	67 - 90	3.4 - 4.5	91 - 68	53	+	6 - 4.5	+	0.07 - 0.05	+
3	84 - 116	2.6 - 3.6	72 - 52	37	0.05	4.9 - 3.6	0.07	0.05 - 0.038	482
4	125 - 163	1.8 - 2.4	49 - 37	32	0.06	3.3 - 2.5	0.071	0.035 - 0.027	495
5	163 - 211	1.4 - 1.8	37 - 29	23	*	*	*	*	*
6	211 - 275	1.1 - 1.4	29 - 22	18	0.10	2.2 - 1.5	0.1.4	0.021 - 0.016	709
7	275 - 373	0.8 - 1.1	22 - 16	12	0.20	1.5 - 1.1	0.29	0.016 - 0.012	1128
8	385 - 500	0.6 - 0.8	16 - 12	9	0.40	1.07 - 0.82	0.234	0.011 - 0.0009	1569
9	602 - 720	0.4 - 0.5	10 - 8.5	6	0.64	0.68 - 0.57	0.641	0.0007 - 0.0006	4305
10	787 - 950	0.3 - 0.4	7.7 - 6.4	5	1.2	0.53 - 0.43	0.940	0.0006 - 0.00	-

(1) FWHM of the Gaussian dirty beam of the individual antennas.
(2) Largest angular scale structure that can be recoverable from observations.
(3) Continuum sensitivity for a one-hour exposure.
(4) and (6) FWHM of the synthesized dirty beam (see Section 2.1) in the compact and extended configuration, respectively.
(5) and (7) Brightness temperature sensitivity, for 1-hour observation with a 50-antenna array arranged in compact or extended configuration, respectively.
$*$ available on a limited number of antennas.
+ To be developed in future.

The data analyzed in this Thesis were carried out during ALMA Early Science Cycle 3 program for NGC613 and during ALMA Cycle 4 for NGC1808, whose capabilities are different from the ALMA full Array, as described in the following Sections.

4.3.2 ALMA Cycle 3 capabilities

ALMA Cycle 3[3] had a duration of 12 months (October 2015-September 2016). In this Cycle, ALMA had the following capabilities: thirty-six $12m$ antennas for interferometric observations, ten 7 m antennas (ACA) and two 12 m antennas for single-dish observations (TP Array); receiving bands 3, 4, 6, 7, 8, 9 and 10 with wavelengths between $0.32 - 3.6$ mm (corresponding to a frequency range of $84 - 950$ GHz); the array configurations allow baselines ranging from 160 m to 10 km (but not for all receiving bands). Table 4.2 collects main capabilites of ALMA Cycle 3.

[3]https://almascience.eso.org/documents-and-tools/cycle3/

Table 4.2: ALMA Cycle 3 Capabilities

Cycle 3 Receiver					Most Compact		Most Extended	
Band	ν (GHz)	λ (mm)	FoV ($''$)	Sensitivity[(1)] (mJy/beam)	Angular Resolution ($''$)	Maximum Scale ($''$)	Angular Resolution (mas)	Maximum Scale ($''$)
3	84−116	2.6−3.6	73−53	0.095	3.8−2.8	21−22	92−66	1.25−0.91
4	125−163	1.84−2.4	48−38	0.11	2.6−2.0	20−15	62−47	0.84−0.65
6	211−275	1.1−1.4	29−22	0.12	1.5−1.2	12−9	36−28	0.50−0.38
7	275−373	0.8−1.1	22−16	0.21	1.2−0.86	9.0−6.6	48−36	0.64−0.47
8	385−500	0.6−0.8	16−12	0.40	0.84−0.6	6.4−4.9	84−64	2.2−1.7
9	602−720	0.4−0.5	10−8.5	1.59	0.53−0.45	4.1−3.4	53−45	1.4−1.2
10	787−950	0.3−0.4	7.8−6.5	3.87	0.41−0.34	3.1−2.6	41−34	1.1−0.87

(1) 1σ rms in an integration time of 60s.

4.3.3 ALMA Cycle 4 capabilities

ALMA Cycle 4[4] had a duration of 12 months (October 2016-September 2017). In this Cycle, ALMA had the following capabilities: forty antennas in the $12m$ Array, plus ten $7m$ and three $12m$ antennas in the ACA configuration; receiver Bands 3, 4, 6, 7, 8, 9 and 10 with wavelengths between $0.35 - 3.0$ mm (corresponding to a frequency range of $100 - 937$ GHz); the array configurations allow baselines ranging from 156 m to 12.6 km (but not for all receiving bands). In table 4.3 we collect the main capabilites of ALMA Cycle 4.

Table 4.3: ALMA Cycle 4 Capabilities

Cycle 3 Receiver					Most Compact		Most Extended	
Band	ν (GHz)	λ (mm)	FoV ($''$)	Sensitivity[(1)] (mJy/beam)	Angular Resolution ($''$)	Maximum Scale ($''$)	Angular Resolution (mas)	Maximum Scale ($''$)
3	84−116	2.6−3.6	73−53	0.095	4.4−3.2	34−25	78−57	0.93−0.68
4	125−163	1.84−2.4	48−38	0.13	3.0−2.3	23−18	53−41	0.63−0.48
6	211−275	1.1−1.4	29−22	0.13	1.8−1.4	14−11	31−24	0.37−0.29
7	275−373	0.8−1.1	22−16	0.24	1.35−0.99	10.6−7.8	43−32	0.48−0.35
8	385−500	0.6−0.8	16−12	0.46	0.96−0.74	7.6−5.8	53−41	0.46−0.36
9	602−720	0.4−0.5	10−8.5	2.3	0.61−0.51	4.8−4.0	34−29	0.30−0.25
10	787−950	0.3−0.4	7.8−6.5	5.2	0.47−0.39	3.7−3.1	22−26	0.23−0.19

(1) 1σ rms in an integration time of 60s.

[4]https://almascience.eso.org/documents-and-tools/cycle4/

4.4 ALMA Science Archive

The ALMA *Science Archive* (ASA)[5] contains all public and proprietary data of PI-proposal observations. ASA has a complex and hierarchical structure, the so-called *Observing project*, as shown in Fig. 4.4[6].

Figure 4.4: Scheme of an Observing Project. Each level of the block diagram corresponds to a precise data acquisition procedure. From *ALMA Science Archive Query*.

At proposal stage the PI makes choices and requests needed to reach his/her purposes. The Observing project is divided into *Science Goals* (SG), i.e., the minimum proposed observational unit including targets in the same sky region that roughly share the same calibration, PI-proposal requests and spectral setup. Sensitivity goals are defined on SG basis. The smallest unit for data processing is called *Observing Unit Set* (OUS).
Each SG is divided into a *Group*. It can contain several configurations to be combined in data processing (e.g., several arrays), each of them is a *Member*. A Member can contain multiple executions of *Scheduling Blocks*. It is the minimum scheduling entity.
Each SG is converted into a Scheduling Block, i.e., the minimum observational unit including targets in the same sky region and their calibrators to be observed with the same instrumental setup. They are the minimum set of instructions to perform an observation. Different configurations cannot stay in the same SB. It is possible that an SB has to be repeated to reach the requested sensitivity. Each repetition of the observation of a SB is called *Execution Block*. This is the minimum observing unit and the minimum data reduction unit, but might not be enough to reach the PI requests. It is the minimum archive

[5]https://almascience.eso.org/asax/
[6]https://almascience.eso.org/documents-and-tools/latest/documents-and-tools/science-archive-manual

unit, i.e., the smallest entity used for observing. The SB/Member/Group are the smallest structures that contain science observations that need to be observed processed/combined together to produce calibrated science products.

4.4.1 Data Quality Assurance

The goal of ALMA *Quality Assurance* (QA) is to deliver to the PI a reliable final data product that has reached the desired control parameters outlined in the SG, that is calibrated to the desired accuracy and free of calibration or imaging artifacts.
ALMA QA happens on four levels:

- **QA0**: near-real time verification of weather and hardware issues carried out on each execution block immediately after the observation.
- **QA1**: verification of longer-term observatory health issues like absolute pointing and flux calibration.
- **QA2**: offline calibration and imaging (using CASA software, see later Section 4.5.1) of a completely observed Member OUS. This procedure is performed by expert analysts with the help of semi-automatic procedures, based on common practice. The calibration can be *Manual* or based on the *Pipeline*. The imaging so far is always manual. This step is limited to verify the achievement of the PI requests for each Member OUS. Finally, the results are archived and given to the PI.
- **QA3**: PIs may request re-reduction, problem fixes and possibly re-observation. This is an optional step.

4.4.2 Data format

The ALMA *Science Data Model* (ASDM) is the final archived product from each observation. ASDM has an unique hexadecimal name and contains the meta-data (headers, descriptions of the observation setup, etc), and the binary data (the raw data, i.e., the raw visibility).
The first step of any data processing is importing the ASDM in the format suitable for the software used, i.e., CASA software. *Measurement Set* (MS) is constituted by several tables referring each other and collecting most (not all) the information in the ASDM.
For each project the main deliverables are Raw Data, Calibration Scripts and Tables. The resulting calibrated data is considered science-ready. As a consequence of the process, only data that passed QA2 are in the archive. Also imaging products are delivered, as result of QA2 processing, but images in the archive are provided as starting point on the way to obtain the final images and a valuable basis for archive researchers, i.e., they are not considered science-ready.

4.5 The adopted software

In this Section we describe the softwares used for the interferometric analysis of the studied galaxies.

4.5.1 The CASA software

The *Common Astronomy Software Applications* (CASA)[7] package is the primary data processing software for the ALMA and VLA, and is frequently used also for other radio telescopes. CASA is a comprehensive software package to calibrate, image, and analyze radio astronomical data from interferometers (e.g., MeerKAT) as well as single dish telescopes (e.g., IRAM-30m, APEX).
The CASA infrastructure is built on top of CASA-core consists of many tools that are implemented in C++ and used with an Interactive Python interface as data reduction tasks. This structure provides flexibility to process the data via task interface or as a python script. In addition to the data reduction tasks, many post-processing tools are available for more flexibility and special purpose reduction needs.
Any kind of interferometric data can be converted with specific tools in a CASA data format, the so-called *Measurement Set* (MS). The structure of MS is a nested-table-based: the principal table, called *MAIN*, which is substructure itself, contains auxiliary information about the observation (e.g., sources, pointing, atmosphere, antennas).
The many columns of MAIN table contain the main information relative to the observation, in particular: the *DATA* column, which contains the information about the raw visibilities; the *Scratch* columns storing the modification to the raw data, such as *Corrected Data*, which contain the calibrated data, and the *Model*, which holds the information about model visibilities.
Using the CASA version 5.1.1-5 software, we inspected available data, created interferometric data cubes and extracted the moments. The three moment are: the *0 moment*, i.e, the integrated intensity map, the *first moment*, i.e, the intensity velocity map and the *second moment*, i.e, the intensity velocity dispersion map. In this Thesis we analyzed the *0 moment*, as explained later in Section 5.1.

4.5.2 The GILDAS and IRAF softwares

Grenoble Image and Line Data Analysis Software (GILDAS)[8] is a collection software oriented toward (sub-)millimeter radioastronomical applications, either single-dish or interferometer. It is one of the numerous image processing systems used in Astronomy and has been adopted as the IRAM standard data reduction package. It is written in Fortran-90/95, with a few parts in C/C++ (mainly keyboard interaction, plotting, widgets).
GILDAS has two different data types: images and tables. Images are data sets of up to 4 dimensions, with a header specifying, for example, the coordinate system, the type of projection used and spectroscopic information. Tables are essentially like 2-D images and the one of relevant information is the number of lines and columns in the table.
Using GILDAS/Mapping version jan21a, we have analyzed calibrated ALMA CO-line and continuum maps, extracted information useful for the analysis, and performed the imaging producing the maps shown in this Thesis.
Image Reduction and Analysis Facility (IRAF)[9] is a general purpose software system for the reduction and analysis of scientific data. The IRAF system provides a good selection of programs for general image processing and graphics applications, plus a large selection

[7] *https://casa.nrao.edu/*
[8] *https://www.iram.fr/IRAMFR/GILDAS/*
[9] *http://iraf.noao.edu*

of programs for the reduction and analysis of optical astronomy data. Using IRAF version 2.16.1, we have performed simple operations on the images and also check some procedures done in the GILDAS environment.
The ALMA data analysis in this Thesis was performed on cluster of the ALMA Regional Center of the INAF Istituto di Radioastronomia, Bologna. This is one of the seven nodes that constitute the European network that provides technical and scientific support to ALMA users.

4.6 The ALMA data selection

In this Section we will illustrate the available ALMA data for NGC613 and NGC1808 and discuss their advantages and disadvantages, in order to justify the choice of the dataset analyzed in this Thesis.
Data were downloaded from ALMA Science Archive[10]. We checked that they data granted the requisites of rms and angular resolution requested by PI and able to satisfy our scientific goals. The inspected data are collected in Table 4.4.

Source	**Band**	**Line**	**Cycle**	ν (GHz)	λ (mm)	**Beam**	**PI**
NGC613	3 84 − 116 GHz	CO(1–0)	2	115.271	2.60	0.7″ 58pc	Y. Miyamoto
	7 **275−373 GHz**	**CO(3–2)**	**3**	**345.796**	**0.87**	**0.14″** **11.6pc**	F. Combes
	275−373 GHz	CO(3–2)	4	345.796	0.87	0.08″ 6.6pc	F. Combes
NGC1808	7 275−373 GHz	CO(3–2)	3	345.796	0.87	0.14″ 6.3pc	F. Combes
	7 **275−373 GHz**	**CO(3–2)**	**4**	**345.796**	**0.87**	**0.30″** **13.5pc**	F. Combes

Table 4.4: CO observations of NGC613 and NGC1808 available in the ALMA Science Archive. All these observations have been acquired in a single pointing towards the galaxy center. Data in bold are those used in this Thesis.

The CO(1–0) emission line observations, available only for NGC613, allow a direct measure of the H_2 mass (see later Section 5.1) but a lower angular resolution than CO(3–2) data (see Section 4.1). The CO(3–2) emission line observations offer a higher angular resolution;

[10]https://almascience.nrao.edu/asax/

however, in this case we have to assume a line ratio $R_{13} = L_{CO(1-0)}/L_{CO(3-2)}$ to estimate H_2 mass from CO(3–2) observations (see Section 5.2). Since our goal is to spatially resolve the nuclear region of NGC613 and NGC1808, we decided to use CO(3–2) observations.
For NGC613, unfortunately, Cycle 4 CO(3–2) data seem to be not usable (after a double check[11]) and for this reason we decided to use CO(3–2) data available from Cycle 3. Instead, for NGC1808 we used Cycle 4 CO(3–2) data. We also mention that CO(3–2) Cycle 3 data of NGC1808 only show hint of detection.
In Tables 4.5 and 4.6 we collect the main properties of the analyzed data for NGC613 and NGC1808, respectively.

Band	**Cycle**	**Array Configuration**	**Integration Time**	**Beam**	**FoV**	**rms**	**Velocity Resolution**
7	3	TE	1 h	0.14″ 11.6 pc	18″ 1.5 kpc	Line:0.9 mJy/beam at 10 km/s Continuum: 80 μJy/beam	10 km/s

Table 4.5: Main properties of the used ALMA Cycle 3 data of NGC613.

In Cycle 3, NGC613 was observed (project ID:#2015.1.00404.S, PI F. Combes) simultaneously for both the compact (TC, baselines from 15 m to 630 m) and the extended (TE, baselines from 15 m to 1400 m) configurations. The TE configuration, adopted in August 2016 with 41 antennas, is the configuration used in this Thesis. The total integration time, including calibration and overheads, was 1 hr. The synthesized beam is of $\sim 0.14''$ ($\sim 12\ pc$) and the rms sensitivity of 1 $mJy/beam$ in 10 km/s channels (80 $\mu Jy/beam$ in the continuum). In order to redefine the center of the observations, we analyzed the continuum map available thanks to ALMA Band 7 ($275 - 373$ GHz) observations.

Band	**Cycle**	**Array Configuration**	**Integration Time**	**Beam**	**FoV**	**rms**	**Velocity Resolution**
7	4	TM2	11 m	0.30″ 13.5 pc	18″ 0.8 kpc	Line:1.4 mJy/beam at 10 km/s Continuum: 90 μJy/beam	10 km/s

Table 4.6: Main properties of the used ALMA Cycle 4 data of NGC1808.

In Cycle 4, NGC1808 was observed (project ID:#2016.1.00296.S, PI F. Combes) simultaneously for both the compact (TM2, baselines from 15 m to 704 m) and the extended (TM1, baselines from 21 m to 3638 m) configurations, carried out in November 2016 and August

[11]We will send a ticket to the ALMA Helpdesk to report this problem.

2017, respectively. The TM2 configuration was observed with 42 antennas for an integration time of 11 minutes, a synthesized beam of $0.30''$ ($\sim 13.5\ pc$) and the rms sensitivity of 1.4 $mJy/beam$ in 10 km/s channels (90 $\mu Jy/beam$ in the continuum). This is the configuration used in this Thesis.
These observations have been acquired in a *single pointing*, covering a FoV of $18''$, corresponding to 1.5 kpc and 0.8 kpc for NGC613 and NGC1808, respectively. NGC613 and NGC1808 were observed in dual polarization mode with 1.875 GHz total bandwidth per baseband, and channel spacing of 0.488 MHz corresponding to ∼0.8 km/s. The spectra were then smoothed to 11.7 MHz (∼10.2 km/s) for NGC613, and to 11 MHz (∼10.16 km/s) for NGC1808 in order to build the final channel maps we used.

The maps used in this work are corrected for primary beam attenuation (see Section 4.2). We stress that very limited CO(3–2) emission was detected outside the full width half power primary beam, for both sources. The *missing-flux problem* can affect the high-frequency observations (e.g., in ALMA Band 7). However, the velocity gradients are very high in galaxy nuclei and the size of the emission in each velocity channel is not expected to be extended. For these reasons, the *missing-flux problem* should not affect CO-line measurements significantly. The *missing-flux problem* could instead affect the continuum map. This effect can be solved (or mitigated) by combining interferometric observations with single-dish observations (e.g. $NOEMA + IRAM - 30\ m$, Combes et al. 2009, Casasola et al. 2011), and for ALMA by combining data from the main array of 12 m diameter antennas with those of the compact ACA array and/or with those of the single ALMA antennas used as single-dish (e.g., see Leroy et al. 2021).

The data presented in the following have passed the QA2 phase (see Section 4.4.1 for details on QA2), hence they are already calibrated and reduced.

Chapter 5

ALMA data analysis

5.1 CO as molecular gas tracer

Molecular gas is critical in determining the formation, morphology, and evolution of galaxy disks. It is within the giant molecular clouds (GMCs) that interstellar gas is transformed into next generations of stars, and the most massive stars are responsable for most of the galactic luminosity. The molecular hydrogen (H_2) lacks a dipole moment and typical temperatures ($\sim$15 – 25 K) in GMCs are too low to excite quadrupole or vibrational transitions. For these reasons, the carbon monoxide (CO, the second most abundant molecule in the interstellar medium, ISM) emission lines are the most straightforward and reliable tracer of H_2 in galaxies (e.g., Carilli & Walter 2013). Its strong rotational transitions emit lines through collisions with H_2 and CO has a weak permanent dipole moment and a ground rotational transitions with a low excitation energy. The CO rotational transitions are observed in the (sub-)millimeter range (e.g., CO(1–0) at 2.6 mm, CO(2–1) at 1.3 mm, CO(3–2) at 0.87 mm).
The standard relation between the observed CO intensity and the column density of H_2 is given by

$$N(H_2) = X_{CO} I(CO\,,\, J = 1 \rightarrow 0), \tag{5.1}$$

where $N(H_2)$ is the column density in unit of cm^{-2}, $I(CO)$ is the CO integrated line intensity in units of $K\ km\ s^{-1}$, $J = 1 \rightarrow 0$ indicates the transition from the (rotationally) excited state to the ground one, and X_{CO} is the CO-to-H_2 conversion factor (e.g., Bolatto et al. 2013). We used the value of $X_{CO} = 2 \times 10^{20}\ cm^{-2}\ (K\ km\ s^{-1})^{-1}$, recommended for Milky Way-like disks (e.g., Bolatto et al. 2013). The CO-to-H_2 conversion factor can also be expressed in terms of α_{CO} defined as:

$$\alpha_{CO} = \frac{M(H_2)}{L'_{CO}}, \tag{5.2}$$

where $M(H_2)$ is the mass of H_2 in $M_\odot$ and L'_{CO} is the CO line luminosity in $K\ km\ s^{-1}\ pc^2$ (Narayanan et al. 2012). The value of $X_{CO} = 2 \times 10^{20}\ cm^{-2}\ (K\ km\ s^{-1})^{-1}$ corresponds to $\alpha_{CO} = 3.2\ M_\odot\ (K\ km\ s^{-1}\ pc^2)^{-1}$. As is usual in the literature, we refer to the CO-to-H_2 conversion factor both in terms of X_{CO} and α_{CO}.
From the integrated intensity CO(3–2) map, i.e., the moment 0 map, we computed the CO integrated flux density (see Section 5.2.2) and, from it, the CO luminosity. Following

Solomon & Vanden Bout (2005), the CO luminosity L'_{CO} can be computed as

$$L'_{CO} = 3.25 \times 10^7 \left(\frac{S(CO)dV}{Jy\ km\ s^{-1}}\right) \left(\frac{\nu_{rest}}{GHz}\right)^{-2} \left(\frac{D_L}{Mpc}\right)^2 (1+z)^{-1}\ [K\ km\ s^{-1}\ pc^2], \quad (5.3)$$

where $S(CO)dV$ is the integrated line flux density, ν_{rest} is the rest frame frequency, z is the redshift and D_L is the luminosity distance.

5.2 NGC613 analyzed maps

In this Section we will present the analyzed maps for the galaxy NGC613. As anticipated in Section 4.6, we focused on the study of the CO(3–2) emission line with the aim of characterizing the distribution of the molecular gas in the innermost region of NGC613. These data have already been published in Combes et at. (2019) and Audibert et al. (2019).
We will present our analysis and corresponding results, comparing them with those present in the literature. Our goal is to calculate the H_2 column density ($N(H_2)$), as traced by CO, in order to compare it with the value obtained in X-ray analysis performed in Section 3.3. We obtained $N(H_2)$ values for three regions centered on the nucleus of NGC613: *i)* within the FoV of ALMA Band 7 observations, *ii)* within the region occupied by the molecular torus, *iii)* within a very central region available from the literature.

5.2.1 Continuum map

The continuum map was used to redefine the position of the central AGN. This is possible when the nucleus has a strong point-like emission in the radio continuum.
Figure 5.1 shows the 345 GHz continuum map obtained towards the nucleus of NGC613. The center of NGC613 is originally taking from NED[1] (RA: 01h 34m 18.170s, Dec: -29d 25m 06.10s). These coordinates, which are those commonly adopted for NGC613 (e.g., Combes et al. 2019, Audibert et al. 2019), are identified in Fig. 5.1 with the black cross. We detected a central continuum point-like source emission (RA: 01h 34m 18.19s, Dec: -29d 25m 06.60s) which is represented in the right panel of Fig 5.1 by the blue star. The center of the observations is not coincident with the peak of the continuum emission: we measured this shift to be $\Delta s \simeq 0.6''$ (mainly in RA). The displacement between the center provided by NED and the center of the continuum emission that we found can be ascribed to an approximation of the coordinates provided by NED. The AGN position we found is consistent with those derived by Combes et al. (2019) and Audibert et al. (2019).
The left panel of Fig. 5.1 shows the central $10'' \times 10''$ of NGC613. The continuum emission is distributed in a clumpy ring of radius $\sim 4''$ corresponding to a star forming ring, observed in K-band (e.g., Böker et al. 2008). The right panel of Fig. 5.1 shows the zoom of the central $2'' \times 2''$ of NGC613, where the peak of the continuum emission is well defined. We assumed that the continuum emission peak corresponds to the position of the central black hole, as commonly done in similar studies (e.g., Casasola et al. 2011, Combes et al. 2013, Combes et al. 2019).
From the ALMA continuum map at 345 GHz we have estimated an integrated flux of $(2.50 \pm 0.25)\, mJy$ compatible with $(2.4 \pm 0.1)\ mJy$ obtained by Audibert et al. (2019).

[1] https://ned.ipac.caltech.edu/

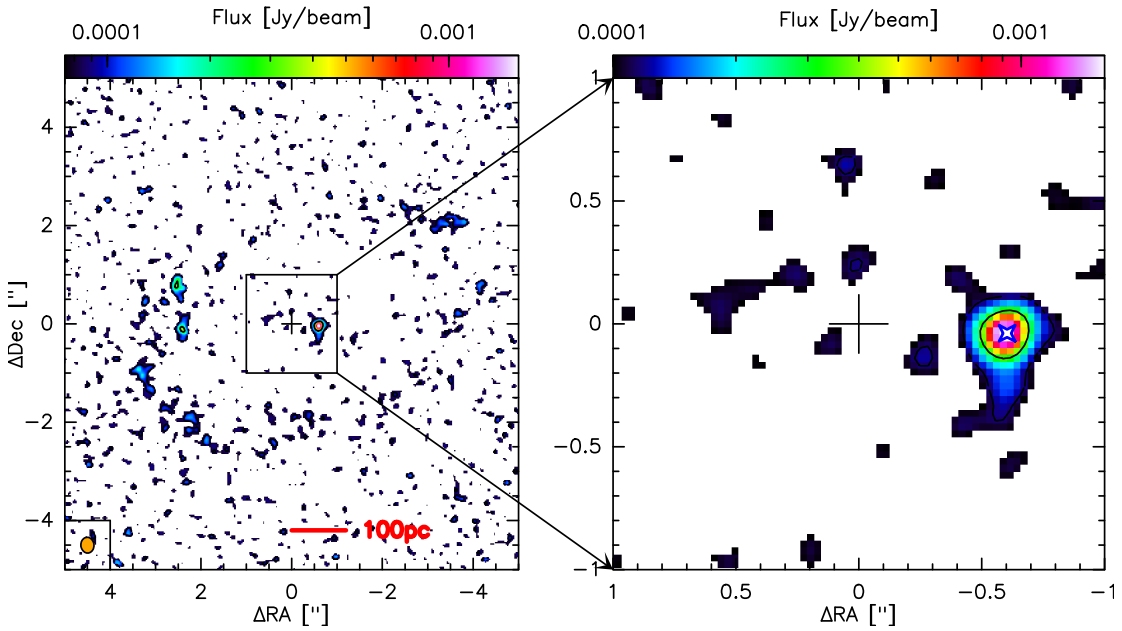

Figure 5.1: Continuum emission at 345 GHz towards the nucleus of NGC613. *Left panel*: central $10'' \times 10''$. *Right panel*: zoom of the central $2'' \times 2''$. The center of the observations is represented by the black cross in both panels. The peak of the continuum emission, i.e., the "new" galaxy center, is represented by the blue star (see discussion in Section 5.2.1). The beam size ($0.16'' \times 0.14''$) is shown as an the orange ellipse in the bottom-left corner of the left panel. The color scale is in $Jy/beam$.

5.2.2 CO(3–2) emission line map

In order to identify the molecular torus, which is expected at the center of galaxies as NGC613, we used the CO(3–2) emission line map, shown in Fig. 5.2. It shows the molecular gas distribution traced by the CO(3–2) emission line in the inner $14'' \times 14''$ ($\sim$FoV) of NGC613. In this map we observe a nuclear emission with a well-defined central peak and a spiralling structure with two arms. The ring structure is well-defined, despite the gas is not homogeneously distributed along the ring itself (see also Miyamoto et al. 2017, Combes et al. 2019, Audibert et al. 2019).

We derived an integrated emission of the CO(3–2) line within the FoV of $S(CO)dV = (1276 \pm 75) Jy\ km/s$, which is consistent with the value of $(1307 \pm 121)\ Jy\ km/s$ derived from Audibert et al. (2019) for ALMA Cycle 4 Band 7 data (see Table 4.4). From equation (5.3), we obtained $L'_{CO} = (1.02 \pm 0.06) \times 10^8\ (K\ km\ s^{-1}\ pc^2)$ within the FoV.

We evaluated the H_2 mass under two assumptions: the CO-to-H_2 conversion factor α_{CO}=3.2 $M_\odot$ $(K\ km\ s^{-1}\ pc^2)^{-1}$ from Bolatto et al. (2013), a typical value for Milky Way and disk galaxies (see Section 5.1), and α_{CO}=0.8 $M_\odot$ $(K\ \ km\ s^{-1}\ pc^2)^{-1}$ from Bolatto et al. (2013), a typical value for ultra-luminous infrared galaxies (ULIRGs, $L_{FIR} > 10^{12}\ L_\odot$). Moreover, we assumed an intensity line ratio $R_{13} = L'_{CO(1-0)}/L'_{CO(3-2)} = 2$ (e.g., Tacconi et al. 2013), for both assumptions of α_{CO}.

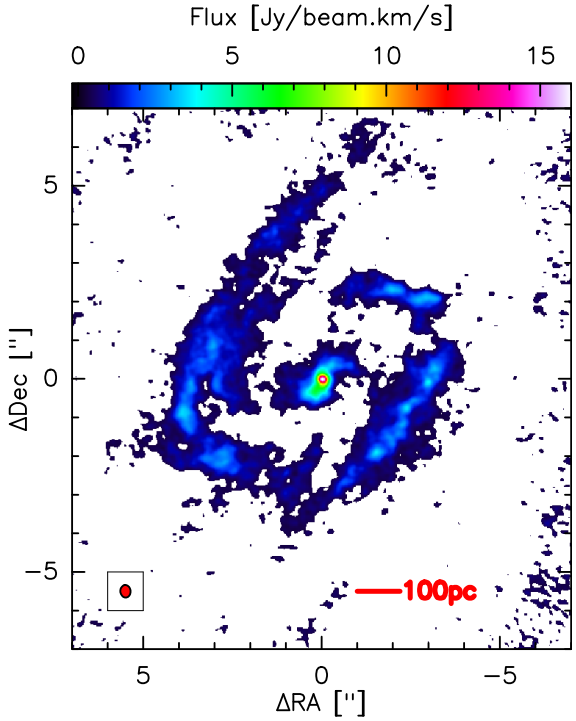

Figure 5.2: The CO(3–2) integrated intensity map of NGC613 in the central $14'' \times 14''$. The beam size ($0.16'' \times 0.14''$) is shown as red ellipse in the bottom-left corner. The color scale is in $Jy/beam\ km/s$.

From the L'_{CO}, we obtained $M(H_2)$ as

$$M(H_2) = \alpha_{CO} L'_{CO} R_{13} = \begin{cases} (6.53 \pm 0.38) \times 10^8\ M_\odot & \text{for } \alpha_{CO} = 3.2\ M_\odot\ (K\ km\ s^{-1}\ pc^2)^{-1}, \\ (1.63 \pm 0.10) \times 10^8\ M_\odot & \text{for } \alpha_{CO} = 0.8\ M_\odot\ (K\ km\ s^{-1}\ pc^2)^{-1}. \end{cases} \tag{5.4}$$

$M(H_2)$ do not takes into account the helium contribution. Taking into account the helium contribution (or, more in general, that of heavier elements), the value of $M(H_2)$ should be multiplied by a factor of 1.36 (see, e.g., Schruba et al. 2011).
We derived the column density $N(H_2)$ within the FoV from the corresponding surface density $\Sigma(H_2)$ as

$$\Sigma(H_2) = \begin{cases} (4.11 \pm 0.24) \times 10^{-35}\ \dfrac{M_\odot}{pc^2} & \text{for } \alpha_{CO} = 3.2\ M_\odot\ (K\ km\ s^{-1}\ pc^2)^{-1}, \\ \\ (1.03 \pm 0.60) \times 10^{-35}\ \dfrac{M_\odot}{pc^2} & \text{for } \alpha_{CO} = 0.8\ M_\odot\ (K\ km\ s^{-1}\ pc^2)^{-1}. \end{cases} \tag{5.5}$$

From equation (5.5), we derived the H_2 density column $N(H_2)$ as

$$N(H_2) = \begin{cases} (2.44 \pm 0.14) \times 10^{22}\ cm^{-2} & \text{for } \alpha_{CO} = 3.2\ M_\odot\ (K\ km\ s^{-1}\ pc^2)^{-1}, \\ (6.12 \pm 0.36) \times 10^{21}\ cm^{-2} & \text{for } \alpha_{CO} = 0.8\ M_\odot\ (K\ km\ s^{-1}\ pc^2)^{-1}, \end{cases} \tag{5.6}$$

The assumption made to derive $N(H_2)$ within the FoV is based on the uniform distribution of gas within the region under analysis, and therefore it tends to underestimate $N(H_2)$,

given the gas distribution shown in Fig. 5.2.
Let us focus on the nuclear region only. In Fig. 5.3 we show the zoom of the molecular gas distribution in the inner $2'' \times 2''$ of NGC613. This nuclear structure is morphologically separated from the outermost ring (see Fig. 5.2). The kinematics analysis of this nuclear structure shows that it is also decoupled from the rest of molecular gas emission (see Audibert et al. 2019). This kinematic decoupling of the nuclear region with respect to the outer parts is observed also in the dense gas traced by the HCO^+(4–3) emission line (see, for instance, Fig. 7 in Combes et al. 2019). Given its position and the amount of gas present in this region, this structure can be interpreted as the molecular gas torus of NGC613.

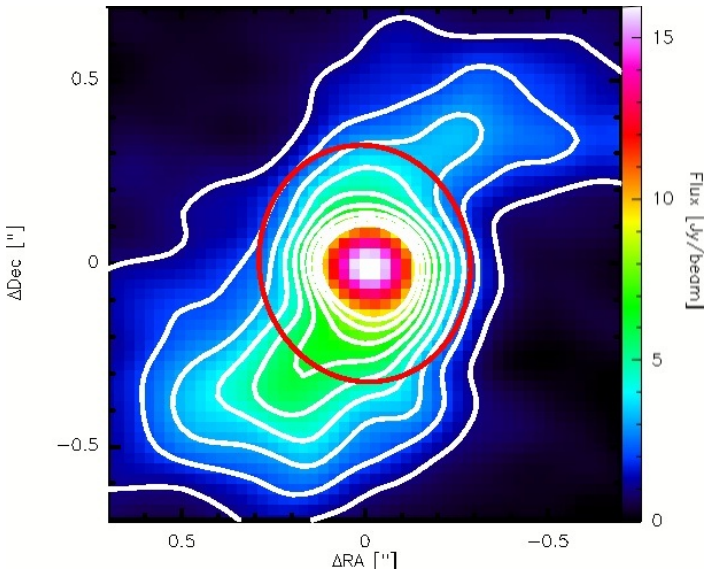

Figure 5.3: The CO(3–2) emission within the inner $2'' \times 2''$ of NGC613. The white intensity contours start from 3σ ($1\sigma = 0.34\ Jy/beam$) and move by integer multiples. The red ellipse corresponds to the defined molecular gas torus (see text for details). The color scale is in $Jy/beam\ km/s$.

We identified the torus in the CO(3–2) data through ellipse-fitting with the adopted center as the continuum point source. We found that the torus is twice the size of the beam and estimated a radius of $(15 \pm 4)\ pc$. The derived radius of the torus is consistent, within errors, with the one measured in Combes et al. (2019) ($r = (14 \pm 3)\ pc$), under similar assumptions. We derived an integrated emission of the CO(3–2) emission line within the region occupied by the torus of $S(CO)dV = (64 \pm 4) Jy\ km/s$ corresponding - based on equation (5.3) - to $L'_{CO} = (5.10 \pm 0.30) \times 10^6\ (K\ km\ s^{-1}\ pc^2)$. From L'_{CO}, we obtained $M(H_2)$ by

$$M(H_2) = \alpha_{CO} L'_{CO} R_{13} = \begin{cases} (3.26 \pm 0.19) \times 10^7\ M_\odot \text{ for } \alpha_{CO} = 3.2\ M_\odot\ (K\ km\ s^{-1}\ pc^2)^{-1}, \\ (8.16 \pm 0.48) \times 10^6\ M_\odot \text{ for } \alpha_{CO} = 0.8\ M_\odot\ (K\ km\ s^{-1}\ pc^2)^{-1}. \end{cases} \tag{5.7}$$

Following the method adopted by Gilli et al. (2014), we assumed a spherical symmetry for the molecular gas torus of NGC613. According to Ruffa et al. (2018), Circosta et al. (2019) and D'Amato et al. (2020), the H_2 column density could be roughly estimated multiplying the H_2 density (i.e., $M(H_2)/\frac{4}{3} \times \pi \times r^3$) by the radius of torus. With these prescriptions,

we obtained:

$$N(H_2) = \begin{cases} (2.27 \pm 0.13) \times 10^{24}\ cm^{-2} \text{ for } \alpha_{CO} = 3.2\ M_\odot\ (K\ km\ s^{-1}\ pc^2)^{-1}, \\ (5.68 \pm 0.33) \times 10^{23}\ cm^{-2} \text{ for } \alpha_{CO} = 0.8\ M_\odot\ (K\ km\ s^{-1}\ pc^2)^{-1}. \end{cases} \quad (5.8)$$

Finally, we explored the nuclear region of radius $r = 3.1\ pc$, corresponding to the beam ($0.04''$) of ALMA Cycle 4 CO(3–2) data presented by Combes et al. (2019, see also Table 4.4 of this Thesis). We obtained molecular gas mass values for the nuclear region of $r = 3.1\ pc$ of:

$$M(H_2) = \begin{cases} (7.35 \pm 0.18) \times 10^{6}\ M_\odot \text{ for } \alpha_{CO} = 3.2\ M_\odot\ (K\ km\ s^{-1}\ pc^2)^{-1}, \\ (1.84 \pm 0.05) \times 10^{6}\ M_\odot \text{ for } \alpha_{CO} = 0.8\ M_\odot\ (K\ km\ s^{-1}\ pc^2)^{-1}, \end{cases} \quad (5.9)$$

corresponding to $N(H_2)$ values, under the assumption of spherical symmetry (as done for the torus) of:

$$N(H_2) = \begin{cases} (1.20 \pm 0.03) \times 10^{25}\ cm^{-2} \text{ for } \alpha_{CO} = 3.2\ M_\odot\ (K\ km\ s^{-1}\ pc^2)^{-1}, \\ (2.99 \pm 0.08) \times 10^{24}\ cm^{-2} \text{ for } \alpha_{CO} = 0.8\ M_\odot\ (K\ km\ s^{-1}\ pc^2)^{-1}. \end{cases} \quad (5.10)$$

5.3 NGC1808 analyzed map

In this Section we will present the analyzed maps for NGC1808. As done for NGC613, we focused on the CO(3–2) emission line and we obtained the $N(H_2)$ values for three regions centered on the nucleus of NGC1808. These data have already been published in Combes et at. (2019) and presented in Audibert et al. (2020, submitted).

5.3.1 Continuum map

We used the continuum map to redefine the positions of AGN. In Fig. 5.4 we show the 345 GHz continuum map obtained for the central region of NGC1808.
The galaxy center is taken from NED (RA: 05h 07m 42.340s, Dec: -37d 30m 46.98s) and these coordinates are represented by the orange cross in Fig. 5.4. The peak of the continuum emission (RA: 05h 07m 42.329s, Dec: -37d 30m 45.88s) is indicated with the blue star in the right panel Fig. 5.4. We measured the displacement between the center of the observations and the peak of emission to be $\Delta s \simeq 0.5''$ (mainly in Dec). We assumed that the position given by the peak of the continuum emission is coincident with the position of the AGN and we defined it as the "new" map center. The AGN position we derive is consistent with that adopted by Combes et al. (2019) and Audibert et al. (2020).
The left panel of Fig. 5.4, displaying the inner $14'' \times 14''$ of NGC1808, shows that the continuum emission is distributed in an incomplete ring of radius of $\sim 5''$. In the right panel of Fig. 5.4, we see the zoom of the inner $7'' \times 7''$, where the central point-like nuclear component is well-defined.

From ALMA continuum map at 345 GHz we estimated an integrated flux of $(6.10 \pm 0.61)\ mJy$, compatible with $(6.78 \pm 0.68)\ mJy$ obtained by Audibert et al. (2020, submitted).

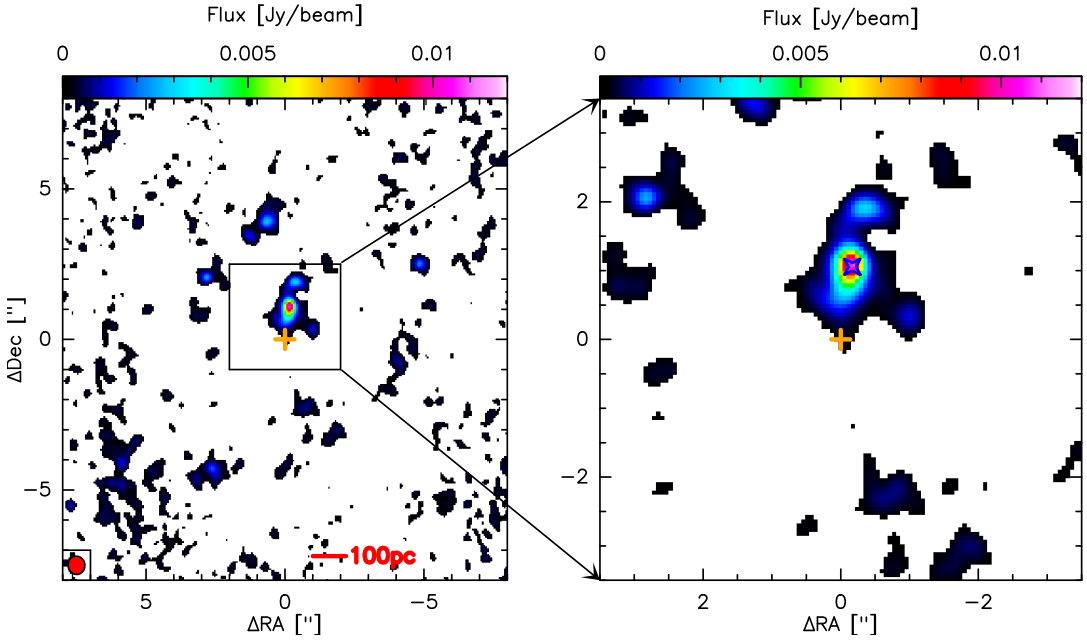

Figure 5.4: Continuum emission at 345 GHz towards the center of NGC1808. *Left panel*: central $14'' \times 14''$. *Right panel*: zoom of the inner $7'' \times 7''$. The center of the observations is represented by the orange cross in both panels. The peak of the continuum emission, i.e., the "new" galaxy center, is represented by the blue star in the right panel (see discussion in Section 5.3.1). The beam size ($0.30'' \times 0.31''$) is shown as the red ellipse in the bottom-left corner of the left panel. The color scale is in $Jy/beam$.

5.3.2 CO(3–2) emission line map

We analyzed the CO(3–2) emission line map in order to identify the molecular gas torus of NGC1808. Figure 5.5 displays the inner $20'' \times 20''$ of the CO(3–2) distribution. This map shows that the CO(3–2) gas has a central peak, two well-defined spiral arms at $\sim 3''$ from the center, and a single arm at $\sim 6''$ from the center.

We estimated an integrated emission of the CO(3–2) line within the FoV of $S(CO)dV = (3348 \pm 368) Jy\ km/s$. From equation (5.3), we derived the CO luminosity of $L'_{CO} = (7.85 \pm 0.86) \times 10^7\ (K\ km\ s^{-1}\ pc^2)$, consistent with the CO luminosity derived from Audibert et al. (2020, submitted).
We derived the H_2 mass under the same assumptions used for NGC613. From the L'_{CO}, we obtained $M(H_2)$ within the FoV as

$$M(H_2) = \alpha_{CO} L'_{CO} R_{13} = \begin{cases} (5.02 \pm 0.55) \times 10^8\ M_\odot & \text{for } \alpha_{CO} = 3.2\ M_\odot\ (K\ km\ s^{-1}\ pc^2)^{-1}, \\ (1.26 \pm 0.13) \times 10^8\ M_\odot & \text{for } \alpha_{CO} = 0.8\ M_\odot\ (K\ km\ s^{-1}\ pc^2)^{-1}. \end{cases} \quad (5.11)$$

where $M(H_2)$ does not take into account the helium contribution.

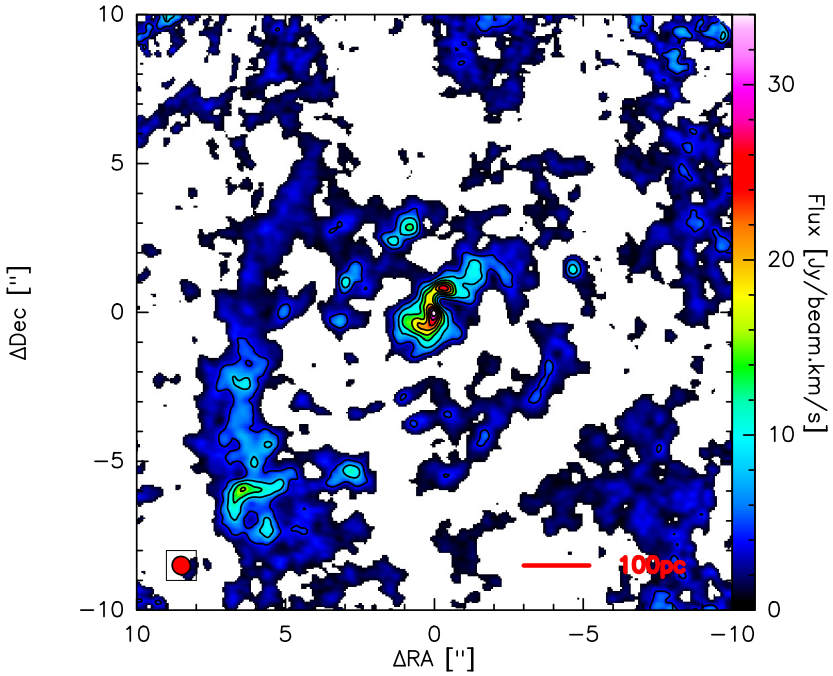

Figure 5.5: The CO(3–2) integrated intensity map in the inner $20'' \times 20''$ of NGC1808. The beam size ($0.30'' \times 0.31''$) is shown as red ellipse in the bottom-left corner. The intensity contours start from 3σ ($1\sigma = 0.13\ Jy/beam$) and move by steps of 30. The color scale is in $Jy/beam\ km/s$.

We derived the column density $N(H_2)$ within the FoV from the corresponding surface density $\Sigma(H_2)$ as

$$\Sigma(H_2) = \begin{cases} (1.02 \pm 0.11) \times 10^{-34} \ \dfrac{M_\odot}{pc^2} \ \text{ for } \alpha_{CO} = 3.2\ M_\odot\ (K\ km\ s^{-1}\ pc^2)^{-1}, \\ \\ (2.56 \pm 0.28) \times 10^{-35} \ \dfrac{M_\odot}{pc^2} \ \text{ for } \alpha_{CO} = 0.8\ M_\odot\ (K\ km\ s^{-1}\ pc^2)^{-1}. \end{cases} \tag{5.12}$$

From equation (5.12), we derived the H_2 density column $N(H_2)$ as

$$N(H_2) = \begin{cases} (6.06 \pm 0.66) \times 10^{22}\ cm^{-2} \ \text{ for } \alpha_{CO} = 3.2\ M_\odot\ (K\ km\ s^{-1}\ pc^2)^{-1}, \\ (1.52 \pm 0.17) \times 10^{21}\ cm^{-2} \ \text{ for } \alpha_{CO} = 0.8\ M_\odot\ (K\ km\ s^{-1}\ pc^2)^{-1}, \end{cases} \tag{5.13}$$

Also in this case, the assumption adopted to derive $N(H_2)$ within the FoV tends to underestimate $N(H_2)$, given the gas distribution shown in Fig. 5.5.
Then, we focused in the central inner $4'' \times 4''$ region, shown in Fig. 5.6. This map shows the central nuclear structure, morphologically separated and kinematically decoupled from the outermost ring (Audibert et al. 2020, submitted). This structure can be interpreted as the molecular gas torus expected in NGC1808. We identified the torus in the CO(3–2) data through ellipse-fitting with the adopted center as the continuum point source. We found that the size of the torus is comparable to that of the beam and estimated a radius for the torus of $(5 \pm 1)\ pc$. This value is consistent with that derived by Combes et al. (2019) ($r = (6 \pm 2)\ pc$), under similar assumptions.

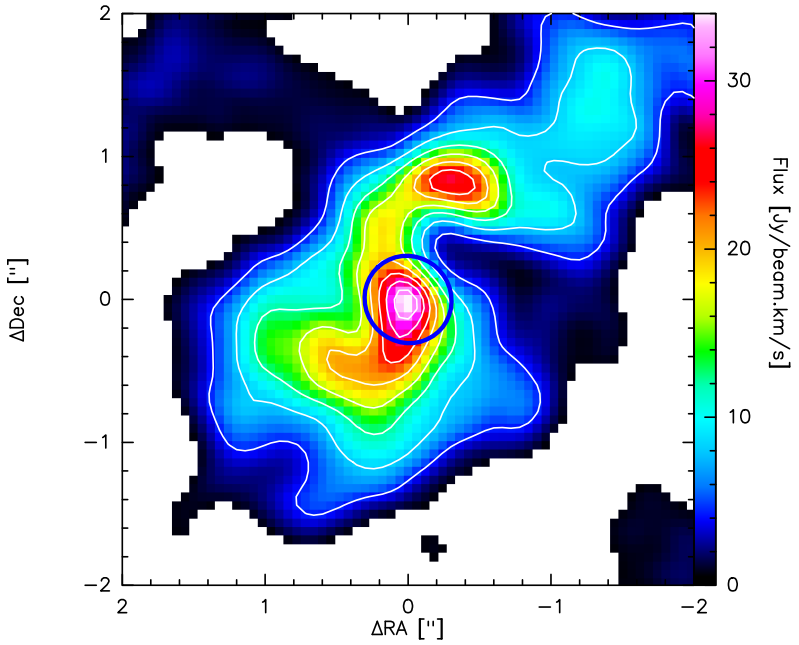

Figure 5.6: The CO(3–2) emission within the inner $4'' \times 4''$ of NGC1808. The white intensity contours starting from 3σ and moving by integer multiples. The blue ellipse corresponds to the defined molecular gas torus (see text for details). The color scale is in $Jy/beam\ km/s$.

For the region occupied by the torus, we obtained an integrated emission of the CO(3–2) line of $S(CO)dV = (66 \pm 27) Jy\ km/s$ corresponding to $L'_{CO} = (1.54 \pm 0.17) \times 10^6\ (K\ km\ s^{-1}\ pc^2)$. From L'_{CO}, we obtained $M(H_2)$

$$M(H_2) = \alpha_{CO} L'_{CO} R_{13} = \begin{cases} (9.86 \pm 1.08) \times 10^6\ M_\odot \text{ for } \alpha_{CO} = 3.2\ M_\odot\ (K\ km\ s^{-1}\ pc^2)^{-1}, \\ (2.46 \pm 0.27) \times 10^6\ M_\odot \text{ for } \alpha_{CO} = 0.8\ M_\odot\ (K\ km\ s^{-1}\ pc^2)^{-1}. \end{cases} \tag{5.14}$$

Following the analysis of NGC613, we assumed a spherical symmetry for the molecular torus of NGC1808 and we obtained the H_2 column density:

$$N(H_2) = \begin{cases} (5.86 \pm 0.64) \times 10^{24}\ cm^{-2} \text{ for } \alpha_{CO} = 3.2\ M_\odot\ (K\ km\ s^{-1}\ pc^2)^{-1}, \\ (1.46 \pm 0.16) \times 10^{24}\ cm^{-2} \text{ for } \alpha_{CO} = 0.8\ M_\odot\ (K\ km\ s^{-1}\ pc^2)^{-1}. \end{cases} \tag{5.15}$$

Finally, we analyzed the nuclear region of radius $r = 1.6\ pc$ and we obtained molecular gas mass of:

$$M(H_2) = \begin{cases} (3.67 \pm 0.40) \times 10^5\ M_\odot \text{ for } \alpha_{CO} = 3.2\ M_\odot\ (K\ km\ s^{-1}\ pc^2)^{-1}, \\ (9.17 \pm 1.01) \times 10^4\ M_\odot \text{ for } \alpha_{CO} = 0.8\ M_\odot\ (K\ km\ s^{-1}\ pc^2)^{-1}, \end{cases} \tag{5.16}$$

corresponding to $N(H_2)$, under the assumption of spherical symmetry, of:

$$N(H_2) = \begin{cases} (2.27 \pm 0.25) \times 10^{24}\ cm^{-2} \text{ for } \alpha_{CO} = 3.2\ M_\odot\ (K\ km\ s^{-1}\ pc^2)^{-1}, \\ (5.67 \pm 0.62) \times 10^{23}\ cm^{-2} \text{ for } \alpha_{CO} = 0.8\ M_\odot\ (K\ km\ s^{-1}\ pc^2)^{-1}. \end{cases} \tag{5.17}$$

5.4 Radial distribution of gas

Typically, molecular gas (H_2) and atomic gas (HI) in spiral galaxies have a complementary distribution in galaxy disks. Molecular gas traced by CO observations - as done in this Thesis - is abundant in the central regions of galaxies and exponentially decreases towards the outside, vice versa the HI is very low in the center and increase in the outer parts. Figure 5.7 shows the different distribution of H_2 (turquoise curve) and HI (grey curve) gas for the nearby galaxy NGC5457 (M101) hosting an AGN as NGC613 and NGC1808. Based on the observed H_2 and HI gas profiles and taking into account that we are focusing on the central region of both galaxies where we expect $N(HI) \sim 0$, we can assume:

$$N(HI) \sim 0 \;\rightarrow\; N(H_2) \sim N_H.$$

where $N(H_2)$ values are those determined thanks to the analysis of ALMA data performed in this Thesis. This value can be directly compared with the hydrogen column density obtained in the X-ray analysis (see Section 3.3).

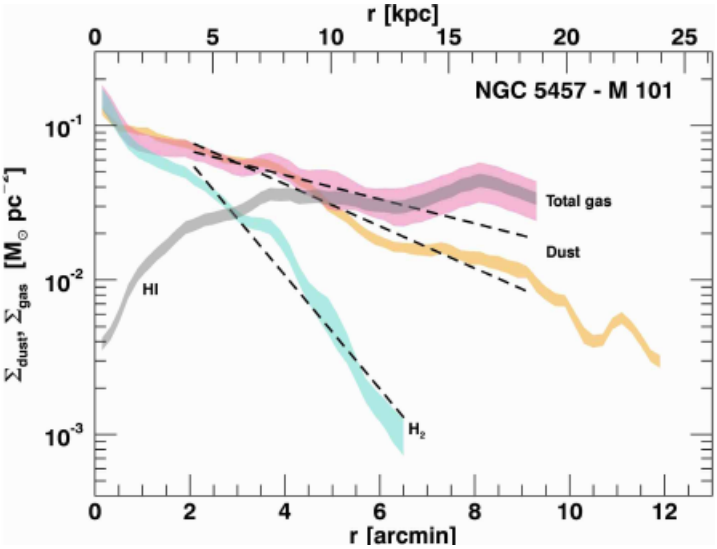

Figure 5.7: Surface density profiles for the mass of dust (orange), molecular gas (turquoise), atomic gas (grey), and total gas (pink) of the galaxy NGC5457, from Casasola et al. (2017). The gas-mass profiles have been corrected for the dust-to-gas mass ratio.

Summing up, in this section we have carried out the estimates of $N(H_2)$ ($\sim N(H)$) for two different values of α_{CO} and, for the very central regions, under the assumption of spherical symmetry of gas. This approach provides a range of values of $N(H_2)$ allowing for wider comparison with the results obtained in the X-ray band.
In Tables 5.1 and 5.2 we report the values of N_H obtained from the millimetric and X-ray analyses for NGC613 and NGC1808, respectively.
The X-ray values of N_H reported in Table 5.1 are obtained from *Chandra* and XMM-*Newton* best-fit models, `MYTorus` decoupled in face-on configurations. Notice that the values obtained from the X-ray analysis and the values obtained from the ALMA analysis (considering the beam region and $\alpha_{CO} = 0.8$ $(K\ km\ s^{-1}\ pc^2)^{-1}$), are compatible within the errors.

NGC613				
	Region	$\alpha_{(CO)}$ $(K\ km\ s^{-1}\ pc^2)^{-1}$	$M(H_2)$ $(M_\odot)$	N_H (cm^{-2})
ALMA This Thesis	$r = 0.8\ kpc$ (FoV)	3.2 0.8	$(6.53 \pm 0.38) \times 10^8$ $(1.63 \pm 0.10) \times 10^8$	$(2.44 \pm 0.14) \times 10^{22}$ $(6.12 \pm 0.36) \times 10^{21}$
	$r = 15\ pc$ (torus)	3.2 0.8	$(3.26 \pm 0.19) \times 10^7$ $(8.16 \pm 0.48) \times 10^6$	$(2.27 \pm 0.13) \times 10^{24}$ $(5.68 \pm 0.33) \times 10^{23}$
ALMA Combes et al. (2019)	$r = 3.1\ pc$ (beam)	3.2 0.8	$(7.35 \pm 0.18) \times 10^7$ $(1.84 \pm 0.05) \times 10^6$	$(1.20 \pm 0.03) \times 10^{25}$ $(2.99 \pm 0.08) \times 10^{24}$
Chandra This Thesis	$r = 0.5\ kpc$			$(2.90 \pm 0.06) \times 10^{24}$
XMM-*Newton* This Thesis	$r = 2.6\ kpc$			$(2.83 \pm 0.07) \times 10^{24}$

Table 5.1: Comparison of ALMA and X-ray data for NGC613. The X-ray values of "global average" column density N_H are obtained from the `MYTorus` decoupled in face-on configurations, both in *Chandra* and in XMM-*Newton*. All the errors reported at the 1σ confidence level.

NGC1808				
	Region	$\alpha_{(CO)}$ $(K\ km\ s^{-1}\ pc^2)^{-1}$	$M(H_2)$ $(M_\odot)$	N_H (cm^{-2})
ALMA This Thesis	$r = 0.4\ kpc$ (FoV)	3.2 0.8	$(5.02 \pm 0.55) \times 10^8$ $(1.26 \pm 0.13) \times 10^8$	$(6.06 \pm 0.66) \times 10^{22}$ $(1.52 \pm 0.17) \times 10^{22}$
	$r = 5\ pc$ (torus)	3.2 0.8	$(9.86 \pm 1.08) \times 10^6$ $(2.46 \pm 0.27) \times 10^6$	$(5.86 \pm 0.64) \times 10^{24}$ $(1.46 \pm 0.16) \times 10^{24}$
ALMA Combes et al. (2019)	$r = 1.6\ pc$ (beam)	3.2 0.8	$(3.67 \pm 0.40) \times 10^5$ $(9.17 \pm 1.01) \times 10^4$	$(2.27 \pm 0.25) \times 10^{24}$ $(5.67 \pm 0.62) \times 10^{23}$
Chandra This Thesis	$r = 0.5\ kpc$			$(2.1 \pm 0.05) \times 10^{23}$
XMM-*Newton* This Thesis	$r = 1.2\ kpc$			$(1.6 \pm 0.02) \times 10^{23}$

Table 5.2: Comparison of ALMA and X-ray data for NGC1808. X-ray N_H are obtain from best-fit models for the source regions, both in *Chandra* and in XMM-*Newton*. All the errors reported at the 1σ confidence level.

The X-ray values of N_H reported in Table 5.2 are obtained from *Chandra* and XMM-*Newton* phenomenological best-fit models for the source regions. In contrast to NGC613, for NGC1808 only phenomenological models have been used. These models do not allow the characterization of the "global average" column density, but only of the one along the line of sight. By confronting the line of sight column density, which suggests local properties of the material, with the global column density obtained in ALMA observations, we can infer the presence of local overdensities or underdensities. This can give some hints on the patchy structure of the torus. In our case, the local N_H is much smaller than the global one (with a factor spanning from $\sim 1/5$ to $\sim 1/20$), hence suggesting a local underdensity along the line of sight.

Chapter 6

Conclusions and perspectives

According to the Unified Model (Antonucci 1993), the line of sight of Type 2 AGN intercepts obscuring material forming the so-called dusty torus. This originates the obscuration observed in the X-ray band. However, the torus has also recently been studied, on parsec scales, through molecular data in nearby galaxies, especially through ALMA (e.g., Garcia-Burillo et al. 2014, Combes et al. 2019). Our Thesis project starts from these considerations, in order to provide indications on the torus as characterized by X-ray observations, coupled with the outcomes coming from millimeter observations. In particular, we started from Combes' et al. 2019 sample, in which the selected galaxies host low-luminosity AGN and have a wide range of activity types (Seyferts 1 to 2, LINERs), and barred or ringed morphologies. As such, the original sample may be considered as a collection of interesting case studies to pave the way for future studies on more homogeneous and more refined samples of AGN. Among the sources which are present in the starting sample, we analyzed two sources, NGC613 (z = 0.0049) and NGC1808 (z = 0.0033), on the basis of the availability of high quality X-ray and molecular data.
On the one hand, from X-ray band observations we estimate the obscuration likely ascribed to the torus; on the other hand, from millimetric observations we investigate, through intensity maps, the distribution of the molecular gas, traced by the CO. The major uncertainties provided by the ALMA analysis concern the assumption of the CO-to-H_2 conversion factor, while those derived in the X-ray analysis include limited photons statistics and modeling.
The main goal of this Thesis is therefore to derive the properties of the tori through multi-band analysis. This multi-frequency analysis allows us to correlate the obscuration at high energies with the molecular gas at low energies, in order to elucidate physical and geometrical properties of the tori in NGC613 and NGC1808.

Results and discussion

The X-ray and millimeter properties of NGC613 and NGC1808 derived in this Thesis are suggestive of clumpy structure of the molecular tori for both sources.
The X-ray analysis was carried out using the data available from *Chandra* and XMM-*Newton* satellites. The analyses for both sources were performed in the energy ranges of $0.3-7$ keV for *Chandra* observations and $0.3-10$ keV for XMM-*Newton* observations. The X-ray spectral analyses of NGC613 and NGC1808 were conducted in slightly different ways, because of the different number of counts available for the two sources. In particular, in the hard band

for NGC613 we have ~ 1500 counts in a region of $r = 6''$ in *Chandra* and ~ 5000 counts in a region of $r = 33''$ in XMM-*Newton*, while for NGC1808 we have ~ 1300 counts in a region of $r = 11''$ in *Chandra* and ~ 5000 counts in a region of $r = 37''$ in XMM-*Newton*. Both phenomenological and physically motivated models (`MYTorus` and `borus`) were adopted for NGC613, while only phenomenological ones were used for NGC1808. The former are used to reproduce the typical spectral components of AGN, hence, providing constrains on the overall emission from the source; the latter are used to reproduce the geometric properties of AGN, both locally and globally. In other words, the physically motivated models allows us to decouple the column density along the line of sight from the "global average" column density of the torus. However, such models, based on Monte-Carlo simulations, require relatively higher number of counts. For this reason it was not possible to adopt `MYTorus` and `borus` for NGC1808.

From the X-ray spectral analysis, we obtained photon indices ($\Gamma = 2.23^{+0.12}_{-0.13}$, for NGC613 and $\Gamma = 1.93^{+0.26}_{-0.25}$ for NGC1808) compatible with typical values observed and theorized in AGN. Even if the purpose of this analysis was focused on the investigation of the geometry of the obscuring material, we also studied the properties of the soft X-ray emission, in order to have a wider description for both sources. For NGC613, we found that the contribution to the soft emission comes from several components: the fraction of photons that are scattered by the surrounding medium, rather than being absorbed, is lower than 1% of the main emission component, consistent with the average value obtained for obscured AGN (e.g., Marchesi et al. 2018); the 0.3−2 keV emission is well fitted using two thermal components, originated by the presence of diffuse structured gas also in the nuclear region, with temperatures of $kT_1 \sim 0.4\ keV$ and $kT_2 \sim 1.1\ keV$. For NGC1808, the gas obscuration below 0.5 keV is reproduced by a further absorption component with an hydrogen column density $N_{H,gas} \sim 10^{21}\ cm^{-2}$. This component takes into account the absorption given by the gas on galactic scales (see, e.g., the dust lanes observed in HST images by Flood & Mutchler 1997). The 0.3−3 keV emission is due to gas heated by SNRs and/or hot bubbles in the central star forming region and is represented by a thermal component with a temperature of $kT \sim 0.6\ keV$; we also detected two emission lines, which are expected in good quality spectra of obscured sources, associated to MgXI and SiXIII (also found in other obscured AGN, e.g., Brinkman et al. 2002).

In order to study the geometrical and the physical properties of the tori, we focused our attention both to the hydrogen column density along the line of sight and to the "global average" one. Starting with $N_{N_{l.o.s.}}$ for both sources, we obtained $N_{H_{l.o.s.}}^{NGC613} \sim 0.30 - 0.44 \times 10^{24}\ cm^{-2}$ and $N_{H_{l.o.s.}}^{NGC1808} \sim 0.31 - 0.34 \times 10^{24}\ cm^{-2}$. Since for NGC1808 we used the phenomenological model only, we were unable to estimate the "global average" column density of the torus, but only the column density along the line of sight. The derived column densities, being lower than the threshold of $\sim 10^{24}\ cm^{-2}$, suggest the presence of a Compton-thin material along the l.o.s., which allows us to classify NGC613 and NGC1808 as a Compton-thin galaxy.
The "global average" column density, derived from `MYTorus` models for NGC613 only, results to be $N_H \sim 3 \times 10^{24}\ cm^{-2}$. We then deduced that, while the material along the l.o.s. results to be Compton-thin, the average column density of the torus is above the Compton-thick threshold. This result suggests a scenario in which the source is observed through a

portion of the torus (or collection of clouds) with a lower density with respect to its average density, suggesting that a patchy (or clumpy) structure is preferred to the basic smooth, doughnut-like, geometry. Furthermore, from `borus02` we obtained the torus covering factor of $C_{TOR} \sim 0.30$, corresponding to an half opening angle of $\sim 73°$. The torus of NGC613 has a small covering factor, i.e., it is in a sort of disk-like structure. In Fig. 6.1 we show the stylized representation of the obscuring torus structure of NGC613, taking into account the results of the X-ray spectral modeling.

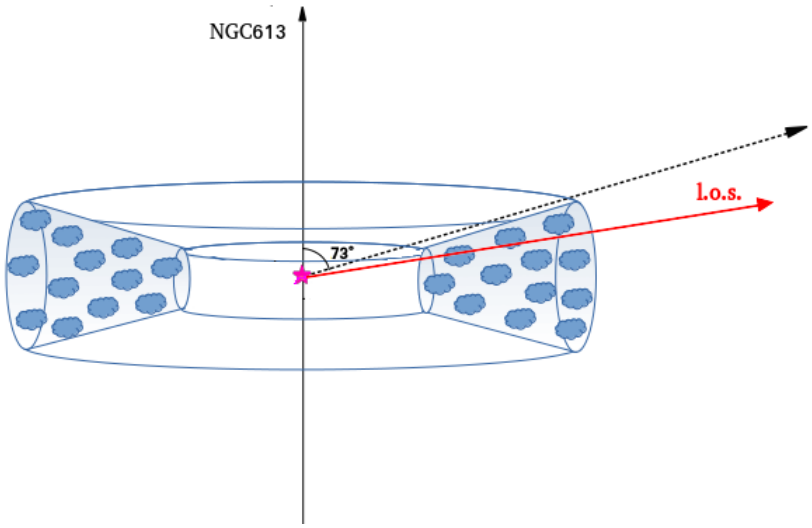

(a)

Figure 6.1: Schematic representation of the obscuring torus of NGC613. The central BH is represented by the magenta star, the torus is represented by the cyan clouds. The black line, the dotted black line and the red line represent the torus axis, the opening angle (associated to the covering factor) and the line of sight, respectively.

The nuclear emission of NGC1808 is likely to be diluted by the contribution of the host galaxy, as we obtained from the study of the luminosity in the X-ray spectral analysis. For a better comprehension the AGN role only, we also studied the SFR of the galaxy. To have an idea of the contribution from stellar processes to the X-ray emission, we calculated the SFR (from literature values of luminosities at different wavelengths) adopting the relations reported by Mineo et al. 2012. We obtained SFR $\sim 5 - 10 M_{\odot}/yr$. We compared the luminosity of the HXRBs with the total X-ray luminosity, in which only the contribution due to the primary emission of the AGN is taken into account. In this way, we singled out the contribution of the AGN to the total emission of the galaxy: HMXBs contribute to the X-ray luminosity up to $\sim 50 - 60\%$ of the total emission of the galaxy in *Chandra* and XMM-*Newton* observations.
In the second part of the thesis, we also analyzed the data available in the millimeter band and computed the amount of molecular gas, traced by CO.
From the CO(3–2) emission line maps, we calculated the column densities in three different regions corresponding to the FoV ($r = 1.5$ *kpc* for NGC613, $r = 0.8$ *kpc* for NGC1808), the torus regions ($r = 15$ *pc* for NGC613, $r = 5$ *pc* for NGC1808) and the beam regions ($r = 3.1$ *pc* for NGC613, $r = 1.6$ *pc* for NGC1808). The last four (two for each source) regions have been determined via ellipse-fitting on CO(3–2) maps. The region corresponding to the

FoV allowed to observe the total CO(3–2) distribution on a larger scale but, because of the assumption of uniform surface density, the $N(H_2)$ values are likely to be underestimated. For the very central regions defined by the torus and the ALMA beam, we assumed that the molecular gas is distributed uniformly in a sphere (i.e., spherical symmetry). Therefore, we focused on the beam regions only, in order to investigate the innermost $N(H_2)$ distributions. Indeed, the beam scale in ALMA corresponds to the expected torus scale in X-ray band. We used two values of the α_{CO} conversion factor, 0.8 and 3.2 $(K\ km\ s^{-1}\ pc^2)^{-1}$, typical for ULIRGs and Milky Way disks, respectively. This approach allows us for wide comparison between ALMA and X-ray results.
In Table 6.1 we report the values of N_H for the beam regions, with the two α_{CO} assumptions, for both sources.

Source	Region	$\alpha_{(CO)}$ $(Kkms^{-1}pc^2)^{-1})$	N_H (cm^{-2})
NGC613	$r = 3.1\ pc$ (beam)	3.2 $(M_\odot)$	$(1.20 \pm 0.03) \times 10^{25}$
		0.8 $(M_\odot)$	$(2.99 \pm 0.08) \times 10^{24}$
NGC1808	$r = 1.6\ pc$ (beam)	3.2 $(M_\odot)$	$(2.27 \pm 0.25) \times 10^{24}$
		0.8 $(M_\odot)$	$(5.67 \pm 0.62) \times 10^{23}$

Table 6.1: The hydrogen column density N_H for the beam regions in both NGC613 and NGC1808. All the errors are reported at 1σ confidence level.

For NGC613, the hydrogen column density of the beam region obtained from ALMA observation, under the assumption of $\alpha_{CO} = 0.8\ (K\ km\ s^{-1}\ pc^2)^{-1}$ is compatible, within the errors, with those found in the X-ray spectral analysis for both X-ray datasets.
For NGC1808, the column density values obtained from the X-ray spectral analysis are lower than the values found in ALMA. This is expected, since, actually, the two values of column density do not correspond exactly to the same type of information. In particular, the values obtained from the X-ray spectral analysis consider the N_H along the line of sight only, hence giving a "local" information. The values from ALMA refer to the average column density of the torus, hence corresponding to a "global" information. However, the comparison of the local and global densities are used as a hint for the identification of overdense (or underdense) regions that suggest a non-uniform distribution of the gas in the torus. We want to stress that multi-band analysis is crucial for the study for molecular tori. In particular, while for NGC613 we were able to obtain global properties, for NGC1808 we derived only the local ones. However, the global information obtained in the millimeter band allowed us to compare the l.o.s. column density with the average one, so that we have been able to infer geometrical properties of the torus.

For both sources, we found that both the line of sight gas column densities, responsible for the absorption of X-rays, and the molecular gas column densities derived from CO(3–2) transitions, have high values. This suggests that the neutral gas line of sight column

densities of the molecular tori, imaged by ALMA with $\sim$ 12$-$14 pc resolution for both studied galaxies, contribute significantly to the obscuration of X-rays.

Future perspectives

We performed our analysis on two of the seven galaxies of the sample analyzed by Combes et al. (2019). Because of the heterogeneity of this sample, it would be very interesting to investigate all the other sources, through multi-band analyses. The case of NGC1808, in particular, has shown how crucial multi-frequency studies are. They not only allow us to cross-check data and results, but also to complement for unavailable data or analyses, as for the example described above. With this mind, it would be interesting to gather data from *Nuclear Spectroscopic Telescope Array* (NuSTAR), operating in a wide energy range (3$-$79 keV) and with a large collecting area ($\sim$ 850 cm^2 at 9 keV and $\sim$ 60 cm^2 at $\sim$78 keV). Thanks to the wide energy range, we could be able to better characterize the powerlaw at high energies; at the moment there are no available *NuSTAR* data for the two sources we examined in this Thesis. The high collecting area would allow us to obtain data with a large number of counts that could permit to implement physically motivated models to those sources with not enough data from *Chandra* and XMM-*Newton* (as was the case of NGC1808).

In recent years, several multi-wavelength studies were carried out to investigate the properties of the obscuring material in AGN (see, e.g., da Silva et al.2020, Esparza-Arredondo et al. 2021, García-Burillo et al. 2021). Various models have been developed to describe the structure, distribution and the kinematics of this material, in order to constrain its physical and geometric properties (e.g., Baloković et al. 2018, Buchner et al.2019, Esparza-Arredondo et al. 2019). Esparza-Arredondo et al. (2021) present the results obtained from fitting a sample of AGN using both clumpy and smooth models, to reproduce their mid-IR and X-ray emissions, in order to understand if the same structures can produce both spectral components in AGN. However, the comparison between the X-ray reflector and the dusty torus inferred from mid-IR spectral fitting is quite complex. They found that up to $\sim$78% of the sample is well reproduced by the smooth model at X-ray wavelengths and up to $\sim$69% is well fitted by clumpy models at mid-IR wavelengths. They found at least six scenarios which describe the observational properties of their sample. In particular, in these scenarios, the gas-dust distribution combinations allow three different solutions: clumpy-clumpy, smooth-smooth, and smooth-clumpy. However, the question of how the torus mid-infrared and the X-ray emission are correlated remains an open question.
García-Burillo et al. (2021) present the first results of the *Galaxy Activity, Torus and Outflows Survey* (GATOS). In this first paper in a series, they aim at understanding the properties of the dusty molecular tori and their connection with host galaxies in nearby Seyferts. Furthermore, they expand the range of AGN luminosities covered by other ALMA surveys of Seyferts (such as NUGA) and allow the study of gas feeding and feedback cycle in a combined sample of 19 Seyferts. They found that 13/19 galaxies tend to show an equatorial orientation of their extended components, i.e., close to perpendicular relative to the AGN wind axes. A smaller subset of four galaxies displays a mixed geometry intermediate between polar and equatorial. The dusty molecular tori imaged by ALMA in the GATOS Seyferts have average diameters of $\sim$ 42 *pc*, median molecular gas masses of $\sim 6 \times 10^5 M_\odot$

and median hard X-ray luminosity (2−10 keV) of $\sim 8 \times 10^{42}$ (erg/s).
This emphasizes the necessity to catalogue as many AGN as possible, in order to obtain statistically significant data that could suggest both phenomenological and theoretical descriptions of the intrinsic properties of molecular tori. A starting short-term project could be the completion of the analysis of the seven source in Combes et al. (2019).

Bibliography

[1] M. A. Abramowicz, X. Chen, S. Kato, J. P. Lasota and O. Regev, "Thermal equilibria of accretion disks", Astrophys. J. Lett. **438** (1995), L37, doi:10.1086/187709, [arXiv:astro-ph/9409018 [astro-ph]].

[2] C. Ramos Almeida, N. A. Levenson, J. M. R. Espinosa, A. A. Herrero, A. A. Ramos, J. T. Radomski, C. Packham, R. S. Fisher and C. M. Telesco, "The Infrared Nuclear Emission of Seyfert Galaxies on Parsec Scales: Testing the Clumpy Torus models", Astrophys. J. **702** (2009), 1127-1149 doi:10.1088/0004-637X/702/2/1127, [arXiv:0906.5368 [astro-ph.CO]].

[3] Andrzej A. Zdziarski, Juri Poutanen, W. Neil Johnson, "Observations of Seyferts by OSSE and parameters of their X-ray/gamma-ray sources", doi:10.1086/317046, [arXiv:astro-ph/0006151 [astro-ph]], Astrophys.J. 542 (2000) 703.

[4] R. Antonucci, "Unified models for active galactic nuclei and quasars", Ann. Rev. Astron. Astrophys. **31** (1993), 473-521, doi:10.1146/annurev.aa.31.090193.002353.

[5] Arnaud, K., Dorman, B., Gordon, C., "An X-ray Spectral Fitting Package, User's Guide for Version 12.9.0, HEASARC", 2015.

[6] Asmus D., Gandhi P., Hönig S. F., Smette A., Duschl W. J., 2015, MNRAS, 454, 766.

[7] A. Audibert, F. Combes, S. García-Burillo, L. Hunt, A. Eckart, S. Aalto, V. Casasola, F. Boone, M. Krips, S. Viti, S. Muller, K. Dasyra, P. van der Werf and S. Martín, "ALMA captures feeding and feedback from the active galactic nucleus in NGC 613", A&A, 632, A33, 2019.

[8] A. Audibert et.al (2020), "Smoking-gun evidence of black hole feeding in NGC 1808", arXiv:2011.09133.

[9] B. Aschenbach, U. Briel, F. Haberl, H. Braeuninger, W. Burkert, A. Oppitz, P. Gondoin and D. Lumb, "Imaging performance of the xmm-newton x-ray telescopes", Proc. SPIE Int. Soc. Opt. Eng. **4012** (2000), 731, doi:10.1117/12.391615, [arXiv:astro-ph/0007256 [astro-ph]].

[10] Y. Avni, "Energy spectra of X-ray clusters of galaxies", The Astrophysical Journal, 210:642-646,1976.

[11] Awaki, H., & Koyama, K. 1993. "Ginga observations of Seyfert galaxies" Adv. Space Res., 13, 221.

[12] Baloković et al. (2018), "New Spectral Model for Constraining Torus Covering Factors from Broadband X-Ray Spectra of Active Galactic Nuclei", The Astrophysical Journal 854.1, p. 42.

[13] J. A. Baldwin, M. M. Phillips and R. Terlevich, "Classification parameters for the emission-line spectra of extragalactic objects", Publ. Astron. Soc. Pac. **93** (1981), 5-19, doi:10.1086/130766.

[14] Baloković, M., Brightman, M., Harrison, F. A., et al. 2018, ApJ, 854, 42.

[15] Bajaja, E., Wielebinski, R., Reuter, H.-P., Harnett, J. I., and Hummel, E., "Observations of CO lines in southern spiral galaxies", A&AS, 114, 147, 1995.

[16] Bassani L., Dadina M., Maiolino R., Salvati M., Risaliti G., della Ceca R., Matt G., Zamorani G., "A Three-dimensional Diagnostic Diagram for Seyfert 2 Galaxies: Probing X-Ray Absorption and Compton Thickness", 1999, ApJS, 121, 473

[17] Bauer, F. E. et al., "NuSTAR Spectroscopy of Multi-component X-Ray Reflection-from NGC 1068", ApJ812, 116, p. 116., 2015, doi:10.1088/0004-637X/812/2/116, [arXiv:1411.0670 [astro-ph.HE]].

[18] Bell E. F., 2003, ApJ, 586, 794.

[19] N. Bennert, H. Falcke, H. Schulz, A. S. Wilson and B. J. Wills, "Size and structure of the narrow-line region of quasars", Astrophys. J. Lett. **574** (2002), L105-L110, doi:10.1086/342420, [arXiv:astro-ph/0206334 [astro-ph]].

[20] Bianchi S., Maiolino R., Risaliti G., "AGN Obscuration and the Unified Model", Advances in Astronomy, 2012,782030, 2012.

[21] Blandford, R. D., and Znajek, R. L. "Electromagnetic extraction of energy from Kerr black holes", 1977, MNRAS, 179, 433

[22] R. D. Blandford and D. G. Payne, "Hydromagnetic flows from accretion discs and the production of radio jets", Mon. Not. Roy. Astron. Soc. **199** (1982), 883.

[23] A. J. Blustin, M. J. Page, S. V. Fuerst, G. Branduardi-Raymont and C. E. Ashton, "The Nature and origin of Seyfert warm absorbers", Astron. Astrophys. **431** (2005), 111, doi:10.1051/0004-6361:20041775, [arXiv:astro-ph/0411297 [astro-ph]].

[24] R. Boissay, C. Ricci and S. Paltani, "A hard X-ray view of the soft excess in AGN", Astron. Astrophys. **588** (2016), A70, doi:10.1051/0004-6361/201526982. [arXiv:1511.08168 [astro-ph.HE]].

[25] Böker, T., Falcón-Barroso, Knapen J. H., Schinnerer E., Allard E., Ryder S., "Stellar Populations as Building Blocks of Galaxies", 2007, in Vazdekis A., Peletier R., eds, IAU Symposium Vol. 241, pp 497-498, doi:10.1017/S1743921307008873.

[26] Böker, T., Falcón-Barroso, J., Schinnerer, E., Knapen, J. H., and Ryder, S. "A SINFONI view of galaxy centers: Morphology and kinematics of five nuclear star-formation rings", 2008, AJ, 135, 479

[27] Bolatto, A. D., Wolfire, M., and Leroy, A. K. "The CO-to-H2 conversion factor", 2013, ARA&A, 51, 207.

[28] W. N. Brandt and D. M. Alexander, "Cosmic X-ray surveys of distant active galaxies: The demographics, physics, and ecology of growing supermassive black holes", Astron. Astrophys. Rev. **23** (2015) no.1, 1 doi:10.1007/s00159-014-0081-z [arXiv:1501.01982 [astro-ph.HE]].

[29] Brightman and Nandra (2011), "An XMM-Newton spectral survey of 12 μm selected galaxies-I. X-ray data", Monthly Notices of the Royal Astronomical Society 413.2, pp. 1206-1235.

[30] Brinkman, AC et al. (2002). "The soft X-ray spectrum from NGC 1068 observed with LETGS on Chandra". A&A 396.3, pp. 761-772.

[31] Brusa, M., et al., "High-redshift Quasar in the COSMOS Survey: the space density of z>3 X-ray selected QSOs", 2009, ApJ, 693, 8, 2009, [arXiv:0809.2513 [astro-ph]], doi: 10.1088/0004-637X/693/1/8 .

[32] Buchner, J., Brightman, M., Nandra, K., et al. 2019, A&A, 629, A16.

[33] D Burlon, M Ajello, J Greiner, A Comastri et al., "Three-year swift-BAT survey of active galactic nuclei: reconciling theory and observations?", The Astrophysical Journal, Volume 728, Number 1, 2011.

[34] Burtscher, Leonard et al., "A diversity of dusty AGN tori-Data release for the VLTI/MIDI AGN Large Program and first results for 23 galaxies", Astronomy & Astrophysics 558, A149, 2013.

[35] Busch, G., Eckart, A., Valencia-S., M., et al. 2017, A&A, 598, A55.

[36] Carilli, C., L. and Walter, F. "Cool gas in high-redshift galaxies", 2013, ARA&A, 51, 105.

[37] V. Casasola, L. K. Hunt, F. Combes, S. Garcia-Burillo and R. Neri, "Molecular Gas in NUclei of GAlaxies (NUGA) XIV. The barred LINER/Seyfert 2 galaxy NGC 3627", Astron. Astrophys. **527** (2011), A92, doi:10.1051/0004-6361/201015680, [arXiv:1101.2626 [astro-ph.CO]].

[38] Casasola V., L. P. Cassarà, S. Bianchi, S. Verstocken, E. Xilouris, L. Magrini, M. W. L. Smith, I. De Looze, M. Galametz, S. C. Madden, M. Baes, C. Clark, J. Davies, P. De Vis, R. Evans, J. Fritz, F. Galliano, A. P. Jones, A. V. Mosenkov, S. Viaene and N. Ysard, "Radial distribution of dust, stars, gas, and star-formation rate in DustPedia face-on galaxies", A&A 605, A18 (2017), doi:10.1051/0004-6361/201731020.

[39] Castangia P., Tarchi A., Henkel C., Menten K. M., "New HO masers in Seyfert and FIR bright galaxies II. The intermediate luminosity range", 2008, A&A,479, 111.

[40] Castangia, P., Panessa, F., Henkel, C., Kadler, M., and Tarchi, A. "New Compton-thick AGN in the circumnuclear H2O maser hosts UGC 3789 and NGC 6264", 2013, MNRAS, 436, 3388.

[41] G. Chartas, C. Rhea, C. Kochanek, X. Dai, C. Morgan, J. Blackburne, B. Chen, A. Mosquera and C. MacLeod, "Gravitational Lensing Size Scales for Quasars", Astron. Nachr. **337** (2017) no.4/5, 356-361, doi:10.1002/asna.201612313, [arXiv:1509.05375 [astro-ph.HE]].

[42] X. m. Chen, M. A. Abramowicz, J. P. Lasota, R. Narayan and I. Yi, "Unified description of accretion flows around black holes", Astrophys. J. Lett. **443** (1995), L61, doi:10.1086/187836, [arXiv:astro-ph/9502015 [astro-ph]].

[43] C. Circosta, C. Vignali, R. Gilli, A. Feltre, F. Vito, F. Calura, V. Mainieri, M. Massardi, C. Norman, "The X-ray emission of z>2.5 active galactic nuclei can be obscured by their host galaxies", [arXiv:1901.07108 [astro-ph]]. doi:10.1051/0004-6361/201834426, A&A 623, A172 (2019).

[44] Collison, P. M., Saikia, D. J., Pedlar, A., Axon, D. J., Unger, S. W. 1994, MNRAS, 268, 203.

[45] Comastri, "Compton-thick AGN: the dark side of the X-ray background", Supermassive Black Holes in the Distant Universe, Springer, pp. 245–272, 2004.

[46] F. Combes, S. García-Burillo, A. Audibert, L. Hunt, A. Eckart, S. Aalto, V. Casasola, F. Boone, M. Krips, S. Viti, K. Sakamoto, S. Muller, K. Dasyra, P. van der Werf and S. Martin, "ALMA observations of molecular tori around massive black holes", 2019, A&A, 623, A79.

[47] M. Contini, "The LLAGN in the centre of the Galaxy", Mon. Not. Roy. Astron. Soc. **418** (2011), 1935, doi:10.1111/j.1365-2966.2011.19612.x, [arXiv:1104.1282 [astro-ph.GA]].

[48] Czerny, Bozena and Martin Elvis, "Constraints on quasar accretion disks from the optical/ultraviolet/soft X-ray big bump" The Astrophysical Journal 321, pp. 305–320, 1987.

[49] M. Dadina, "BeppoSAX observations in the 2–100 keV band of the nearby Seyfert galaxies: an atlas of spectra", A&A 461, 1209–1252 (2007), doi: 10.1051/0004-6361:20065734.

[50] Dadina, Mauro, "Seyfert galaxies in the local Universe (z 0.1): the average X-ray spectrum as seen by BeppoSAX". Astronomy & Astrophysics 485.2, pp. 417–424, 2008.

[51] M. Dadina, C. Vignali, M. Cappi, G. Lanzuisi, G. Ponti, B. De Marco, G. Chartas and M. Giustini, "XMM-Newton reveals a Seyfert-like X-ray spectrum in the z = 3.6 QSO B1422+231", Astron. Astrophys. **592** (2016), A104, doi:10.1051/0004-6361/201628467, [arXiv:1605.08549 [astro-ph.GA]].

[52] Q. D'Amato, R. Gilli, C. Vignali, M. Massardi, F. Pozzi, G. Zamorani, C. Circosta, F. Vito, J. Fritz, G. Cresci, V. Casasola, F. Calura, A. Feltre, V. Manieri, D. Rigopoulou, P. Tozzi, C. Norman, "Dust and gas content of high-redshift galaxies hosting obscured AGN in the CDF-S". [arXiv:2003.08631 [astro-ph]], doi:10.1051/0004-6361/201936175, A&A 636, A37 (2020).

[53] V. Das, D. M. Crenshaw, S. B. Kraemer and R. P. Deo, "Kinematics of the narrow-line region in the seyfert 2 galaxy ngc 1068: dynamical effects of the radio jet", Astron. J. **132** (2006), 620-632, doi:10.1086/504899, [arXiv:astro-ph/0603803 [astro-ph]].

[54] P. da Silva, Roberto B. Menezes, João E. Steiner, "The nuclear region of NGC 613. I - Multiwavelength analysis". [arXiv:2001.07328 [astro-ph]], doi:10.1093/mnras/staa007 (2020).

[55] W. Davis, and Ari Laor, "The radiative efficiency of accretion flows in individual active galactic nuclei". The Astrophysical Journal, 728:98 (19pp), 2011, doi:10.1088/0004-637X/728/2/98.

[56] Davies, R. L., Groves, B., Kewley, et al., "Dissecting galaxies: separating star formation, shock excitation and AGN activity in the central region of NGC 613", 2017, MNRAS, 470, 4974

[57] C De Breuck et al. "CO emission and associated HI absorption from a massive gas reservoir surrounding the z= 3 radio galaxy B3 J2330+ 3927", A&A, Volume 401, pp 911 - 925, 2003.

[58] De Marco, B et al., "Discovery of a relation between black hole mass and soft X-ray time lags in active galactic nuclei", Monthly Notices of the Royal Astronomical Society 431.3, pp. 2441–2452, (2013).

[59] de Vaucouleurs, G., de Vaucouleurs, A., Corwin, Jr., H. G., et al. 1991, "Third eference Catalogue of Bright Galaxies", Volume I: Explanations and references. Volume II: Data for galaxies between 0h and 12h. Volume III: Data for galaxies between 12h and 24h.

[60] Dahlem, M., Aalto, S., Klein, U., et al. 1990, A&A, 240, 237.

[61] Dahlem, M., Hartner, G. D., & Junkes, N. 1994, ApJ, 432, 598.

[62] D. Donato, G. Ghisellini, G. Tagliaferri and G. Fossati, "Hard x-ray properties of blazars", Astron. Astrophys. **375** (2001), 739, doi:10.1051/0004-6361:20010675, [arXiv:astro-ph/0105203 [astro-ph]].

[63] B. T. Draine and H. M. Lee, "Optical properties of interstellar graphite and silicate grains", Astrophys. J. **285** (1984), 89-108, doi:10.1086/162480.

[64] Draine, "Interstellar dust grains". Annual Review of Astronomy and Astrophysics 41.1, pp. 241–289, (2003a).
- "Scattering by interstellar dust grains. I. Optical and ultraviolet". The Astrophysical Journal 598.2, p. 1017, (2003b)..

[65] J. Ebrero, J. S. Kaastra, G. A. Kriss, L. Di Gesu, E. Costantini, M. Mehdipour, S. Bianchi, M. Cappi, R. Boissay and G. Branduardi-Raymont, *et al.* "Anatomy of the AGN in NGC 5548. VI. Long-term variability of the warm absorber", Astron. Astrophys. **587** (2016), A129, doi:10.1051/0004-6361/201527808, [arXiv:1601.02385 [astro-ph.HE]].

[66] Eisenberger P. and Marra W.C., "X-Ray Diffraction Study of the Ge(001) Reconstructed Surface", Physical Review Letters. 46: 1081–4, (1981).

[67] M. Elitzur, "The Toroidal Obscuration of Active Galactic Nuclei", New Astron. Rev. **52** (2008), 274-288, doi:10.1016/j.newar.2008.06.010. [arXiv:0805.3699 [astro-ph]].

[68] Elmegreen B. G., "Starbursts by gravitational collapse in the inner Lindblad resonance rings of galaxies", 1994, ApJ, 425, L73

[69] Esparza-Arredondo, D., González-Martín, O., Dultzin, D., et al. 2019, ApJ, 886, 125.

[70] Esparza-Arredondo et al. 2021. "The dust-gas AGN torus as constrained from X-ray and mid-infrared observations". arXiv:2104.11263 [astro-ph.GA]

[71] Fabbiano G., 1989, ARA&A, 27, 87.

[72] Fabbiano G., 2006, ARA&A, 44, 323.

[73] A. C. Fabian, "Broad iron lines in AGN and x-ray binaries", Astrophys. Space Sci. **300** (2005), 97-105, doi:10.1007/s10509-005-1203-x, [arXiv:astro-ph/0412224 [astro-ph]].

[74] A. C. Fabian and G. Miniutti, "The X-ray spectra of accreting Kerr black holes", [arXiv:astro-ph/0507409 [astro-ph]].

[75] A. C. Fabian, A. Lohfink, E. Kara, M. L. Parker, R. Vasudevan, C. S. Reynolds, "Properties of AGN coronae in the NuSTAR era", Monthly Notices of the Royal Astronomical Society, Volume 451, Issue 4, 21 August 2015, Pages 4375–4383, 2015.

[76] Fanaroff, Bernard L and Julia M Riley, "The morphology of extragalactic radio sources of high and low luminosity", Monthly Notices of the Royal Astronomical Society 167.1, 31P–36P, (1974).

[77] Falcón-Barroso J., Böker T., Schinnerer E., Knapen J. H., Ryder S., 2008, in Bureau M., Athanassoula E., Barbuy B., eds, IAU Symposium Vol. 245, Formation and Evolution of Galaxy Bulges. pp 177–180 (arXiv 0709.0353), doi:10.1017/S1743921308017584

[78] Falcón-Barroso, J., Ramos Almeida, C., Böker, T., et al. "The circumnuclear environment of NGC 613: a nuclear starburst caught in the act?", 2014, MNRAS, 438,329

[79] P. Ferrando, A. F. Abbey, B. Altieri, M. Arnaud, P. Bennie, M. Dadina, M. Denby, S. Ghizzardi, R. G. Griffiths and N. La Palombara, *et al.* "Status of the epic/mos calibration", [arXiv:astro-ph/0202372 [astro-ph]].

[80] L. Ferrarese and D. Merritt, "A Fundamental relation between supermassive black holes and their host galaxies", Astrophys. J. Lett. **539** (2000), L9, doi:10.1086/312838, [arXiv:astro-ph/0006053 [astro-ph]].

[81] Flood, J., Mutchler, M.. "Hubble Space Telescope imaging of the nuclear starburst galaxy NGC 1808". American Astronomical Society, Vol. 29, p.1330, 1997.

[82] Forbes, D.A., Boisson, C., & Ward, M.J., 1992, MNRAS, 259, 293.

[83] G. Fossati, L. Maraschi, A. Celotti, A. Comastri and G. Ghisellini, "A Unifying view of the spectral energy distributions of blazars", Mon. Not. Roy. Astron. Soc. **299** (1998), 433-448, doi:10.1046/j.1365-8711.1998.01828.x, [arXiv:astro-ph/9804103 [astro-ph]].

[84] García-Burillo et al. 2014. "ALMA resolves the torus of NGC 1068: continuum and molecular line emission". doi: 10.3847/2041-8205/823/1/L12, ApJLetters.

[85] García-Burillo et al. 2021. "The Galaxy Activity, Torus and Outflows Survey (GATOS) I. ALMA images of dusty molecular tori in Seyfert galaxies." arXiv:2104.10227 [astro-ph.GA]

[86] Gaskell, C Martin, "The case for cases B and C: intrinsic hydrogen-line ratios of the broad-line region of active galactic nuclei, reddenings and accretion disc sizes", Monthly Notices of the Royal Astronomical Society 467.1, pp. 226–238, (2017).

[87] Ghisellini et al., "The contribution of the obscuring torus to the X-ray spectrum of Seyfert galaxies: a test for the unification model", Monthly Notices of the Royal Astronomical Society 267.3, pp. 743–754, (1994).

[88] Giacconi, Riccardo et al., "Evidence for x-rays from sources outside the solar system", Physical Review Letters 9.11, p. 439, 1962.

[89] Gilli, R. et al., "The contribution of AGN to the X-ray background: the effect of iron features", New Astronomy 4, pp. 45–57, (1999), doi: 10.1016/S1384-1076(99) 00004-4.

[90] R. Gilli, A. Comastri and G. Hasinger, "The synthesis of the cosmic X-ray background in the Chandra and XMM-Newton era", Astron. Astrophys. **463** (2007), 79, doi:10.1051/0004-6361:20066334, [arXiv:astro-ph/0610939 [astro-ph]].

[91] Gilli, "The cosmic X-ray background: abundance and evolution of hidden black holes". arXiv preprint arXiv:1304.3665, 2013.

[92] Gilli et al., "ALMA reveals a warm and compact starburst around a heavily obscured supermassive black hole at z= 4.75", Astronomy & Astrophysics 562, A67, 2014.

[93] Gitti, M., Lecture notes for the course "Laboratorio di Astrofisica", MSc degree in Astrophysics, 2020, UNIBO.

[94] Goulding, A. D. and Alexander, D. M. 2009, MNRAS, 398, 1165.

[95] Haardt F., Maraschi L., 1991,ApJ,380, L51.

[96] Haardt F., Maraschi L., 1993,ApJ,413, 507.

[97] Haardt F., Maraschi L., Ghisellini G., 1994,ApJ,432, L95.

[98] Harrison C., "Observational constraints on the influence of active galactic nuclei on the evolution of galaxies", Ph.D. thesis, Durham Universit, 2014.

[99] Heckman, T. M., Armus, L., & Miley, G. K. 1990, APJS, 74, 833.

[100] R. C. Hickox and M. Markevitch, "Absolute measurement of the unresolved cosmic X-ray background in the 0.5-8 keV band with Chandra", Astrophys. J. **645** (2006), 95-114, doi:10.1086/504070, [arXiv:astro-ph/0512542 [astro-ph]].

[101] R. C. Hickox and D. M. Alexander, "Obscured Active Galactic Nuclei", Ann. Rev. Astron. Astrophys. **56** (2018), 625-671, doi:10.1146/annurev-astro-081817-051803, [arXiv:1806.04680 [astro-ph.GA]].

[102] Hine, RG and MS Longair, "Optical spectra of 3CR radio galaxies", Monthly Notices of the Royal Astronomical Society 188.1, pp. 111–130, (1979).

[103] Hirashita H., Buat V., Inoue A. K., 2003, A&A, 410, 83.

[104] L. C. Ho and J. Kormendy, "Supermassive black holes in active galactic nuclei", doi:10.1888/0333750888/2365, [arXiv:astro-ph/0003267 [astro-ph]].

[105] Hummel, E., Jorsater, S., Lindblad, P. O., and Sandqvist, A. 1987, A&A, 172, 51.

[106] Hummel, E. and Jorsater, S. 1992, A&A, 261, 85.

[107] Ichimaru, SETSUO, "Bimodal behavior of accretion disks-Theory and application to Cygnus X-1 transitions", The Astrophysical Journal 214, pp. 840-855, (1977).

[108] Iglesias-Páramo J., Buat V., Donas J., Boselli A., Milliard B., 2004, A&A, 419, 109.

[109] Iglesias-Páramo J. et al., 2006, ApJS, 164, 38.

[110] K. Iwasawa, R. Gilli, C. Vignali, A. Comastri, W. N. Brandt, P. Ranalli, F. Vito, N. Cappelluti, F. J. Carrera and S. Falocco, *et al.* "The XMM deep survey in the CDF-S II. a 9-20 keV selection of heavily obscured active galaxies at z>1.7", Astron. Astrophys. **546** (2012), A84, 2012, doi:10.1051/0004-6361/201220036, [arXiv:1209.0916 [astro-ph.CO]].

[111] Jaffe, Walter et al., "MIDI observations of the nuclear obscuring torus in NGC 1068", Proceedings of the International Astronomical Union 2004.IAUS222, pp. 37-39, (2004).

[112] Jiménez-Bailon, E., Santos-Lleo, M., Dahlem, M., et al. 2005, A&A, 442, 861.

[113] Junkes, N. & Zinnecker, H. & Hensler, Gerhard & Dahlem, M. & Pietsch, W., "NGC 1808: X-ray emission from the nuclear starburst". Astronomy and Astrophysics, 294, 8-22, (1995).

[114] Jungwiert, B., Combes, F., and Axon, D. J. 1997, A&AS, 125, 479.

[115] J. S. Kaastra, R. Mewe, D. A. Liedahl, S. Komossa and A. C. Brinkman, "X-ray absorption lines in the seyfert 1 galaxy ngc 5548 discovered with chandra-letgs", Astron. Astrophys. **354** (2000), L83, [arXiv:astro-ph/0002345 [astro-ph]].

[116] P.M.W. Kalberla, W.B. Burton, Dap Hartmann, E.M. Arnal, E. Bajaja, R. Morras, W.G.L. Poppel, "The Leiden/Argentine/Bonn (LAB) Survey of Galactic HI: Final data release of the combined LDS and IAR surveys with improved stray-radiation corrections", Astron.Astrophys.440:775-782,2005, doi:10.1051/0004-6361:20041864 .

[117] E. Kara, W. N. Alston, A. C. Fabian, E. M. Cackett, P. Uttley, C. S. Reynolds and A. Zoghbi, "A global look at X-ray time lags in Seyfert galaxies", Mon. Not. Roy. Astron. Soc. **462** (2016) no.1, 511-531 doi:10.1093/mnras/stw1695 [arXiv:1605.02631 [astro-ph.HE]].

[118] V. P. Kasliwal, M. S. Vogeley and G. T. Richards, "Extracting Information from AGN Variability", Mon. Not. Roy. Astron. Soc. **470** (2017) no.3, 3027-3048, doi:10.1093/mnras/stx1420, [arXiv:1607.04299 [astro-ph.GA]].

[119] K. I. Kellermann, R. Sramek, M. Schmidt, D. B. Shaffer and R. Green, "VLA observations of objects in the Palomar Bright Quasar Survey", Astron. J. **98** (1989), 1195-1207 doi:10.1086/115207

[120] Kellermann, K. I., Sramek, R., Schmidt, M., Shaffer, D. B., and Green, R. 1989, AJ, 98, 1195.

[121] Kondratko, P. T., Greenhill, L. J., Moran, J. M., et al. 2006, ApJ, 638, 100.

[122] Koribalski, B., Dahlem, M., Mebold, U., & Brinks, E. 1993, A&A, 268, 14.

[123] Kotilainen, J. K., Forbes, D. A., et al. 1996, A&A, 313, 771.

[124] I. V. Kotov, H. Neal, and P. O'Connor, "Pair creation energy and Fano factor of silicon measured at 185 K using55Fe x-rays, in High Energy, Optical, and Infrared Detectors for Astronomy VIII", Vol. 10709, edited byA. D. Holland and J. Beletic, International Society for Optics and Photonics(SPIE, 2018) pp. 362 – 372.

[125] Krolik, Julian H and Mitchell C Begelman, "Molecular tori in Seyfert galaxies-Feeding the monster and hiding it", The Astrophysical Journal 329, pp. 702–711, 1988.

[126] Lanzuisi, G., Civano, F., Elvis, M., et al. 2013, MNRAS, 431,978.

[127] G. Lanzuisi, R. Gilli, M. Cappi, M. Dadina, S. Bianchi, M. Brusa, G. Chartas, F. Civano, A. Comastri and A. Marinucci, *et al.* "NuSTAR Measurement of Coronal Temperature in Two Luminous, High-redshift Quasars", Astrophys. J. Lett. **875** (2019) no.2, L20 doi:10.3847/2041-8213/ab15dc [arXiv:1904.04784 [astro-ph.HE]].

[128] A. Laor, "What is the broad line region?, ASP Conf. Ser. **311** (2004), 169 [arXiv:astro-ph/0312415 [astro-ph]].

[129] Laustsen, S., Madsen, C., & West, R.M. 1987, "Exploring the Southern Sky". Springer (NY).

[130] Ledlow, Michael J and Frazer N Owen, "Optical Properties of Rich-Cluster Radio Galaxies", Energy Transport in Radio Galaxies and Quasars. Vol. 100, p. 359, 1996.

[131] Leroy et al. 2021, "PHANGS-ALMA Data Processing and Pipeline", arXiv:2104.07665 [astro-ph.IM].

[132] Liang E. P. T., 1979,ApJ,231, L111.

[133] Liu, J.F. and Bregman, J. N. 2005, ApJS, 157, 59.

[134] Malkan et al. "The ultraviolet excess of Seyfert 1 galaxies and quasars", The Astrophysical Journal 254, pp. 22–37, 1982.

[135] K. Mitsuda, H. Inoue, K. Koyama, K. Makishima, M. Matsuoka, Y. Ogawara, K. Suzuki, Y. Tanaka, N. Shibazaki and T. Hirano, "Energy spectra of low-mass binary X-ray sources observed from TENMA", Publ. Astron. Soc. Jap. **36** (1984), 741-759.

[136] K. O. Mason, A. A. Breeveld, R. Much, M. Carter, F. A. Cordova, M. S. Cropper, J. Fordham, H. Huckle, C. Ho and H. Kawakami, *et al.* "The XMM-Newton optical/UV monitor telescope", Astron. Astrophys. **365** (2001), L36-L44, doi:10.1051/0004-6361:20000044, [arXiv:astro-ph/0011216 [astro-ph]].

[137] Magdziarz, Pawełand Andrzej A Zdziarski, "Angle-dependent Compton reflection of X-rays and gamma-rays", Monthly Notices of the Royal Astronomical Society 273.3, pp. 837–848, 1995.

[138] Marchesi et al. (2018). "Compton-thick AGNs in the NuSTAR Era". The AstrophysicalJournal 854.1, p. 49.

[139] R. Mewe, E. H. B. M. Gronenschild and G. H. J. van den Oord, "Calculated X-radiation from optically thin plasmas. 5.", Astron. Astrophys. Suppl. Ser. **62** (1985), 197-254.

[140] C. Misner, Kip Thorne, John Archibald Wheeler, pp. 875–876 of Gravitation, San Francisco: W. H. Freeman. (1973).

[141] Miyamoto Y., Nakai N., Seta M., Salak D., Nagai M., Kaneko H., 2017, Publications of the Astronomical Society of Japan, 69, 83.

[142] Miyamoto Y., Seta M., Nakai N., Watanabe Y., Salak D., Ishii S., 2018, Publications of the Astronomical Society of Japan, 70, L1.

[143] R. Morrison and D. McCammon, "Interstellar photoelectric absorption cross-sections, 0.03-10 keV", Astrophys. J. **270** (1983), 119 doi:10.1086/161102

[144] Murphy & Yaqoob, "An X-ray spectral model for Compton-thick toroidal reprocessors", Monthly Notices of the Royal Astronomical Society 397.3, pp. 1549–1562, (2009).

[145] Narayan, Ramesh and Insu Yi, "Advection-dominated accretion: A self-similar solution", arXiv astro-ph/9403052, 1994.

[146] Narayanan, D., Krumholz, M. R., Ostriker, E. C., and Hernquist, L. 2012, MNRAS, 421, 3127.

[147] M. Nenkova, Z. Ivezic and M. Elitzur, "Dust emission from active galactic nuclei", Astrophys. J. Lett. **570** (2002), L9, doi:10.1086/340857, [arXiv:astro-ph/0202405 [astro-ph]].

[148] Netzer, Hagai, "The physics and evolution of active galactic nuclei", Cambridge University Press, 2013.

[149] H. Netzer, "Revisiting the Unified Model of Active Galactic Nuclei", Ann. Rev. Astron. Astrophys. **53** (2015), 365-408, doi:10.1146/annurev-astro-082214-122302, [arXiv:1505.00811 [astro-ph.GA]].

[150] I. Okamoto, "Electromagnetic extraction of energy from Kerr black holes", Publ. Astron. Soc. Jap. **58** (2006), 1047, doi:10.1093/pasj/58.6.1047, [arXiv:astro-ph/0506302 [astro-ph]].

[151] A. G. Pacholczyk and W. R. Stoeger, S.J., "Active galactic nuclei. 5. X-ray variability and the black hole cluster paradigm", Astrophys. J. **434** (1994), 435, doi:10.1086/174745.

[152] Padovani, P. et al., "Active galactic nuclei: what's in a name?", A&ARv25,2, p. 2., 2017, doi:10.1007/s00159-017-0102-9, arXiv:1707.07134.

[153] M. Pereira-Santaella, A. M. Diamond-Stanic, A. Alonso-Herrero and G. H. Rieke, "The Mid-Infrared High-Ionization Lines from Active Galactic Nuclei and Star-Forming Galaxies", Astrophys. J. **725** (2010), 2270-2280, doi:10.1088/0004-637X/725/2/2270, [arXiv:1010.5129 [astro-ph.CO]].

[154] G. C. Perola, G. Matt, M.Cappi, F.Fiore, M. Guainazzi, L. Maraschi, P. O. Petrucci, and L. Piro, "Compton reflection and iron fluorescence in BeppoSAX observations of Seyfert type 1 galaxies", A&A 389, 802-811 (2002), doi: 10.1051/0004-6361:20020658.

[155] P.O. Petrucci, A. Merloni, A. Fabian, F. Haardt, E. Gallo, "The effects of a Comptonizing corona on the appearance of the reflection components in accreting black hole spectra", Monthly Notices of the Royal Astronomical Society, Volume 328, Issue 2, December 2001, Pages 501–510,

[156] Phillips, A.C. 1993, AJ, 105, 486.

[157] E. Piconcelli and M. Guainazzi, "Xmm-newton discovery of soft x-ray absorption in the high-z superluminous blazar rbs 315", Astron. Astrophys. **442** (2005), L53, doi:10.1051/0004-6361:200500189, [arXiv:astro-ph/0509488 [astro-ph]].

[158] Pier, Edward A and Julian H Krolik, "Infrared spectra of obscuring dust tori around active galactic nuclei. II. Comparison with observations", The Astrophysical Journal 418, p. 673, 1993.

[159] M. A. Prieto, J. Reunanen, K. R. W. Tristram, N. Neumayer, J. A. Fernandez-Ontiveros, M. Orienti and K. Meisenheimer, "The spectral energy distribution of the central parsecs of the nearest AGN", Mon. Not. Roy. Astron. Soc. **402** (2010), 724, doi:10.1111/j.1365-2966.2009.15897.x, [arXiv:0910.3771 [astro-ph.CO]].

[160] S. I. Raimundo, A. C. Fabian, R. V. Vasudevan, P. Gandhi and J. Wu, "Can we measure the accretion efficiency of Active Galactic Nuclei?", Mon. Not. Roy. Astron. Soc. **419** (2012), 2529, doi:10.1111/j.1365-2966.2011.19904.x, [arXiv:1109.6225 [astro-ph.CO]].

[161] Ramesh Narayan, Insu Yi, "Advection-Dominated Accretion: Self-Similarity and Bipolar Outflows", Astrophysics (astro-ph), arXiv:astro-ph/9411058, doi:10.1086/175599.

[162] C. Ramos Almeida and C. Ricci, "Nuclear obscuration in active galactic nuclei", Nature Astronomy volume 1, pages 679-689 (2017).

[163] M. S. Rice, P. Martini, J. E. Greene, R. W. Pogge, J. C. Shields, J. S. Mulchaey and M. W. Regan, "Spatially-resolved narrow line region kinematics in active galactic nuclei", Astrophys. J. **636** (2006), 654-673, doi:10.1086/498091, [arXiv:astro-ph/0509568 [astro-ph]].

[164] G. Risaliti, R. Maiolino and M. Salvati, "The Distribution of absorbing column densities among seyfert 2 galaxies", Astrophys. J. **522** (1999), 157-164, doi:10.1086/307623, [arXiv:astro-ph/9902377 [astro-ph]].

[165] G. Risaliti and M. Elvis, "A Panchromatic view of AGN", Astrophys. Space Sci. Libr. **308** (2004), 187, doi:10.1007/978-1-4020-2471-9_6, [arXiv:astro-ph/0403618 [astro-ph]].

[166] C. S. Reynolds, "Accretion processes in AGN: The X-ray View", arXiv:astro-ph/0605368 (2005).

[167] I. Ruffa, C. Vignali, A. Mignano, R. Paladino, and K. Iwasawa, "The role of molecular gas in the nuclear regions of IRAS 00183-7111. ALMA and X-ray investigations of an ultraluminous infrared galaxy", Astronomy & Astrophysics manuscript no. 32268 (2018).

[168] Saikia, D.J., et al. 1990, MNRAS, 245, 397.

[169] Salak, D., Tomiyasu, Y., Nakai, N., et al. 2017, ApJ, 849, 90.

[170] Salak, D., Tomiyasu, Y., Nakai, N., et al. 2018, ApJ, 856, 97

[171] Schmidt and Maarten, "Space distribution and luminosity functions of quasars", The Astrophysical Journal 162, p. 371, 1970.

[172] Sérsic, J.R., & Pastoriza, M., 1965, PASP 77, 287.

[173] Seyfert, Carl K, "Nuclear Emission in Spiral Nebulae", The Astrophysical Journal 97, p. 28, 1943.

[174] N. I. Shakura and R. A. Sunyaev, "Black holes in binary systems. Observational appearance", Astron. Astrophys. **24** (1973), 337-355.

[175] M. Schmidt, "3C 273 : A Star-Like Object with Large Red-Shift", Nature **197** (1963) no.4872, 1040, doi:10.1038/1971040a0.

[176] A. Schruba, A. K. Leroy, F. Walter, F. Bigiel, E. Brinks, W. J. G. de Blok, G. Dumas, C. Kramer, E. Rosolowsky and K. Sandstrom, *et al.* "A Molecular Star Formation Law in the Atomic Gas Dominated Regime in Nearby Galaxies", Astron. J. **142** (2011), 37, doi:10.1088/0004-6256/142/2/37. [arXiv:1105.4605 [astro-ph.CO]].

[177] T. Shanks, B. Ansarinejad, R. M. Bielby, I. Heywood, N. Metcalfe, L. Wang "The nature of sub-millimetre galaxies I: A comparison of AGN and star-forming galaxy SED fits", arXiv:2010.07934 astro-ph.GA (2020).

[178] Shtykovskiy P. E., Gilfanov M. R., 2007, Astron. Lett., 33, 437.

[179] Silva L., Granato G.L., Bressan A. and Danese L., "Modeling the Effectsof Dust on Galactic Spectral Energy Distributions from the Ultraviolet to the Millimeter Band", ApJ, 509:103–117, 1998.

[180] Smith, A. G., "The Multiple Timescales of AGN Variability", in Astronomical Society of the Pacific Conference Series, Vol. 110, Blazar Continuum Variability, ed. H. R. Miller, J.R. Webb, & J. C.Noble, 3, 1996.

[181] Solomon, P. M. and Vanden Bout, P. A. 2005, ARA&A, 43, 677.

[182] H. C. Spruit, "Accretion disks". arXiv:1005.5279 [astro-ph.HE] [astro-ph.SR] (2010).

[183] Tacconi, L. J., Neri, R., Genzel, R., et al. 2013, ApJ, 768, 74.

[184] Telfer, Randal C et al., "The rest-frame extreme-ultraviolet spectral properties of quasi-stellar objects", The Astrophysical Journal 565.2, p. 773, 2002.

[185] Tombesi, Francesco et al., "Unification of X-ray winds in Seyfert galaxies: from ultra-fast outflows to warm absorbers". Monthly Notices of the Royal Astronomical Society 430.2, pp. 1102-1117, 2013.

[186] K. R. W. Tristram and M. Schartmann, "On the size-luminosity relation of AGN dust tori in the mid-infrared", Astron. Astrophys. **531** (2011), A99, doi:10.1051/0004-6361/201116867. [arXiv:1105.4875 [astro-ph.CO]].

[187] C. M. Urry and P. Padovani, "Unified schemes for radio-loud active galactic nuclei", Publ. Astron. Soc. Pac. **107** (1995), 803, doi:10.1086/133630, [arXiv:astro-ph/9506063 [astro-ph]].

[188] Yuichi Terashima and Andrew S. Wilson 2003. The American Astronomical Society. All rights reserved. Printed in U.S.A.The Astrophysical Journal, Volume 583.

[189] Vasudevan R. V., Fabian A. C., Gandhi P., Winter L. M., Mushotzky R. F., 2010, MNRAS, 402, 1081.

[190] D. E. Vanden Berk *et al.* [SDSS], "Composite quasar spectra from the Sloan Digital Sky Survey", Astron. J. **122** (2001), 549-564, doi:10.1086/321167, [arXiv:astro-ph/0105231 [astro-ph]].

[191] S. Veilleux & D. Osterbrock, "Spectral classification of emission-line galaxies", The Astrophysical Journal Supplement Series, 63:295-310, 1987.

[192] Veron-Cetty M.-P., Veron P., 1986, A&AS, 66, 335.

[193] C. Vignali, "Obscured accretion from AGN surveys", IAU Symp. **304** (2014), 132-138, doi:10.1017/S1743921314003548, [arXiv:1401.5061 [astro-ph.GA]].

[194] Vito, F. et al., "The hard X-ray luminosity function of high-redshift (3 < z . 5) active galactic nuclei", MNRAS 445, pp. 3557–3574, 2014, doi: 10.1093/mnras/stu2004, arXiv: 1409.6918.

[195] Weedman, Daniel W, "Seyfert galaxies", Annual review of astronomy and astrophysics 15.1, pp. 69-95, 1977.

[196] M. C. Weisskopf, B. Brinkman, C. Canizares, G. Garmire, S. Murray and L. P. Van Speybroeck, "An overview of the performance and scientific results from the Chandra X-ray Observatory (CXO)", Publ. Astron. Soc. Pac. **114** (2002), 1-24, doi:10.1086/338108, [arXiv:astro-ph/0110308 [astro-ph]].

[197] J. Wilms, A. Allen and R. McCray, "On the Absorption of X-rays in the interstellar medium", Astrophys. J. **542** (2000), 914-924, doi:10.1086/317016, [arXiv:astro-ph/0008425 [astro-ph]].

[198] J. H. Woo and C. M. Urry, "AGN black hole masses and bolometric luminosities", Astrophys. J. **579** (2002), 530-544, doi:10.1086/342878, [arXiv:astro-ph/0207249 [astro-ph]].

[199] Yaqoob (2012), "The nature of the Compton-thick X-ray reprocessor in NGC 4945", Monthly Notices of the Royal Astronomical Society 423.4, pp. 3360-3396.

[200] Yaqoob et al. (2015), "A Compton-thin solution for the Suzaku X-ray spectrum of the Seyfert 2 galaxy Mkn 3", Monthly Notices of the Royal Astronomical Society 454.1, pp. 973-990.

[201] - Zhao et al. (2019(a)). "COMPTON-THICK AGN IN THE NuSTAR ERA II: A DEEP NuSTAR AND XMM-Newton VIEW OF THE CANDIDATE COMPTON THICK AGN IN NGC 1358". ApJ, 870, 60.
- Zhao et al. (2019(b)). "COMPTON-THICK AGN IN THE NuSTAR ERA IV: A DEEP NuSTAR AND XMM-Newton VIEW OF THE CANDIDATE COMPTON THICK AGN IN ESO 116-G018". ApJ, 871, 182.

Acknowledgements

I apologize but I need to write my personal acknowledgements in my mother tongue.
In primo luogo vorrei ringraziare il Prof. Cristian Vignali per essere stato sempre reperibile (anche ad orari improponibili), per essere stato il primo ad aver creduto in questo lavoro, per la sua passione e dedizione che sono per me di ispirazione, per il suo sostegno e contributo fondamentali per la riuscita del lavoro. Un grazie speciale al Dott. Mauro Dadina ed alla Dott.ssa Viviana Casasola, per tutto quello che mi avete insegnato, per avermi supportato, sopportato ed accompagnato in questo lungo periodo di tesi.
Ringrazio la mia famiglia che ha sempre condiviso con me gioie ed dolori, per avermi sempre dato la libertà di scelta, per avermi sempre incoraggiata, appoggiata e sostenuta nelle mie decisioni, per i sacrifici fatti che mi hanno permesso di realizzare questo piccolo grande sogno. Grazie per avermi fatto diventare quella che sono, per avermi dato la forza anche quando mi mancava, e per avermi fatto sempre e comunque sentire immensamente amata.
Ringrazio tutti i miei amici e le mie amiche che hanno condiviso con me questi lunghi anni, che mi hanno sopportato (più che supportato) nei miei sfoghi e nelle mie pazzie. Siete stati e siete tutti veramente preziosi.
Ringrazio me stessa per non aver mollato, per essere caduta ed aver trovato la forza di rialzarmi, per la mia determinazione, dedizione, passione e combattività che alla fine sono state più forti delle mie paure, delle mie debolezze e delle mie ansie.
Ringrazio il mio compagno di vita Carlo senza il quale non sarei arrivata qui oggi. Grazie per avermi accompagnata, passo dopo passo, a questo traguardo, per aver sopportato come nessun'altro il mio stress, i miei nervosismi e le mie pazzie di questo lungo periodo universitario. Ma soprattutto grazie perché assieme a te la vita è più bella.

A Te e per Te, che manchi come l'aria...